Spring 1-1-2012

Gravity Waves and their Effects on the Mean State and Variability of Mars' Atmosphere

John E. Creasey

University of Colorado at Boulder, jcreasey@wildblue.net

Recommended Citation

Creasey, John E., "Gravity Waves and their Effects on the Mean State and Variability of Mars' Atmosphere" (2012). *Aerospace Engineering Sciences Graduate Theses & Dissertations*. 41.
https://scholar.colorado.edu/asen_gradetds/41

Gravity Waves and their Effects on the Mean State and Variability

of Mars' Atmosphere

by

John E. Creasey

B.S., University of Virginia, 1991

M.S.E.E., Villanova University, 1997

M.S., University of Colorado at Boulder, 2003

A thesis submitted to the

Faculty of the Graduate School of the

University of Colorado in partial fulfillment

of the requirements for the degree of

Doctor of Philosophy

Department of Aerospace Engineering Sciences

2012

This thesis entitled:
Gravity Waves and their Effects on the Mean State and Variability of Mars' Atmosphere
written by John. E Creasey
has been approved for the Department of Aerospace Engineering Sciences

_____

Jeffrey M. Forbes

_____

Jeffrey P. Thayer

Date _____

The final copy of this thesis has been examined by the signatories, and we find that
both the content and the form meet acceptable presentation standards of scholarly
work in the above mentioned discipline.

Creasey, John E. (Ph. D., Aerospace Engineering Sciences)

Gravity Waves and their Effects on the Mean State and Variability of Mars' Atmosphere

Thesis directed by Prof. Jeffrey M. Forbes

Data from the Mars Global Surveyor (MGS) spacecraft has revealed the presence of gravity waves in Mars' lower atmosphere and thermosphere. From perturbations in radio occultation temperature profiles of the lower atmosphere, global distributions of gravity wave potential energy density were calculated. The potential energy density distributions served as the basis to compute gravity wave source momentum flux used in a Mars dynamical model, marking the first time that a numerical study of Mars' gravity waves was observationally constrained. The gravity wave source spectrum is believed to include a stationary component from topographic forcing and a non-stationary component from atmospheric tides with large zonal wavenumbers. The model used was a Mars-specific version of the Hybrid Lindzen-Matsuno gravity wave parameterization that was created and integrated into the time-dependent, two-dimensional QNLM model for Mars. Due to the non-stationary waves in the gravity wave spectrum, the effect on predicted zonal wind and temperature fields was profound, particularly in the upper atmosphere above 100 km altitude where Mars' atmosphere is poorly observed. At solstice, the middle atmosphere zonal jets were closed near 80 km, and upper atmosphere zonal winds were significantly diminished from 120-140 m s^{-1} to near zero. Meridional circulation increased to over 50 m s^{-1} at altitudes where gravity wave breaking occurred, and adiabatic heating above the winter pole was enhanced. The model results were particularly sensitive to the prescribed phase speed distribution, and multiple phase speed spectra were evaluated to assess sensitivity. The effects of the non-stationary tidal components in the gravity wave spectrum indicate that Mars' GCMs may be underestimating their contribution to middle and upper atmosphere forcing, but open questions remain with respect to the phase speed distribution of non-stationary components and the relative contribution to momentum flux of stationary and non-stationary waves. Direct measurements of wind speed are needed to better constrain the gravity wave spectrum and validate predicted results.

Dedication

To my children, Eleanor and William.

May you never stop learning, growing, and exploring.

Acknowledgements

I would like to acknowledge the support and guidance of my committee: Jeff Forbes, Brian Argrow, Scott Palo, Scot Rafkin, and Jeff Thayer. To my advisor, Jeff Forbes, I am forever grateful for the support, motivation, and patience throughout this journey. As a full-time worker and full-time dad, I do not think it would have been possible for me to complete this dissertation with any other advisor. Your positive words of encouragement kept me going when the tunnel seemed very dark.

Most importantly, I would like to thank my wife Nicola and children Ellie and Will for the love, sacrifice, and support over the many years that "daddy is working on his Ph. D". Thank you for letting me pursue this dream. I look forward to the extra time we can spend together.

Contents

Tables

Table

Figures

Figure

Chapter 1

Introduction

Studies of small-scale disturbances in Earth's atmosphere date back to the first observations of traveling ionospheric disturbances (TIDs) and meteor trails [*Munro*, 1948; *Munro*, 1950; *Beynon*, 1948]. *Hines* [1960] interpreted these observed motions as internal atmospheric gravity waves and provided the theoretical foundation for gravity waves and their effects on the middle atmosphere. Gravity waves are now known to be an essential contributor to the dynamics of Earth's atmosphere on all meteorological scales. To satisfy heat and momentum budgets and obtain a realistic simulation of the middle atmosphere wind and temperature structure, gravity wave effects must be included in dynamical models. Because the horizontal scales of gravity waves are too small to be resolved within large-scale dynamical models, their effects on the general circulation are typically parameterized, with model inputs constrained by observations.

On Earth, a variety of ground-based and spaced-based observational techniques have been used to detect and quantify gravity waves. These techniques include radiosondes, infrared and microwave limb sounders, long-duration balloon flights, lidar, and radar - each of which is sensitive to gravity wave energy over a portion of the gravity wave spectrum. Often these measurements can be combined with other data to provide a more detailed picture of the atmospheric conditions at the time the gravity wave was observed. These observational studies are important not only to constrain the inputs used in modeling studies, but also to validate the results of theoretical studies and very-high-resolution models [*Alexander et al.*, 2010].

Gravity waves are a ubiquitous feature of planetary atmospheres, not just Earth's. Gravity waves have been detected in the atmospheres of Mars [*Seiff and Kirk*, 1977; *Hinson et al.*, 1999; *Creasey et al.*, 2006a, 2006b], Venus [*Young et al.*, 1987; *Hinson and Jenkins*, 1995; *Peralta et al.*, 2008], Titan [*Hinson and Tyler*, 1983], and Jupiter [*Young et el.*, 1997]. For Earth, it is well established that gravity waves affect the thermal structure and mean circulation of the middle and upper atmosphere by transporting momentum and energy upward from the source regions in the troposphere. Because gravity waves in the atmosphere grow exponentially with height, small-amplitude disturbances near the surface can have a profound effect at heights where dissipation occurs, as momentum and heat are deposited into the mean flow. Similar effects are anticipated for Mars.

The response of Mars' atmosphere to gravity wave forcing is not nearly as well established as for Earth. *Barnes* [1990] and *Théodore et al.* [1993] used simplified dynamical models to show that breaking gravity waves could produce enough force on the mean zonal flow to close off the winter westerly jet and generate significant adiabatic warming at winter high-latitudes. Numerical simulations with general circulation models (GCM) of the Mars' atmosphere, however, have produced mixed results. Where *Joshi et al.* [1995] found that gravity wave drag dominates the momentum balance of the middle atmosphere, *Forget et al.* [1999] found gravity wave drag to be poorly constrained above 40 km altitude, and *Angelats i Coll et al.* [2005], using an improved version of the *Forget et al.* [1999] GCM, found that gravity waves decelerate the zonal winds but do not strongly affect the structure of the zonal mean wind and temperature fields. These modeling efforts suffered from (1) a lack of observations to validate the predicted wind and temperature fields, (2) no observational constraints on the gravity wave forcing, and (3) a gravity wave source spectrum limited to consider only orographically generated waves.

Using data from the Mars Global Surveyor (MGS) spacecraft to constrain gravity wave forcing in a dynamical model of Mars, this thesis addresses the last two of these shortcomings. Occultation measurements from the MGS Radio Science (RS) experiment provide a set of globally distributed temperature profiles of Mars' lower atmosphere that reveal the vertical wave structures of atmospheric gravity waves [*Creasey et al.*, 2006a]. Modeling work by *Miyoshi et al.* [2011] has since identified the

small-scale waves observed in the MGS RS dataset to be a combination of both gravity waves and high wavenumber tidal components. Because the propagation, energy transport, and dissipation of tides and gravity waves are treated the same [*Lindzen*, 1981], the term gravity wave is used in this study to identify small-scale buoyancy waves of all sources. When applicable, this study differentiates the small-scale waves as tidal and non-tidal gravity waves. With help from the linear theory of gravity waves, wave energy density and momentum flux can be calculated from the temperature observations to provide a global distribution of gravity wave energy in the lower atmosphere. As an input to a time-dependent, two-dimensional model of Mars atmosphere, the observed gravity wave distribution serves as the basis for investigating how gravity waves affect the mean structure and variability of Mars' atmosphere. This study marks the first Mars' modeling study constrained by observations of gravity wave forcing.

1.1   Background

1.1.1   Atmospheric Gravity Waves

In a stably stratified fluid, density increases with depth, or in the case of the atmosphere, decreases with height. An important characteristic of a stably stratified fluid is the ability to support and propagate wave motions. Gravity waves, generated when a fluid parcel displaced vertically undergoes buoyancy oscillations, are one such motion. In the atmosphere, lee waves and atmospheric tides are others. Gravity waves are also referred to as buoyancy waves since buoyancy is the restoring force in the wave motion. In terms of scale, horizontal wavelengths of atmospheric gravity waves are on the order of tens of kilometers to a few thousand kilometers, orders of magnitude smaller than Earth's large-scale diurnal and semidiurnal tides. Atmospheric tides with larger zonal wavenumbers have horizontal scales on the same order as gravity waves and can be observationally inseparable from gravity waves forced by typical sources such as wind flow over topography.

Although the gravity wave field is comprised of a spectrum of waves of varying magnitude, frequency, and direction, gravity waves are best explained with the monochromatic wave solution to the linearized forms of the fundamental equations of conservation of momentum, mass, and energy [e.g.

Fritts and Alexander, 2003; *Nappo*, 2002]. One key result of the solution is the dispersion relation, which relates the wave frequency to the horizontal and vertical wavenumbers:

$$\hat{\omega}^2 = \frac{N^2(k^2 + l^2) + f^2\left(m^2 + \frac{1}{4H^2}\right)}{k^2 + l^2 + m^2 + \frac{1}{4H^2}}.$$ (1.1)

Here $\hat{\omega} = \omega - k\bar{u} - l\bar{v}$ is the wave intrinsic frequency, the frequency that would be observed in a reference frame moving with the background flow $(\bar{u}, \bar{v})$; k, l, and m are the zonal, meridional, and vertical wavenumbers respectively; $N = (g\,\partial\ln\theta/\partial z)^{1/2}$ is the Brunt-Väisälä frequency, or buoyancy frequency, where θ is potential temperature; $f = 2\Omega\sin\phi$ is the Coriolis parameter, where Ω is the planet's rotation rate and ϕ is latitude; and H is the atmospheric scale height.

Another important quantity is wave group velocity. Group velocity transports wave energy through space. Following a disturbance, it is the energy transport that creates the wave; the wave does not create the energy transport. Group velocity is defined as

$$\left(c_{gx}, c_{gy}, c_{gz}\right) = \left(\frac{\partial\omega}{\partial k}, \frac{\partial\omega}{\partial l}, \frac{\partial\omega}{\partial m}\right).$$ (1.2)

For vertical transport, this becomes

$$c_{gz} = \frac{-m(\hat{\omega}^2 - f^2)}{\hat{\omega}\left(k^2 + l^2 + m^2 + \frac{1}{4H^2}\right)}.$$ (1.3)

Vertical group velocity is defined as positive for upward energy propagation.

From the dispersion relation and the group velocity equations, some important properties of gravity waves can be inferred. For $m^2 \gg 1/4H^2$, the dispersion relation simplifies and rearranges to

$$m^2 \approx \frac{k^2(N^2 - \hat{\omega}^2)}{\hat{\omega}^2 - f^2}.$$ (1.4)

For vertically propagating waves, (k, l, m) are real, and correspondingly, the squares of the wavenumbers must be positive. With $m^2 > 0$ and intrinsic frequency assumed to be positive definite, equation (1.4) defines the range of permissible intrinsic frequencies of vertically propagating gravity waves: $|f| < |\hat{\omega}| < N$. Looking now at the group velocity equation, m must be negative for upward energy

4

www.manaraa.com

propagation. In other words, for a gravity wave transporting energy from a source region near the surface upward in the atmosphere, wave phase propagation is downward. In this thesis, upward wave propagation refers to upward energy transport.

The gravity wave's vertical flux of horizontal momentum, referred to hereafter as momentum flux, is given by

$$(F_x, F_y) = \rho\left(\overline{u'w'}, \overline{v'w'}\right) , \tag{1.5}$$

where ρ is atmospheric density, primed quantities are perturbations to the background state, and overbars represent time-averaging over a wavelength or wave period. Following the non-interaction theorem of *Eliassen and Palm* [1961], gravity waves conserve momentum if they propagate without dissipation through a background atmosphere that varies only in the vertical direction. Thus, as a gravity wave propagates upward, wave amplitude grows exponentially as density decreases.

The vertical propagation of the gravity wave depends on the wave's characteristics, the background wind, and the buoyancy characteristics of the atmosphere. If a wave encounters a critical level where the phase speed of the wave approaches the speed of the background wind, the wave will be absorbed by the background flow and not propagate further. This critical-level filtering allows some waves to continue to grow and transport energy and momentum higher into the atmosphere, while restricting others. A wave will also be subjected to dissipation processes, such as turbulent diffusion, molecular diffusion, radiative cooling, and ion friction. At large wave amplitudes, the turbulent breakdown of convectively unstable regions leads to wave saturation. This wave saturation and associated turbulent diffusion is referred to as gravity wave breaking and is responsible for the most important gravity wave effects in the middle atmosphere [*Lindzen*, 1981; *Fritts*, 1984]. Unlike gravity wave breakdown, molecular diffusion, radiative cooling, and ion friction act independently of wave amplitude. On Earth, molecular diffusion is a significant dissipation mechanism for gravity waves that reach the upper mesosphere and thermosphere.

If momentum flux remains constant with height (i.e. if there is no dissipation), the wave does not exert a force on the mean state. If a wave is being dissipated, however, the divergence of momentum flux results in a nonzero force on the mean state given by, in the zonal direction,

$$f_x = -\frac{1}{\rho}\frac{\partial F_x}{\partial z} \, , \qquad (1.6)$$

where f_x is the acceleration imparted to the mean flow. This quantity is sometimes referred to as gravity wave drag. The dissipation of the wave is the mechanism for gravity waves to deposit horizontal momentum from near the surface into the middle and upper atmosphere. The direction of the forcing depends on the intrinsic phase speed of the wave, $c_i = c - \bar{u}$, with the acceleration of the flow towards the phase speed of the gravity wave. For a zonally propagating gravity wave, a dissipating wave with positive (negative) intrinsic phase speed exerts a net eastward (westward) force on the background flow.

1.1.2   Gravity Waves in Earth's Atmosphere

In Earth's atmosphere, gravity waves are primarily excited by wind flow over topography, convective activity, and wind shear instabilities. Other sources likely to be important are frontal processes, localized body forcing, and wave-wave interactions [*Fritts and Alexander*, 2003]. The most commonly recognized source is wind flow over topography, with gravity waves resulting from the vertical displacement of the atmosphere as it moves over land barriers such as the Rocky Mountains or the Andes Mountains. This orographic forcing produces stationary gravity waves, or mountain waves, with near-zero phase speeds. However, if Doppler shifted by the background wind, these waves may have non-zero intrinsic frequencies and be able to propagate upstream or downstream relative to the mean flow, allowing for the transport of momentum and energy horizontally away from the source. Convective activity produces gravity waves through time-varying thermal forcing associated with the release of latent heat. In the tropics, far from topography and regions of shear instabilities, gravity wave energy in the stratosphere has been correlated with satellite-based estimates of deep convective activity [*Forbes*, 1996]. Unlike orographically-generated waves, convection can generate gravity waves across the full range of phase speeds, wave frequencies, and horizontal and vertical wavelengths. Gravity waves can also be

6

generated when an instability develops in a stratified flow. The necessary condition for dynamical instability is given by the Richardson number, $Ri = N^2/(\partial u/\partial z)^2 < 1/4$. The Richardson number represents the ratio of the production of turbulence by buoyancy, the restoring force, to the production of turbulence by velocity shear. For gravity waves generated by wind shear instability, Howard's semi-circle theorem tells us the phase speed of the wave must lie between the minimum and maximum wind speed [*Howard*, 1961].

Gravity waves play a significant role in the mean circulation and temperature structure of Earth's atmosphere. Gravity waves transport momentum and energy from the source region in the lower atmosphere to the mesosphere and lower thermosphere, generate turbulence and mixing at these heights as waves become unstable, and deposit momentum to influence the large-scale wind and temperature fields. The effects of gravity waves in the mesosphere have been established in a series of studies by *Lindzen* [1981], *Holton* [1982], *Holton* [1983], and *Garcia and Solomon* [1985]. These studies built upon earlier works which recognized the need for dynamical processes to account for features in the observed wind and temperature fields, notably the reversal of the meridional temperature gradient, departure of the atmosphere from radiative equilibrium, and the closure of the mid-latitude jets [*Hines*, 1963; *Leovy*, 1964]. The conclusion was that a strong zonal drag force was required to satisfy both the heat and momentum budgets of the mesosphere.

Gravity waves that break and deposit momentum in the mesosphere apply a forcing to the zonal mean flow that, at solstice, reverses the direction of the zonal mean jets, which are established via radiative balances in the lower and middle atmosphere. The breaking gravity waves exert a net westward (eastward) force on the eastward (westward) jet in the winter (summer) hemisphere. The force in general opposes the background winds. The zonal forcing, combined with the Coriolis force, drives a meridional circulation with strong upwelling (downwelling) and adiabatic cooling (subsidence heating) in the summer (winter) hemisphere, driving the mesopause region far from radiative equilibrium. The meridional temperature gradient is reversed in the mesosphere and lower thermosphere such that the warmest (coolest) temperatures are found near the winter (summer) pole. The mean meridional

7

circulation is also important for the transport of constituents, such as ozone and ozone-destroying chemicals, in the upper atmosphere.

Although the effects of gravity waves are most significant in the mesosphere, gravity waves also play a role in the stratosphere and influence the structure and variability of tidal and planetary waves. In the stratosphere, gravity wave amplitudes are smaller than those that reach the mesosphere, as amplitudes may not have grown sufficiently large for turbulent breakdown. Gravity wave effects in the stratosphere are secondary, with the majority of the wave-driven circulation effects coming from planetary-scale waves. From *Alexander et al.* [2010], gravity wave forcing in the tropics helps drive the quasibiennial oscillation (QBO) in zonal winds, may contribute to the semiannual oscillation (SAO) of zonal winds, and can influence the formation and ice content of cirrus clouds. In extratropical regions, gravity wave forcing dominates the equator-to-pole meridional transport circulation (Brewer-Dobson circulation) at spring-summer transitions [*Alexander and Rosenlof*, 2003], helps the transition from winter westerlies to summer easterlies [*Scaife et al.*, 2002], and provides additional warming above the winter pole [*Garcia and Boville*, 1994].

Gravity waves interact with large-scale tidal and planetary waves, leading to variability of planetary-scale motions. Gravity waves can influence the amplitudes of tidal waves [*Miyahara and Forbes*, 1991], with seasonal variations in tidal amplitudes correlated to mean wind filtering of gravity waves [*Meyer*, 1999a; *Mayr et al.*, 1998]. Other studies have suggested that gravity wave breaking in the mesosphere enhances planetary wave excitation [*McLandress and Ward*, 1994] and that filtering of gravity waves by mesospheric planetary waves enables the penetration of the quasi 2-day and quasi 16-day waves into the thermosphere [*Meyer*, 1999b].

1.1.3 Mars Global Surveyor (MGS) Mission

Mars Global Surveyor (MGS) was launched on November 7, 1996 and arrived at Mars on September 11, 1997. After an extended aerobraking period, MGS achieved near-circular, sun-synchronous orbit in March 1999 to start its mapping mission. The mapping orbit had an average altitude of 378 km, crossing the equator ascending (descending) at 1400 (0200) local time. MGS's scientific

8

mission continued until November 2, 2006 when a battery failure, caused by an error in a data update to the spacecraft's on-board software, led to the loss of the spacecraft.

From *Albee et al*. [2001], the formal science objectives of MGS were to (1) characterize surface morphology at high spatial resolution to quantify surface characteristics and geological processes, (2) determine the composition and map the distribution of surface minerals, rocks, and ices and measure surface thermophysical properties, (3) determine globally the topography, geodetic figure, and gravitational field, (4) establish the nature of the magnetic field and map the crustal remnant field, (5) monitor global weather and thermal structure of the atmosphere, and (6) study surface-atmosphere interaction by monitoring surface features, polar caps, polar thermal balance, atmospheric dust, and condensate clouds over a seasonal cycle. To meet these objectives, the MGS spacecraft, shown in Figure 1.1, carried a scientific payload consisting of the Mars Orbiter Camera (MOC), Mars Orbiter Laser Altimeter (MOLA), Thermal Emission Spectrometer (TES), Magnetometer / Electron Reflectometer package, and the Ultrastable Oscillator (USO) for Radio Science (RS) experiments [*Albee et al*., 2001]. The payload was designed to explore Mars for a full Martian year, approximately two Earth years, with a complementary set of observations of the atmosphere, surface, and interior.

MOC's imaging system [*Malin et al*., 1992; *Malin et al*., 2001] consisted of a narrow-angle camera for high spatial resolution images of the surface, resolving objects as small as 0.5 meters across, and two wide-angle cameras for lower spatial resolution images of the surface and atmosphere, similar to weather photographs of Earth. MOLA [*Zuber at al*., 1992; *Smith et al.*, 2001a] measured the round-trip time of flight of a laser pulse from the spacecraft to the surface, which when combined with accurate spacecraft position and velocity, created a highly accurate global topographic map of Mars with vertical accuracy within about 30 centimeters. TES [*Christensen et al*., 1992; *Christensen et al*., 2001] used thermal infrared spectroscopy to study the atmosphere, including the thermal structure of the atmosphere and composition and distribution of atmospheric dust, and map the mineral composition of the surface. MAG/ER [*Acuña et al*., 1998; *Mitchell*, 2001] contained two vector magnetometers to measure the magnetic field in the vicinity of the MGS spacecraft, which quickly established that Mars does not now

9
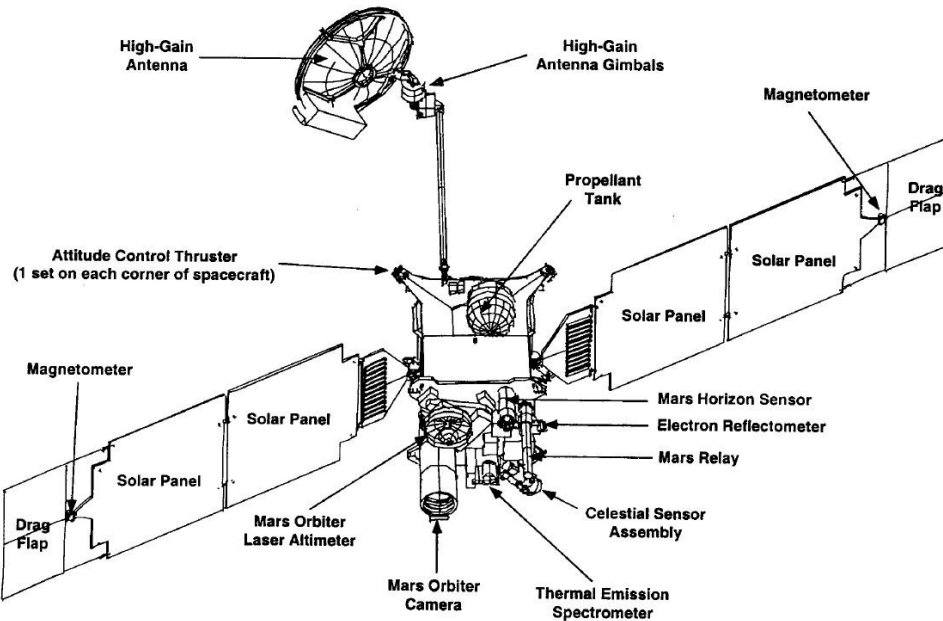
Figure 1.1: Mars Global Surveyor (MGS) spacecraft.

have a global magnetic field like Earth, and an electron reflectometer to characterize surface magnetic features. The USO, combined with the tracking stations of the Deep Space Network (DSN), enabled detection of small Doppler shifts in the radio communication with the spacecraft during occultation by the atmosphere [*Tyler et al.*, 1992; *Hinson et al.*, 1999]. From the occultation measurements were derived electron density profiles of the ionosphere and temperature-pressure profiles of the lower atmosphere. In addition to the instruments above, the MGS accelerometer (ACC) was used as a scientific instrument during the aerobraking phases of the mission to provide density observations of the upper atmosphere.

Two datasets from MGS were utilized in this thesis in the investigation of atmospheric gravity waves: ACC density measurements of Mars' thermosphere and RS temperature profiles of the lower atmosphere. Examination of small-scale density perturbations inferred from the ACC data revealed wave-like structures consistent with gravity waves at thermospheric heights [*Creasey et al.*, 2006b], while perturbations in the temperature profiles from the RS experiment provided a global distribution of gravity wave activity in the lower atmosphere from the surface to roughly 35 km altitude [*Creasey et al.*, 2006a]. The vertical resolution of the RS profiles was sufficient to delineate gravity waves with vertical

wavelengths between 2.5 and 25 km. Details on the RS and ACC datasets and their applications to the gravity wave investigation are discussed in Chapters 2 and 3 respectively.

1.2 Motivation

With the influx of atmospheric measurements from recent Mars missions, there exists a significant opportunity to make a major advance in our understanding of gravity waves in Mars' atmosphere and their role in influencing the zonal mean state of the atmosphere. This opportunity was the motivation behind this work. This research, for the first time, used observational data to (a) quantify the gravity wave energy emanating from the lower atmosphere of Mars, (b) characterize the small-scale density variations in the thermosphere in the context of gravity waves, and (c) provide constraints on gravity wave forcing in a dynamical model of Mars' atmosphere. Overall, this research will lead to a better fundamental understanding of Mars' atmosphere in terms of the conversion and transport of energy and momentum by small-scale waves and in terms of the effects of small-scale waves on the global circulation. To examine the effects of gravity waves, this research developed a gravity wave parameterization consistent with the sources and characteristics of the gravity waves observed and incorporated this parameterization into a time-dependent, two-dimensional dynamical model of Mars' atmosphere. By clarifying the role of gravity waves in Mars' upper atmosphere, the modeling work will be of value to comprehensive GCMs that attempt to specify and predict atmospheric densities for various mission operations purposes such as aerobraking, aerocapture, and entry, descent, and landing (EDL). It should be noted that the observational data cannot fully quantify all components of the gravity wave spectra, such as phase speed, wave frequency, and horizontal wavelength. Those components that cannot be specified or inferred from the data were either estimated using linear gravity wave theory or evaluated using sensitivity studies. Similarly, because the background wind field is not known, background wind distributions for different Mars seasons have been used to test the gravity wave parameterization. Similar to the integrated observational and numerical studies for Earth, it is anticipated that future missions to Mars will measure the atmosphere wind field such that better constraints can be placed on gravity wave parameterizations. In addition to measurements of wind speed, this thesis identifies other data needed

from future Mars missions, such as measurements of additional gravity wave characteristics, to improve upon the gravity wave characterization and parameterization started here.

1.3   Research Objectives

Given the global scale of gravity wave observations now available, the research objectives were as follows.

1. Characterize the structure and distribution of gravity waves in Mars' lower and upper atmosphere.

2. Establish the effects of gravity waves on the mean circulation, temperature, and density structure of the middle and upper atmosphere of Mars consistent with the gravity wave fluxes observed in the lower atmosphere.

To meet the objectives, the following science questions were addressed.

1. What are the characteristics of the wave structures observed in MGS radio occultation vertical temperature profiles?

2. How do gravity wave energy densities observed in the lower atmosphere vary with latitude, longitude, season, and local time of day?

3. Do the distributions of observed gravity wave energy densities provide insight on how gravity waves are generated at Mars?

4. How do density perturbations observed in the thermosphere vary with latitude, longitude, season, and local time of day?

5. Do the characteristics of waves seen in the thermosphere differ from those of gravity waves observed in the lower atmosphere?

6. What are the effects of gravity waves on zonal mean wind and temperature variations in the middle and upper atmosphere of Mars?

7. How high in Mars' atmosphere do the effects of gravity waves extend?

8. What are the dependencies of the mean circulation and structure to various characteristics of the source spectrum (i.e. phase speed distribution)?

1.4   Outline of Thesis

The remainder of this thesis is organized as follows. Chapter 2 discusses the MGS RS dataset and the derivation of global distributions of gravity wave energy from RS temperature profiles. Chapter 3 discusses the MGS ACC dataset and provides an analysis of gravity wave structures observed in thermospheric density profiles. Chapter 4 describes the gravity wave parameterization developed in this research, the QLM model used to assess the effects of gravity waves on the mean structure and circulation of the atmosphere, and the derivations of model inputs from observed gravity wave energy distributions. Chapter 5 analyzes the results of the model runs and discusses the effect of gravity waves on Mars' atmosphere. Chapter 6 concludes the thesis by summarizing the results and discussing potential follow-on research.

Chapter 2

Mars Global Surveyor (MGS) Radio Science (RS) Data Analysis

A radio occultation (RO) experiment measures the perturbations in Doppler frequency produced by refractive bending in an atmosphere between a transmitter and receiver. The resulting profile of refractivity versus radius can be reduced to profiles of atmospheric number density, pressure, and temperature, making radio occultation a powerful technique for remotely investigating a planet's atmosphere. The basic requirements for a radio occultation system are a transmitter with sufficient frequency stability and a receiver with sufficient sensitivity to measure the small Doppler shifts in the received signal. Also required are precise knowledge of the locations of the transmitter and receiver, knowledge of the structure and composition of the occulting atmosphere, and a mission design that permits a limb sounding geometry.

The radio occultation technique has been used to study the atmospheres of all planets in the solar system, with the exceptions of Mercury and Pluto, and the atmospheres of the moons Titan, Io, and Triton. The method has also been applied to cometary atmospheres and planetary rings. The first major success of the radio occultation method was with Mariner-4, which determined the surface pressure of Mars to be approximately 4 mbar and almost entirely carbon dioxide [*Kliore et al*., 1965]; previous consensus was a surface pressure on the order of 100 mbar, with oxygen believed likely to be a major constituent. Since that time, radio science experiments have been a part of nearly all planetary missions. For missions to the outer planets, such as the Voyager missions and Pioneer missions, the occultation was often a one-time opportunity based on the geometry of the flyby. Much of our early knowledge of the structure of the ionospheres and neutral atmospheres of the outer planets was based on the radio science

14

www.manaraa.com

data collected in these experiments. For an orbiting spacecraft carrying a radio occultation experiment, the missions provided frequent occultation measurements over many years. A properly designed and supported radio science campaign for an orbiter mission can generate thousands of individual temperature and pressure profiles, providing global coverage and capturing seasonal variations in the atmosphere. The vertical profiles of temperature, pressure, and number density provide direct measurements of the state of the atmosphere and contribute to our understanding of the atmosphere's structure and circulation. In addition, if there is sufficient vertical resolution in the collected profiles, the measurements also support the investigation of gravity waves. Such is the case with the MGS RS experiment.

MGS was not the first spacecraft mission to provide radio occultation measurements of Mars' atmosphere. The radio occultation measurement from the Mariner-4 flyby provided a much more accurate estimate of Mars surface pressure and temperature [*Kliore et al*., 1965], which significantly changed our understanding of the composition and structure of Mars' atmosphere. Additional occultation measurements were taken during the Mariner 1969 flyby mission with the Mariner 6 and 7 spacecraft, providing data on the structure of the dayside ionosphere [*Fjeldbo et al*., 1970] and additional surface pressure and temperature data points [*Kliore et al*., 1972]. Mariner 9, the first orbiter mission to Mars, took over 200 occultation measurements during its primary and extended mission, including extensive data in the north and south polar regions, where temperatures indicated the polar caps may at least in part consist of water ice [*Kliore et al*., 1973]. Mariner 9 surface pressure data suggested the shape of Mars was more oblate than believed and indicated a pronounced north-south asymmetry in planetary radii [*Kliore et al., 1972*; *Kliore et al*., 1973]. The Viking 1 and 2 missions conducted further occultation experiments from 1976 to 1978. Viking collected atmospheric measurements ranging in latitude from 74°S to 73°N, enabling investigation of Mars' atmosphere on a near-global scale over a full Martian year [*Fjeldbo et al*, 1977; *Lindal et al*., 1979]. When compared to Mariner 9 and Viking, the improvements with MGS in terms of occultation data quantity and quality were significant [*Hinson et al*., 1999]. Compared to Viking, spatial and temporal resolution was enhanced by a factor of 12 due to the reduced orbit period. The shorter wavelength of the X-band radio system also improved vertical resolution by a

15

factor of 2 which, when combined with a ~10X stronger signal, reduced uncertainties in retrieved temperatures and pressures by a factor of 3-5.

Of more recent Mars missions, only MGS and the Mars Express orbiter have carried radio science packages suitable for radio sounding of the neutral atmosphere and ionosphere. The Mars Express Orbiter Radio Science (MaRS) experiment, which derives its carrier frequencies from an Earth-based hydrogen maser source, is expected to improve the altitude extent and vertical resolution of temperature and pressure profiles as compared to MGS [*Pätzold et al*., 2004]. MaRS profiles, which were not available for this research, could be applied to future work to improve the gravity wave energy distribution. Mars Reconnaissance Orbiter (MRO) and Mars Odyssey (MO) carry radio science packages for the investigation of the Martian gravity field using range and range rate measurements [*Zuber et al*., 2007], but the radio systems are not adequate for occultation measurements.

2.1   Radio Occultation Technique

The geometry of the radio occultation experiment for a planetary mission is shown in Figure 2.1. The refractive bending angle, α, has been exaggerated for illustrative purposes. Radio transmissions from a moving transmitter pass through the planetary atmosphere and are received by a distant receiver on Earth that is also in motion. The ray path curves within the planet's atmosphere in response to refractive index gradients, resulting in a net angular deflection in the transmitted signal and a Doppler shift in the received frequency. The deflection and Doppler shift vary as the orbit propagates and the path through the atmosphere changes. Assuming the atmosphere is spherically symmetric, the geometry is reconstructed using the Doppler shift measurement and knowledge of the positions and velocities of the transmitter and receiver. The assumption of spherical asymmetry provides a unique solution because it implies that the refraction is constrained to the plane containing the transmitter, receiver, and center of symmetry [*Ahmad and Tyler*, 1999].

Vertical profiles of pressure and temperature are retrieved using methods based on geometrical optics [*Fjeldbo et al*., 1971]. In order to isolate the perturbations to those caused by the planetary atmosphere, the received signal is first processed to remove time-varying Doppler shifts caused by the

16
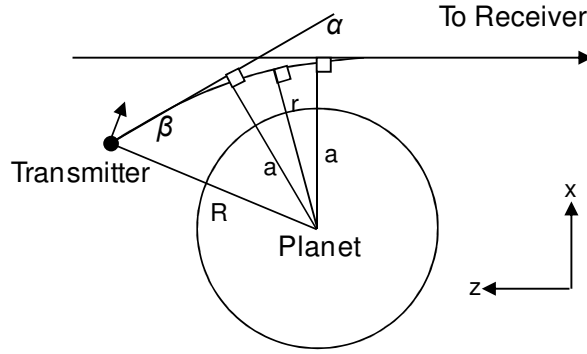
Figure 2.1: Radio occultation geometry.

motions of the transmitter and receiver. In the case of MGS, the motions of the spacecraft and Earth were removed using a reference signal that contained only the Doppler shifts expected in the absence of Mars' atmosphere [*Hinson et al.*, 1999]. The result is a profile of the observed Doppler shift, f_d, caused by refractive bending, versus time. Assuming only motions of spacecraft velocity and not including relativistic effects, the relationship between the Doppler shift and bending angle can be expressed as

$$f_d \approx \frac{v_x \sin \alpha}{\lambda} + \frac{v_z (1 - \cos \alpha)}{\lambda}, \tag{2.1}$$

where v_x and v_z are the components of spacecraft velocity in Figure 2.1 and λ is the vacuum wavelength of the transmitted signal. For each measurement of f_d, we can also compute the corresponding impact parameter, a, the perpendicular distance between the incoming ray path and the center of curvature of the atmosphere,

$$a = R \sin \beta, \tag{2.2}$$

where, as shown in Figure 2.1, R is the radius to the transmitter and β is the angle between the transmitter position vector and the signal transmission. Equations (2.1) and (2.2) allow us to express $f_d(t)$ as $\alpha(a)$.

The Abel transform converts the profile of bending angle versus impact parameter to a profile of refractive index, μ, versus radius, r [*Fjeldbo et al.*, 1971]. Following *Hinson et al.* [1999], an atmosphere with refractive index profile $\mu(r)$ deflects a ray with impact parameter a_j by

17

$$\alpha(a) = -2a_j \int_{r_j}^{\infty} \frac{d \ln \mu}{dr} \frac{dr}{\sqrt{(\mu r)^2 - a_j^2}} \,. \tag{2.3}$$

At the point of closest approach, equation (2.3) has an exact inverse:

$$\ln \mu_j = \frac{1}{\pi} \int_{a_j}^{\infty} \frac{\alpha(a) da}{\sqrt{a^2 - a_j^2}} \,, \tag{2.4}$$

where the radius is given by

$$r_j = \frac{a_j}{\mu_j} \,. \tag{2.5}$$

For a mixture of nonpolar gases, refractive index, $\mu(r)$, is related to number density, $n(r)$, by

$$n = \frac{\mu - 1}{\bar{\kappa}} \,, \tag{2.6}$$

where

$$\bar{\kappa} = \sum_i f_i \kappa_i \,, \tag{2.7}$$

summed over all gases in the mixture. Here f_i and κ_i are the mixing ratio and refractive volume of gas i. For Mars, $\bar{\kappa} = 1.804 \times 10^{-29}$ m^3, calculated from Viking Lander composition measurements and laboratory measurements of the principal constituents [*Hinson et al.*, 1999]. Assuming hydrostatic balance, pressure, p, is calculated from number density using

$$\frac{\partial p}{\partial r} = -n\bar{m}g \,, \tag{2.8}$$

where $\bar{m}$ is the mean molecular mass of the atmosphere and g is the acceleration due to gravity. Integrating (2.8) gives the expression for $p(r)$:

$$p(r) = n_0 k T_0 + m \int_r^{r_0} n(r')g(r')dr' \,. \tag{2.9}$$

r_0 defines an arbitrary finite upper limit for radius. At this radius, number density is known, but T_0 must be estimated as a boundary condition. The temperature profile is obtained from the ideal gas equation:

18

$$T(r) = \frac{p(r)}{n(r)k},\tag{2.10}$$

where k is the Boltzmann constant. For gravity wave investigations using radio occultation measurements, the derived temperature profiles are most relevant, as the equation for gravity wave potential energy is calculated using the temperature perturbation.

2.2 MGS RS Experiment

2.2.1 System Description

The MGS RS experiment consisted of the radio system on-board the spacecraft and the radio and tracking system of NASA's Deep Space Network (DSN). The system used for MGS was essentially the same as that designed for the Mars Observer spacecraft, which was lost just prior to Mars orbital insertion in 1993. The spacecraft and ground systems were designed and configured to work together to ensure data accuracy and quality of results. *Tyler et al*. [2001] describes the elements of the spacecraft and ground systems.

There were two types of radio science observations carried out during the mapping phase of the mission: occultation measurements for study of the atmosphere and spacecraft tracking measurements for study of the gravity field. Occultation measurements were taken with the spacecraft's transponder in non-coherent mode, with the frequency reference provided by the temperature-controlled ultrastable oscillator (USO). The USO, which consisted of a quartz crystal resonator contained in a temperature-controlled titanium dewar, was used to generate the X-band carrier frequency of 8423.2 MHz. The frequency stability of the USO, characterized by the square root of the Allan variance, was measured to be better than 2×10^{-13} over observed intervals of 1 to 1000 s, which marked an order of magnitude improvement over the oscillators used by Voyager and Galileo [*Tyler et al*., 1992]. MGS carried another separate oscillator which could generate a non-coherent downlink, but its frequency stability 6-7 orders of magnitude less than the USO made it unsuitable for occultation measurements. Gravity field measurements were taken with the spacecraft's transponder in coherent mode, where the transmitted carrier frequency was derived from the received uplink carrier frequency. The coherent mode frequency
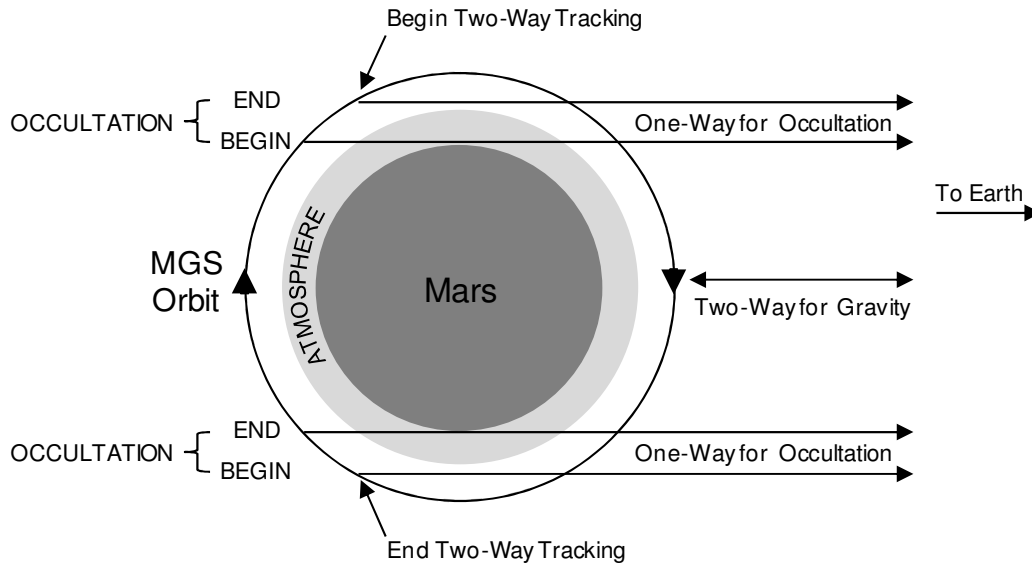
Figure 2.2: Geometry for radio science observations [*Tyler et al*., 2001].

reference provided by the ground station, typically sourced from a hydrogen maser, was more stable than the USO [*Tyler et al*., 1992]. Despite the better frequency stability, coherent mode was not used for occultation measurements for two reasons. First, the time required to establish coherent two-way communications would have resulted in a loss of occultation data. Second, processing of coherently acquired data would have been more complicated, as the uplink and downlink signals pass through Mars' atmosphere on different ray paths.

As described in *Tyler et al*. [2001] and *Hinson et al*. [1999], the spacecraft radio system was configured for occultation measurements with the transponder in non-coherent mode, with modulation off to improve carrier signal strength, with the frequency reference provided by the USO, and with the signal radiated through the high-gain antenna (HGA). This configuration was maintained for about 10 minutes near entry to or exit from occultation. Each observation included extinction of the signal by the surface and a baseline interval above the ionosphere for data calibration and error analysis. The signal was received at Earth in open-loop mode by one of the 34-m or 70-m DSN antennas located in California, Australia, and Spain. After downconverting, filtering to a 2.5-kHz bandwidth, and digitizing, the

occultation data was sent to the Jet Propulsion Laboratory (JPL) for processing by the Radio Science investigation team.

2.2.2   Radio Occultation Data Products

There were two datasets derived from the MGS RS radio occultation measurements: temperature-pressure profiles of the neutral atmosphere and electron density profiles of the ionosphere. The datasets are available online in NASA's Planetary Data System (PDS) per Table 2.1.

Table 2.1: MGS Radio Occultation PDS Datasets

Dataset	Data	Number of Profiles	Location
MORS_1101	Neutral Atmosphere Temperature-Pressure	21,243	http://starbrite.jpl.nasa.gov/pds/viewProfile.jsp?dsid=MGS-M-RSS-5-TPS-V1.0
MORS_1102	Ionosphere Electron Density	5600	http://starbrite.jpl.nasa.gov/pds/viewProfile.jsp?dsid=MGS-M-RSS-5-EDS-V1.0

Each sounding of the neutral atmosphere yielded a vertical profile of temperature, pressure, and number density versus radius and geopotential extending from the surface to the 10-Pa pressure level [*Hinson*, 2008]. An example profile is shown in Figure 2.3. Each data file also provided a 1σ estimate of uncertainty in the derived quantities at each height. From *Hinson et al.* [1999], typical uncertainties ranged from 0.4% or 1 K near the surface to 6% or 10K at the 10-Pa pressure level, or roughly 40-50 km altitude. The 10-Pa pressure level corresponded to the radius upper limit, r_0, used in retrieving the temperature and pressure profiles.

The vertical resolution, determined from the geometrical optics diffraction limit and Nyquist sampling considerations, was approximately $\sqrt{\lambda D}$, where λ is the wavelength of the signal and $D = R\cos\beta$ is the distance from the spacecraft to the limb of Mars. The vertical resolution was different for each measurement, as D changed for each occultation geometry. Minimum, mean, and maximum vertical resolutions were found to be 278 m, 783 m, and 1248 m respectively.
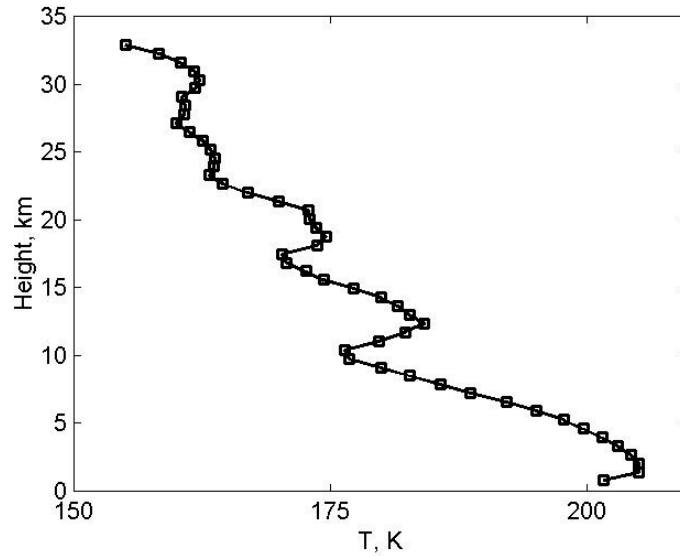
Figure 2.3: Temperature profile 9139G18A in the Tharsis region at 18°N and 113°W. Square symbols represent the raw data points.

Because occultation measurements were optimized for sounding the neutral atmosphere, electron density profiles of the ionosphere were obtained for only the limited set of radio occultation measurements where solar zenith angle was less than about 90 degrees at the measurement location. Each electron density profile provided a table of electron number density versus radius at altitudes from roughly 90 km to 200 km with sample spacing of about 1 km. The electron density profiles have been analyzed by *Bougher et al.* [2001] and *Bougher et al.* [2004], who linked ionospheric waves to non-migrating tides in the neutral atmosphere, and by *Cahoy et al.* [2006], who suggested that thermal tides modulate the neutral density, which controls the height of the ionosphere. The electron density profiles were not used in this research.

2.2.3   Radio Occultation Data Summary

From January 1998 through September 2006, MGS conducted 21,243 radio soundings of the Martian neutral atmosphere, each providing a vertical profile of temperature, pressure, and number density versus radius and geopotential. Profiles are available for all local times of day, all seasons, and over multiple Martian years. Table 2.2 and Table 2.3 show the distribution of occultation measurements

across areocentric longitude, L_s, and latitude with respect to local true solar time (LTST). One hour of

LTST is 1/24th of a sol.

Table 2.2: Radio occultation measurement distribution by local time of day (LTST) versus solar longitude, L_s. Values shown are number of vertical profiles.

LTST	L_s (deg)				Total
	0 +/- 45	90 +/- 45	180 +/- 45	270 +/- 45	
2200-0200	0	0	0	427	427
0200-0600	3819	5149	935	1096	10,999
0600-1000	1894	494	1259	990	4637
1000-1400	30	892	1888	581	3391
1400-1800	0	91	680	969	1740
1800-2200	0	0	12	37	49
Total	5743	6626	4474	4100	21,243

Table 2.3: Radio occultation measurement distribution by local time of day (LTST) versus latitude. Values shown are number of vertical profiles.

LTST	Latitude (deg)						Total
	90°S-60°S	60°S-30°S	30°S-0°	0°-30°N	30°N-60°N	60°N-90°N	
2200-0200	424	3	0	0	0	0	427
0200-0600	369	1542	1427	1217	2629	3815	10,999
0600-1000	573	0	0	0	37	4027	4637
1000-1400	1294	0	0	0	0	2097	3391
1400-1800	91	0	0	0	0	1649	1740
1800-2200	17	24	8	0	0	0	49
Total	2768	1569	1435	1217	2666	11,588	21,243

Local time coverage of the occultation measurements was geometrically constrained by the near-polar, sun-synchronous orbit. As reflected in Table 2.3, latitudes between 60°S and 60°N were available only at local times between 0300 and 0600 hours. Conversely, daytime measurements were taken at latitudes poleward of 60 degrees. Temporal and seasonal coverage was limited by a number of operational factors, including solar noise, spacecraft anomalies, and orbit geometry. Increased noise levels in the occultation measurements precluded profile retrieval near solar conjunction, resulting in

collection gaps of periods from 14 to 79 days near the solar conjunctions in 2000, 2002, 2004, and 2006. For much of the mission, a problem with one of the pointing gimbals in the HGA restricted occultation measurements in the southern hemisphere. The impact can be seen in the significantly greater number of measurements in north polar versus south polar regions. Spacecraft anomalies, where the spacecraft stopped collecting scientific data in response to flight hardware or software problems, and HGA motion, due to solar array repositioning and HGA rewinding, also prevented profile retrieval at various times in the mission. In addition, at three times during the mission, the MGS orbit plane was nearly broadside as seen from Earth. During these periods, which lasted as long as 170 days, atmospheric occultation occurred in a highly grazing geometry or did not occur at all, and profiles are not available.

After reviewing all profiles collected, it was decided for this research to use the subset of 10,999 profiles with local times between 0200 and 0600. These nighttime profiles were well-suited for calculating temperature perturbations. In the nighttime profiles, there often existed a temperature inversion below 10 km altitude, but above that, temperature generally decreased with height, allowing the use of a third-order curve fit to represent background temperature. Geographic locations of the 10,999 profiles are shown in Figure 2.4. Spacing was not uniform, as seen in the heavy concentration of measurements poleward of 60°N, but sufficient spatial coverage existed to support a global analysis of the data. Daytime profiles, on the other hand, sometimes contained strong inversions at altitudes greater than 10 km and general erratic behavior. The poor curve fit for background temperature led to artificially created or enhanced perturbations. Measurements taken outside of 0200-0600 local time also did not enhance geographic coverage, since they were restricted to polar regions. Gravity wave energy densities in polar regions were calculated for all local times and found to be comparable, indicating minimal impact (benefit) in excluding (including) daytime polar profiles in the research. Thus, due to the limited benefit of the data weighed against the difficulties in processing some of the profiles, daytime measurements were not used in this study. One limitation in this research, then, is the inability to assess diurnal variations in gravity wave activity. The diurnal comparison would only be possible in polar regions,

24
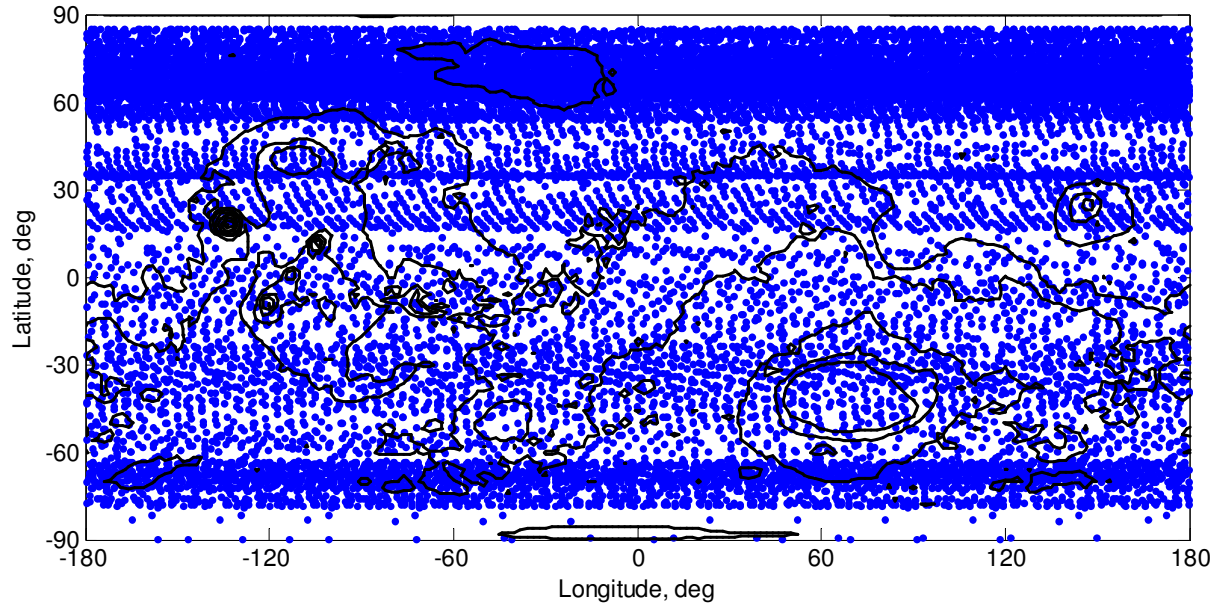
Figure 2.4: Distribution of radio occultation measurements relative to Martian topography. Each marker represents a vertical temperature profile derived from one sounding of the neutral atmosphere.

where sufficient data exists, and could be an opportunity for future study focusing on polar atmospheric processes.

MGS's radio occultation measurements spanned nearly five full Martian years, starting in the second half of Martian Year (MY) 23 and continuing through the first half of MY28. The definition of Martian year comes from *Clancy et al.* [2000] where MY1 started on April 11, 1955. Figure 2.5 shows the timeline of occultation measurements by latitude. The availability of nearly five full years of measurements enabled year-to-year comparisons of gravity wave activity. Mars seasons can be readily inferred from the figure because each Martian year starts on northern spring equinox, $L_s = 0°$. However, the time axis if expressed in L_s would be slightly non-linear since Mars months, defined as 30° in L_s, range from 46 to 67 sols due to the eccentricity of Mars' orbit.

The MGS radio occultation dataset [*Hinson*, 2008] has been used in the investigation of gravity waves [*Creasey et al.*, 2006a], forced atmospheric waves [*Hinson et al.*, 2001], thermal tides and water ice clouds [*Hinson and Wilson*, 2004], and transient eddies [*Hinson and Wilson*, 2002; *Hinson*, 2006]. *Hinson et al.* [2008] also used MGS occultation measurements in combination with a concurrent set of
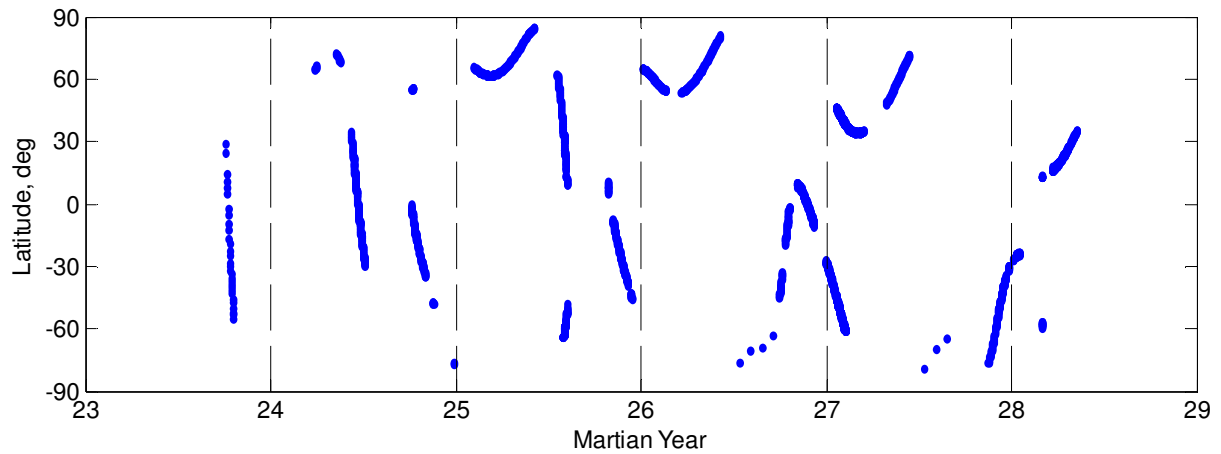
Figure 2.5: Distribution of MGS radio occultation measurements from January 1998 to September 2006, encompassing Martian Years 23 through 28.

Mars Express occultation measurements to identify and characterize two tidal modes in the occultation data.

2.3   Gravity Wave Potential Energy Density

In the temperature profile in Figure 2.3, the existence of a wave structure with a vertical wavelength of roughly 7 km can be readily observed. These wave-like temperature perturbations indicated the probable presence of gravity waves and were typical of the stronger atmospheric variations observed in the radio occultation data. Each temperature profile derived from an occultation measurement has been individually analyzed to quantify the wave energy associated with the temperature perturbations.

The analysis of the occultation measurements followed the approach used by *Tsuda et al.* [2000] and *Eckermann et al.* [1994] as applied in the terrestrial atmosphere to GPS radio occultation profiles and radiosonde data respectively. The approach is based on the linear theory of gravity waves such that it is possible to estimate total gravity wave energy from temperature observations only. For each profile, gravity wave potential energy per unit mass was calculated from the temperature perturbation relative to the background temperature:

26

$$E_p = \frac{1}{2} \frac{g^2}{N^2} \left(\frac{T'}{\overline{T}} \right)^2 . \qquad (2.11)$$

In this equation, g is acceleration due to gravity, N is the Brunt-Väisälä frequency given by

$$N^2 = \frac{g}{\overline{T}} \left(\frac{\partial \overline{T}}{\partial z} + \frac{g}{c_p} \right), \qquad (2.12)$$

$\overline{T}$ is the background temperature, T' is the temperature perturbation, and c_p is specific heat at constant pressure. Other than c_p, all are functions of height. Appendix A contains the derivation of the gravity wave potential energy equation (2.11) from the equations of state and the first law of thermodynamics.

Total gravity wave energy is the sum of gravity wave potential and kinetic energy: $E_0 = E_p + E_k$. From *Van Zandt* [1985] and *Fritts and Alexander* [2003], the ratio of kinetic to potential energy is presumed constant, making E_0 linearly proportional to E_p. Assuming a universal spectrum of gravity waves, the relationship between kinetic and potential energy is given by the spectral index, $p = E_k/E_p$. Based on observations of the gravity wave spectrum [e.g. *Van Zandt*, 1982; *Tsuda et al.*, 1999], the generally accepted value on Earth for p is 5/3. Assuming a similar spectral index for Mars, which we will evaluate later, we can estimate total gravity wave energy from the potential energy of each temperature profile retrieved.

Gravity wave potential energy density was calculated as a function of height over the range from 10 km to 30 km. The lower limit was chosen to avoid the boundary layer temperature inversion which was present in many of the profiles and extended from the surface to as high as 7.5 km altitude. The upper limit was constrained to 30 km altitude to maintain data consistency across all profiles, since the maximum altitude of the 10-Pa level varied with the underlying topography.

The vertical resolution was roughly constant across a profile but varied from measurement to measurement due to changing occultation geometries. To maintain consistency in processing and simplify spectral analysis of vertical wavelength, each temperature profile was first interpolated to a constant vertical grid with vertical spacing of 1250 m. Per Nyquist sampling theorem, this spacing established a 2.5 km lower limit on vertical wavelengths that could be resolved from the temperature

27
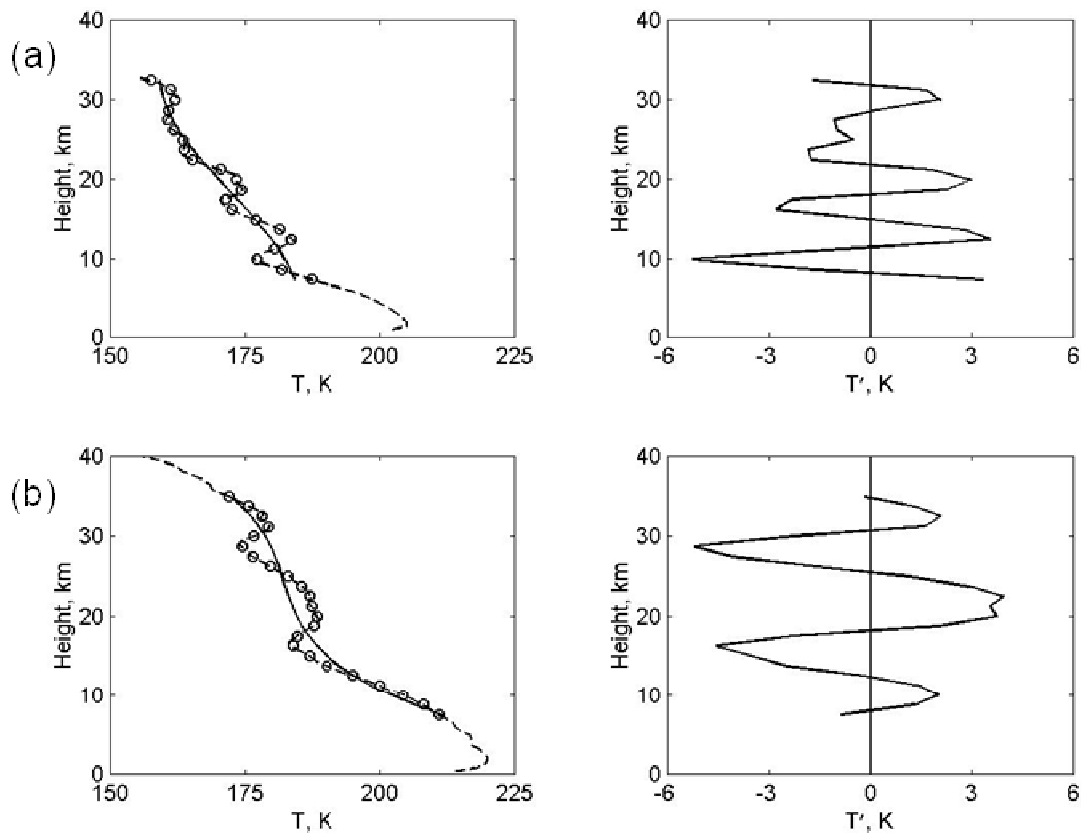
Figure 2.6: Selected temperature profiles (a) 9139G18A in the Tharsis region at 18°N and 113°W and (b) 9153V26A at 3°S and 160°E. In the plots on the left, the dashed line extending from the surface is the raw temperature data derived from the occultation experiment, the circles along the dashed line represent the interpolated data points with constant vertical spacing of 1250 m, and the solid line is the background temperature defined by a least-squares cubic polynomial curve fit. The plots on the right side show the calculated temperature perturbation profile.

perturbation profile. Since most of the perturbation energy occurred at longer vertical wavelengths, it is believed that the imposed constant grid did not filter any significant gravity waves.

The background temperature profile, $\bar{T}$, was found for each occultation measurement by applying a least-squares third-order curve fit to the constant-grid temperature data. The curve fit was applied to the temperature profile between 7.5 km and 32.5 km altitude. The curve fit was extended to allow for edge effects to occur outside the 10-30 km height range used in the gravity wave potential energy calculation. An additional effect of the third order curve fit was that it filtered vertical wavelengths greater than the

vertical span of data fitted, or in this case wavelengths greater than 25 km. Since typical vertical wavelengths of gravity waves in Earth's lower atmosphere have been observed to be ~5-12 km [*Alexander et al.*, 2008; *Wang and Alexander*, 2010] and the wavelength analysis of the perturbation profiles showed no dominant wavelengths greater than 18 km (Figure 2.10 (b)), it was presumed that the third order fit did not remove gravity wave components significant to the zonal mean circulation. The temperature perturbation T' was determined by subtracting the background temperature from the observed temperature: $T' = T - \bar{T}$. Figure 2.6 demonstrates the calculation of temperature perturbation from the retrieved temperature profile. These cases were selected to highlight wave activity seen in the temperature perturbation profile, with vertical wavelengths roughly (a) 7 km and (b) 12 km.

Using equation (2.11), gravity wave potential energy density, E_p, was calculated as a function of height. The Brunt-Väisälä frequency used in the calculation was locally determined using equation (2.12) as opposed to using a mean value. A single value of E_p for each profile was obtained by averaging E_p over a height range of interest. *Creasey et al*. [2006a] reported gravity wave potential energy density from 10-30 km. The simulations discussed later in Chapter 5 used momentum flux derived from gravity wave potential energy densities from 10-15 km.

2.4   Global Distribution of Gravity Wave Potential Energy

The global distribution of gravity wave potential energy density was determined by averaging E_p values in an area 15° in latitude by the equivalent distance in longitude. Average values were calculated every 5° in latitude and longitude. The global distribution of E_p in the 10-30 km height region is shown in Figure 2.7. Zonally averaged E_p is shown in Figure 2.8. The distribution includes 10,841 temperature profiles, as 158 profiles were removed from further analysis due to not meeting the maximum height limitation (153) or difficulties in calculating background temperature (5).

Figure 2.7 shows that gravity wave activity was observed predominantly in the Martian tropics, where it was distributed asymmetrically in longitude with a slight bias towards the northern hemisphere. Within the tropics, wave energy was high in the mountainous Tharsis region, presumably due to

29

topography. However, wave energy was equally high over the low-lying Isidis Planitia, with elevated activity also observed in the tropics near Chryse Planitia and Amazonis Planitia. Outside the tropics, measurements revealed enhanced wave activity over the southern hemisphere extending close to the southern pole, a result expected due to the greater orographic variance in this hemisphere. Gravity waves were intermittent in the northern hemisphere above 50°N, but not altogether absent. Roughly 5% and 1% of all measurements taken above 50°N yielded E_p values greater than 5 J kg^{-1} and 10 J kg^{-1} respectively.

The standard deviations shown in Figure 2.8 reflect the variability in the data. On Earth, gravity waves have been observed to occur intermittently in large amplitude wave packets [e.g. *Alexander et al.*, 2010], and it appears the same behavior applies on Mars. Inspection of the potential energy density distributions confirmed the distributions were not Gaussian and that large amplitude waves contributed significantly to the mean. Variance was greatest just north of the equator in the latitude bands containing the Tharsis region. Variance was also appreciably larger in the southern hemisphere than the northern hemisphere, correlating better with the southern hemisphere's higher orographic variance than the mean E_p value. In particular, energy density standard deviation, as compared to the mean, was significantly higher near 50°S-60°S, where elevated wave activity had been observed near the western edges of Hellas Planitia and Argyre Planitia. In general, quantifying gravity wave intermittency is a concern for accurately estimating gravity wave momentum flux from observations [*Alexander et al*., 2002; *Alexander et al*., 2010]. Due to the dispersion relation, waves with greater group velocity (i.e. energy transport) may be less likely to be observed. As discussed later in this section, this may lead to larger energy densities reported in the tropics from slow-moving, less-energetic waves.
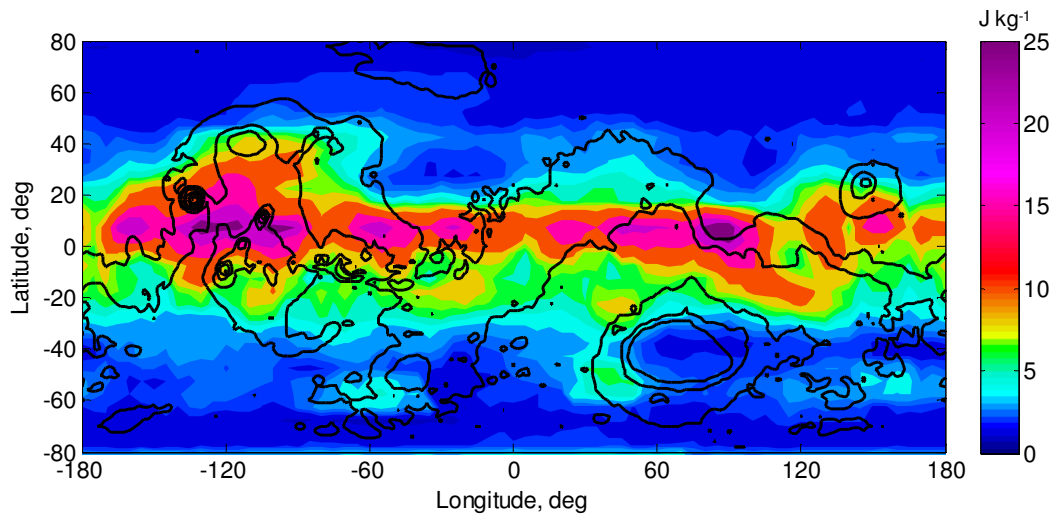
Figure 2.7: Global distribution of E_p, gravity wave potential energy per unit mass, at 10-30 km height for all values of L_s.
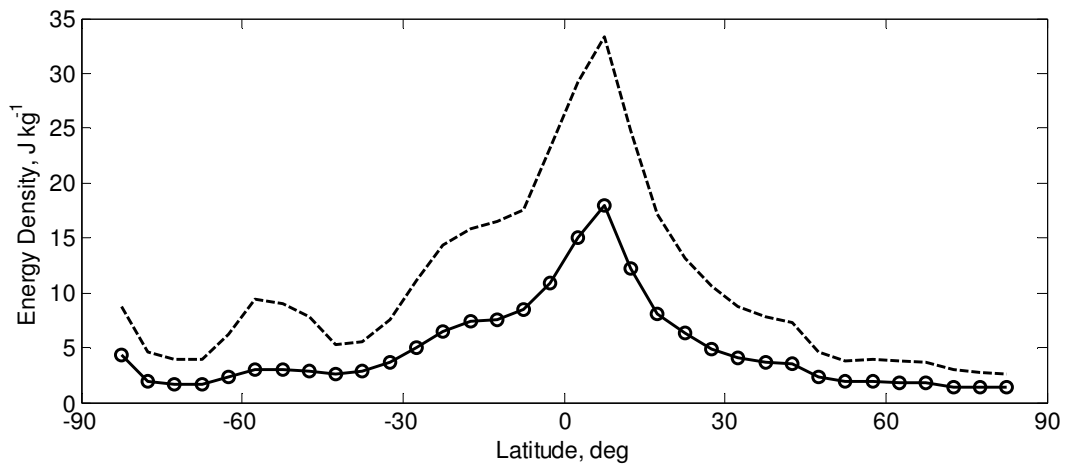
Figure 2.8: Zonal average of E_p, gravity wave potential energy per unit mass, at 10-30 km height for all values of L_s. The circles and solid line represent the zonal mean. The dashed line is one standard deviation above the mean.
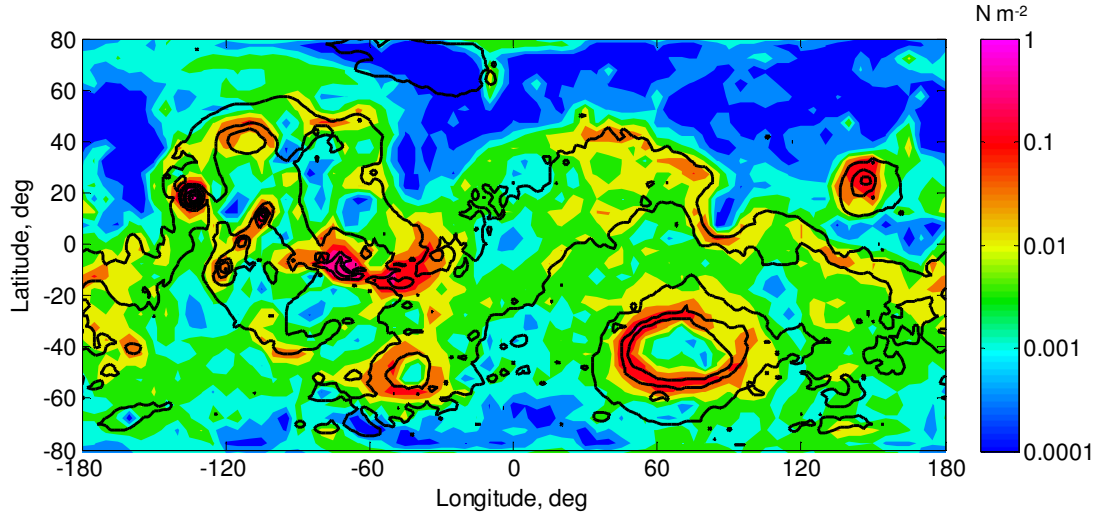
Figure 2.9: Global distribution of surface stress, based on wind flow over topography.

2.4.1   Gravity Wave Sources

If gravity wave activity was due primarily to orographic forcing, *Creasey et al*. [2006a] expected that the geographical distribution of wave energy would be correlated to the surface stress derived from the underlying topography. Surface stress is a representation of wind flow over topography, which is the basis for the gravity wave forcing schemes used in several Mars GCMs, including the LMD GCM behind the Mars Climate Database [*Lewis et al*., 1999; *González-Galindo et al*., 2009b]. From *Palmer et al*. [1986], surface stress, τ, is defined as

$$\tau = \kappa\rho NU\sigma^2 \, , \tag{2.13}$$

where τ is the magnitude of the low level wind, κ is a tunable parameter used here with a constant value of 10^{-4} m^{-1}, and σ^2 is the subgrid-scale orographic variance. Using seasonally-averaged near-surface wind speed and atmospheric pressure from the Mars Climate Database [*Lewis et al*., 1999] and orographic variance calculated from MGS MOLA data [*Delacourt et al*., 2003], surface stress was calculated for all locations as shown in Figure 2.9. As expected, surface stress is considerably higher in areas of significant topography, such as near the Tharsis volcanoes and Elysium Mons. If orographic forcing was the sole source of gravity wave excitation, the distribution of surface stress in Figure 2.9 would more closely

resemble the wave energy density distribution in Figure 2.7. This result implies that (1) forcing mechanisms other than orographic forcing are responsible for the small-scale wave activity observed in the Martian tropics and (2) simulations that employ a gravity wave parameterization or forcing scheme based only on wind flow over topography may not be adequately representing the geographic distribution of gravity wave activity.

Miyoshi et al. [2011] has suggested that the global distribution of gravity waves reported here and in *Creasey et al.* [2006a] also included the small-scale tides. They performed a space-time Fourier analysis on the results of the Mars GCM of *Moudden and McConnell* [2005] and found that in the lower atmosphere tidal components having large zonal wavenumbers were significant along with stationary components excited by topography. The 2° by 2° grid scale of the *Moudden and McConnell* [2005] model allowed investigation of small-scale waves with horizontal wavelength greater than 200 km. Except for the stationary component, non-tidal gravity wave components were negligibly small. Evidence of tidal components in the MGS occultation data had previously been reported in *Hinson and Wilson* [2004]. From a subset of 440 MGS occultation measurements, *Hinson and Wilson* [2004] suggested that large temperature inversions that occur above the Martian tropics occurred due to zonally modulated thermal tides. They noted that inversions were strongest and occurred most frequently above elevated terrain, in particular Tharsis. They also noticed, with the exception of Tharsis, that inversions were stronger in the southern tropics than the northern tropics. As noted earlier, this research did not attempt to differentiate between tidal and non-tidal gravity waves. From *Lindzen* [1981], the unstable breakdown of tides and gravity waves are treated similarly, and the sub-grid scale of the observed waves means they may not already be resolved in dynamical models.

As noted in *Miyoshi et al.* [2011], their GCM results did not explain all of the features of the MGS-derived potential energy distributions. Other non-orographic gravity wave sources must be considered, and we look to Earth for analogous behavior. On Earth, tropospheric convection generates significant gravity wave energy at low latitudes [*Fritts and Alexander*, 2003; *Alexander et al.*, 2006]. The distribution of gravity wave energy has been found to correlate with rainfall rate indicating that gravity

33

waves are mainly generated by cumulus convection [e.g. *Miyoshi and Fujiwara*, 2009]. For Mars, *Miyoshi et al*. [2011] did not consider gravity waves forced by convection since convective activity in Mars' atmosphere is much weaker than Earth's and the intense convective storms seen in Earth's tropics do not have a Martian analog. Convective gravity waves on Earth are not always tied to rainfall. *Kuettner et al*. [1987] reported widespread gravity wave systems over convective boundary layers (CBL) in the presence of vertical wind shear. Cloud tops were found to present an obstacle to the surrounding airflow similar to topographic obstacles launching gravity waves. If Mars' CBL, which extends to 8-10 km (4-6 km) altitude where surface elevation is high (low) [*Hinson et al*., 2008b], was a source region for gravity waves, the energy may be present in the radio occultation data. Geostrophic adjustment is another potential source of gravity wave activity [*Zhu and Holton*, 1987; *Fritts and Luo*, 1992]. Gravity wave excitation accompanies the restoration of balanced flow, such as the geostrophic adjustment of an ageostrophic jet. *Fritts and Luo* [1992] suggested that Earth's jet stream may be a significant source of low-frequency gravity waves. Shear generation and wave-wave interactions are other gravity wave sources cited for Earth [*Fritts and Alexander*, 2003], although both were unlikely to be observed in the radio occultation data. The expected horizontal scales of gravity waves excited by unstable shears are an order of magnitude less than the observability constraint of the radio occultation experiment, and nonlinear wave-wave interactions are typically associated with middle atmosphere gravity wave forcing as opposed to near the surface. Another potential source is the non-local deep transport (NLDT) mechanisms associated with Mars' topography and dust storms [*Rafkin*, 2012]. Rapid and deep thermal circulations forced by topography may cause vertical disturbances in a stable layer to excite gravity waves.

In summary, the gravity wave spectrum at Mars is expected to be comprised of both stationary and non-stationary components. Stationary components due to topographic forcing combined with non-stationary components due to tidal gravity waves explain much of the distribution of observed gravity wave energy. Other non-orographic sources of gravity waves are also plausible such as dry convective activity at boundary layers, geostrophic adjustment, and non-local deep transport. These mechanisms

34

may account for some of the differences between the observed *Creasey et al.* [2006a] distributions and modeled *Miyoshi et al.* [2011] distributions, although observational data is not available to investigate further.

2.4.2   Comparison to Earth

For Earth, *Tsuda et al.* [1999] derived a similar global distribution of gravity wave potential energy density using radio occultation data from the Global Positioning System/Meteorology (GPS/MET) experiment. The *Tsuda et al.* [1999] E_p distribution at 20-30 km altitude also showed significant gravity wave energy across the tropics over both landmass and water. *Alexander et al.* [2002] investigated the possibility that the equatorial maximum in the Tsuda distributions was due to short vertical wavelength Kelvin wave modes. Kelvin wave variance has a predictable latitudinal width that varies in proportion to vertical wavelength. *Alexander et al.* [2002] found that the width was much narrower than the observed distribution about the equator and concluded that Kelvin waves alone could not explain the equatorial maximum in the GPS data. A similar argument could be made for the Mars MGS gravity wave distribution where elevated gravity wave energy extended past the tropics and the zonally averaged peak was offset from the equator. At mid-latitudes in *Tsuda et al.* [1999], larger (smaller) E_p values were found in the winter (summer) hemisphere and over the continents (Pacific Ocean). Elevated gravity wave energy was not observed in areas of significant topography. Mean E_p values near Japan were estimated to vary from 4-8.5 J kg^{-1} over a year, with maximum in winter and minimum in summer.

Ern et al. [2004] derived global distributions of Earth's gravity wave activity using temperature profiles retrieved from the Cryogenic Infrared Spectrometers and Telescopes for the Atmosphere (CRISTA) instrument flown on two Shuttle missions. The temperature perturbation distribution showed perturbations larger in the tropics than at mid-latitudes, similar to the trend seen in *Tsuda et al.* [1999] for Earth and this research for Mars, with the largest perturbations seen in the southern hemisphere near Antarctica and the tip of South America. Using an estimate of horizontal wavelength determined from two or more adjacent temperature profiles, *Ern et al.* [2004] were able to calculate the vertical flux of

horizontal momentum. *Ern et al.* [2004] developed a relationship between momentum flux and energy density which for mid-frequency gravity waves can be written as

$$F_x = \bar{\rho} \frac{\lambda_z}{\lambda_x} E_p, \tag{2.14}$$

where λ_x and λ_z are gravity wave horizontal and vertical wavelengths respectively. The global distribution of momentum flux showed extremely high momentum flux in the southern hemisphere poleward of 40°S, near South America and Antarctica in particular. In the tropics and northern sub-tropics, only patches of high momentum flux were found. According to equation (2.14), the differences in the distributions of perturbation energy and momentum flux in the tropics are first-order attributed to the longer horizontal wavelengths observed in the tropics. From *Alexander et al.* [2002], longer horizontal wavelengths near the equator are expected due to latitudinal variations in the Coriolis parameter. Because gravity wave intrinsic frequencies exist between the Coriolis parameter and the Brunt-Väisälä frequency, very low intrinsic wave frequencies are allowed near the equator as the Coriolis parameter approaches zero. From the dispersion relation, low frequency waves will tend to have longer horizontal wavelengths. Vertical group velocity also decreases with wave intrinsic frequency. If the source is intermittent, the wave will also have a higher probability of being observed as it propagates more slowly through the altitude region being observed.

Alexander et al. [2008] and *Wang and Alexander* [2010] have produced maps of gravity wave parameters and momentum flux for Earth. *Alexander et al.* [2008] performed a wavelet analysis on adjacent temperature profiles from the High Resolution Dynamics Limb Sounder to determine the vertical and horizontal wavelengths of a gravity wave. Following *Ern at al.* [2004], momentum flux was estimated using equation (2.14). Momentum flux was distributed globally similarly to *Ern et al.* [2004], but the absolute values were lower by a factor of ~5 [*Alexander et al.*, 2010]. *Wang and Alexander* [2010] extended the method of *Alexander et al.* [2008] to three dimensions by analyzing multiple GPS occultation temperature profiles that occur in the same latitude, longitude, and time cell. *Wang and Alexander* [2010] calculated global distributions of temperature perturbation, vertical wavelength,

36

horizontal wavelength, the ratio of intrinsic frequency to the Coriolis parameter, momentum flux, and for the first time, horizontal propagation direction. Observed temperature perturbations were again larger in the tropics, but the perturbation amplitudes of 0.8-1.1 K were roughly a factor of 2 lower than *Ern et al.* [2004]. The distribution of momentum flux showed gravity wave hot-spots over South America, Scandinavia, and southeast Africa. It was suggested that the larger momentum flux over the Amazon in South America was due to strong convective activity. Other than the hot-spot regions, momentum flux in the tropics was not elevated.

The methods used in the recent estimates of global gravity wave distribution on Earth are also applicable to Mars. From the temperature perturbation profile of the MGS radio occultation measurement, vertical wavelength could readily be calculated. Unfortunately, other gravity parameters were not known, since the spatial and temporal distribution of MGS occultation measurements did not permit the two-dimensional or three-dimensional approach used by *Ern at al.* [2004], *Alexander et al.* [2008] and *Wang and Alexander* [2010]. Instead, the gravity wave parameters needed to determine momentum flux were estimated using gravity wave theory. Chapter 4 describes the method used to calculate gravity wave momentum flux from MGS potential energy density.

2.5 Evaluation of Vertical Wavelengths

For each temperature perturbation profile that had a maximum perturbation greater than 1 K, the dominant vertical wavelength was determined by taking the Fourier transform of the perturbation profile and then choosing the 1 km wavelength bin with the highest power. The normalized composite power spectrum and distribution of dominant vertical wavelengths are shown in Figure 2.10. The mean and median vertical wavelengths were 14.9 km and 14.0 km respectively. The distribution of dominant wavelength was bimodal with maxima near 8-10 km and 13-15 km, suggesting the potential existence of multiple, discrete wave sources or propagation conditions.
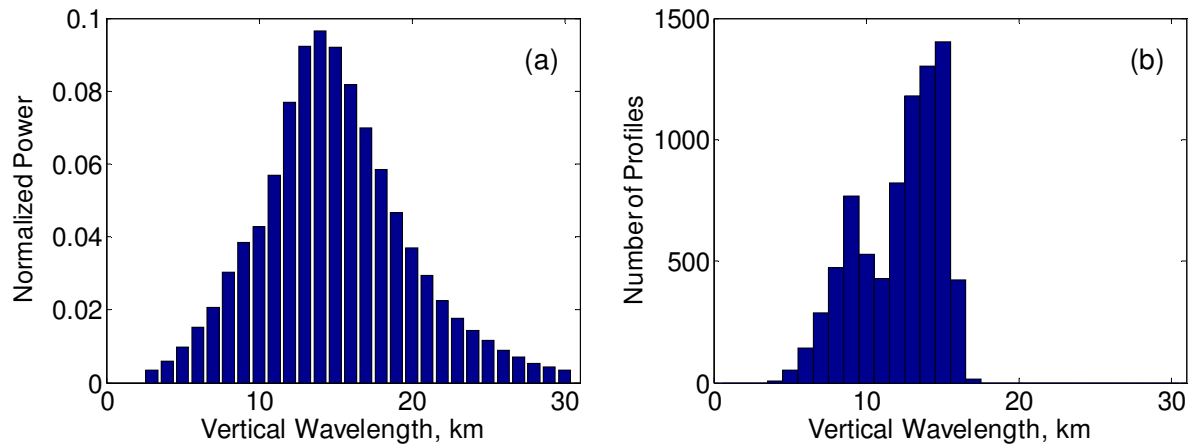
Figure 2.10: Global vertical wavelength distribution. (a) Wave power spectrum computed for applicable temperature perturbation profiles using Fourier analysis. Individual power spectrums were summed and then normalized. (b) Dominant vertical wavelength determined for each profile by the 1-km bin with the highest power.

The wavelength distributions were repeated for latitude bands of 90°S to 30°S, 30°S to 30°N, and 30°N to 90°N to look for latitudinal or hemispherical dependencies. The mean vertical wavelengths were 15.1-km, 14.9-km, and 14.7-km respectively. Based on *Alexander et al.* [2008] and *Wang and Alexander* [2010], a pronounced latitudinal dependence was expected. For Earth, *Alexander et al.* [2008] found vertical wavelengths on the order of 7-12 km with wavelengths increasing from the equator to high latitudes in the winter hemisphere. *Wang and Alexander* [2010] reported a similar trend from equator to pole, but with dominant vertical wavelengths of ~5-8 km. The *Ern et al.* [2004] vertical wavelength distribution, however, did not show a strong dependence on latitude. *Alexander et al.* [2008] suggested the *Ern et al.* [2004] result may have been due to the higher vertical resolution of the CRISTA data, which may have observationally filtered shorter-wavelength waves believed to exist near the equator. With a vertical resolution comparable to the HIRDLS instrument, such an argument cannot be made for the MGS occultation measurements.

The correlation of vertical wavelength to gravity wave potential energy density was also investigated. Mean vertical wavelength was found to increase with potential energy density. For profiles with $E_p < 2$ J kg^{-1}, mean vertical wavelength was 14.3 km; this result increased steadily to 15.4 km for

38

profiles with $E_p > 20$ J kg^{-1}. Also, for $E_p < 2$ J kg^{-1}, dominant vertical wavelengths of 8-10 km occurred nearly as often as wavelengths of 13-15 km. By $E_p > 20$ J kg^{-1}, the occurrences of 8-10 km dominant wavelengths were negligible. The wavelength distributions indicate that higher potential energy densities were generally associated with longer vertical wavelengths. Compared to Earth, this result is consistent with *Ern et al.* [2004] and *Alexander et al.* [2008] for the strong temperature perturbations and longer vertical wavelengths observed over Antarctica and the tip of South America.

The vertical wavelengths inferred from the *Miyoshi et al.* [2011] tidal gravity waves were consistent with the vertical wavelengths calculated from the MGS radio occultation data. Using the *Lindzen* [1967] definition of equivalent depth, horizontal and vertical wavelengths were calculated for diurnal, semidiurnal, and higher mode tidal components with large zonal wavenumbers as shown in Table 2.4 for the equator. The solar thermal tidal fields are represented by $A_{n,s} \cos(n\,\Omega\,t + s\lambda - \phi_{n,s})$ where s is the zonal wavenumber and n is the subharmonic of a sol.

Table 2.4: Horizontal and vertical scales of tidal gravity waves at the equator.

Zonal Wavenumber, s	Horizontal Wavelength (km)	Vertical Wavelength (km)			
		$n = 1$	$n = 2$	$n = 3$	$n = 4$
10	2133	7.8	11.7	15.5	19.3
15	1600	3.6	5.3	6.9	8.5
20	1067	2.2	3.1	4.0	4.9
40	533	0.7	0.9	1.2	1.4

For vertical wavelengths between 8 and 15 km, the *Miyoshi et al.* [2011] tidal gravity waves would correspond to teridiurnal and higher components with zonal wavenumbers of roughly 10-15, or semidiurnal or diurnal components at lower zonal wavenumbers. As will be shown later, components with zonal wavenumbers $s < 10$ may be pushing against the observational constraints of the data.

2.6   **Yearly and Seasonal Variations**

Figure 2.11 shows the individual gravity wave potential energy densities derived from retrieved temperature profiles over the nearly five full Martian years of observations. E_p results shown were
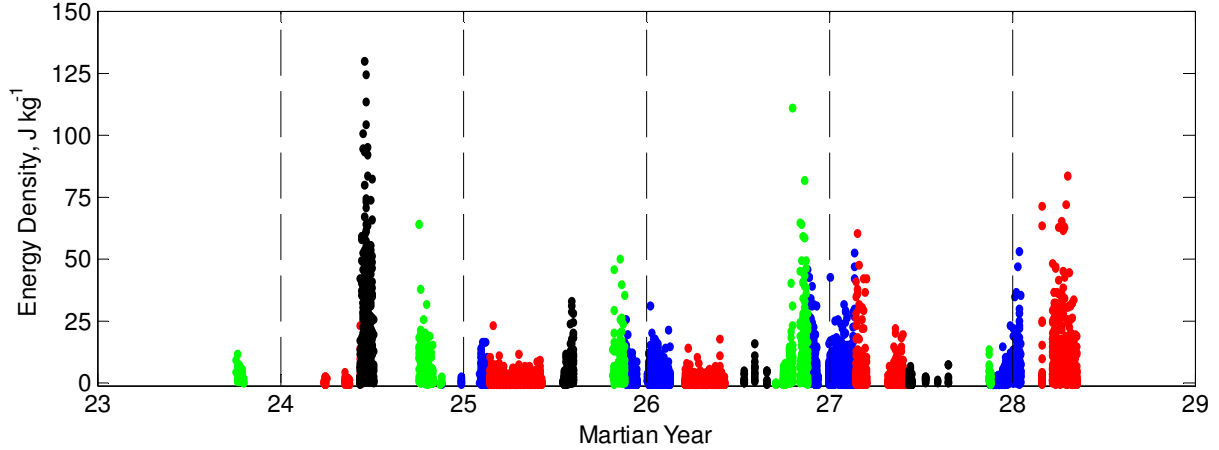
Figure 2.11: Distribution of gravity wave potential energy density by Martian year. Each data point represents the potential energy density of a retrieved temperature profile averaged over the 10-15 km height range. Markers are color-coded by Mars season: blue is northern spring (L_s=0 +/- 45 deg), red is northern summer (L_s=90 +/- 45 deg), black is northern winter (L_s=180 +/- 45 deg), and green is northern autumn (L_s=270 +/- 45 deg).

averaged over the 10-15 km height range and were used later in the momentum flux calculations. Figure 2.11 has been color coded by Mars season, where the seasons were defined for this study as 45° in solar longitude on either side of northern hemisphere spring equinox ($L_s = 0°$), summer solstice ($L_s = 90°$), autumn equinox ($L_s = 180°$), and winter solstice ($L_s = 270°$). As discussed earlier, coverage gaps in the timeline were due to periods of solar noise, spacecraft anomalies, and poor occultation geometries.

Table 2.5: Year-to-year variability in mean potential energy density at 10-15 km height.

	Martian Year						All
	23	24	25	26	27	28	
Number of occultation measurements	30	957	2934	2908	3127	1020	10,976
Mean potential energy density (J kg^{-1})	3.4	11.3	2.3	3.2	2.6	7.5	3.9

Year-to-year variability was evident, as quantified in the range of mean potential energy density in Table 2.5. In particular, MY24 saw a period at L_s =135-161 degrees where many temperature profiles had a pronounced temperature inversion at heights greater than 10 km. The larger inversions resulted in temperature perturbations as high as ~4-5 K, which equated to potential energy densities around or above

100 J kg^{-1}. Temperature profiles leading into this period registered low values of potential energy density, implying a relatively sudden onset in observed gravity wave energy.   Unfortunately, occultation measurements were not again possible until L_s=264 degrees, 170 Earth days later, due to the orbit's broadside viewing geometry. When measurements resumed, gravity wave energy was reduced, and the intervening behavior can only be guessed. In general, the majority (over 80%) of retrieved profiles had potential energy densities less than 5 J kg^{-1}, which corresponded to a temperature perturbation of ~1 K. Larger-amplitude waves, with higher energy densities, did not occur randomly throughout the MGS mission but instead occurred in distinct periods spanning multiple Martian months. Figure 2.11 also shows that periods of both background-level potential energy (< 5 J kg^{-1}) and elevated potential energy (> 5 J kg^{-1}) occurred across all seasons.

For the most part, sufficient MGS occultation measurements existed to quantify the global potential energy density by Mars season.   When filtering by season, there were geographical gaps in coverage, but missing data points in the zonal average were interpolated from adjacent latitudes or extrapolated using the zonal average over a full Martian year.

41
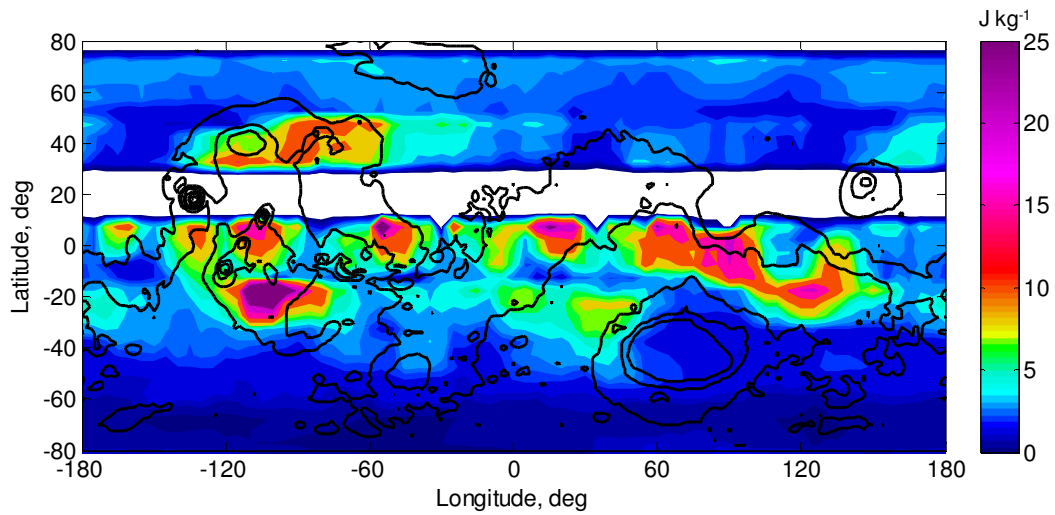
Figure 2.12: Global distribution of E_p, gravity wave potential energy per unit mass, at 10-15 km height for northern spring, L_s=0 +/- 45 deg. White areas represent locations with no data available.
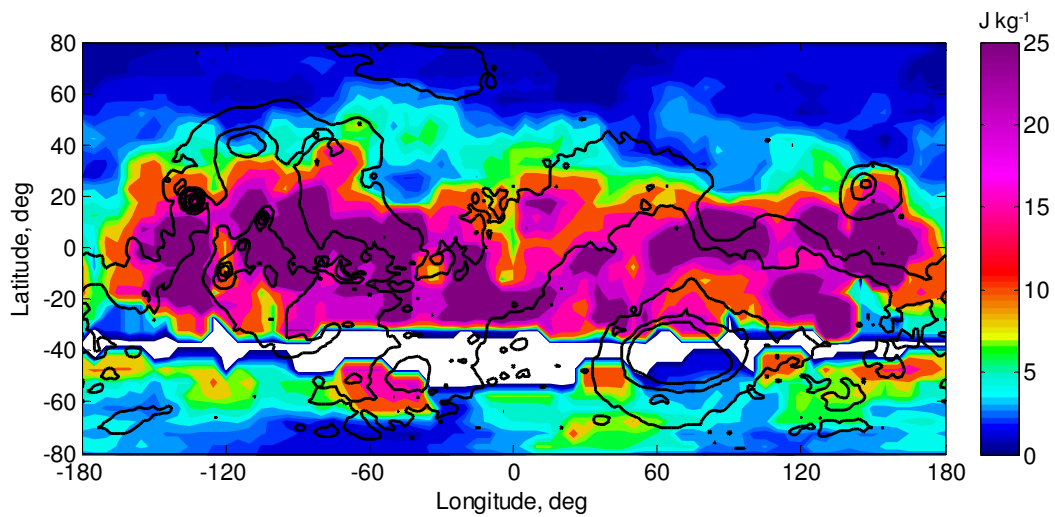
Figure 2.13: Global distribution of E_p, gravity wave potential energy per unit mass, at 10-15 km height for northern autumn, L_s=180 +/- 45 deg.

Figure 2.12 and Figure 2.13 show the global distributions of potential energy density for northern spring equinox and northern autumn equinox respectively. Potential energy density was significantly higher near northern autumn versus northern spring, particularly in the Martian tropics where mean potential energy density was higher by a factor of 3 (22.6 J kg^{-1} versus 7.7 J kg^{-1}). However, it was anticipated that similar results would be observed near spring and autumn equinox due to similarities in the magnitude and direction of low-level zonal winds [*Forget et al*., 1999; *Collins et al*., 1997]. The differences in energy density imply potential differences in forcing, source spectra or low-level winds, such that (1) larger amplitude gravity waves were forced, (2) waves were generated at different phase speeds that were then able to propagate through the background wind field, or (3) critical levels were encountered at low-levels in northern spring, but not in northern autumn. Unfortunately, additional data did not exist to evaluate any of these possibilities. The differences may also be attributed simply to year-to-year variability. The occultation measurements taken in MY24 from L_s=135-161 contributed significantly to the mean potential energy density for northern autumn. In following Martian years, northern autumn mean potential energy densities were noticeably reduced.
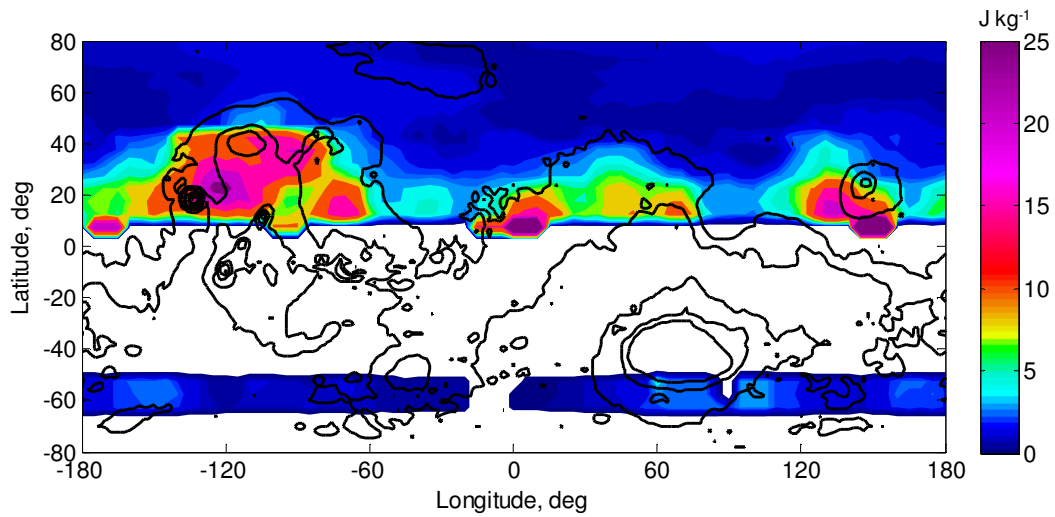
Figure 2.14: Global distribution of E_p, gravity wave potential energy per unit mass, at 10-15 km height for northern summer, L_s=90 +/- 45 deg.
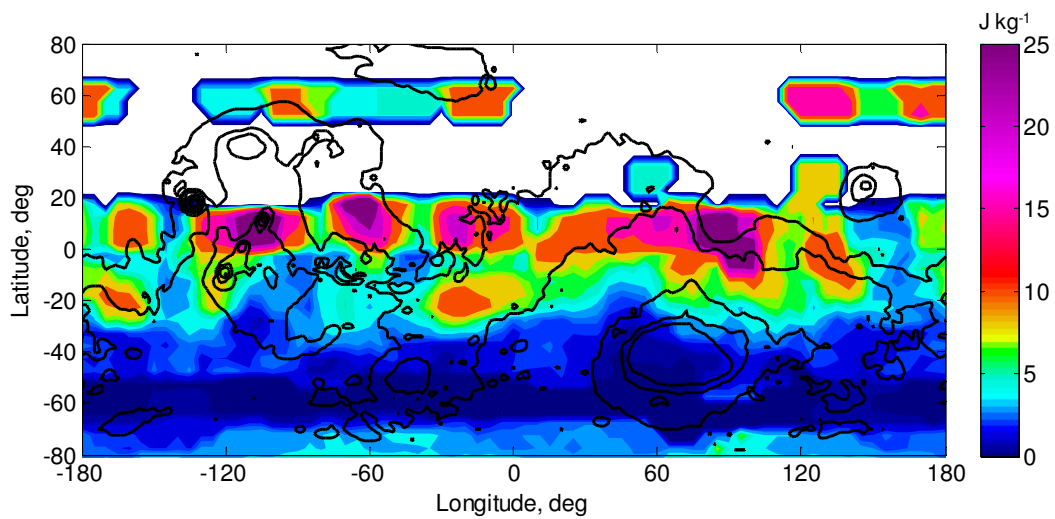
Figure 2.15: Global distribution of E_p, gravity wave potential energy per unit mass, at 10-15 km height for northern winter, L_s=270 +/- 45 deg.

Occultation measurements in northern summer (Figure 2.14) and northern winter (Figure 2.15) were limited primarily to the summer hemispheres. The exceptions were measurements taken in the tropics up to 20°N in northern winter and a band of measurements at 60° latitude in the winter hemisphere of both northern summer and northern winter. In northern summer, elevated gravity wave energies were observed in Tharsis near Olympus Mons and near Isidis Planitia. In northern winter, elevated gravity wave energies occurred slightly poleward of the equator in the winter hemisphere and were distributed in longitude. In particular, larger amplitude waves were observed near the Tharsis volcanoes. Slightly elevated activity was also observed in northern winter near the south pole. With the absence of winter hemisphere measurements, this study was unable to contrast by hemisphere the energy densities observed with respect to the expected zonal mean eastward (winter) and westward (summer) jets [*Théodore et al.*, 1993; *Forget et al.*, 1999; *Joshi et al.*, 1995; *Forbes and Miyahara*, 2006]. It was anticipated that preferential filtering by background winds would result in different energy density profiles between the winter and summer hemispheres. Although Figure 2.15 shows appreciably greater gravity wave activity near 60°N in northern winter, this band of data is comprised of a small set of 9 measurements collected over a two-day span in MY24. Such an increase may be indicative of a mid-latitude winter maximum in gravity wave activity, similar to the winter maximum in Earth's stratosphere determined from radar observations [*Vincent and Reid*, 1983; *Tsuda et al.*, 1990; *Sato*, 1994], or it may be a temporal event coincident with the occultation measurements. The southern winter measurements near 60°S were not elevated. Mean and maximum potential energy densities were 1.6 J kg^{-1} and 4.9 J kg^{-1} in southern winter near 60°S, compared to 9.5 J kg^{-1} and 21.6 J kg^{-1} in northern winter near 60°N. At summer middle latitudes (30°-60°), mean potential energy density was slightly higher in northern summer compared to southern summer (2.4 J kg^{-1} versus 1.9 J kg^{-1}) due to large contributions from measurements near Tharsis.
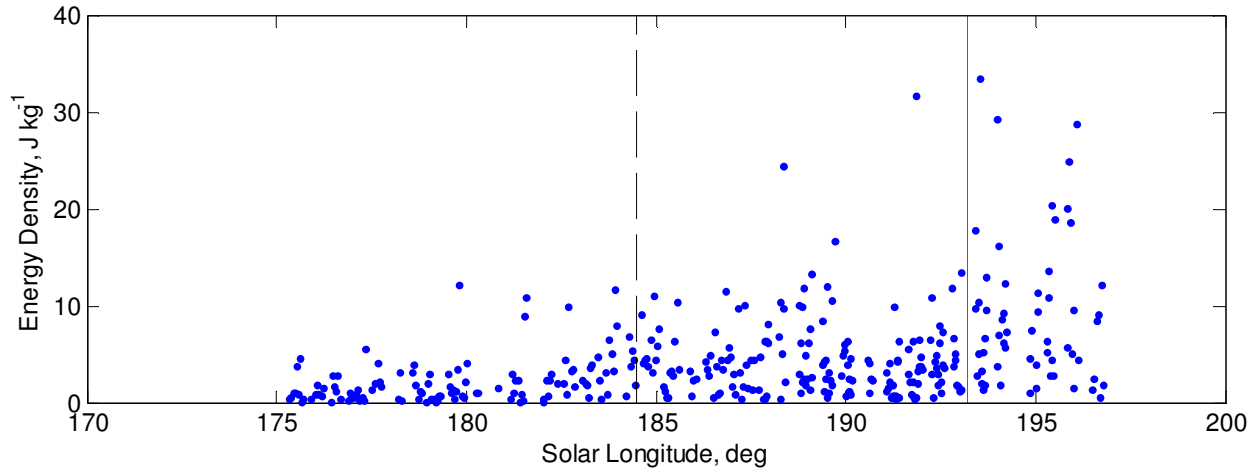
Figure 2.16: Distribution of gravity wave potential energy density at 10-15 km height during the onset of the 2001 planet-encircling dust storm. The dashed vertical line marks the start of the local dust storm near Hellas basin. The dust storm had intensified and expanded to engulf Mars by the solid vertical line.

Another factor considered in evaluating trends in gravity wave energy was the occurrence of global or planet-encircling dust storms. Planet-encircling dust storms on Mars occur near perihelion (L_s=251 deg) when solar heating is at a maximum. The global dust storms begin as small, localized dust storms that intensify and expand over a one or two week period to cover the entire planet [*Zurek*, 1982]. During a global dust storm, significantly elevated concentrations of atmospheric dust can extend up to 50 km altitude [*Anderson and Leovy*, 1978; *Clancy et al.*, 2003; *Smith*, 2003; *Clancy et al.*, 2010] and remain elevated for months [*Conrath*, 1975; *Martin and Richardson*, 1993]. These storms not only transport dust globally over the entire planet, but the atmospheric loading enhances solar heating and leads to a significantly altered thermal structure and atmospheric circulation [e.g. *Conrath*, 1975; *Pollack et al.*, 1979]. The MGS mission witnessed only one planet-circling dust storm while in orbit around Mars. That dust storm started in June 2001 (L_s=185 deg) and engulfed Mars for months [*Smith et al.*, 2002]. The onset of the 2001 storm occurred during a period of active occultation experiments, and the potential energy densities for the retrieved profiles are shown in Figure 2.16. There appeared to be a general upward trend in energy density as the storm expanded, but the data was limited by the small number of profiles retrieved before occultation measurements were suspended early in the storm when the MGS

orbit was nearly broadside as viewed from Earth. Regional and local dust storms, such as reported in *Smith et al*. [2000], are common occurrences on Mars during dust season. This study did not attempt to correlate gravity wave energy in the lower atmosphere with local and regional dust storm activity. However, as discussed in the next chapter, density profiles from the MGS accelerometer were analyzed to search for evidence of gravity waves at thermospheric heights [*Creasey et al*., 2006b] during the Noachis Terra regional dust storm that occurred in Phase I of aerobraking in 1997.

2.7   Wave Dissipation

In the absence of dissipation, the amplitude of a vertically-propagating gravity wave is expected to grow with height according to $\rho^{-1/2}$, as atmospheric density decreases [*Lindzen*, 1981]. From equation (2.11), one would also expect a corresponding increase in potential energy density due to the growth in temperature perturbation amplitude. In the MGS temperature profiles, mean potential energy density did not steadily increase with height, indicating that some gravity waves became saturated and were breaking down or encountered a critical level and were filtered by the background wind.

Evidence of gravity wave saturation can be seen in both example profiles in Figure 2.6, where temperature perturbation amplitudes were near constant or decreased with height. From *Lindzen* [1981] and *Holton* [1982], a wave begins to break at the level where the local temperature lapse rate is dry adiabatic:

$$-\frac{d(\bar{T} + T')}{dz} = \Gamma_d \,, \tag{2.15}$$

where $\Gamma_d \equiv g/c_p$ is the dry adiabatic lapse rate. This condition for wave breaking was met in the example profiles. Based on a large subset of profiles individually inspected, it was believed that gravity wave breaking and momentum deposition was common in Mars' lower atmosphere as larger amplitude waves became unstable. Evidence of critical-level filtering, where the phase speed of the gravity wave approaches the speed of the background flow, was not readily apparent in the temperature profiles inspected. That is not to say that critical level filtering did not occur; rather, critical levels were not actively searched for since the phase speed of the wave, the horizontal propagation direction of the wave,

and the background wind field were all not known. In short, a quantitative analysis of gravity wave dissipation was not performed on the MGS temperature profiles. Instead, the modeling effort for this research used momentum flux values calculated from potential energy densities at the lower edge of the height range investigated (10-15 km). This allowed the gravity wave parameterization to determine wave breaking and critical-level filtering in the lower atmosphere, rather than have those effects embedded and hidden in the source magnitude data.

The possibility that trapped mountain waves, or lee waves, were observed in the data was also investigated. Lee waves extend downwind from the generating obstacle and are trapped between the surface and a reflecting upper level. At Mars, lee wave clouds were frequently observed in Mariner 9 images between 40°N and 60°N latitude [Briggs and Leovy, 1974]. Using the Scorer parameter, an analysis was performed to assess whether conditions were suitable for trapped or evanescent mountain waves to exist. The Scorer parameter, L, defined as

$$L^2 = \frac{N^2}{u^2} - \frac{1}{u}\frac{d^2u}{dz^2}, \qquad (2.16)$$

where u is the background wind speed, indicates vertical trapping of linear waves generated at the surface [Scorer, 1949]. In equation (2.16), the first term on the right hand side is the stability term, and the second term is the curvature term. A mountain wave, formed by flow over topography, will propagate vertically if $L^2 > k^2$, where k is the horizontal wavenumber of the mountain ridge. Assuming the contribution from the curvature term is negligible, the minimum horizontal wavelength that will propagate vertically is given by

$$\lambda > 2\pi\frac{u}{N}, \qquad (2.17)$$

where λ is the horizontal wavelength determined from the zonally varying topography. Equation (2.17) shows that shorter horizontal wavelengths may be trapped by strong background winds or a layer with low static stability.

Because the low-level wind speed and direction were not known, the Scorer parameter could not be evaluated for individual temperature profiles. Instead, the Scorer parameter was evaluated for a

48

stressful case using the magnitude of the background zonal wind taken from the Mars Climate Database [*Lewis et al.*, 1999]. Using a typical value of N=0.6 x 10^{-2} s^{-1} for Mars [*Read and Lewis*, 2004] and an expected maximum low-level wind speed u~50 m s^{-1} at 9.6 km altitude from the Mars Climate Database, the minimum horizontal wavelength for a vertically propagating mountain wave was found to be 52 km. However, following *Preusse et al.* [2008], the minimum observable horizontal wavelength for occultation measurements was estimated at 50-100 km for vertical wavelengths between 7 and 14 km, the vertical wavelengths typically observed in MGS temperature perturbation profiles. It was therefore expected that vertically trapped waves would be observationally filtered in an occultation experiment under expected atmospheric conditions.

2.8   Measurement Errors

Errors were introduced in the retrieved temperature profiles during the occultation measurement and at several locations during the profile retrieval. Errors can be classified as random errors or systematic errors. Random errors occurred due to thermal noise, computational uncertainties, and random fluctuations in the propagation path [*Ahmad and Tyler*, 1999]. In the MGS profile retrieval process, the effects of the neutral atmosphere exceeded the noise level by a factor of 600 [*Hinson et al.*, 1999]. Thermal noise increased with height and became excessive above the 10 Pa level (~40-50 km), establishing the upper altitude limit for profile retrieval. In the ionosphere, thermal noise dominated above 200 km.

Systematic errors were highly correlated over an occultation measurement and arose from a number of sources, including HGA motion, perturbations in the radio signal from the solar wind and terrestrial atmosphere, reconstruction of the spacecraft trajectory, and departures from spherical symmetry, a key assumption in the profile retrieval algorithm [*Tyler et al.*, 1992; *Ahmad and Tyler*, 1999]. If known and characterized, systematic errors can be removed or reduced. HGA motions were evaluated and either modeled or deemed negligible [*Tyler et al.*, 1992]. The phase bias from the interplanetary plasma and terrestrial atmosphere was removed through signal processing, while the effects of the terrestrial troposphere and ionosphere were removed using calibration data from the DSN tracking

49

stations [*Tyler et al*., 1992]. The spacecraft trajectory was well known using precision orbits determined by the MGS RS gravity investigators [*Yuan et al*., 2001] resulting in a characteristic uncertainty in radius of ~1 m [*Tyler et al*., 2001]. Finally, the validity of the spherical symmetry assumption was addressed during profile retrieval.

Mars is far from spherical due to the planetary shape, atmosphere rotation rate, and complex gravity field. From *Ahmad and Tyler* [1999], large scale meridional gradients are possible on Mars, and surfaces of constant refractivity are tilted by as much as 4.5 mrad above 20 km altitude. If not accounted for in the retrieval process, a 3.0 mrad tilt would lead to a temperature error of 1.2%, or 2.4 K at 200 K. In the profile retrieval process, the assumption of spherical symmetry is invoked multiple times. If local spherical symmetry breaks down, errors are introduced each time the assumption is used. *Hinson et al*. [1999] modified their profile retrieval method to assume symmetry about the local center of curvature of the geoid rather than the planet's center of mass. Winds, however, can create a horizontal gradient in the shape of the atmosphere, leading to the loss of spherical symmetry. The effects of the wind field cannot be removed since the local winds at the time of the occultation measurement were not known. *Hinson et al*. [1999] noted that this did not appear to be an issue in the initial set of MGS temperature profiles retrieved. From *Hinson* [2008], the best source of information about the data quality of the temperature profiles are the uncertainties included with each profile. Uncertainties varied with height, from as low as 0.2% or ~0.4 K at the surface to 6% or 10 K at the 10 Pa level [*Hinson et al*., 1999; *Tyler et al*., 2001]. Across the 10,999 profiles used in this study, the mean temperature uncertainties were 1.2 K at 10 km and 1.6 K at 15 km height. The uncertainties were found to be highly correlated across a profile; if random in nature, the data would have been unusable for gravity wave investigations, even at the lowest heights.

Chapter 3

Mars Global Surveyor (MGS) Accelerometer (ACC) Data Analysis

The orbit insertion maneuver at Mars left MGS in a highly elliptical orbit with a periapsis altitude of 263 km and an apoapsis altitude of approximately 54,000 km. To achieve a low-altitude circular orbit around Mars, MGS used the aerobraking technique to slow the orbit with drag from the atmosphere. Aerobraking had previously been used successfully by Magellan at Venus [*Lyons*, 1994] and was required for MGS after the mission switched to the smaller Delta II launch vehicle and large propulsive maneuvers to reduce the orbit were no longer an option [*Albee et al*., 2001]. During aerobraking operations, the periapsis altitude was dropped deeper into the thermosphere with relatively small propulsive maneuvers at apoapsis. As the spacecraft dipped into the atmosphere to slow the orbit, the z-axis accelerometer in the spacecraft's IMU (Inertial Measurement Unit) obtained measurements of thermospheric density. The density profiles not only supported density predictions for follow-on aerobraking passages but also provided scientific data on the structure of Mars' upper atmosphere. During the aerobraking period, divided into two phases due to a broken solar array, 800 density profiles were obtained at altitudes ranging from 170 km to 110 km and across different seasons, latitudes, and local times of day [*Keating et al*., 2002]. The MGS thermospheric density profiles have mostly been used to study the propagation of thermal tides into the thermosphere [e.g. *Forbes and Hagan*, 2000; *Forbes et al*., 2002; *Withers et al*., 2003], but small-scale variations in the density profiles have also provided evidence of gravity waves [*Creasey et al*., 2006b; *Fritts et al*., 2006]. Much of this chapter has been reported in *Creasey et al.* [2006b], the first paper to quantify gravity wave variance in Mars' thermosphere. Due to spatial and temporal differences, the data analysis in this chapter was not quantitatively applicable to the follow-on

51

modeling work but is presented here to describe the observed gravity wave activity at thermospheric heights.

3.1   MGS ACC Measurements

3.1.1   Aerobraking Operations

Prior to the arrival of MGS at Mars, very little was known about the aerobraking regime of Mars' upper atmosphere. Data was limited to the entry profiles recorded on earlier Mars' lander missions. The lack of knowledge of the structure of the upper atmosphere was a challenge to the operations team to determine appropriate and safe depths for the spacecraft for each aerobraking passage. Aerobraking operations were further complicated by a damaged solar array panel, where the extent of the damage was not fully known until aerobraking was underway [*Albee et al.*, 2001]. Following solar array deployment during the cruise stage, it was clear that one solar array panel was not locked in the deployed position. Due to a failure in the damper arm that had prevented the panel from deploying fully, it was decided to aerobrake in a modified configuration with the orientation of the panel reversed.

MGS aerobraking began on the third orbit of Mars in September 1997. On orbit 15 in early October, excessive flexing of the damaged solar panel indicated there had also been damage to the yoke of the panel. The orbit periapsis was raised above aerobraking altitudes, and the entire aerobraking sequence was replanned to avoid high pressures that could result in loss of mission. Aerobraking resumed in November 1997 with less dynamic pressure on the solar panels. The density profile collected by the z-axis accelerometer during each pass through the atmosphere was critical in planning the next aerobraking passage, as the spacecraft trajectory for the next orbit was adjusted to a safe depth based on atmospheric density predicted from the previous density profile. The damaged solar panel also induced an oscillation in the spacecraft bus and the z-axis accelerometer which, when removed, reduced the spatial resolution of the science data. To achieve the optimal orbit for science observations where local time was 1400 (0200) on ascending (descending) passes, aerobraking was divided into two phases separated by a six month period. Phase I lasted from November 1997 through March 1998, with Phase II from September 1998 through February 1999. MGS eventually reached its near-circular mapping orbit in

52

March 1999, an entire Earth year later than planned. One benefit of the extended aerobraking period was an increase in the number of thermospheric density observations. Compared to the original mission profile, significantly more density profiles were collected, with greater temporal and spatial variation.

3.1.2   ACC Density Profiles

Acceleration measured by the z-axis accelerometer was used to compute the profile of atmospheric density encountered during each aerobraking passage into the upper atmosphere. The z-axis accelerometer was one of four accelerometers (x, y, z, and skew), along with four gyros, contained within the spacecraft's IMU located on the nadir deck. The z-axis accelerometer was the primary accelerometer used for density retrieval since the spacecraft was oriented with the z axis along the velocity vector during aerobraking. Atmospheric density was recovered using Newton's second law and the equation for the atmospheric drag force:

$$\rho = \frac{2ma_z}{V^2 C_z A}, \tag{3.1}$$

where m is the mass of the spacecraft, a_z is the acceleration due to aerodynamic forces, V is the spacecraft velocity, C_z is the drag coefficient of the spacecraft, and A is the spacecraft cross-sectional area normal to the velocity vector. The acceleration due to aerodynamic forces was only one component of the measured acceleration. Other acceleration terms included instrument bias, gravity gradient, thruster activity, and angular and translational motions [*Tolson et al.*, 1999]. Contributions from other accelerations and biases were removed from the measured acceleration. The accelerometer was sampled 10 times per second with a sensitivity of 0.332 mm s^{-1} per quantized count, which was 38 times more sensitive than the accelerometers on the Viking entry probes [*Tolson et al.*, 1999]. Data noise, after orbit 18 when all samples were transmitted, was constant throughout the aerobraking period due to active thermal control of the IMU and no pre-processing of data [*Tolson et al.*, 2007]. For operations, acceleration was determined every one second. For science investigations, data was reduced to density profiles averaged every 7 and 40 seconds and reported each second [*Keating et al.*, 2002]. The 40-s profile filtered out localized atmospheric wave activity to better estimate mean structure [*Keating et al.*,

53
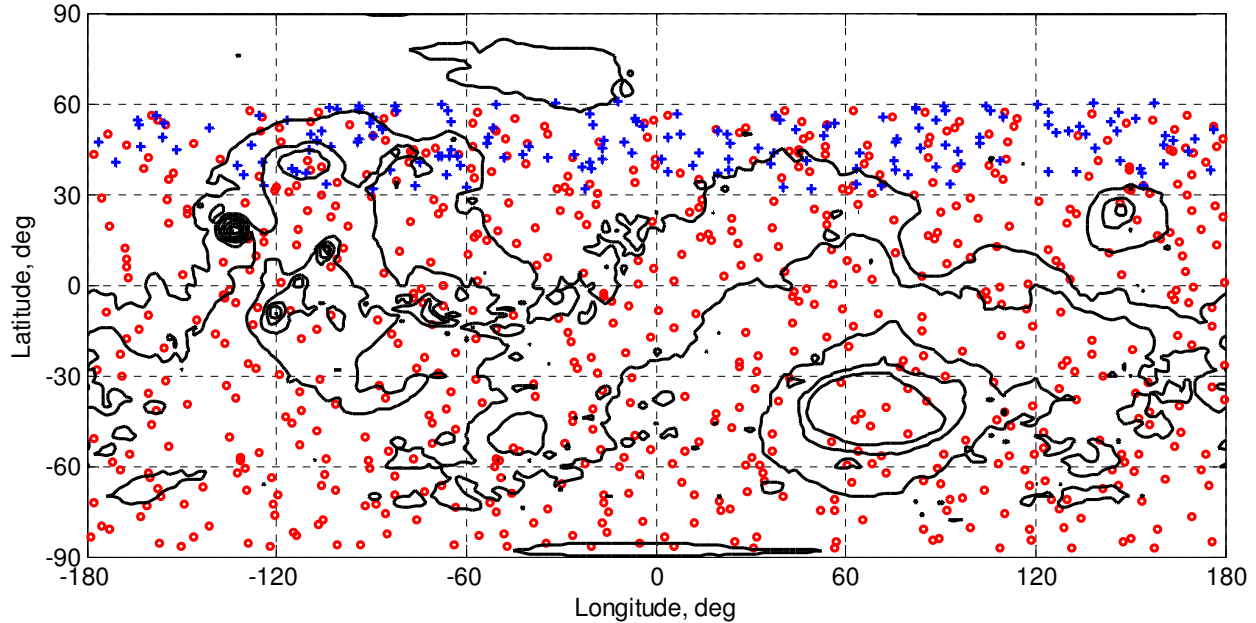
Figure 3.1: Distribution of accelerometer measurements relative to Martian topography. Each marker represents the periapsis location for one orbit, with blue plus symbols indicating Phase I and red circles indicating Phase II. Contour intervals are spaced every 3000 m.

1998]. The 7-s running mean removed the contribution from the oscillation induced by the damaged solar array, which had a mean value of approximately zero since the solar array panel returned to the same orientation relative to the spacecraft bus at the end of the aerobraking pass. If not for the solar panel oscillation, the high resolution data would have been reported every 1-s, as was done in the Mars Odyssey (ODY) mission [*Tolson et al.*, 2005]. Even though the 7-s averaging reduced the spatial resolution of the data, the 7-s running mean still retained significant small-scale structure.

The MGS accelerometer measurements, obtained from the NASA Planetary Data System [*Keating et al.*, 2002], have provided 800 inbound-outbound density profiles ranging from about 100 km to 170 km altitude and covering latitudes from 60°N to the south pole. The typical pass in the detectable atmosphere lasted roughly 400-s and spanned 30 degrees in latitude [*Tolson et al.*, 1999]. Figure 3.1 shows the relatively even geographical distribution of measurements. Phase I measurements were taken in northern late autumn and early winter in MY 23 at latitudes from 30°N to 60°N, while Phase II measurements spanned northern early spring to southern winter in MY 24 at latitudes from 60°N to 87°S.
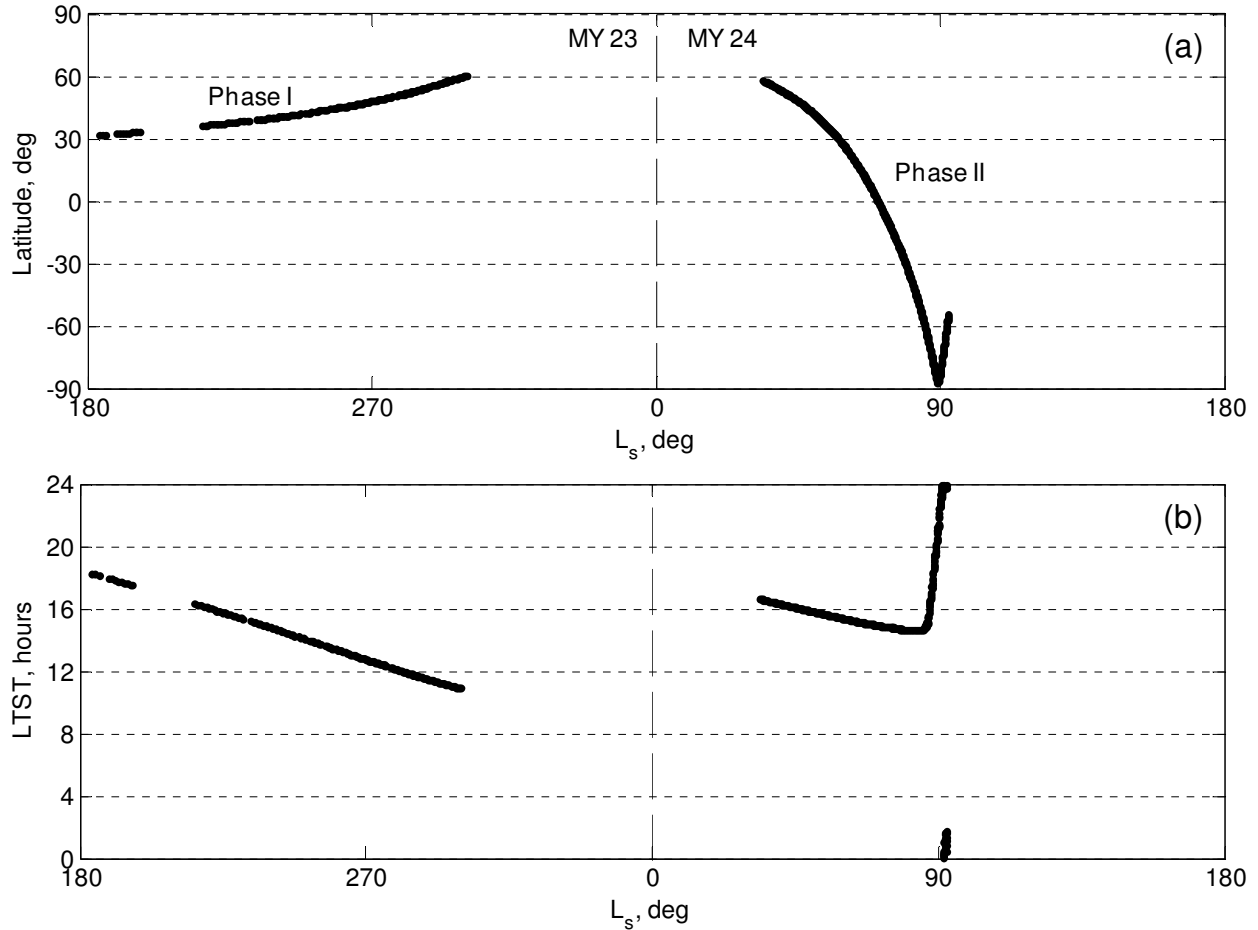
Figure 3.2: Latitude (a) and LTST (b) distribution of accelerometer measurements during Phase I and Phase II of MGS aerobraking.

Local true solar times ranged from approximately 1100 to 1800 in Phase I and from 1500 to 0200 in Phase II. Figure 3.2 shows the progression of L_s, periapsis latitude, and LTST during Phases I and II of aerobraking. All orbits with valid density profiles were used in this research, with the notable exclusion of profiles collected on orbits 911-961. Although these profiles possessed strong wave-like perturbations (red data points in Figure 3.4), they had been identified on the PDS site as anomalous due to a problem with one of the on-board computers [*Tolson et al*., 2000]. 1σ measurement uncertainties were included with all density profiles. Measurement errors were lowest at periapsis and increased with altitude.

The 7-s and 40-s running means for an example accelerometer profile are shown in Figure 3.3 (a). Data are shown for 100 seconds on either side of periapsis which represents the time span used in the
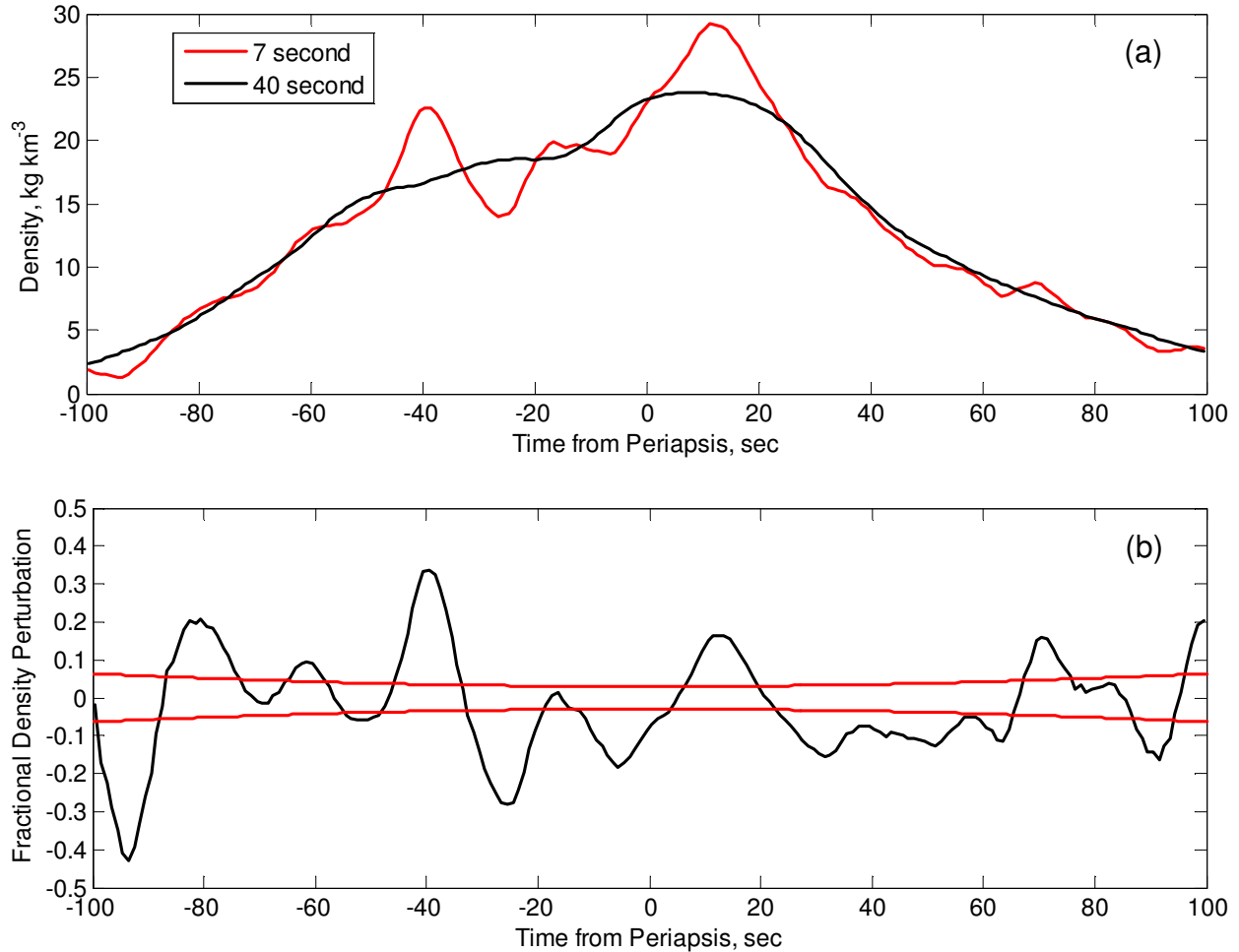
Figure 3.3: Example accelerometer profile P0179 showing (a) the 7-second and 40-second averaged density data, and (b) the corresponding fractional density perturbation. The red lines in (b) depict the 1σ measurement uncertainties.

density perturbation analysis later. Periapsis occurred at time equal zero with negative (positive) times indicating the inbound (outbound) density profile. For a typical mid-latitude density profile, 200-s about periapsis corresponded to roughly 12-15 degrees in latitude, 2 degrees in longitude, and 700-900 km along the orbital track. The height span for the reduced 200-s profile ranged from 15 km at the start of the aerobraking sequence to less than 1 km at the end.

The 40-s averaged density data included the background state plus atmospheric waves with near-horizontal scales greater than a few hundred km. In other words, it was not possible to separate the mean state from the large-scale waves using the density profile alone. The density at aerobraking altitudes

showed great variation over time, including large orbit-to-orbit differences. Upper atmosphere density at fixed altitude, latitude, and local time varied by factors of 2 or more as a function of longitude [*Withers et al.*, 2003]. The variability reflected the ability of energy to propagate upward from the lower atmosphere into the thermosphere. Using the 40-s averaged data, *Keating et al.* [1998] identified an unexpected periodicity of density versus longitude with peaks near 90°E and 270°E and interpreted the result as a wave-2 stationary planetary wave. *Forbes and Hagan* [2000], *Joshi et al.* [2000], and *Wilson* [2000] argued the observed structure was a non-migrating tide, specifically the diurnal Kelvin wave, that appeared as quasi-stationary due to the restricted sampling in local time, and their modeling studies confirmed the result. The modeling by *Forbes and Hagan* [2000] also indicated that significant global wind and temperature perturbations accompanied the density oscillations. Wave-2 structure observed during ODY aerobraking provided further evidence the diurnal Kelvin wave reaches the Mars' thermosphere [*Wang et al.,* 2006]. Further modeling studies [*Forbes et al.*, 2002; *Wilson*, 2002; *Withers et al.*, 2003; *Angelats i Coll et al.*, 2004] supported MGS observations that both wave-2 ($n = 1$, $s = -1$), and wave-3 ($n = 2$, $s = -1$) were the major contributors to the planetary-scale density variations in the thermosphere, where $n = 1$ (2) for the diurnal (semidiurnal) tide, s is the zonal wavenumber, and $n = 1$, $s = -1$ corresponds to the diurnal Kelvin wave. *Bougher et al.* [2001] also identified the $n = 2$, $s = -1$ tidal mode as the most likely cause of the wave-3 harmonic observed in the upper atmosphere electron density profiles. From *Forbes et al.* [2002], the non-migrating tides arise primarily from zonal asymmetries in near-surface solar forcing associated with Mars' topography. *Withers et al.* [2003] decomposed Mars' topography from the MGS MOLA instrument into zonal harmonics and found zonal wavenumbers of 1 through 4, consistent with the non-migrating tidal modes observed in the ACC density profiles.

3.2   Density Perturbation Analysis

The variability present in the 7-s averaged density profiles was due to small-scale gravity waves propagating into the thermosphere [*Creasey et al.*, 2006b; *Fritts et al.*, 2006]. The variations were seen not only during MGS aerobraking, but also in the 1-s density profiles captured during ODY and Mars Reconnaissance Orbiter (MRO) aerobraking at Mars [*Tolson et al.*, 2007]. To evaluate the structure of

these waves, the data analysis followed the approach used by *Fritts et al.* [1989, 1993] with Space Shuttle accelerometer data collected during Earth reentry and by *Kasprzak et al.* [1988] with PVO spectrometer data collected during orbiter entry at Venus. Following *Fritts et al.* [1989, 1993], the observed structure were presumed to be due to horizontal rather than vertical variations. The density perturbation ρ' was calculated by subtracting the mean density $\bar{\rho}$, taken here to be the 40-s averaged density data, from the 7-s averaged data. The fractional density perturbation, $\rho'/\bar{\rho}$, normalized the perturbations to the mean density. Mean and quadratic trends were removed from the fractional density perturbation profile. The quadratic trend was an artifact of the density gradient difference caused by the non-circular aerobraking orbit and the data averaging. Figure 3.3 (b) shows the fractional density perturbation corresponding to the density profile in (a) and is representative of the small-scale structure seen in many density profiles. Fractional density perturbations, which commonly exceeded 30% and at times were above 50%, were much stronger than those observed on Earth. Significant fractional density perturbations observed during Shuttle reentry were only on the order of 1-5% [*Fritts et al.*, 1989].

Measurement uncertainties, which included errors due to data noise and natural variability, were evaluated using the 1σ errors in the 40-s density data [*Keating et al.*, 2002]. Figure 3.3 (b) depicts the measurement uncertainty associated with the example profile. Height-averaged measurement errors of 0.2 to 0.6 kg km^{-3} were consistent with *Tolson et al.* [2000] and corresponded to 2% and 10% of mean density at heights of 110 km and 140 km respectively.

Wave spectral power was evaluated using Parseval's relation for the discrete Fourier transform (DFT) [*Oppenheim and Schafer*, 1989] which relates a discrete-time signal's total energy to its total spectral energy:

$$\sum_{n=-\infty}^{\infty} |x[n]|^2 = \frac{1}{2\pi}\int_0^{2\pi} |X(\omega)|^2 d\omega \,, \tag{3.2}$$

where $x[n]$ is the discrete-time signal, the fractional density perturbation profile in this case, and $X(\omega)$ is the spectrum of the signal. This approach was also used by *Forbes et al.* [1995] investigating wave structures in density profiles of Earth's thermosphere. In the present research, the figure of merit was the

58
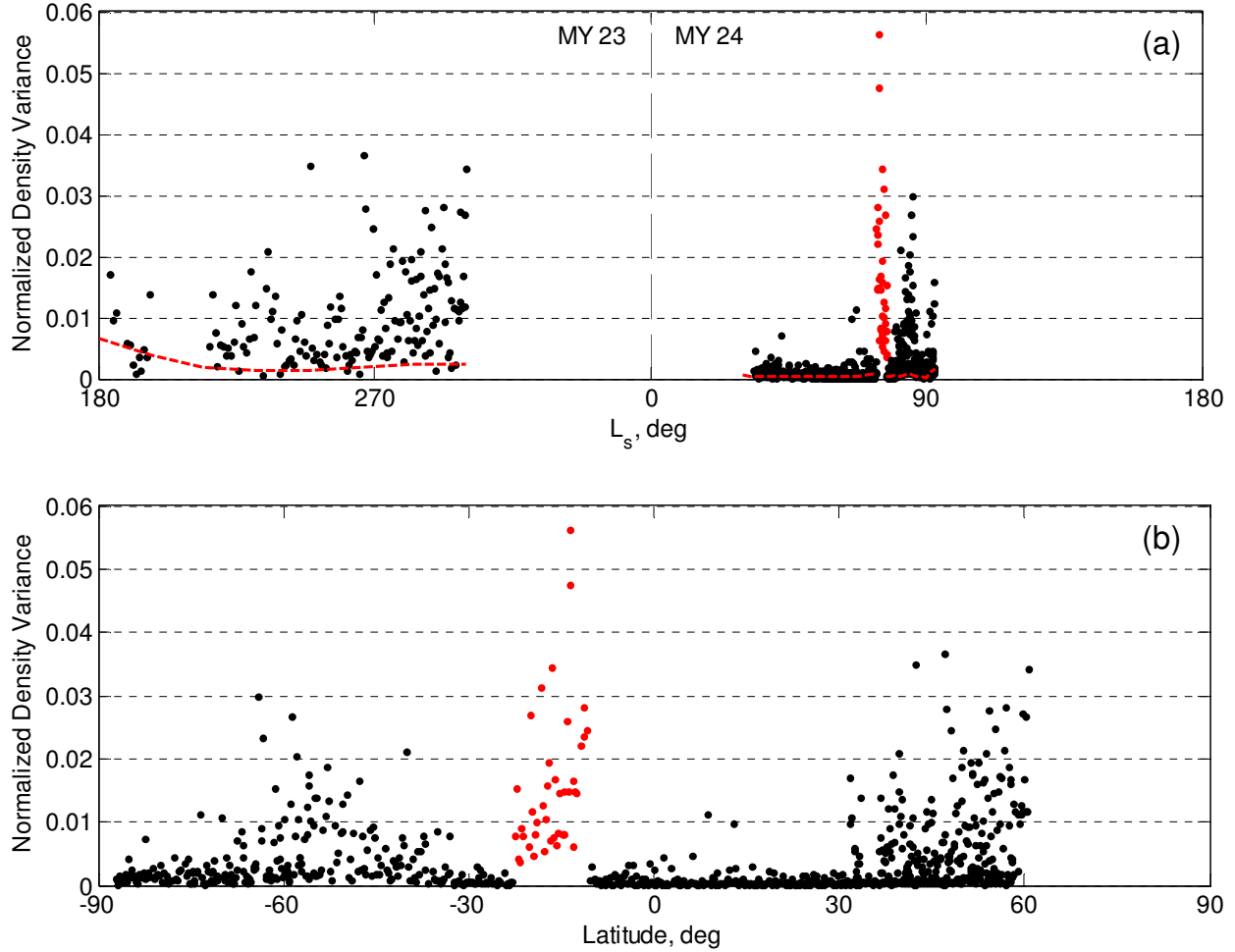
Figure 3.4: Fractional density perturbation variance computed for each profile as a function of (a) Martian year and (b) latitude. Red markers indicate unused data on orbits 911-961. The dashed red lines in (a) represent the density profile measurement uncertainty.

variance of the zero-mean fractional density perturbation, which from equation (3.2) is equal to the spectral power across the observed spatial frequencies. Observed wavelengths were constrained by the data averaging to roughly 50-200 km. The 40-s running mean filtered out most of the energy from wave structures with wavelengths greater than approximately 200 km, and from the Nyquist sampling theorem, the 7-s running mean established a minimum wavelength of 50-60 km.

3.3   Evaluation of Gravity Wave Activity

The fractional density perturbation variance was calculated for each density profile as a measure of the small-scale wave activity encountered in the upper atmosphere during the aerobraking passage.

Figure 3.4 shows the variance calculated as functions of both Martian year and latitude. The dashed red lines represent the variance due to measurement error. Red data points were marked as anomalous in the PDS dataset and are not discussed in the results. In panel (a), elevated density perturbations occurred throughout Phase I and in the latter part of Phase II with a relatively quiet period for the first half of Phase II. Panel (b) shows that elevated perturbations occurred over middle latitudes (roughly 35°-60° latitude) in both hemispheres with much lower variance in the tropics and in high southern latitudes. No correlation was found between the location of elevated density perturbations in the thermosphere and the temperature perturbations in the lower atmosphere reported in Chapter 2 and in *Creasey et al*. [2006a], where gravity wave energy was observed to be much stronger over the Martian tropics and, to a lesser degree, over areas of significant topography.

Given the progression of the measurements through areocentric longitude, latitude, and LTST, periods of density perturbations could be contrasted by season, hemisphere, and local time. Figure 3.5 compares fractional density perturbations at northern mid-latitudes, at the same local time, but in different seasons. In this figure, the fractional density perturbations of all profiles in a given period are plotted on top of one another to provide a visual indication of the magnitude and scale of the observed perturbations. Panel (a) occurred during Phase I of aerobraking from orbits 5-66 starting at northern autumn equinox in MY 23 and lasting through late northern autumn. Panel (b) occurred during Phase II from orbits 674-718 in late northern spring in MY 24. In both panels, the latitude range was the same (32°N to 40°N), and the local times were late afternoon. Significant small-scale wave activity was observed during northern autumn, where mean perturbation variance was 13 times higher than in northern spring. In northern spring, density fluctuations were mostly within the 1σ measurement error. These results may be explained by filtering by the zonal mean winds associated with the middle atmosphere jets. From the Mars Climate Database [*Forget et al*., 1999], westward propagating waves may have encountered a critical level in late spring but been allowed to propagate upward to the thermosphere against the eastward zonal winds in autumn. The eastward mid-latitude jet in the northern hemisphere intensifies from autumn to winter. In the ODY aerobraking density profiles that occurred at northern latitudes in winter, *Fritts et*
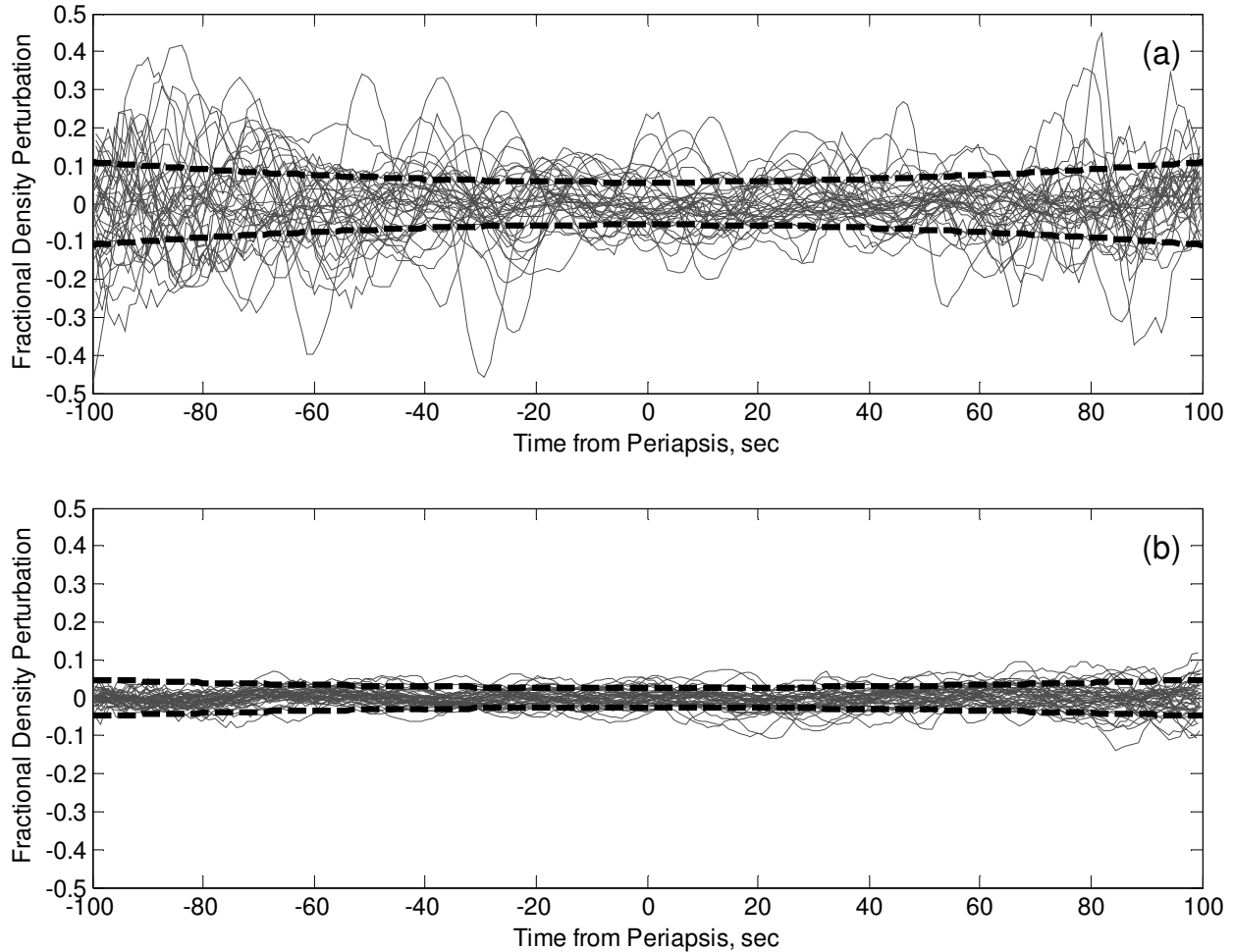
Figure 3.5: Seasonal contrast of fractional density perturbations between (a) northern autumn and (b) northern spring. Profiles in (a) occurred on orbits 5-66, at 32°N-40°N periapsis latitude, 1500-1800 LTST, and L_s 183-237°. Profiles in (b) occurred on orbits 674-718, at 32°N-40°N periapsis latitude, 1530-1600 LTST, and L_s 51-57°. Dashed lines depict 1σ measurement errors.

al. [2006] reported large fractional density perturbations, occasionally as large as 60%, in the thermosphere. Given that similar eastward mid-latitude jets were likely encountered, the propagation of gravity waves to the thermosphere in MGS northern autumn and ODY northern winter indicates consistent gravity wave forcing or spectral characteristics between datasets.

The results were also consistent with the gravity wave energy densities observed in the lower atmosphere. From Figure 2.12 and Figure 2.13, the global distribution of potential energy density at 10-15 km altitude was greater in northern autumn than in northern spring. The differences in wave energy in

the lower atmosphere may have been due to seasonal-dependent gravity wave sources, filtering by the intervening winds, or a combination of both. As pointed out by *Fritts et al.* [2006], however, the gravity waves observed by *Creasey et al.* [2006a] in the MGS radio occultation data were likely not the same waves observed in aerobraking density profiles in Mars' thermosphere. The minimum horizontal wavelength observable in radio occultation measurements is on the order of 100-200 km [*Preusse et al.*, 2008], while the 40-s averaging in the thermospheric density profiles observationally filtered out wavelengths of 200 km and greater. Also, from momentum flux calculations in *Fritts et al.* [2006], vertical wavelengths were estimated at ~45-85 km, much greater than the 8-15 km vertical wavelengths associated with the observed lower atmosphere gravity waves. The relatively short horizontal scale and long vertical scale of the thermospheric waves were consistent with the *Miyoshi et al.* [2011] excitation of non-tidal gravity waves associated with the breaking and dissipation of diurnal or semidiurnal tides in the middle atmosphere. Because of the differences in spatial scales, there was no observational evidence either way that the gravity waves observed in the lower atmosphere propagate to the thermosphere. The gravity waves may be of middle/upper atmospheric origin as in *Miyoshi et al.* [2011], but other sources in the lower atmosphere may have been involved. Assuming a universal spectrum of gravity waves [e.g. *ZanVandt*, 1982], it is plausible to suggest the gravity wave forcing that excited the waves seen in the radio occultation temperature profiles in the lower atmosphere was also responsible for the small-scale wave structure observed in the thermosphere.

Figure 3.6 compares fractional density perturbations in (a) northern hemisphere winter to (b) southern hemisphere winter. In each case, the gravity waves were expected to have propagated through the eastward winter zonal jet to reach the thermosphere. Latitude bands were comparable (54°N to 60°N versus 54°S to 65°S), but local times differed slightly (1100 versus 1500 LTST). Although density perturbations were elevated in both hemispheres, mean variance was 50% higher in the northern hemisphere. Given the higher orographic variance in the southern hemisphere at these latitudes, this result suggested that small-scale waves observed in the thermosphere may not be heavily influenced by the underlying topography. The difference in variance may also be explained by year-to-year variability

as panel (a) occurred in Phase I of aerobraking in MY 23, while panel (b) was from Phase II in MY24. Figure 3.6 also provides a local time contrast during southern winter. During Phase II of aerobraking, the progression of periapsis around the south pole allowed density profiles to be collected at high southern latitudes over a wide range of local times. Fractional density perturbation profiles in panel (b) occurred 8-12 sols before southern winter solstice (L_s = 84-86°) near 1500 LTST, while the profiles in panel (c) were collected a few sols after the solstice (L_s = 91-93°) near 0200 LTST. The latitude band was the same for both sets of profiles. At 1500 LTST, variance was two times greater than at 0200 LTST, which may be evidence of a difference between daytime and nighttime filtering by tidal related winds.

Because the above comparisons occurred in mutually exclusive time periods and in some cases different Martian years, it is possible that the results were influenced by temporal events. One such event during Phase I of aerobraking was the Noachis dust storm, which began as a localized disturbance in the Noachis Terra region in the southern hemisphere and precipitated rapid heating and expansion of the atmosphere. Although the effects of the storm were observed globally and lasted from orbits 50-100 (L_s = 225-260°), the storm was classified as regional since the area of high dust opacity remained confined to Noachis and adjacent regions [*Keating et al*., 1998]. During the dust storm onset and decay, thermospheric mass densities increased three-fold due to atmospheric expansion, and dust opacities in the northern hemisphere, where aerobraking passages occurred during the storm, increased by a factor of 2 [*Bougher et al*., 1999]. *Bougher et al*. [1999] believed that planetary, tidal, and gravity wave effects would be important in large dust storms to account for the additional dynamical heating not provided by the lower atmosphere. However, as seen in Figure 3.4, no noticeable change in perturbation variance was observed in this time period when compared to the periods immediately before and after. Further, no correlation was found with the regional and local dust storms reported by *Smith et al*. [2000], although it should be noted that the TES instrument, used to determine dust opacity, was not operated during Phase II of aerobraking.
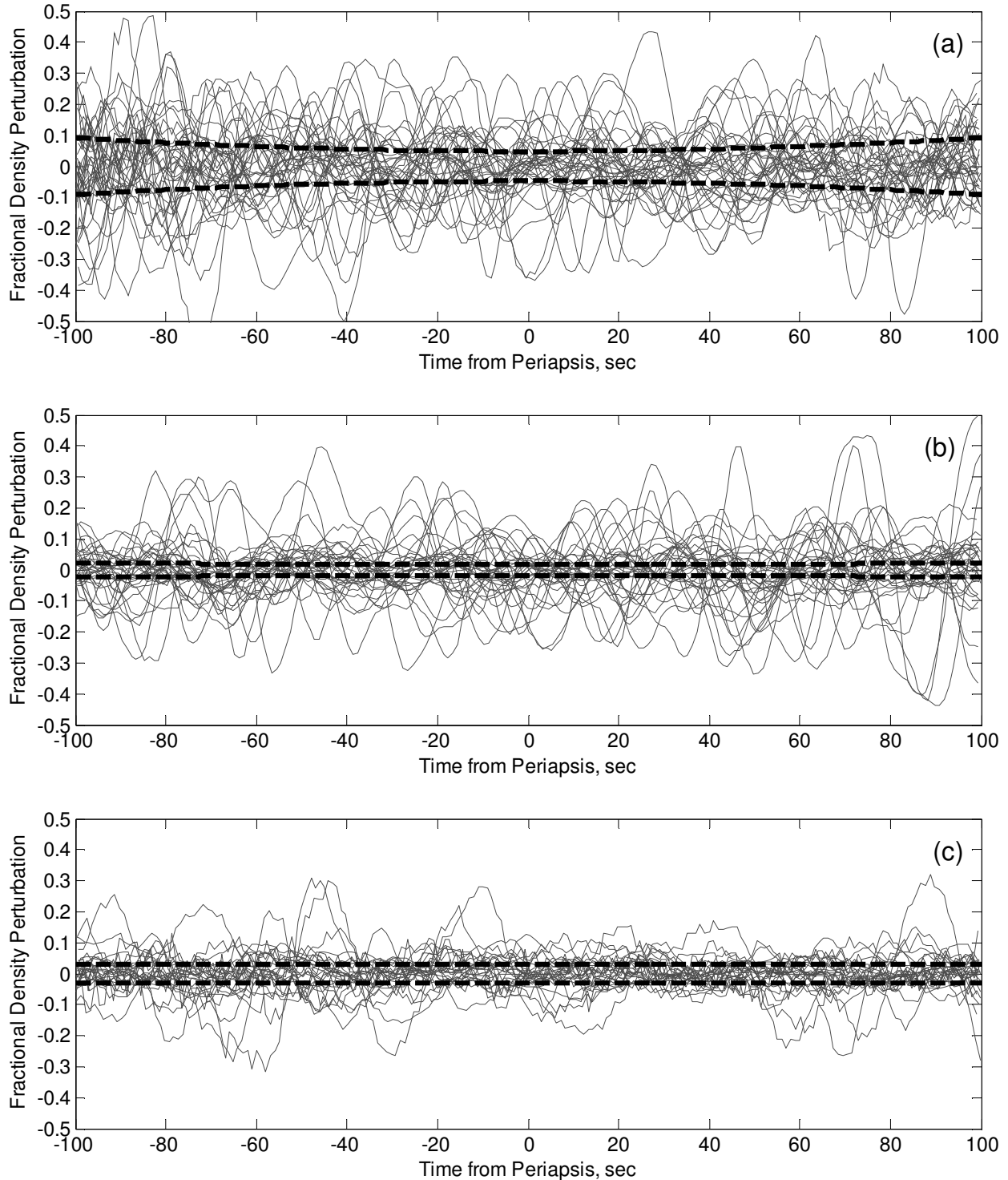
Figure 3.6: Hemisphere contrast between (a) northern hemisphere winter and (b) southern hemisphere winter, and local time contrast between (b) daytime and (c) nighttime. Profiles occurred on (a) orbits 158-201, at 54°N-60°N periapsis latitude, 1100-1200 LTST, and L_s 286-300° (24-47 sols past northern winter solstice), (b) orbits 1081-1115, at 54°S-65°S periapsis latitude, 1500 LTST, and L_s 84-86° (8-12 sols before southern winter solstice), and (c) orbits 1254-1283, at 54°S-65°S periapsis latitude, 0200 LTST, and L_s 91-93°. Dashed lines depict 1σ measurement errors.

64

3.4   Summary

The MGS Accelerometer provided observational evidence that gravity waves not only reach thermospheric heights but cause significant fluctuations in the density field. The data enabled contrasts of gravity wave activity by season, hemisphere, and local time of day which may prove useful in future studies of Mars' thermosphere. The data began to answer the science questions related to thermospheric gravity waves, but further data is required to better understand thermospheric gravity wave sources and the intervening wind field. Overall, however, the data was not suitable to further constrain gravity wave forcing in the follow-on modeling work which assumed gravity waves of lower atmosphere origin only. Due to differences in horizontal and vertical scales, the gravity waves observed in the thermosphere were not the same types of waves observed the lower atmosphere temperature profiles. The gravity waves may have differed further with respect to propagation direction, phase speed, and wave frequency. How the lower atmosphere gravity waves and thermospheric gravity waves relate could not be determined. As implied by *Miyoshi et al.* [2011], the gravity waves in the thermosphere may have been of middle atmosphere origin and unrelated to gravity wave activity in the lower atmosphere.

Chapter 4

Model Descriptions and Inputs

The interactions of gravity waves with the mean flow occur on scales much smaller than the resolutions of current dynamical models, where resolutions are limited by computational capabilities. Horizontal scales of gravity waves are typically measured in tens to hundreds of kms, while the horizontal resolutions of existing models for Mars, as well as for Earth, are on the order of 3.75 to 5 degrees in latitude and longitude [e.g. *Lewis et al*., 1999; *Forbes and Miyahara*, 2006] which corresponds to roughly 200-300 km at Mars' equator. In order for gravity waves to be included in the dynamical model in a physically meaningful way, their effects must be parameterized. In other words, the dynamics of individual gravity waves are not modeled directly. Instead, the parameterization models the propagation, energy transport, and dissipation of a spectrum of gravity waves given assumptions on the wave characteristics and fluxes of the gravity wave field emanating from the source region. For Mars, existing gravity wave parameterizations have not been constrained by observed gravity wave fluxes, since until *Creasey et al*. [2006a] this data was not available. As such, the parameterized effects of gravity waves in Mars modeling studies to date may not be accurate in terms of effect and magnitude.

For Earth, there exists a number of gravity wave parameterization schemes used in general circulation models [e.g. *Lindzen*, 1981; *Matsuno*, 1982; *Hines*, 1997; *Alexander and Dunkerton*, 1999; *Medvedev and Klaassen*, 2000; *Meyer*, 1999a, 1999b; *Yiğit et al*., 2008]. In adapting such parameterizations for Mars, the underlying gravity wave theory remains unchanged. Thus, a gravity wave parameterization applied to Earth is mechanically similar to the same parameterization applied to Mars. Although gravity wave parameterization schemes can be significantly different, they are similar in their

use of the dispersion relation, the WKB approximation, and upward energy propagation from linear gravity wave theory. Their differences lie in the treatment of the disturbances as spectrally discrete or continuous and in the mechanism by which the gravity waves are dissipated as linear or nonlinear.

This chapter describes the gravity wave parameterization developed for this research and incorporated into the Mars dynamical model of *Forbes and Miyahara* [2006]. This chapter also discusses how inputs to the gravity wave parameterization were defined for the model runs in Chapter 5, including how the gravity wave vertical flux of horizontal momentum was determined directly from the potential energy distributions calculated in Chapter 2.

4.1   Gravity Wave Parameterization

This research developed a Mars-specific version of the hybrid Lindzen-Matsuno gravity wave parameterization originally applied to the study of gravity wave and planetary-scale wave interactions on Earth [*Meyer*, 1999a, 1999b]. This hybrid scheme is based on the linear saturation parameterization of *Lindzen* [1981] and the atmospheric transmission parameterization of *Matsuno* [1982]. Prior to this research, Mars modeling studies mostly used Lindzen schemes for dissipation [*Barnes*, 1990; *Théodore et al.*, 1993; *Joshi et al.*, 1995; *Forget et al.*, 1999; *Collins et al.*, 1997] or modeled small-scale wave effects as Rayleigh friction [*Forbes and Miyahara*, 2006]. In more recent work, the GCM used by *Hartogh et al.* [2005] employed the spectral parameterization of *Medvedev and Klaassen* [2000], while *Medvedev et al.* [2011] used the scheme of *Yiğit et al.* [2008], which included the effects of eddy and molecular diffusion, in addition to nonlinear dissipation, thermal conduction, and ion drag. With the exception of *Medvedev et al.* [2011], these models extended in altitude only to the middle atmosphere or lower thermosphere.

4.1.1   Lindzen Parameterization

In the Lindzen scheme [*Lindzen*, 1981], a wave propagates vertically with exponential amplitude growth until an altitude is reached where the wave becomes convectively unstable. Above this saturation level, the wave will break or destabilize, generating small-scale turbulence that prevents further growth of the wave with height. The momentum carried by the wave will be deposited into the mean flow, and the resulting zonal force can be calculated.

From *Lindzen* [1981] and *Holton* [1982], the condition for wave saturation is met at the height, z_b, where the local temperature lapse rate produced by the combined wave and mean temperature fields is dry adiabatic. This wave saturation condition, from equation (2.15), can be rewritten as:

$$\left|\frac{dT'}{dz}\right| = \frac{N}{(\bar{u}-c)^{3/2}}\frac{B\Gamma e^{z/2H}}{k(u_0-c)^{1/2}} = \Gamma, \tag{4.1}$$

where B is the wave amplitude, $\Gamma = \Gamma_d - \bar{\Gamma}$ is the difference between the dry adiabatic and basic state lapse rates, $\bar{u}(z)$ is the mean zonal wind field, and u_0 is the zonal wind speed at the wave source level. The breaking level is determined implicitly from equation (4.1):

$$z_b = 3H\ln\left(\frac{|\bar{u}-c|}{\tilde{u}}\right), \tag{4.2}$$

where $\tilde{u}$ is a measure of the horizontal perturbation amplitude defined as

$$\tilde{u} = \sqrt[3]{\frac{2N\overline{u'w'}}{k}}, \tag{4.3}$$

where $\overline{u'w'}$ is the averaged vertical flux of horizontal momentum. Above z_b, turbulent diffusion produced by wave breaking limits the growth of wave amplitude. To maintain thermal balance, the eddy diffusion, ν_{eddy}, that satisfies the saturation condition is given by

$$\nu_{eddy} = \frac{k(\bar{u}-c)^4}{N^3}\left[\frac{1}{2H} - \frac{3}{2}\frac{d\bar{u}/dz}{(\bar{u}-c)}\right]. \tag{4.4}$$

Equation (4.4) is valid above the breaking level, z_b, unless a critical level ($\bar{u} = c$) is encountered. The *Holton* [1982] formulation includes a constant, A, in equation (4.4) to account for spatial and temporal averaging of gravity wave effects. In practice, the constant is typically treated as a tunable parameter to achieve a desired forcing in the mesosphere. In this study, the eddy diffusion profiles are not tuned (i.e. $A = 1$). The momentum flux divergence, f_x, produced by wave saturation is

$$f_x = -\frac{N^2}{(\bar{u}-c)}\nu_{eddy}. \tag{4.5}$$

68

The momentum flux divergence accelerates or decelerates the zonal mean flow towards the phase speed of the wave. Equations (4.4) and (4.5) are valid for $z_b < z < z_c$, where z_c is the critical level where intrinsic phase speed is zero.

4.1.2 Matsuno Parameterization

The Matsuno parameterization scheme [*Matsuno*, 1982] is based on the *Plumb and McEwan* [1978] formulation for the instability of a standing forced wave and assumes eddy and molecular viscosity are present everywhere in the atmosphere. Dissipation through eddy or molecular diffusion deposits momentum in the middle atmosphere and thermosphere. The acceleration due to the divergence of wave momentum flux is

$$f_x = -\frac{1}{\rho}\frac{\partial F_x}{\partial z}, \tag{4.6}$$

where F_x is the zonal component of momentum flux transported by the wave and is given by

$$F_x = 2 \int\limits_0^{c_{max}} \int\limits_0^{\pi} F_\theta(c,\theta,z) \cos\theta \, d\theta \, dc. \tag{4.7}$$

Here F_θ represents the vertical flux of horizontal momentum in the direction of angle θ due to a wave component of phase speed c and can be expressed as

$$F_\theta(c,\theta,z) = F_\theta(c,\theta,z_0)\tau(c,\theta,z_0,z). \tag{4.8}$$

where τ is the transmissivity of the atmosphere to a given wave given by

$$\tau(c,\theta,z_1,z_2) = \exp\left[-\int_{z_1}^{z_2} \frac{2\nu(z')N^3}{k[c - \bar{u}(z')\cos\theta]^4}dz'\right], \tag{4.9}$$

where $\nu(z)$ is the vertical diffusion profile and z_1 and z_2 define the height range considered. In the absence of eddy or molecular viscosity, transmissivity equals 1. Transmissivity approaches 0 (complete attenuation) as viscosity increases or as intrinsic phase speed approaches zero.

The Matsuno parameterization assumes that eddy diffusion is based on the attenuation of the gravity waves themselves, and the source mechanism for the turbulence is not addressed. Instead of calculating eddy diffusion, the vertical profile of eddy diffusion is prescribed.

69

4.1.3   Hybrid Lindzen-Matsuno (HLM) Parameterization

The hybrid Lindzen-Matsuno gravity wave parameterization used in *Meyer* [1999a, 1999b] combines the middle atmosphere mechanical forcing of the Lindzen parameterization with the upper atmosphere molecular diffusion of the Matsuno parameterization. The Lindzen scheme is useful in the middle atmosphere, but does have limitations. It does not include the effects of molecular dissipation on waves in the upper atmosphere and does not address critical level interactions. The Matsuno scheme complements the Lindzen scheme by addressing these shortcomings. In the Matsuno formulation, the mechanisms for eddy diffusion are not addressed and eddy diffusion must be prescribed. These limitations prevent it from being implemented as a standalone parameterization. Used together, however, the two schemes model both gravity wave eddy diffusion and molecular diffusion from the source level into the thermosphere. The Lindzen scheme dominates in the middle atmosphere and lower thermosphere, while the Matsuno scheme is important in the thermosphere where molecular diffusion dominates and near critical levels.

The HLM parameterization models a spectrum of waves discretely. Each wave is defined by its phase speed and magnitude at the source level. The phase speed, c, cannot be determined from radio occultation measurements and must be estimated from typical values used for Earth (see Section 4.3.4). Using equation (4.3), the source magnitude, $\tilde{u}$, is determined directly from the vertical flux of horizontal momentum, $\overline{u'w'}$, which was calculated from the potential energy densities derived from radio occultation temperature profiles (see Section 4.3.3). Because the diffusion from one wave can affect the growth and breaking level of another wave, multiple iterations are needed until the solution has converged. In the HLM formulation, the transmissivity of the atmosphere to a given wave affects its breaking level such that equation (4.2) becomes

$$z_b = 3H \ln\left(\frac{|\bar{u} - c|}{\tau^{2/3}\tilde{u}}\right), \tag{4.10}$$

with $\tau = 1$ for conservative propagation for the first iteration. Eddy diffusion is calculated above the breaking level until a critical level is encountered or the saturation condition is no longer satisfied. If the

combined wave and mean lapse rate change such that the saturation condition is not met, the wave resumes exponential growth until a secondary breaking level or critical level is reached. To avoid abrupt changes in the forcing at the breaking level, an exponential decay is applied below the breaking level over approximately one scale height. The transmissivity profile for a given wave is determined using equation (4.9) with $\nu = \nu_{mol} + \nu_{eddy}$. Here the vertical profile of molecular diffusion, ν_{mol}, is defined by $\nu_{mol} = 3.128\, T^{0.69}\rho^{-1}$ x 10^{-7} m^2 s^{-1} for the CO_2 Martian atmosphere [*Medvedev et al.*, 2011] where T and ρ, which are functions of height and latitude, are taken from the simulation. If a critical level is encountered, the transmissivity of the wave will go to zero, which is the mechanism in the Matsuno parameterization for depositing momentum when a wave is obliterated by critical level filtering. In successive iterations, wave breaking is re-calculated using the transmissivity profile from the previous iteration. Through equation (4.10), the eddy and molecular diffusion present in the atmosphere act to limit wave amplitude growth and result in slightly higher breaking levels. The eddy diffusion profile is then calculated above the new breaking level, and the process repeats until the diffusion profiles have converged.

The acceleration imparted to the mean flow by each wave is calculated using the final transmissivity profile and equations (4.6) through (4.8). It can be shown for a transmissivity profile where $\nu_{mol} = 0$ and $\nu(z) = \nu_{eddy}(z)$ that these equations reduce to equation (4.5) of the Lindzen scheme. Thus, the vertical profile of acceleration can be calculated from the combined eddy and molecular diffusion, as opposed to managing each separately. This approach is similar to the scheme of *Yiğit et al.* [2008] if only the linear and molecular terms were included.

The HLM parameterization scheme used in this research does have limitations. First, all gravity wave propagations are assumed to be vertical only. Horizontal propagation of gravity waves is ignored. Also, all gravity wave accelerations drive the zonal mean flow only, as gravity wave interactions with the meridional wind are not included. Also not included are possible nonlinear and wave-wave interactions. Finally, like all other gravity wave parameterizations, this parameterization assumes the validity of the

WKB approximation, which states that an approximate solution can be found if the mean state is assumed to vary more slowly in the vertical than does the phase of the wave. Departures from the WKB approximation affect the local validity of the dispersion relation. In the work of *LaPrise* [1993], the WKB approximation was affected by transient influences. However, over an extended duration, the averaged values predicted with the WKB approximation were similar to the results of a full solution model. Thus, in this study, it was assumed that the zonally averaged fields and gravity wave parameters mitigated local violations of the WKB approximation, if any were to exist.

4.2   QNLM Numerical Model

The Mars-specific hybrid Lindzen-Matsuno gravity wave parameterization was incorporated into the time-dependent 2-D (height, latitude) quasi-nonlinear model (QNLM) of Miyahara and Forbes that had already been developed and tested for Mars' atmosphere [*Forbes and Miyahara*, 2006]. QNLM is a global numerical model currently configured for Earth, Mars, and Titan that simulates the propagation of one or more linearly independent planetary-scale waves interactively with the zonal mean flow. The output of the model reflects the contributions of the waves to the zonal mean zonal, meridional, and vertical motions and the zonal mean temperature distribution. Although a mechanistic model and not a full replacement for a full 3-D GCM, the QNLM was sufficient to address the science questions for this research.

4.2.1   Model Description

In the QNLM model, the primitive equation system is separated into a zonally averaged equation system and a perturbation equation system (i.e. mean flow and planetary-scale tidal waves), and the two equation systems are integrated simultaneously until a steady state is reached. The full equation system and boundary conditions can be found in *Miyahara and Wu* [1989]. The wave solution is determined from the zonal mean temperatures and winds induced by solar heating, in addition to the contributions to the zonal mean fields by momentum deposition due to the waves. The zonal mean equations are non-linear, as are the interactions between waves and the mean flow. Wave-wave interactions are neglected, so that waves only interact with other waves indirectly via modifications to the mean flow through

dissipation and momentum deposition. The model can be configured for low, intermediate, and high dust conditions corresponding to normal-incidence optical depths of $\tau = 0.5$, 2.3, and 5.0 respectively [*Leovy and Zurek*, 1979; *Zurek*, 1986]. As optical depth increases, the proportion of solar insolation that thermally drives the atmosphere also increases. To isolate the effects of gravity waves on the mean state of the atmosphere, the model was run under low-dust conditions, and planetary-scale tidal waves (i.e. zonal wavenumbers $s = 1$ or $s = 2$) were not included in the simulation. Longer wavenumber tidal components embedded in the gravity wave energy distributions were captured in the input momentum flux profile.

The global mean atmosphere follows the empirical model of *Stewart* (1987) for southern hemisphere summer solstice ($L_s = 270°$) and average solar and dust conditions. Temperature profiles by Mars season are shown in Figure 4.1. From the surface, temperature decreases linearly to the middle atmosphere, where the temperature field is isothermal. In the thermosphere, temperature increases to an exospheric value of 230-250 K above 170 km. Zonal mean forcing was driven by heating rates which were antisymmetric about the equator at solstice and symmetric about the equator at equinox. The vertical distribution was Gaussian shaped, and from *Forbes and Miyahara* [2006], peak amplitudes and altitudes were chosen to approximate the wind fields from Mars GCMs and the temperature field from MGS TES observations [*Smith et al*., 2001b]. Heating rates were initially configured for $L_s = 270°$ and then seasonally adjusted by modifying the peak altitude in the thermosphere based on seasonal scale height differences and by scaling the heating rate profile by the relative Sun-Mars squared distances. Due to the eccentricity of Mars's orbit, solar flux (W m^{-2}) at perihelion is 40% greater than at aphelion. Radiative cooling was modeled using the Newtonian cooling parameterization from *Forbes et al*. [2002]. Solar average conditions were assumed across all seasons.

Prior to this work, gravity wave drag in QNLM was simulated not through a gravity wave parameterization but rather through Rayleigh friction, with a distribution peaking at 5 sol^{-1} near 80 km, the estimated saturation level for topographic gravity waves in Mars' atmosphere [*Joshi et al*., 1995]. Rayleigh friction schemes provide the zonal drag mechanism to alter the large-scale wind, but they only

73
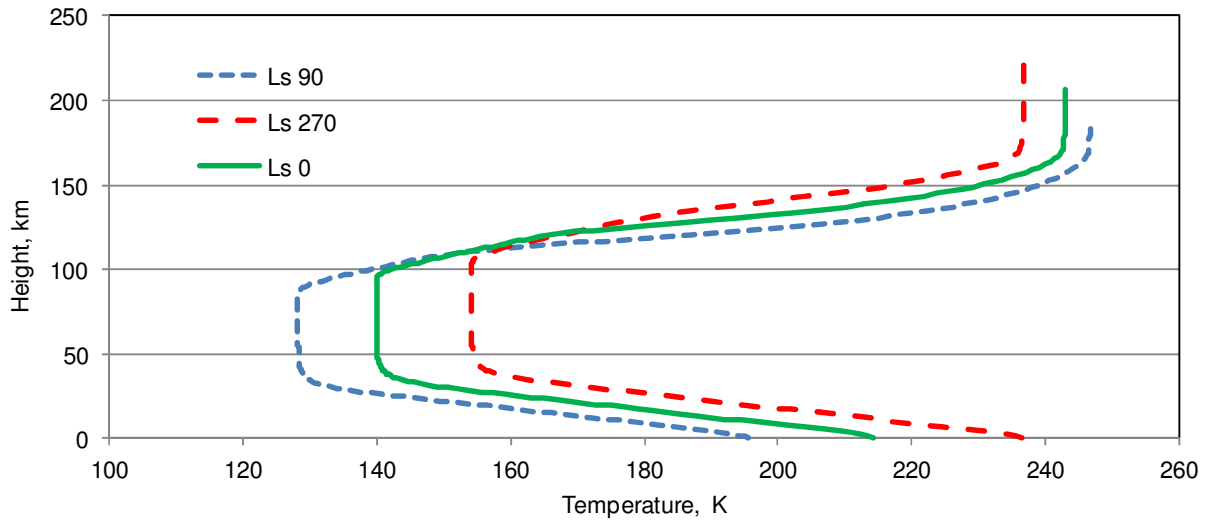
Figure 4.1: Background temperature profile by Mars season at solar average and low dust conditions.

act to decelerate the wind and cannot account for zonal wind reversals. To more realistically represent the spectra, propagation, and dissipation of gravity waves, the hybrid Lindzen-Matsuno gravity wave parameterization replaced the Rayleigh friction scheme. The mean flow was solved simultaneously with the gravity wave parameterization such that the nonlinear zonal mean equations were coupled to the gravity wave parameterization through the forcing term in the zonal momentum equation. Gravity wave forcing modified the zonal mean flow which in turn affected the breaking levels and filtering of the upward propagating gravity waves.

The latitude resolution of the model is 5 degrees, and the vertical resolution is 0.1 scale heights in log-pressure coordinates. The lower boundary of the model is at the surface, and the upper boundary, which varies by season due to differences in atmospheric scale heights, ranged from 190-230 km. The simulation was integrated with a time step of 300 s and was run for 40 days, which was a duration sufficient for a steady state gravity wave solution to be reached. Gravity wave forcing was introduced on day 15 and ramped up to a steady state value by day 25.

74

Figure 4.2: Zonal mean fields for solar longitude $L_s = 270°$ (northern hemisphere winter) with zonal mean forcing only: (a) eastward wind, (b) northward wind, (c) vertical wind, and (d) temperature perturbation from the global mean. Red solid lines are positive quantities; blue dashed lines are negative.

4.2.2   Background Atmosphere

The QNLM model was first run without the gravity wave parameterization to determine the background wind and temperature fields. The model was configured for low dust and solar average conditions, with no large-scale tidal waves to influence zonal mean flow. Rayleigh friction was included in the middle atmosphere to provide some closure of the middle atmosphere jets as predicted by GCMs [e.g. *Forget et al.*, 1999]. The background atmosphere was then compared to the results of previous modeling studies to show that the model captures the main features of the winds and temperature fields predicted by Mars GCMs.

Figure 4.2, which compares to Figure 3 in *Forbes and Miyahara* [2006], shows the modeled zonal mean parameters for northern hemisphere winter (L_s = 270°) with zonal forcing only. Middle atmosphere zonal jets were consistent with *Forbes and Miyahara* [2006], but the strength of the upper atmosphere zonal jets and the pole-to-pole meridional circulation was slightly stronger due to updated thermospheric heating rates. In the middle atmosphere, zonal mean eastward (winter) jets of 100 m s^{-1} and westward (summer) jets of 80 m s^{-1} were consistent in magnitude and location with L_s = 270° cases from *Forget et al.* [1999], *Joshi et al.* [1995], and *Théodore et al.* [1993]. The magnitudes of the zonal jets in *Hartogh et al.* [2005] were about 20 m s^{-1} less in both hemispheres. The zonally averaged temperature fields in *Hartogh et al.* [2005] compared very well to TES temperature observations, which extended from the surface to roughly 40 km altitude. In the absence of direct wind measurements, lower atmosphere temperature measurements provide the best available data to validate GCM results. Zonal jets in the thermosphere were of order 120-140 m s^{-1}. Comparisons for thermospheric wind speeds were difficult, as most of the cited GCMs did not reach beyond the lower thermosphere, and there are no direct wind observations of Mars' upper atmosphere. The Laboratoire de Meteorologie Dynamique (LMD) Mars GCM does extend to 240 km [*González-Galindo et al.*, 2009a, 2009b], and the results from the LMD GCM in *Angelats i Coll et al.* [2005], *González-Galindo et al.* [2009b], and *Medvedev et al.* [2011] suggested a much stronger westward thermospheric jet of 200-220 m s^{-1} extending further into the northern hemisphere. The northward pole-to-pole circulation with upwelling (downwelling) at the south (north) pole was produced by all cited GCMs. The corresponding temperature increase and departure from radiative equilibrium at northern high latitudes at 60-80 km altitude was due to subsidence heating by the descending branch of the global Hadley cell [*Bougher et al.*, 2006; *Forbes and Miyahara*, 2006] and was consistent with observational studies [*Deming et al.*, 1986; *Smith et al.*, 2001b].
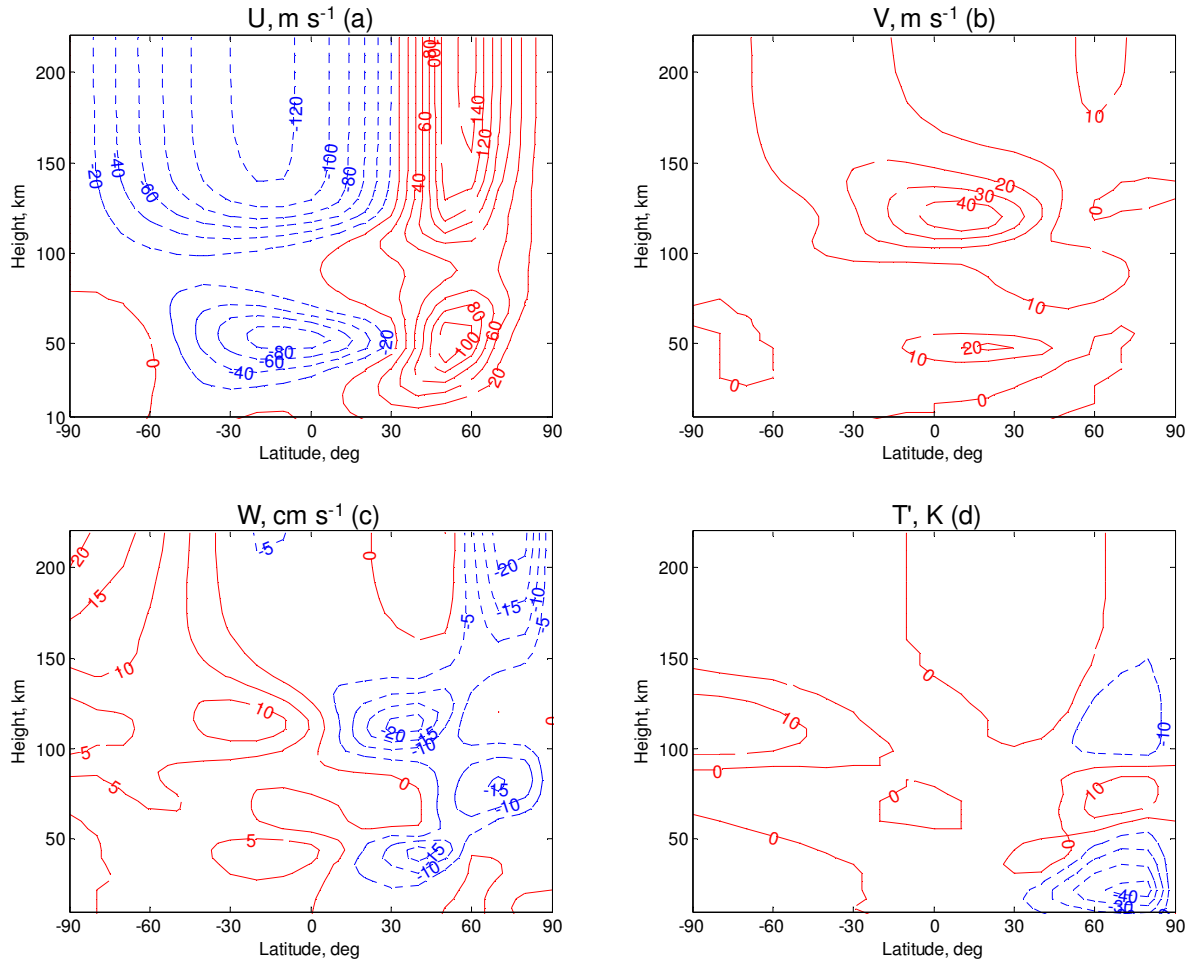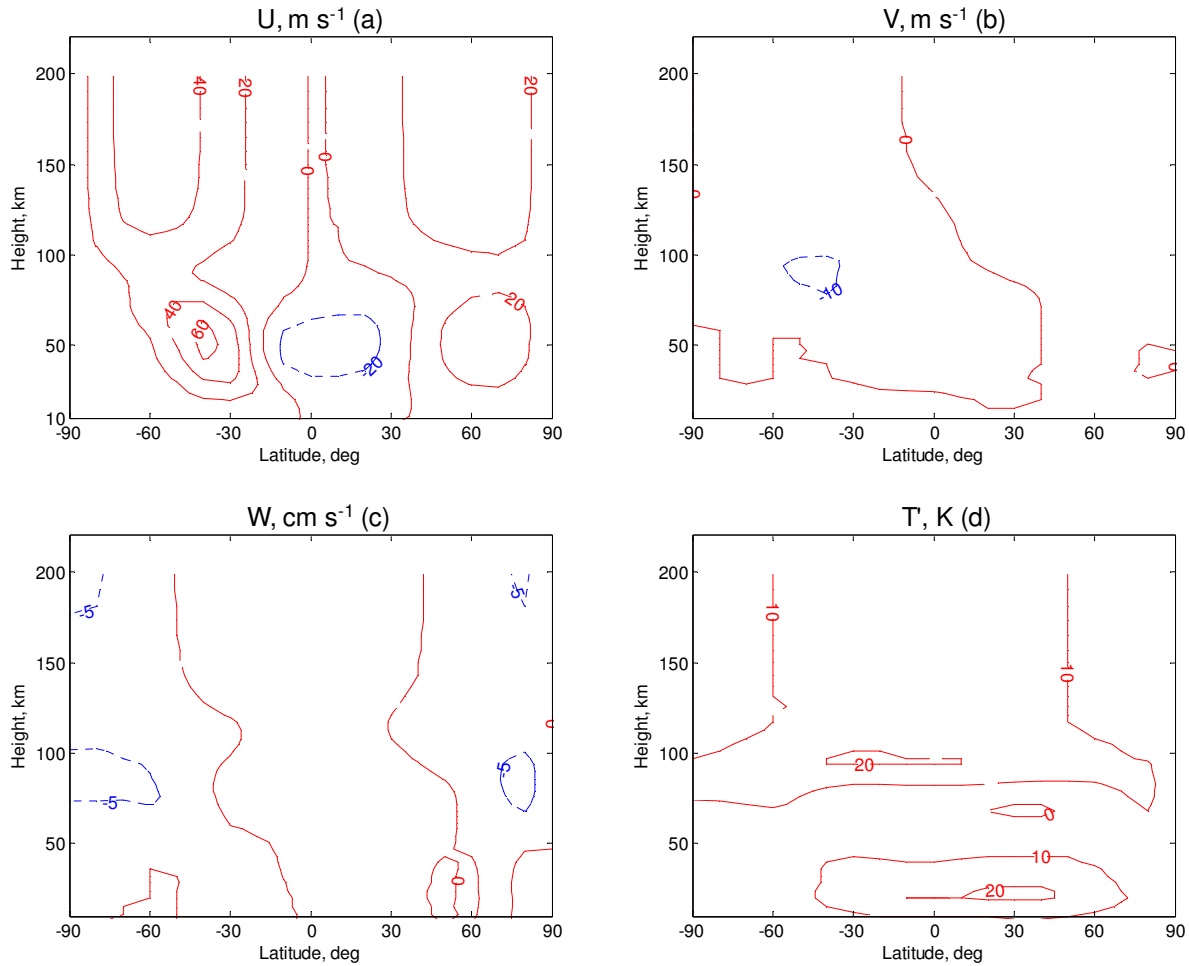
Figure 4.3: Zonal mean fields for solar longitude $L_s = 0°$ (northern hemisphere spring) with zonal mean forcing only: (a) eastward wind, (b) northward wind, (c) vertical wind, and (d) temperature perturbation from the global mean. Red solid lines are positive quantities; blue dashed lines are negative.

Figure 4.3 shows the modeled zonal mean parameters for northern hemisphere spring ($L_s = 0°$) with zonal forcing only. Winds and temperature for northern hemisphere autumn ($L_s = 180°$) were the same as northern spring but with northern and southern hemispheres reversed. Heating rates were symmetric about the equator following $\cos \phi$, where ϕ is latitude, and then linearly adjusted to produce a relatively stronger middle atmosphere jet in the autumn hemisphere. Heating rate peak magnitudes were scaled from the $L_s = 270°$ profile by the ratio of the squared heliocentric distances to account for the reduction in solar flux, as Mars is 10% further from than the Sun at equinox than at northern winter solstice. The zonal mean wind field is characterized by eastward zonal jets in the middle atmosphere of

77

www.manaraa.com

each hemisphere, a relatively weaker westward jet in the middle atmosphere above the equator, and near-symmetric eastward flow in the thermosphere. In the middle atmosphere near 50 km, the eastward jets of 60 m s^{-1} and 20 m s^{-1} in the southern (autumn) and northern (spring) hemispheres respectively and the westward jet of 20 m s^{-1} are consistent in strength and location with *Forbes et al*. [2002]. In *Hartogh et al*. [2005], the middle atmosphere eastward jets were comparable in strength but occurred lower in the atmosphere near 30 km, while a strong westward jet peaked at 160 m s^{-1} near 80 km and extended from pole to pole. The equinox model runs in *Forget et al*. [1999] and *Collins et al*. [1997] produced eastward jets stronger by up to 60 m s^{-1}, comparable in magnitude to the jets in the solstice case, and a broader westward jet that also peaked higher in the atmosphere above the equator. The GCM-predicted behavior of zonal winds in the thermosphere had limited results. *Forbes et al*. [2002] had weak jets, consistent in magnitude with this study, but asymmetric about the equator with an eastward (westward) jet in the autumn (spring) hemisphere. Although the models do not extend above 90-110 km, the results of *Hartogh et al*. [2005], *Forget et al*. [1999], and *Collins et al*. [1997] could be extrapolated to suggest a pole-to-pole westward jet above the equator in the lower thermosphere. There were no GCM results that were fully consistent with the QNLM symmetric eastward zonal winds in the thermosphere, but the sample of published data was small, and there were also no observations of the zonal wind field that contradict the result. Figure 4.3 also shows the formation of a weak meridional circulation in each hemisphere with upwelling near the equator and downwelling near the poles.

4.3   Gravity Wave Source Spectrum

From *Ern et al*. [2004], gravity wave vertical flux of horizontal momentum can be estimated from gravity wave potential energy density using

$$\overline{u'w'} = \frac{\lambda_z}{\lambda_h} E_p \,, \tag{4.11}$$

where λ_z and λ_h are the vertical and horizontal wavelengths of the gravity wave. Vertical wavelengths were calculated from the temperature perturbation profiles, but horizontal wavelengths had to be estimated using the gravity wave dispersion relation bounded by the observational filtering inherent to the

78

radio occultation technique. This section develops the horizontal wavelength profile consistent with gravity wave theory and calculates the zonally averaged momentum flux profiles used in QNLM model runs.

4.3.1 Gravity Wave Observability

Preusse et al. [2008] defined the sensitivity range of limb sounding instruments, which includes the radio occultation technique, to detect gravity waves of certain vertical and horizontal wavelengths. For a given vertical wavelength, the minimum horizontal wavelength was determined from an analytic radiative transfer solution for the sensitivity of the instrument to a sinusoidal perturbation in the atmosphere. For Earth, a 15 km vertical wavelength could be resolved if the horizontal wavelength were at least 300 km, but this result assumed an unfavorable measurement geometry. *Preusse et al.* [2008] then suggested that horizontal wavelengths 50% smaller could be observed under better viewing geometries, reducing the minimum horizontal wavelength to 150 km for a 15 km vertical wavelength. The sensitivity equation in *Preusse et al.* [2002, 2008] was evaluated for Mars taking into account differences in the planet's radius, atmospheric scale height, and atmospheric temperature. The results indicated that a limb sounder at Mars is roughly 25% more sensitive to atmospheric perturbations than at Earth. At the median vertical wavelength of 14 km found in the MGS radio occultation profiles, the minimum observable horizontal wavelengths in Mars atmosphere were expected to be on the order of 100-200 km depending on measurement geometry relative to the wave phase fronts. The minimum observable horizontal wavelength is linearly proportional to vertical wavelength. At 7 km vertical wavelength, for example, the minimum horizontal wavelength was 50-100 km.

The maximum resolvable horizontal wavelength varied by latitude according to the intrinsic frequency of the gravity wave, which was limited by the Coriolis parameter such that $|\hat{\omega}| > |f|$. *Preusse et al.* [2008] determined maximum horizontal wavelength using a limiting value of $|\hat{\omega}/f| = 1.4$, but noted from CRISTA measurements that the ratio remained much larger than 1.4 in general. At 25° latitude on Earth, this ratio corresponded to maximum horizontal wavelengths of 1000 km and 3000 km at vertical wavelengths of 5 km and 15 km respectively. At 50° latitude, maximum horizontal wavelengths

79

reduced by a factor of 2 due to the increase in the Coriolis parameter. These calculations were repeated for Mars with similar results. For a vertical wavelength of 14 km, maximum horizontal wavelengths were found to be 8000 km, 1600 km, and 900 km at the equator, 25° latitude, and 50° latitude respectively. Results at 7 km vertical wavelength were reduced by a factor of 2. With zonal wavenumbers up to $s = 3$ to 6 at the equator, it is plausible that large tidal components were observed in the radio occultation data. However, from Table 2.4, the observed vertical wavelengths indicate that if small zonal wavenumber tidal gravity waves were observed, the components must be a higher subharmonic. As will be shown later, it is not believed that any long horizontal wavelengths were observationally filtered due the sensitivity of the radio occultation technique.

The probability that a wave was detected was also dependent on the time the wave had taken to propagate through the altitude region observed. If there is intermittency in wave forcing [*Alexander et al.*, 2002; *Fritts and Alexander*, 2003], the waves that propagate more slowly have a better chance of being observed. As the minimum allowed intrinsic frequency decreases near the equator ($|\hat{\omega}| > |f|$), the probability of wave detection increases significantly [*Alexander et al.*, 2002]. As intrinsic frequency decreases, vertical group velocity, which transports wave energy, also decreases. Lower vertical group velocity implies longer horizontal wavelengths. Thus, following *Alexander et al.* [2002, 2010], there exists not only a latitude dependency with horizontal wavelength, but also a latitude dependency with probability of observation. Near the equator, the longer horizontal wavelengths, which have a better chance of being detected, transport less energy. In order not to overestimate gravity wave momentum flux from potential energy density, it is important not to underestimate horizontal wavelengths, particularly in the tropics where large potential energy densities were observed.

4.3.2   Horizontal Wavelengths

Previous modeling studies for Mars used horizontal wavelengths in their gravity wave parameterizations on the order of a few hundred kms constant across all latitudes [e.g. *Barnes*, 1990; *Collins et al.*, 1997; *Medvedev et al.*, 2011]. These studies tuned model results to achieve a desired forcing in the mesosphere using a tunable input parameter, which in some cases was the horizontal

wavelength. Besides accounting for intermittency, the tunable parameter compensated for errors in any assumptions on the gravity wave source spectra that might play into the gravity wave drag calculations.

In this study, horizontal wavelength was estimated by combining the momentum flux definitions of *Ern et al.* [2004] and *Fritts and VanZandt* [1993]. In the *Fritts and VanZandt* [1993] representation of a continuous gravity wave spectrum, the gravity wave integrated component momentum flux is:

$$F_{x,y} = (b_x, b_y) D(p, \tilde{f}) E_0 , \qquad (4.12)$$

where (b_x, b_y) represents the zonal anisotropy given by

$$(b_x, b_y) = \int\limits_0^{2\pi} \Phi(\theta)(\cos\theta, \sin\theta)d\theta , \qquad (4.13)$$

$\Phi(\theta)$ expresses the orientation of the wave field, p is the spectral index, $\tilde{f} = f/N$ is the ratio of the Coriolis parameter to the Brunt-Väisälä frequency, $E_0 = E_p + E_k$ is the total gravity wave energy density, and $D(p, \tilde{f})$ is given by

$$D(p, \tilde{f}) = \frac{B_0}{N} \int\limits_f^N \hat{\omega}^{1-p} \left[\left(1 + \frac{f^2}{\hat{\omega}^2}\right) \left(1 - \frac{f^2}{\hat{\omega}^2}\right) \left(1 - \frac{\hat{\omega}^2}{N^2}\right) \right]^{1/2} d\hat{\omega} , \qquad (4.14)$$

where $\hat{\omega}$ is wave intrinsic frequency and $B_0 = (p-1)f^{p-1}[1 - (f/N)^{p-1}]^{-1}$. From *VanZandt* [1985], the ratio of wave kinetic energy to potential energy is equal to the spectral index $p = E_k/E_p$. Using the commonly accepted value of $p = 5/3$ for Earth, total energy can be written as a function of potential energy only: $E_0 = 8E_p/3$. The value of $p = 5/3$ was validated for Mars following the simple model in *Alexander et al.* [2002] comparing the gravity wave potential energy in the tropics to the middle latitudes. The ratio of $E_p(5°)/E_p(35°)$ was 3.7, which tracked almost exactly to the *Alexander et al.* [2002] latitudinal variations associated with $p = 5/3$ when the model was configured for Mars. Combining equation (4.12) with equation (4.8) from *Ern at al.* [2004] yields an equation for horizontal wavelength as a function of vertical wavelength and latitude:

$$\lambda_h = \frac{3}{8} \frac{\lambda_z}{|b_x| D(p, \tilde{f})},$$
(4.15)

This study assumed that all horizontal momentum flux was zonal, and only the zonal component of equation (4.12) was considered. Following *VanZandt and Fritts* [1989], a value of $b_x = -0.2$ was used for the zonal anisotropy of the wave field which corresponded to 60% (40%) of the zonal energy westward (eastward) and which had been inferred from gravity wave activity observed at Earth's tropopause. $D(p, \tilde{f})$ was evaluated numerically at each latitude step in the model. Using the derived median vertical wavelength of 14.0 km across all latitudes, the latitude profile of horizontal wavelength was calculated using equation (4.15) and is shown in Figure 4.4. At the equator, equation (4.15) approaches infinity due to the $\sin\phi$ term in the Coriolis parameter. To avoid this limit, the horizontal wavelength at the equator was assigned the same value as the horizontal wavelength at 5° latitude. The values in Figure 4.4 were well within the observational limits from *Preusse et al*. [2008] and consistent at middle latitudes with the *Fritts et al*. [2006] assertion that the horizontal wavelengths in the MGS radio occultation wave activity were expected to be on the order of 200-400 km.

The inferred horizontal wavelengths by latitude were used not only in the source-level momentum flux calculations but also as an input to the gravity wave parameterization to be used in the breaking level and eddy diffusion calculations in the Lindzen scheme. As λ_h increases (i.e. horizontal wavenumber $k = 2\pi/\lambda_h$ decreases), the gravity wave breaks at a lower altitude, and the associated eddy diffusion and zonal acceleration are reduced.
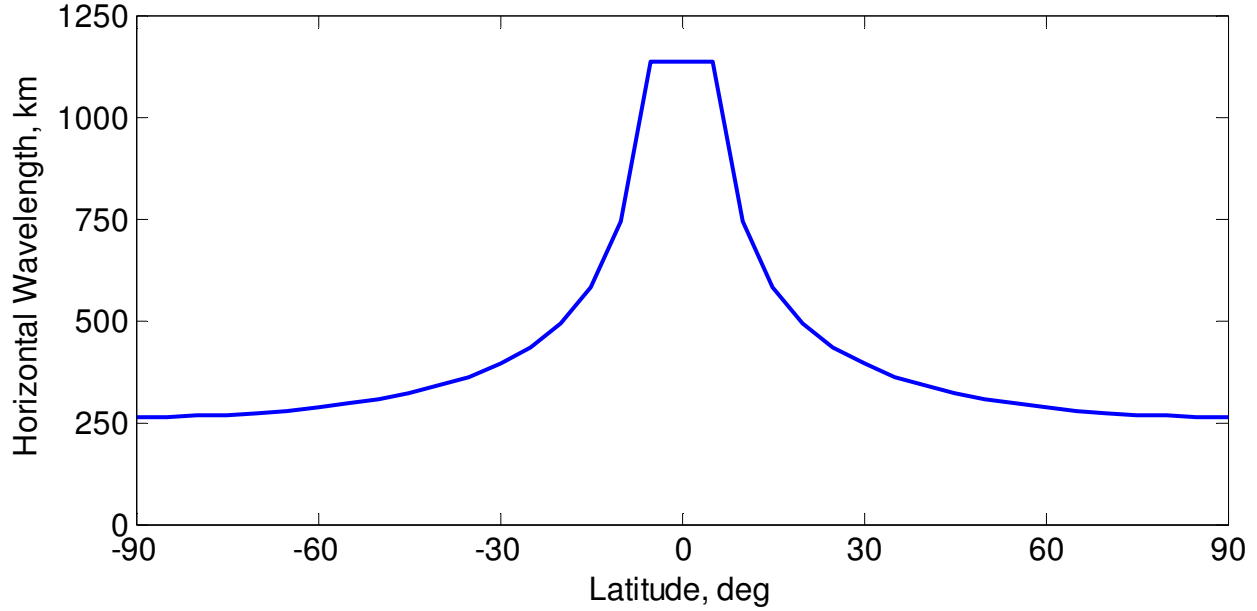
Figure 4.4: Horizontal wavelength by latitude. Horizontal wavelength at the equator was set equal to the value at 5° latitude.

4.3.3   Momentum Flux Calculations

The first step to calculate the momentum flux distribution used in the gravity wave parameterization was to zonally average the seasonal gravity wave potential energy distributions shown in Chapter 2. Figure 4.5 shows the zonally averaged E_p distributions for radio occultation measurements by Mars season. All distributions are shown with the same vertical scale to highlight the differences in wave energies by season. At latitudes where no radio occultation data existed, missing data points were interpolated from adjacent latitudes or extrapolated using the zonal average across all seasons. In cases where sample size was very small, such as northern latitudes at $L_s = 270°$, the zonally averaged data was not used. Otherwise, the data was not modified or smoothed

Zonally averaged momentum flux was calculated directly from equation (4.1) using the zonally averaged potential energy density profile and the horizontal wavelength profile. This approach is similar to the momentum flux calculations used in *Ern et al.* [2004], *Alexander et al.* [2008], *Alexander et al.* [2009], *Preusse et al.* [2008], and *Wang and Alexander* [2010] in the estimation of Earth's gravity wave momentum flux. Because these studies also had knowledge of both the horizontal and vertical

83

wavelengths associated with the temperature profile, they were able to calculate momentum flux for each wave directly from the observed temperature perturbations using equivalent forms of equation (4.1), as opposed to calculating momentum flux from a zonally averaged energy density profile. The momentum flux profiles used in this study are shown in Figure 4.6. The momentum flux source level was defined to be 12.5 km altitude, since the flux levels were derived from potential energy densities between 10-15 km altitude. The application of the latitude-dependent horizontal wavelength had the effect of deemphasizing the wave energy observed near the equator. In northern hemisphere autumn ($L_s = 180°$), the peak of gravity wave flux shifted into the southern hemisphere, where orographic variance is greater. Similarly, momentum flux levels near the poles showed relative increases in southern hemisphere summer and northern hemisphere spring. The northern hemisphere spring profile was particularly interesting, as gravity wave momentum flux remained in a 0.5-1.0 mPa band at all latitudes northward of 30°S.
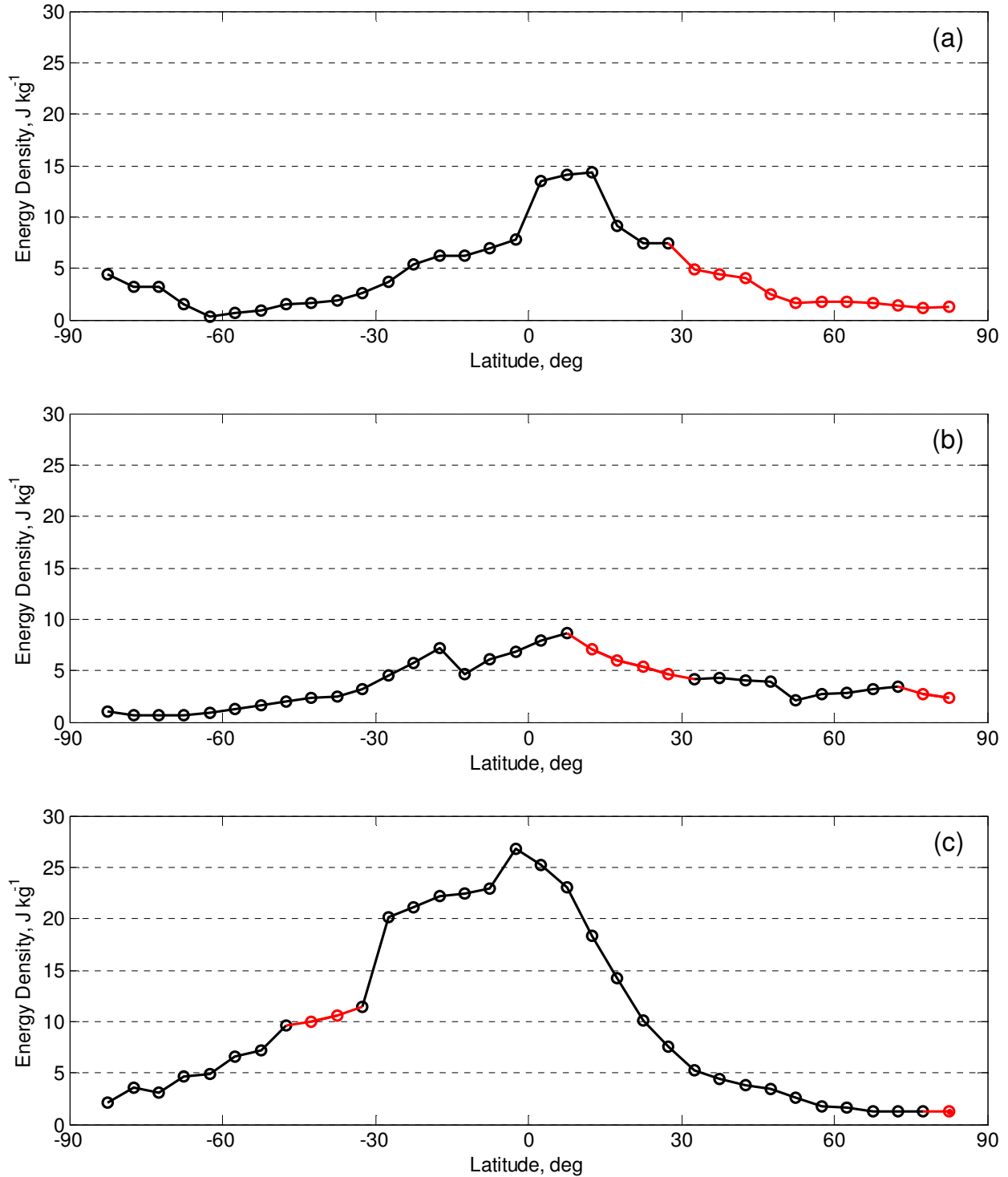
Figure 4.5: Zonally averaged gravity wave potential energy density at 10-15 km altitude for (a) northern hemisphere winter ($L_s = 270°$), (b) northern hemisphere spring ($L_s = 0°$), and (c) northern hemisphere autumn ($L_s = 180°$). Red data points were fitted from adjacent latitudes or the composite zonal average.
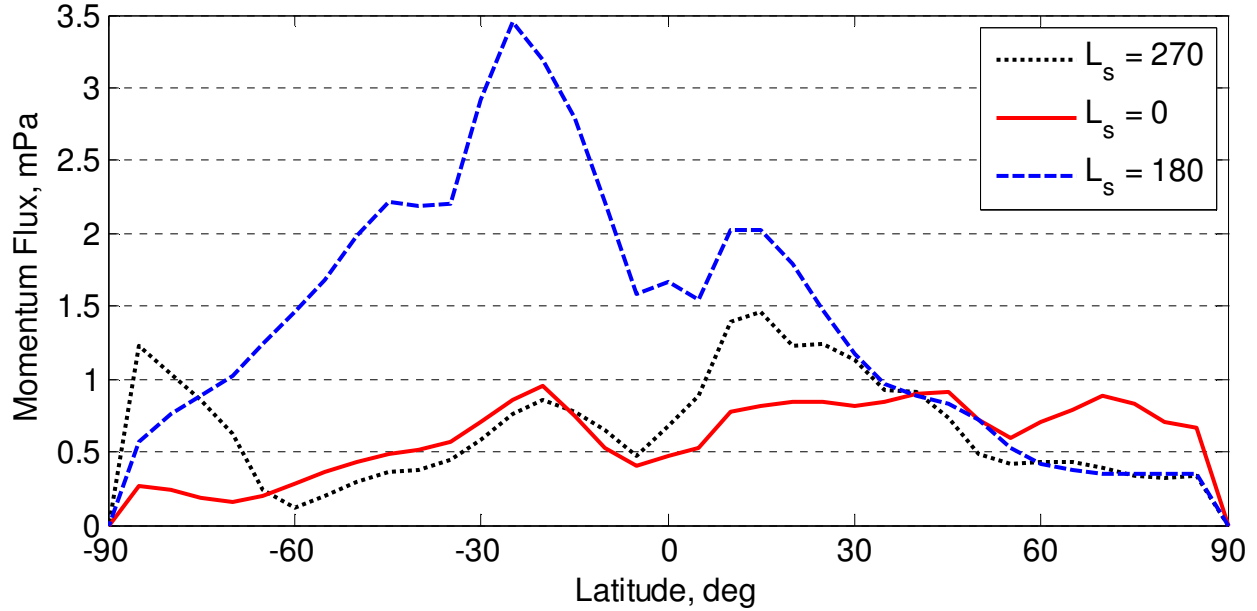
Figure 4.6: Zonally averaged vertical flux of horizontal momentum at 12.5 km altitude for northern hemisphere winter (black dotted line), northern spring equinox (red solid line), and northern hemisphere autumn (blue dashed line).

The values of 0.5-3.5 mPa for gravity wave momentum flux at Mars were in the range of the values observed or calculated for Earth [*Fritts and Alexander*, 2003], although even for Earth, global momentum flux estimates vary significantly. In *Alexander et al*. [2008], mean gravity wave momentum flux derived from HIRDLS data in northern hemisphere summer varied from 0.1-0.2 mPa at high northern latitudes to 0.5-1.0 mPa near the equator and 2-10 mPa at high southern latitudes. The largest mean values were observed over the Antarctic Peninsula and the southern tip of South America. Mean momentum fluxes from CRISTA [*Ern et al*., 2004] at a similar time of year showed a similar global distribution but were higher than HIRDLS by a factor of ~5. *Alexander et al*. [2010] explained the difference as due to sensitivity/aliasing corrections, longer vertical wavelengths used in CRISTA analysis, and intermittency effects. *Wang and Alexander* [2010] estimated Earth global momentum flux derived from GPS radio occultation data to be 0.05-0.33 mPa. This lower result was driven by much longer inferred horizontal wavelengths of 1500-4500 km. The values discussed above are mean values averaged over a period of time. Peak values recorded during mountain wave events were as high as 300 mPa over

Scandinavia, 140 mPa over the Antarctic Peninsula, and over 1000 mPa over South Georgia Island [*Alexander et al.*, 2010].

The uncertainties in the momentum flux distributions were significant, primarily due to the uncertainties in the inferred quantities used in calculating horizontal wavelengths. The λ_h calculation was particularly sensitive to the spectral index and the measure of zonal anisotropy. Small changes in spectral index led to significant changes in horizontal wavelength [*Fritts and VanZandt*, 1993]. Table 4.1 lists the

Table 4.1: Horizontal wavelength and normalized intrinsic frequency by latitude and spectral index.

Latitude (deg)	λ_h (km) / $|\widehat{\omega}/f|$				
	$p = 1.5$	$p = 1.6$	$p = 1.67$	$p = 1.75$	$p = 1.85$
90	79 / 8.7	163 / 4.4	264 / 2.8	487 / 1.7	1023 / 1.2
60	85 / 9.4	175 / 4.7	286 / 3.0	534 / 1/8	1137 / 1.2
30	108 / 12.8	233 / 6.0	394 / 3.6	765 / 2.1	1713 / 1.3
5	239 / 33.3	606 / 13.2	1138 / 7.1	2530 / 3.3	6696 / 1.6

horizontal wavelengths at selected latitudes at different values of spectral index, p. Using the dispersion relation, intrinsic frequency relative to the Coriolis parameter, $|\widehat{\omega}/f|$, was calculated for each horizontal wavelength. The ratio $|\widehat{\omega}/f|$ provided a measure of wave frequency normalized by latitude. Given that the probability of detection was biased towards wave intrinsic frequencies approaching the lower limit established by the Coriolis parameter, it was expected that many of the waves observed were low-intrinsic frequency gravity waves. This result was confirmed by the small values for $|\widehat{\omega}/f|$ in Table 4.1. For Mars, the normalized intrinsic frequencies were slightly higher but consistent with estimates for gravity waves at Earth. For gravity waves detected in Earth GPS radio occultation data, *Wang and Alexander* [2010] found that $|\widehat{\omega}/f|$ ranged from 1.05 to 3.05 and maximized at the equator with corresponding horizontal wavelengths of 1500-4500 km. In Earth radiosonde observations, $|\widehat{\omega}/f|$ was estimated to be between 2 and 4 with λ_h= 500-2000 km [*Alexander et al.*, 2010], and from CRISTA measurements, $|\widehat{\omega}/f| = 1.4$ was found to be the lower bound for that limb-scanning instrument [*Preusse et al.* 2006]. Returning to Table 4.1, the resulting horizontal wavelengths at $p = 1.5$ were expected to be too short to be

consistently resolved in the MGS radio occultation measurements, while at $p = 1.85$, the wavelengths were expected to exceed the upper sensitivity limit at middle and upper latitudes. The horizontal wavelength profiles at $p = 1.6$ and $p = 1.75$ provided reasonable bounds to the expected observability limits. The profiles scaled the source momentum flux profile by factors of approximately 0.5 and 2 respectively and were used in Chapter 5 to evaluate the sensitivity of gravity wave forcing to changes in source spectrum magnitude. According to *VanZandt and Fritts* [1989], as the zonal anisotropy of the wave field increases, wave momentum flux increases. In terms of the horizontal wavelength and momentum flux magnitude calculations used in this study, varying the zonal anisotropy parameter, b_x, would achieve nearly the same result as varying the spectral index, p. Additional sensitivy testing on b_x was not performed since results for $p = 1.6$ and $p = 1.75$ would be similar to results for $|b_x| = 0.4$ and $|b_x| = 0.1$ respectively.

Another potential source of uncertainty was the momentum flux equation. The momentum flux calculation in equation (4.1) uses the midfrequency approximation of the dispersion relation such that intrinsic frequency can be expressed by the horizontal wavenumber. The full equation from *Ern et al*. [2004] is

$$F_x = \left[1 - \frac{\widehat{\omega}^2}{N^2}\right]\left[1 + \frac{1}{m^2}\left(\frac{1}{2H} - \frac{g}{c_s^2}\right)^2\right]^{-1}\left[1 + \left(\frac{f}{m\widehat{\omega}}\right)^2\left(\frac{1}{2H} - \frac{g}{c_s^2}\right)^2\right]^{1/2}\rho\frac{\lambda_z}{\lambda_h}E_p, \qquad (4.16)$$

where c_s is the speed of sound and the first three terms represent the deviation from the midfrequency approximation. In the range of intrinsic frequencies for p between 1.6 and 1.75, the deviation from the midfrequency approximation was calculated to be less than 1% at high latitudes increasing to 2-4% near the equator.

Relative to the uncertainties in the momentum flux calculation, the error estimates in the source energy densities were small. In each MGS radio occultation data file [*Hinson*, 2008], 1σ estimates of temperature, pressure, and radius uncertainty were provided for each measurement. Mean and maximum temperature uncertainties at 10 km altitude were 1.2 K and 5.6 K. At 15 km altitude, mean and maximum

temperature uncertainties had increased to 1.6 K and 9.0 K. Errors in a temperature profile were assumed to be highly correlated instead of random in nature, and inspection of individual temperature profiles supported this assumption. Maximum 1σ temperature uncertainties were on the order of 4-5% of background temperature in the height range used to derive the source spectrum, and from equations (2.11) and (2.12), this contributed a similar percentage uncertainty to potential energy density. The accuracy and reliability of temperatures derived from MGS radio occultation measurements were confirmed in *Hinson et al*. [2004]. By definition, deviations from the third-order curve fit representing background temperature were classified as temperature perturbations. It was not possible to discriminate random noise from a perturbation associated with wave activity. However, temperature perturbation profiles were not random noise sequences. They were highly correlated as evidenced in the results of the spectral analysis of vertical wavelength. It was therefore assumed that the derived temperature perturbations were due to small-scale wave activity. It was also believed that the third-order curve fit for background temperature did not introduce artificial temperature perturbations. The resulting perturbation profiles were zero-mean, and the performance of the curve fit was monitored.

Intermittency effects were not included in the momentum flux distributions. As demonstrated in *Alexander et al*. [2002], intermittency can bias the observed energy densities towards the equator where slower propagating waves have an increased probability of detection. The magnitude of the bias is dependent on the intermittency period of the waves, with longer intermittency periods resulting in overestimation of wave energy density near the equator. Although gravity waves on Earth are presumed to be intermittent by nature [e.g. *Alexander et al*., 2010], data on the intermittency of gravity waves on Mars did not exist. If modeled following *Alexander et al*. [2002], the effect on the source spectrum would have been similar to the effect of increasing the spectral index and horizontal wavelength profile.

4.3.4   Phase Speed Distributions

The HLM parameterization used a discrete spectrum of waves with a range of zonal phase speeds and directions. At each latitude, momentum flux was divided across the spectrum of waves according to

a Gaussian-shaped distribution centered at phase speed $c = 0$ m s^{-1}. Positive (negative) values represent eastward (westward) propagation, and 0 m s^{-1} represents a stationary wave.

From section 2.4.1, the phase speed spectrum is expected to be comprised of both stationary ($c = 0$ m s^{-1}) and non-stationary ($|c| > 0$ m s^{-1}) gravity waves. Stationary gravity waves are excited by wind flow over topography. Non-stationary gravity waves are high wavenumber tidal components [*Miyoshi et al.*, 2011] or are excited by other plausible mechanisms such as dry convection at boundary layers, geostrophic adjustment, or non-local deep transport. The phase speeds of the tidal gravity waves follow $c = \Omega\, a/s$ where Ω is Mars' rotation rate and a is the radius of Mars. Zonal wavenumbers $s = 5, 10, 15,$ and 20 correspond to phase speed magnitudes of 48, 24, 16, and 12 ms s^{-1} respectively. From section 4.3.1, tidal gravity waves with zonal wavenumbers as low as 3 are observable in the radio occultation data at the equator. However, based on the range of observable horizontal wavelengths, zonal wavenumbers from 8 through 35 are considered likely. Observed vertical wavelengths could further constrain the zonal wavenumber per Table 2.4, but the subharmonics of the waves are not known. The tidal component is divided equally between westward (migrating) and eastward (non-migrating) components following the spectral distribution in *Miyoshi et al.* [2011].

Because the gravity wave phase speeds on Mars are not known, multiple simulations with different sets of assumed phase speeds were used. The baseline phase speed spectrum consisted of a purely stationary spectrum (i.e. all momentum flux at $c = 0$ m s^{-1}) that was consistent with Mars GCMs gravity wave forcing schemes. Phase speed spectra with maximum phase speed magnitudes of 20, 60, and 80 m s^{-1} were next evaluated. The first was a modified symmetric version of the -20, 0, +20 m s^{-1} spectrum used by *Holton* [1982] that is representative of stationary gravity waves combined with tidal gravity waves with zonal wavenumber near 10-15. The phase speed spectrum of -60, -40, -20, 0, +20, +40, and +60 m s^{-1} followed the set of phase speeds used by *Meyer* [1999a, 1999b] for Earth's gravity waves and is representative of larger-scale tidal wave gravity waves . A variation of the above spectrum, listed as 60W in Table 4.2, allocated 3 times more momentum flux to westward propagating waves than eastward waves in an attempt to approximate possible low-level filtering of eastward propagating waves

at equinox in both hemispheres or at solstice in the winter hemisphere. The other spectrum investigated was an approximation of the spectrum used by *Medvedev et al*. [2011] for Mars where $c_{max} = 80$ m s^{-1}. The *Medvedev et al*. [2011] spectrum was based on the gravity wave distribution observed in Earth's troposphere and reflected significant levels of convective activity. Convective activity can generate gravity waves throughout the full range of phase speeds [*Fritts and Alexander*, 2003; *Alexander et al*., 2006] and on Earth is typically associated with gravity wave generation over intense storms. As discussed earlier, comparable levels of convective excitation of gravity waves are not expected in Mars' atmosphere. However, the spectrum was retained as part of the sensitivity analysis. Table 4.2 provides a summary of the allocation of momentum flux by phase speed for the different spectra considered.

Table 4.2: Normalized phase speed spectra.

Case (c_{max})	Phase speed (m s^{-1})								
	-80	-60	-40	-20	0	+20	+40	+60	+80
0	-	-	-	-	1.00	-	-	-	-
20	-	-	-	0.29	0.43	0.29	-	-	-
60	-	6.3E-5	0.03	0.21	0.51	0.21	0.03	6.3E-5	-
60W	-	9.5E-5	0.05	0.32	0.51	0.11	0.02	3.2E-5	-
80	1.7E-3	0.02	0.09	0.23	0.32	0.23	0.09	0.02	1.7E-3

4.4   Test Cases

The QNLM model was run for zonal mean wind and temperature fields representing both solstice and equinox conditions. At solstice, the $L_s = 270$ curve from Figure 4.6 was used as the input source momentum flux profile. At equinox, both the $L_s = 0$ and $L_s = 180$ momentum flux profiles were used since source magnitudes differed significantly. At solstice, gravity wave momentum flux was also calculated using different values of spectral index, p. Values of $p = 1.6$ and $p = 1.75$ defined the bounds on momentum flux based on observability constraints on horizontal wavelength. The magnitudes of the resulting momentum flux profiles were roughly a factor of 2 and 0.5 times the nominal momentum flux

calculated with $p = 5/3$. At both solstice and equinox, the phase speed spectrum was varied according to Table 4.2. The results of the model runs are discussed in Chapter 5.

Chapter 5

Effects of Gravity Waves on Mars' Atmosphere

The dynamics of the middle and upper atmospheres of Mars and Earth share many characteristics. The solar radiative environments are comparable, and net differential heating produces similar mean zonal jets [e.g. *Forget et al.*, 1999; *Hartogh et al.*, 2005]. Both atmospheres contain planetary-scale waves as evidenced in observations of Mars' migrating and non-migrating tides [e.g. Forbes et al., 2002; Withers et al., 2003] and stationary planetary waves [*Banfield et al.*, 2003]. From the solutions to Laplace's tidal equation, atmospheric tidal and planetary waves possess similar structure and characteristics in both atmospheres [*Zurek and Haberle*, 1988]. Because the planets' rotation rates are approximately the same, solar tidal periods are nearly the same as well. Also, the similar axial tilt and relatively low orbital eccentricity result in seasonal dependencies on Mars as on Earth.

As discussed in previous chapters, gravity waves have been observed in Mars' lower and upper atmospheres at altitudes that parallel gravity wave observations at Earth. It is expected that gravity waves would be stronger on Mars because topography is very large as compared to Earth and because strong zonal jets are believed to extend to lower altitudes, enabling stronger gravity waves from topographic forcing [*Fritts et al.*, 2006]. Stronger mean winds permit potentially larger gravity wave amplitudes and vertical wavelengths, with increased momentum and energy transport to higher altitudes. Previous modeling studies have suggested that gravity waves play a more dominant role on Mars than on Earth. *Barnes* [1990] found that breaking gravity waves of 100-1000 km horizontal wavelength generated sufficient drag on the zonal mean flow to close off the eastward zonal jet at 40-80 km altitude in the winter hemisphere. The breaking gravity waves also induced significant high-latitude warming consistent

93

with the winter polar warming reported by *Deming et al*. [1986]. The model results of *Théodore et al*. [1993] supported the finding that the temperature inversion at high winter latitudes was due to interaction between gravity waves and the general circulation. *Théodore et al*. [1993] also suggested that gravity wave breaking was responsible for pulling the southern hemisphere westward jet into the northern hemisphere through strong meridional advection of the zonal wind. The results of *Joshi et al*. [1995] and *Collins et al*. [1997] were consistent with the previous modeling studies. *Joshi et al*. [1995] concluded that gravity wave drag dominated the momentum balance of Mars' atmosphere above 60 km altitude and was significant in the Hadley circulation and associated heating below 60 km. In the studies above, gravity waves were allowed to propagate into the middle atmosphere. *Barnes* [1990] used a prescribed background wind to quantify the effects of a breaking gravity wave at Mars. *Théodore et al*. [1993] used a source spectrum with eastward (westward) phase speeds ($|c| = 20$ m s^{-1}) that were able to propagate against the westward (eastward) background flow. Although *Joshi et al*. [1995] used a stationary gravity wave spectrum, it appears his model did not filter gravity waves due to the background wind ($\bar{u} = c$) and allowed them to propagate vertically to their breaking level.

In other modeling studies [*Forget et al*., 1999; *Angelats i Coll et al*., 2005; *Hartogh et al*., 2005], the effects of gravity waves were less pronounced. *Medvedev and Hartogh* [2007] estimated that gravity wave drag in these studies contributed only about 10% of the Eliassen-Palm flux divergence associated with resolved eddies. The GCM results of *González-Galindo et al*. [2009b] used an updated version of the LMD GCM of *Forget et al*. [1999] and *Angelats i Coll et al*. [2005]. The sub-grid scale gravity wave parameterization was the same as earlier versions of the LMD GCM, and the gravity wave results were similar. In these models, gravity wave drag was poorly constrained, and only stationary ($c = 0$ m s^{-1}) gravity waves were considered. As will be shown in this section, the difference in the magnitude of gravity wave effects between the earlier studies and the recent GCM results is due to the ability of the gravity waves to propagate into the middle and upper atmosphere. In GCM results, much of the gravity wave energy is filtered by the background wind at low levels.

94

This chapter presents the zonal mean wind and temperature fields associated with gravity wave forcing from the surface to the upper thermosphere using the Hybrid Lindzen-Matsuno gravity wave parameterization integrated into the Mars QNLM. For the first time, gravity wave forcing was constrained by observations of gravity wave energy in Mars' lower atmosphere. Simulation results are shown for Mars' solstice and equinox conditions and for different phase speed distributions.

5.1 Gravity Wave Forcing on Background Atmosphere

The gravity wave parameterization was configured to run either integrated with QNLM or standalone against prescribed wind and temperature fields. The latter configuration was particularly useful to calculate the zonal accelerations associated with a constant background atmosphere, test the sensitivity of zonal accelerations to gravity wave input parameters, or assess zonal accelerations at the end of a QNLM run.

Figure 5.1 shows the output of the HLM gravity wave parameterization against the wind and temperature fields in Figure 4.2 representing northern hemisphere winter ($L_s = 270°$). The magnitude of the source momentum flux followed the latitude profile for $L_s = 270°$ in Figure 4.6 and was distributed over phase speeds from -60 to 60 m s^{-1}. The contribution of each wave (i.e. phase speed) to the net zonal acceleration is shown in Figure 5.2. Wave breaking due to convective instability began around 30 km altitude in the lower northern latitudes, but generally occurred between 70-100 km altitude. Waves with higher magnitude phase speeds tended to break higher in the atmosphere due to greater intrinsic phase speeds ($c_i = c - \bar{u}$) and smaller wave amplitudes at the source. If a wave reached the thermosphere, it was slowly dissipated through molecular diffusion.
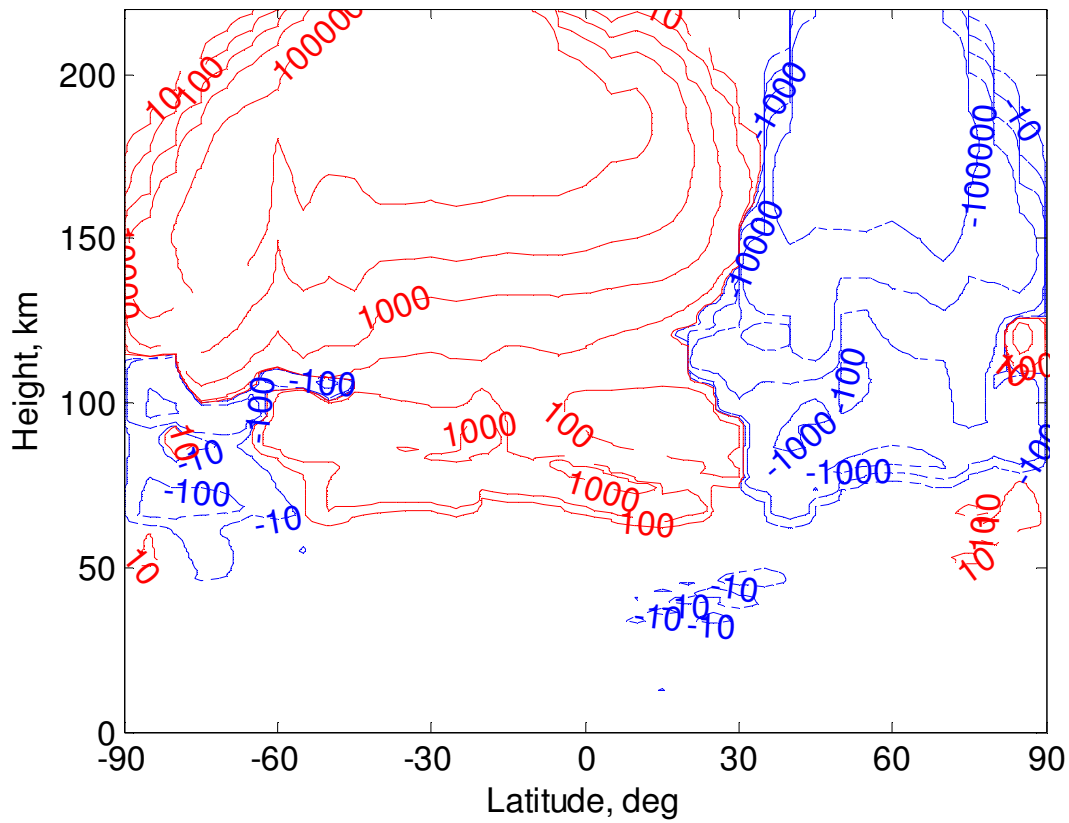
Figure 5.1: Gravity wave acceleration (m s^{-1} sol^{-1}) of the zonal mean flow against the background atmosphere in Figure 4.2 ($L_s = 270°$) with phase speed distribution -60, -40, -20, 0, 20, 40, and 60 m s^{-1}. Red (blue) contour lines depict eastward (westward) acceleration.
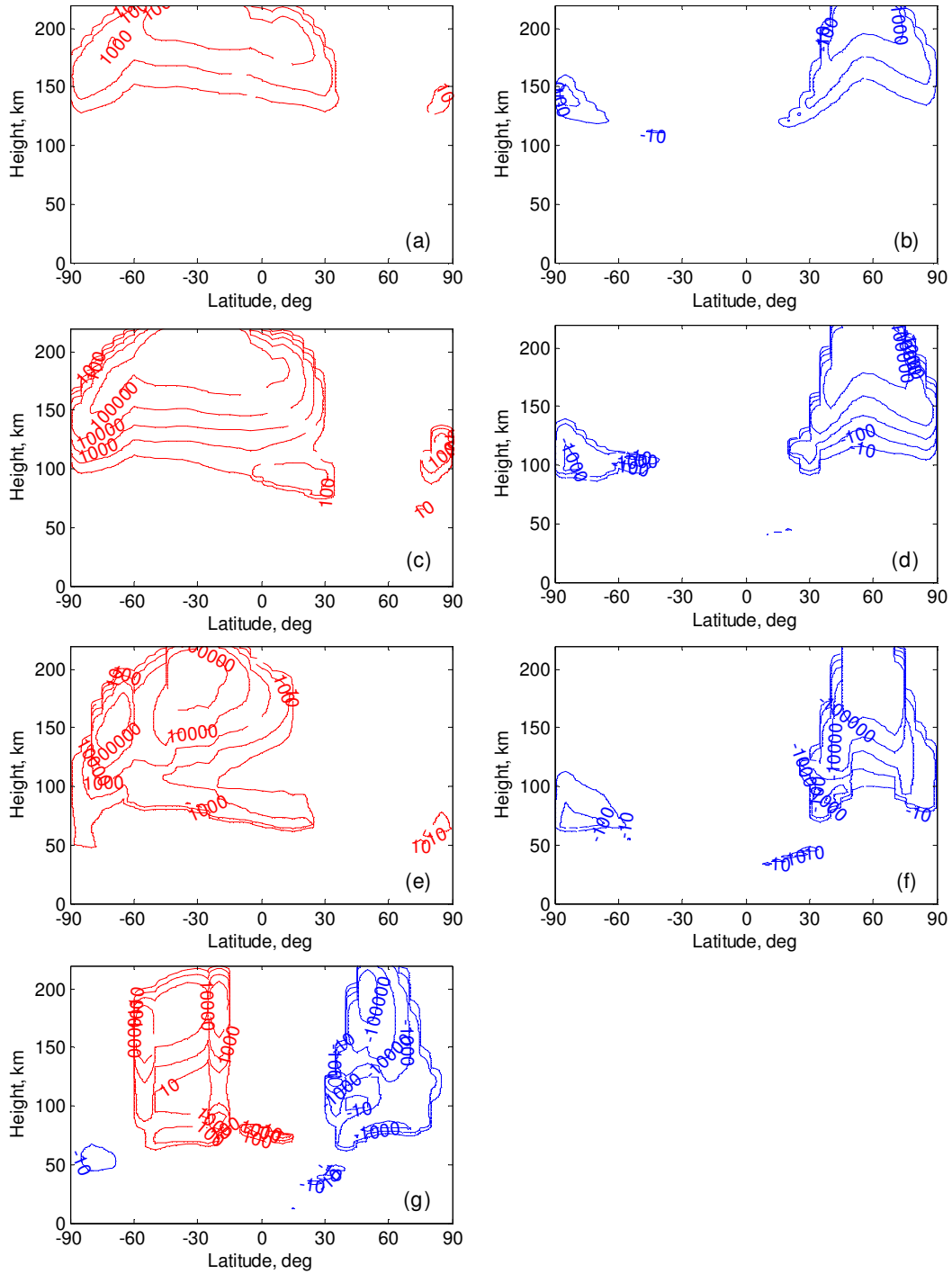
Figure 5.2: Gravity wave acceleration (m s^{-1} sol^{-1}) of the zonal mean flow against the background atmosphere in Figure 4.2 (L_s = 270°) with phase speed distribution (a) 60 m s^{-1}, (b) -60 m s^{-1}, (c) 40 m s^{-1}, (d) -40 m s^{-1}, (e) 20 m s^{-1}, (f) -20 m s^{-1}, and (g) 0 m s^{-1}. Red (blue) contour lines depict eastward (westward) acceleration.

In the middle atmosphere, the zonal accelerations due to wave breaking were consistent with *Barnes* [1990] and *Joshi et al*. [1995]. *Barnes* [1990] predicted gravity wave drag reaching ~900 m s^{-1} sol^{-1} at 60° latitude, while *Joshi et al*. [1995] found peak accelerations of 1000-1500 m s^{-1} sol^{-1} just above the cores of the zonal jets. The *Fritts et al*. [2006] estimate of gravity wave momentum flux (2000 m^2 s^{-2} at 100 km altitude) from perturbations in MGS accelerometer density profiles was also consistent with the zonal accelerations calculated here. Using Mars Climate Sounder temperature retrievals, *Heavens et al*. [2010] identified convective instabilities in the middle atmosphere and interpreted the instabilities to be the result of breaking gravity waves. *Heavens et al*. [2010] estimated momentum flux divergence for a single wave to be 4500 m s^{-1} sol^{-1}, but a relatively short horizontal wavelength of 150 km was assumed. In the thermosphere, the accelerations in Figure 5.1 were exceptionally high but consistent with the gravity wave drag calculated in *Medvedev et al*. [2011]. *Medvedev et al*. [2011] used a constant gravity wave forcing within the range of gravity wave potential energy densities from *Creasey et al*. [2006a]. In both results, the magnitudes of the zonal accelerations exceeded 10^5 m s^{-1} sol^{-1} due to zonal wind distributions that enabled significant gravity wave effects in the thermosphere. While some waves were filtered by the background wind, others were allowed to propagate to the thermosphere due to the large intrinsic phase speeds. With exponential amplitude growth with height, large zonal accelerations were calculated in the thermosphere where momentum had been deposited. In *Medvedev et al*. [2011], the larger accelerations extended lower in the thermosphere than in the HLM results due to the stronger zonal winds taken from the LMD GCM [*González-Galindo et al*., 2009b].

Figure 5.3 shows the output of the HLM gravity wave parameterization against the wind and temperature fields in Figure 4.3 representing northern hemisphere spring ($L_s = 0°$). The magnitude of the source momentum flux followed the latitude profile for $L_s = 0°$ in Figure 4.6 and was distributed over phase speeds from -60 to 60 m s^{-1}. The contribution of each wave to the net zonal acceleration is shown in Figure 5.4. Overall, the magnitudes of the zonal accelerations were lower than in northern hemisphere winter due to the reduced strength of the zonal jets in both the middle atmosphere and thermosphere. Gravity wave breaking due to convective instabilities occurred at lower altitudes (~60-80 km) due to
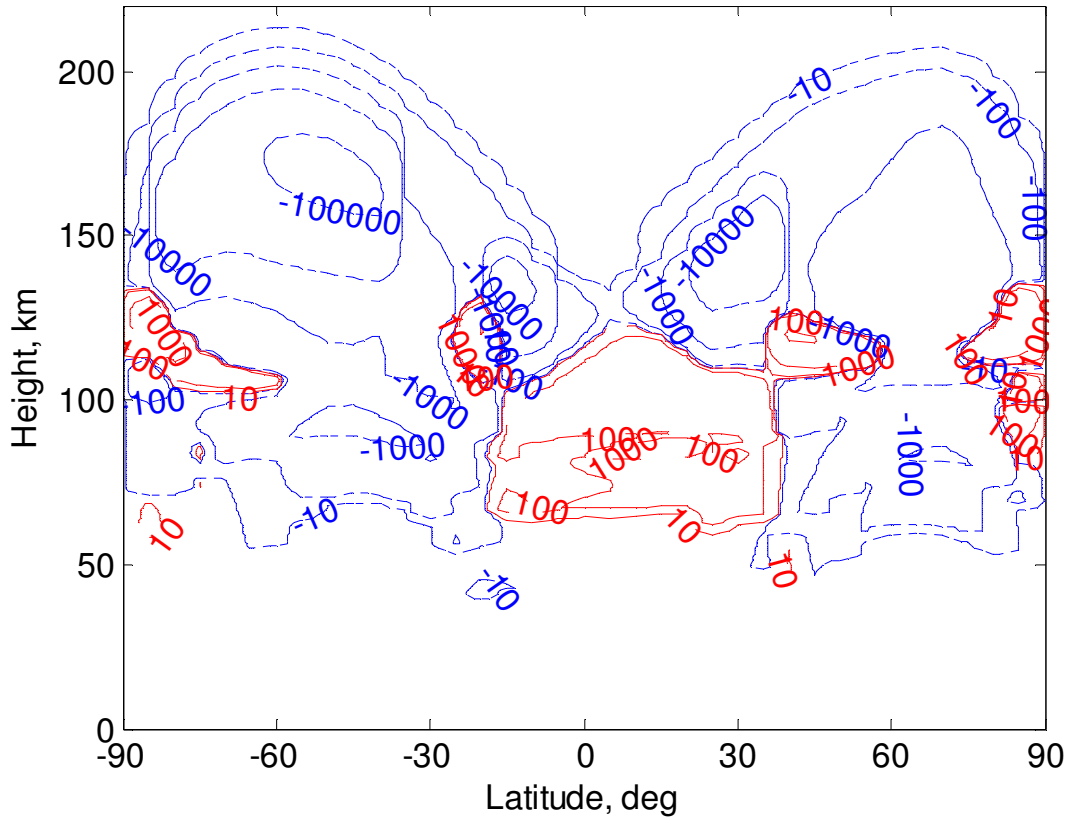
98

Figure 5.3: Gravity wave acceleration (m s^{-1} sol^{-1}) of the zonal mean flow against the background atmosphere in Figure 4.3 ($L_s = 0°$) with phase speed distribution -60, -40, -20, 0, 20, 40, and 60 m s^{-1}. Red (blue) contour lines depict eastward (westward) acceleration.

lower intrinsic phase speeds. With predominantly eastward zonal flow in the thermosphere, only westward propagating gravity waves reached altitudes above 150 km, and only westward momentum was deposited into the mean flow at these altitudes.

Since the zonal accelerations were strongly influenced by the prescribed zonal wind distribution and phase speed distribution, the results of the standalone parameterization runs should be treated cautiously for two reasons. First, there are no observations of the middle and upper atmosphere wind field to validate the background zonal wind or gravity wave phase speed distributions used. Second, the gravity wave effects were not coupled to the background atmosphere. Nevertheless, the calculated zonal accelerations strongly suggested that significant modifications to the mean circulation should be expected.
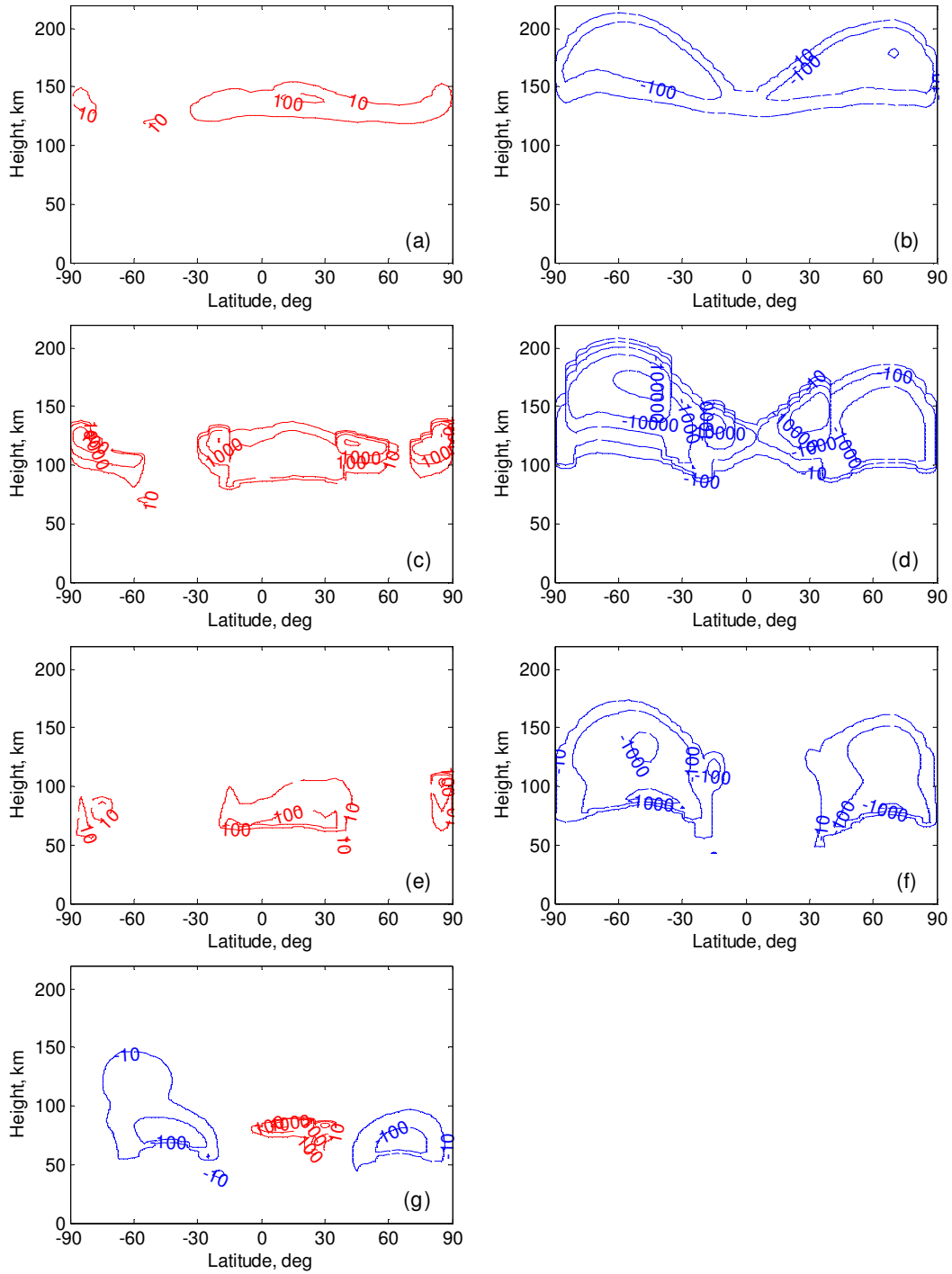
Figure 5.4: Gravity wave acceleration (m s^{-1} sol^{-1}) of the zonal mean flow against the background atmosphere in Figure 4.3 ($L_s = 0°$) with phase speed distribution (a) 60 m s^{-1}, (b) -60 m s^{-1}, (c) 40 m s^{-1}, (d) -40 m s^{-1}, (e) 20 m s^{-1}, (f) -20 m s^{-1}, and (g) 0 m s^{-1}. Red (blue) contour lines depict eastward (westward) acceleration.

5.2   Gravity Wave Effects at Solstice

Figure 5.5 shows the zonal mean wind and temperature fields due to the combined zonal mean and gravity wave forcing at northern hemisphere winter solstice ($L_s = 270°$) and the corresponding differences to the zonal mean parameters from zonal forcing only. The magnitude of the source momentum flux followed the latitude profile for $L_s = 270°$ in Figure 4.6 and included only the stationary component ($c = 0$ m s $^{-1}$). Stationary gravity waves arise from wind flow over topography. This case effectively replicated the gravity wave parameterization used in existing Mars GCMs [*Hartogh et al*., 2005; *González-Galindo et al*., 2009b].

Available observational data to compare against the QNLM results are very limited. Zonally averaged temperature fields from the MGS TES instrument are available for the lower atmosphere below 40 km altitude [*Hartogh et al*., 2005], and the QNLM results capture the salient features of the TES observations. The TES data is slightly warmer (~10 K) at low altitudes above the equator and summer hemisphere and cooler above the winter pole, but these are altitude regions in QNLM that are not affected by gravity waves. Any differences to TES data are due to the specification of the dynamical model. Other than a limited number of Earth-based wind speed measurements identified later in this section, wind speed data is not available to validate model results. Observations above 40 km altitude are likewise not available. Valid comparisons can only be made against GCM results.

The resulting zonal wind field was remarkably similar to GCM results. The strength of the summer hemisphere westward jet and the latitude extent compared very well to *González-Galindo et al*. [2009b], but the peak occurred higher in the atmosphere. In the QNLM simulation, stationary gravity waves encountered a critical level very low in the atmosphere and had no effect on the westward flow. The westward jet was allowed to develop from the lower atmosphere through the thermosphere in the absence of any zonal drag attributed to gravity waves. Compared to *Hartogh et al*. [2005] and *González-Galindo et al*. [2009b], the middle atmosphere winter (eastward) jet was of comparable magnitude, and the jet core occurred at a latitude between the jet cores from the two GCMs. Stationary gravity waves breaking between 50 and 100 km altitude were able to partially close the winter jet and reduce the

101

eastward flow in the thermosphere by up to 80 m s^{-1}. Zonal acceleration peaks of -1000 m s^{-1} sol^{-1} were consistent with early modeling studies by *Barnes* [1990] and *Joshi* et al. [1995]. Peak meridional northward winds increased by 20 m s^{-1} to 60 m s^{-1} and were found near 120 km altitude. Adiabatic heating above the winter pole also increased due to downwelling from the enhanced pole-to-pole Hadley circulation. This case illustrated why gravity wave effects in current Mars GCMs have been deemed to be small. Much of the stationary gravity wave energy is filtered at low levels by the background winds, preventing the momentum from being transported into the middle atmosphere.

It should be noted that GCM results include effects of tidal components within the grid scale resolution of the model. Although the GCMs referenced do not have as high a resolution as the *Moudden and McConnell* [2005] model discussed earlier, it is expected that the GCMs should resolve tidal gravity waves at the zonal wavenumbers discussed in section 4.3.4. Given the LMD GCM of *González-Galindo et al*. [2009b] grid resolution of 5.625° longitude and the *Hartogh et al*. [2005] resolution of 11.25° longitude, first-order the GCMs are able to resolve tidal components up to $s = 37$ and $s = 18$ respectively.
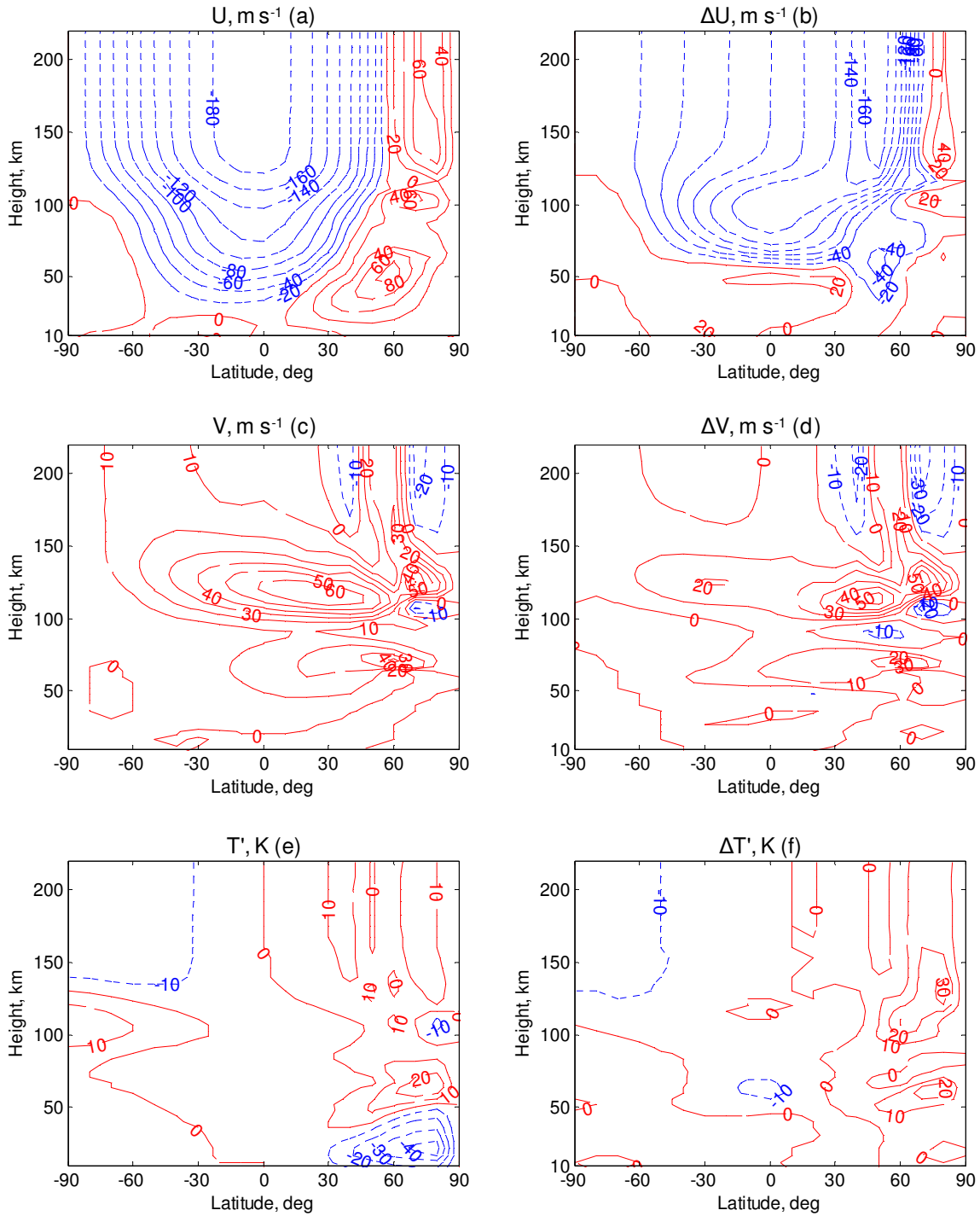
Figure 5.5: Zonal mean fields for $L_s = 270°$ (northern hemisphere winter) with zonal mean and stationary gravity wave forcing: (a) eastward wind, (c) northward wind, and (e) temperature perturbation from the global mean. Differences from zonal mean forcing only are shown in (b), (d), and (f). Red solid lines are positive quantities; blue dashed lines are negative.
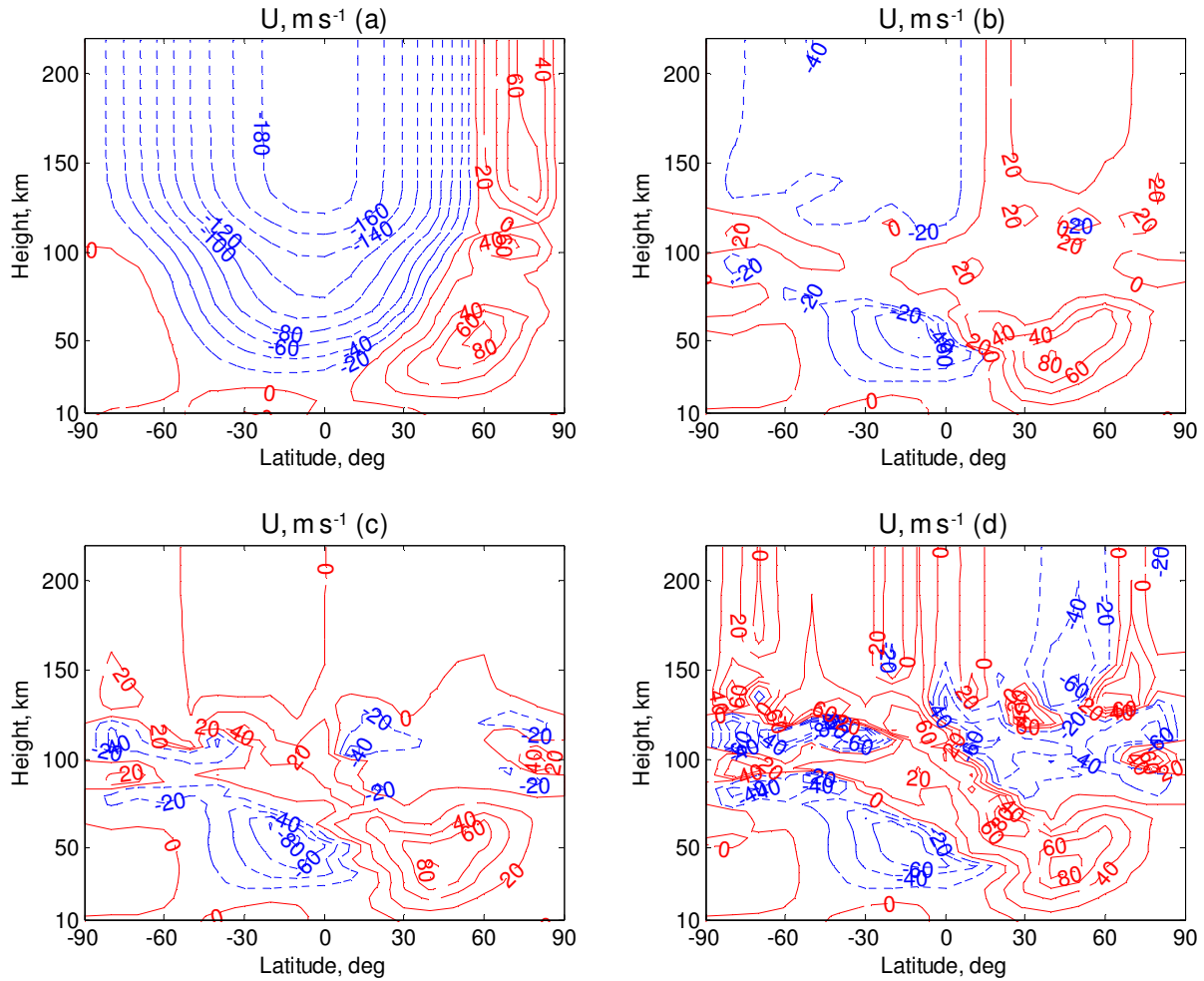
Figure 5.6: Zonal mean eastward wind for $L_s = 270°$ (northern hemisphere winter) with zonal mean and gravity wave forcing with (a) $c = 0$ m s^{-1}, (b) $|c| \leq 20$ m s^{-1}, (c) $|c| \leq 60$ m s^{-1}, and (d) $|c| \leq 80$ m s^{-1}. Red solid lines are positive quantities; blue dashed lines are negative.

5.2.1   Sensitivity to Phase Speed Spectrum

The QNLM model was run with gravity wave forcing using each of the phase speed distributions in Table 4.2. Total source momentum flux was calculated using a spectral index of $p = 5/3$ and was the same for all simulations. The zonal mean fields are shown in Figure 5.6 through Figure 5.8. In each figure, panel (a) shows the wind or temperature field with topographic gravity wave forcing only. The differences across the various phase speed distributions were significant. While gravity wave source

104

amplitudes were an important parameter in determining gravity wave effects, accurate specification of the phase speed spectrum was shown to be more critical since the atmosphere's response was far more sensitive to variations in the phase speed distribution than to variations in source momentum flux magnitudes.

With gravity wave zonal phase speeds of $|c| \leq 20$ m s^{-1}, significant modifications to the mean zonal flow had started to occur. Zonal wind and temperature fields are shown in panel (b) of each figure. In the middle atmosphere, the peak wind speed of both the eastward and westward jets was reduced by approximately 20 m s^{-1}, and both jets were closed near 80 km altitude. Breaking levels of stationary gravity waves occurred mainly between 50 and 75 km altitude, while gravity waves with $|c| = 20$ m s^{-1} were at times able to propagate as high as 150 km altitude before undergoing molecular dissipation. Some of the 20 m s^{-1} waves deposited momentum through wave breaking in the middle atmosphere before propagating into the thermosphere. In the thermosphere, some zonal flow remained, but in general the non-zero phase speed gravity waves did not allow any significant thermospheric zonal flow to develop. This test case included gravity wave momentum flux from tidal gravity waves at horizontal scales expected to be resolved by the Mars GCMs. The differences to GCM wind fields in the middle and upper atmosphere indicate that the forcing in the GCM due to the large wavenumber tidal component may be underestimated. Another possibility is that the phase speed spectrum was not properly prescribed. Either too much momentum flux was allocated to the non-stationary waves in the phase speed spectrum, or the phase speeds (zonal wavenumbers) of the tidal gravity waves were smaller (larger).

With the symmetric phase speed spectrum from -60 to +60 m s^{-1}, the gravity wave effects in both the middle and upper atmospheres were even more significant as shown in panel (c) of each figure. In the middle atmosphere, the eastward winter jet was again closed near 80 km altitude. The strength of the winter jet was reduced by ~25 m s^{-1}, and the location of the jet's peak lowered from 50 to 30 km altitude and moved southward by 10° latitude. The westward jet at low southern latitudes was similarly closed near 80 km. The strength of the westward jet was only reduced by ~10 m s^{-1} and the peak altitude and latitude were not appreciably different, but the incursion of the westward jet into the northern hemisphere

105

was reduced from a maximum of 30°N to 15°N. Between 80 and 120 km altitude, mean flows varied from -40 to 40 m s^{-1} with localized eastward and westward flow in both hemispheres. The resolutions of the model and the phase speed spectrum may have contributed to the irregularities with zonal winds in this altitude band. Gravity waves breaking in the middle atmosphere and lower thermosphere produced zonal accelerations on the order of 100-1000 m s^{-1} sol^{-1}, consistent with *Barnes* [1990] and *Joshi et al.* [1995]. Above 120 km, the thermospheric jets were effectively eliminated. The results can be explained by the zonal forcing distributions in Figure 5.9. Breaking levels were generally lower due to smaller intrinsic phase speeds in the middle atmosphere and lower thermosphere. Only the faster waves with phase speeds $c = \pm 60$ m s^{-1} were able to propagate to the thermosphere. Dissipation through molecular diffusion occurred at lower thermospheric heights as the transmissivity of the atmosphere to a given wave was reduced by the lower intrinsic phase speed. Due to the symmetry of the phase speed spectrum, the eastward and westward momentum deposited in the thermosphere balanced the other over time. By $|c| \leq$ 80 m s^{-1}, there was some evidence of reversal of the thermospheric zonal circulation.

Overall, the results for the modified zonal flow for the $|c| \leq 20$ m s^{-1} and greater spectra were in marked contrast to the results of current Mars GCMs. The most dramatic differences were in the thermosphere where Mars GCMs predict strong westward flow centered in the southern hemisphere, but extending into the middle latitudes of the northern hemisphere. In the solstice case in *González-Galindo et al.* [2009b], which used an updated version of the LMD GCM from *Forget et al.* [1999] and *Angelats i Coll et al.* [2005], the westward jet peaked at over 180 m s^{-1} near 100 km altitude, and strong westward zonal flow continued to 200 km altitude, the top of the model. In the *Hartogh et al.* [2005] GCM simulations, the summer hemisphere westward jet peaked at over 160 m s^{-1} near 80 km altitude and decreased to the top of the model at 110 km. Starting at 90 km altitude, the westward flow extended from pole to pole. *Lellouch et al.* [1991] estimated the horizontal wind speed of Mars' summer (westward) hemisphere jet from Earth-based Doppler shift measurements. Wind speeds of 160 ± 80 m s^{-1} compared favorably to Mars GCMs, but the result from the QNLM simulation was also within the reported measurement uncertainty. Further Doppler shift measurements near 50 km height at solstice by *Moreno*

et al. [2009] were also found to be consistent with the LMD GCM results. Lower atmosphere QNLM results were also in general agreement with wind fields derived from TES temperature fields [*Hartogh et al*., 2005], but observations only extended to 40 km altitude. It is important to note that these measurements did not extend above the middle atmosphere into the regime where most gravity wave effects here were predicted. The behavior of the QNLM middle atmosphere winter jet was in better agreement with Mars GCMs. The strength and location of the jet were very similar to *Hartogh et al*. [2005], although the winter jet in *González-Galindo et al*. [2009b] was 20 m s^{-1} stronger and peaked further north near 60°N latitude. The unbalanced $|c| \leq 60$ m s^{-1} distribution with 3 times more westward momentum flux than eastward momentum flux (not shown) actually increased the magnitude of the middle atmosphere westward jet in the summer hemisphere and left some westward zonal flow in the thermosphere.

In the QNLM simulation, the strong mean meridional circulation driven by solstitial differential heating was further enhanced by gravity wave deceleration of the zonal jets. In the $|c| \leq 60$ m s^{-1} case, the peak circulation increased from 40 m s^{-1} to 50 m s^{-1} near 120 km altitude. From 70-100 km altitude, where gravity wave breaking occurred, the northward flow was significantly increased by 20-30 m s^{-1}. In the upper thermosphere, meridional circulations developed between each pole and 30° latitude in the absence of the zonal wind field. The peak meridional winds of 40 m s^{-1} in the LMD GCM near 100-120 km altitude [*González-Galindo et al*., 2009b] were slightly lower but comparable to the QNLM result. However, the strong meridional circulation in the LMD GCM continued through the thermosphere to the top of the model peaking above 60 m s^{-1} just south of the equator.

The enhanced northward meridional circulation led to increased warming above the winter pole due to adiabatic heating from the descending branch of the Hadley cell, consistent with observations of middle atmosphere polar warming by *Deming et al*. [1986] and *Smith et al*. [2001b] and previous Mars numerical studies [*Barnes*, 1990; *Joshi et al*., 1995; *Hartogh et al*., 2005]. In the QNLM results $|c| \leq 60$ m s^{-1} case, temperatures above the north pole saw an increase of 10-30 K between 50 km and 70 km altitude. Temperatures in the thermosphere above the pole also increased significantly, which was

107

consistent with temperature measurements during Mars Odyssey aerobraking and subsequent Mars GCM simulations [*Bougher et al.*, 2006]. In *Bougher et al.* [2006], the thermospheric polar warming was attributed to the strength of the Hadley circulation, particularly during perihelion polar night conditions. *Bougher et al.* [2006] also suggested that gravity waves may slow the simulated meridional winds and reduce polar warming, opposite to the gravity wave effects observed here. The cooling of the lower atmosphere at 10-50 km altitude above the winter pole was a feature captured in other Mars modeling studies [e.g. *Joshi et al.*, 1995; *Hartogh et al.*, 2005], but significant cooling of the middle atmosphere above the summer pole due to the upwelling circulation of the Hadley cell was not a pronounced feature in Mars GCM results. *González-Galindo et al.* [2009b] showed some cooling above the summer pole at 100-120 km altitude but not a commensurate change at heights where polar warming occurred.

Across the phase speed test cases, the salient features of the meridional wind and temperature fields were in general consistent with the results discussed previously. One item of note was the cooling of the upper thermosphere above the summer pole in the $|c| \leq 80$ m s^{-1} case, presumably due to the penetration of the $c = \pm 80$ m s^{-1} waves to altitudes as high as 220 km. This result reinforced the concept that modifications to the wind and temperature structure of the thermosphere are best accomplished by, if not limited to, fast gravity waves that can propagate freely through the lower atmosphere.
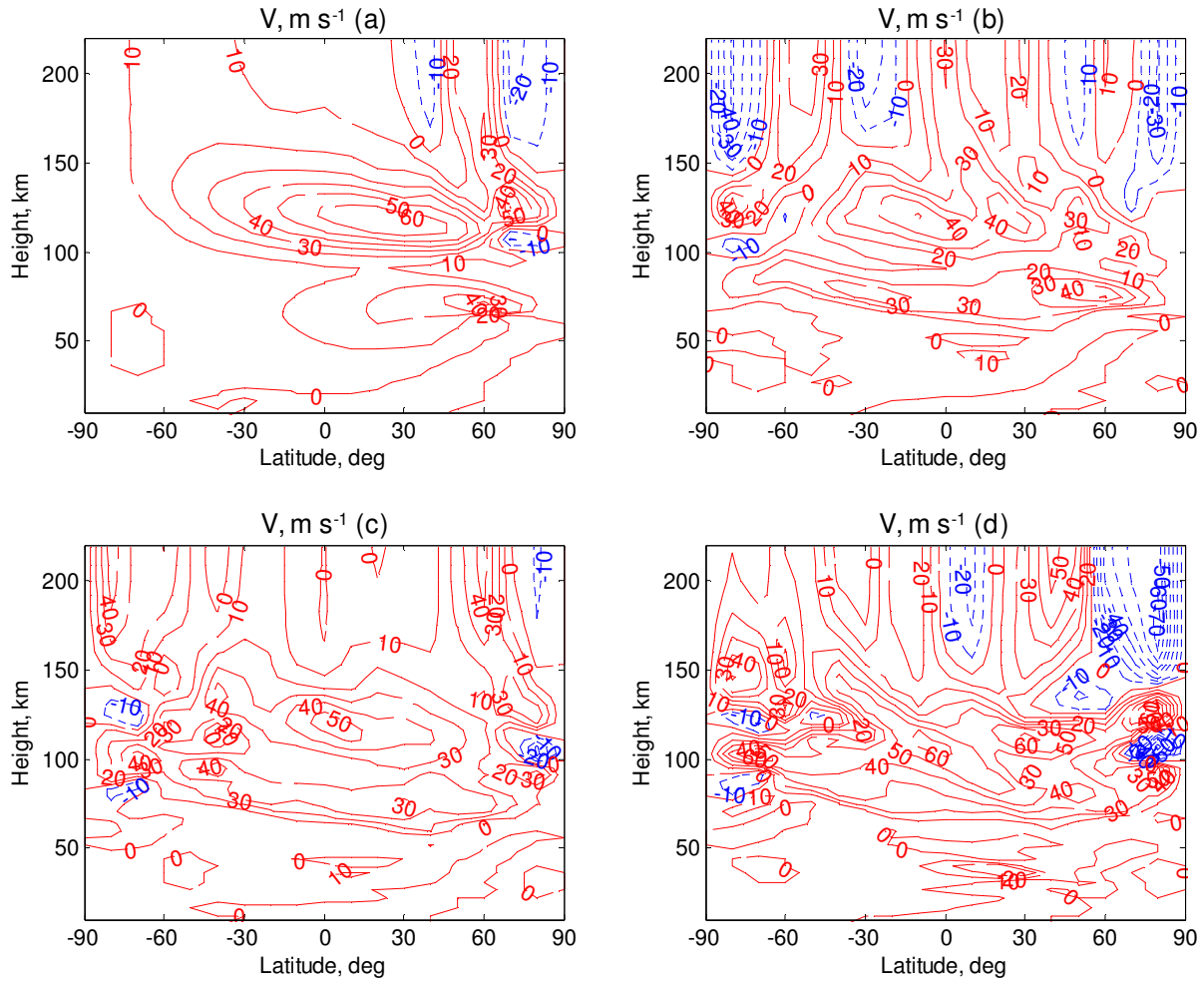
Figure 5.7: Zonal mean northward wind for $L_s = 270°$ (northern hemisphere winter) with zonal mean and gravity wave forcing with (a) $c = 0$ m s^{-1}, (b) $|c| \leq 20$ m s^{-1}, (c) $|c| \leq 60$ m s^{-1}, and (d) $|c| \leq 80$ m s^{-1}. Red solid lines are positive quantities; blue dashed lines are negative.

A significant problem is that the phase speed distribution of tidal and non-tidal gravity waves is not known. Proper specification of the gravity wave phase speed spectrum requires better understanding of the horizontal structure of the gravity waves, the relative contributions of tidal and non-tidal gravity waves in the momentum flux distribution, and upper level wind measurements to validate model results. As seen in this section, non-stationary gravity waves can have profound effects on the zonal mean fields in the middle and upper atmosphere, which are poorly observed. The QNLM results, which used momentum fluxes constrained by observations, show that Mars' GCMs may be underestimating the
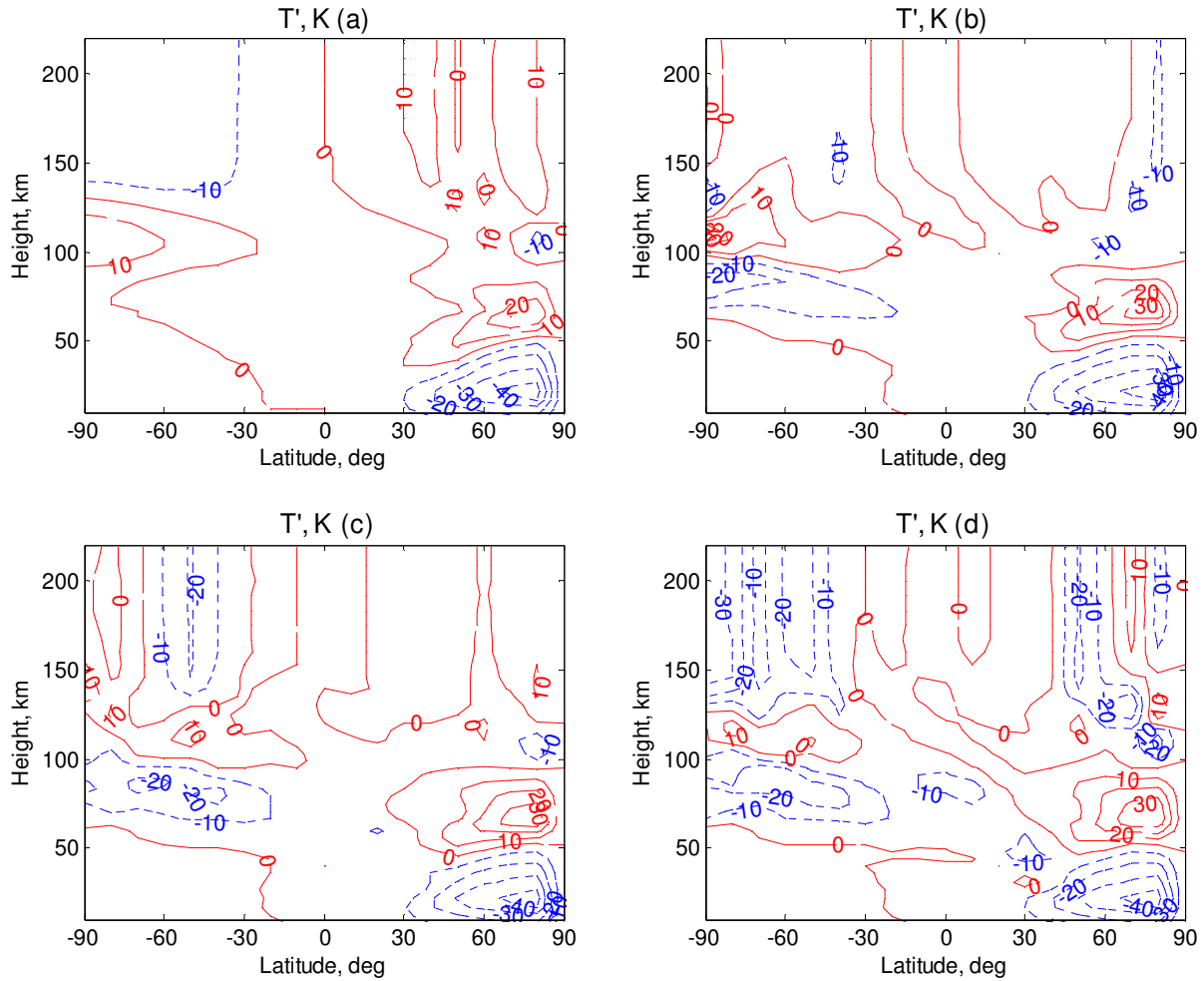
Figure 5.8: Zonal mean temperature perturbation from the global mean for $L_s = 270°$ (northern hemisphere winter) with zonal mean and gravity wave forcing with (a) $c = 0$ m s^{-1}, (b) $|c| \leq 20$ m s^{-1}, (c) $|c| \leq 60$ m s^{-1}, and (d) $|c| \leq 80$ m s^{-1}. Red solid lines are positive quantities; blue dashed lines are negative.

effects of larger wavenumber tidal components on the middle and upper atmosphere. The gravity wave effects due to the stationary component of the gravity wave spectrum are perhaps better understood since the QNLM results confirm predictions by GCMs that much of this wave energy will be filtered by the background winds.
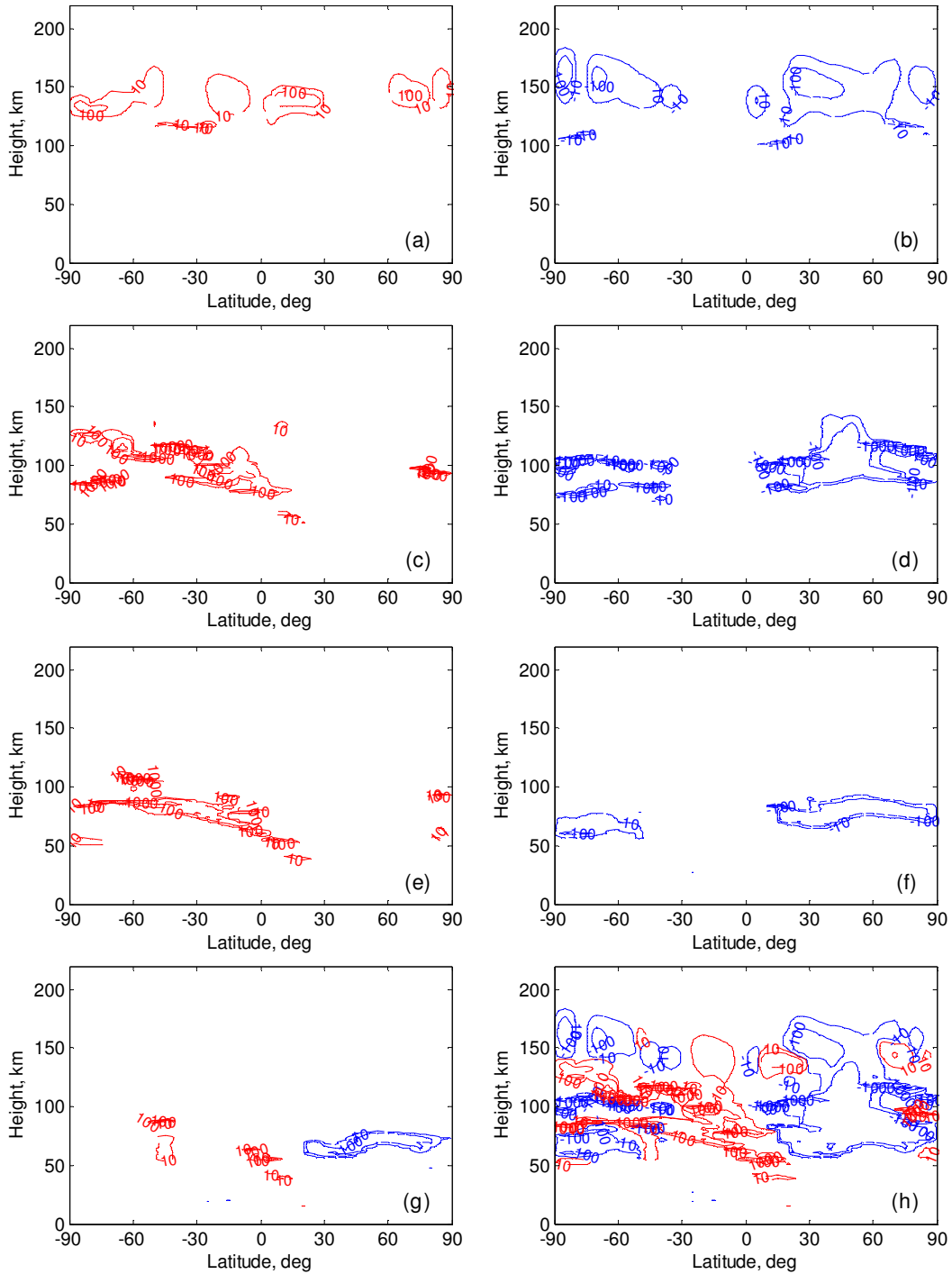
Figure 5.9: Gravity wave acceleration (m s^{-1} sol^{-1}) of the zonal mean flow for L_s = 270° and spectral index p = 5/3 with phase speed distribution (a) 60 m s^{-1}, (b) -60 m s^{-1}, (c) 40 m s^{-1}, (d) -40 m s^{-1}, (e) 20 m s^{-1}, (f) -20 m s^{-1}, (g) 0 m s^{-1}, and (h) all phase speeds. Red (blue) contour lines depict eastward (westward) acceleration.

5.2.2　　　Sensitivity to Source Magnitude

As discussed in section 4.3.3, the gravity wave spectral index was modified to create momentum flux profiles that bounded the expected observability limits of the radio occultation experiment. The differences in source magnitudes were driven solely by the differences of the associated horizontal wavelengths. In Figure 5.10, the zonal mean plots on the left side correspond to the high momentum flux case with $p = 1.6$, while the plots on the right side represent the low momentum flux case with $p = 1.75$. The phase speed distribution ranged from -60 to 60 m s^{-1}. The associated zonal accelerations by phase speed can be found in Appendix C.
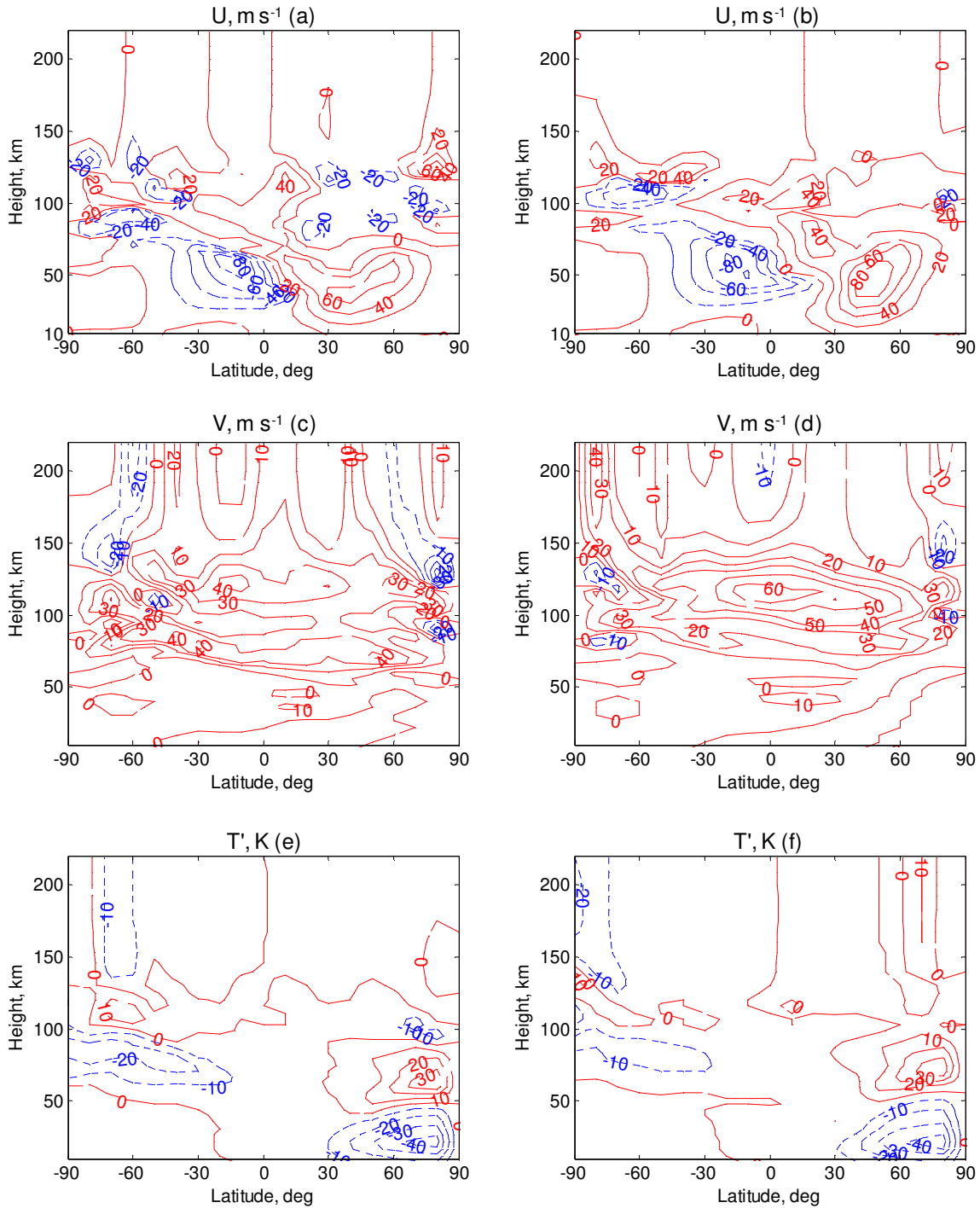
Figure 5.10: Zonal mean fields for $L_s = 270°$ (northern hemisphere winter) with zonal mean and gravity wave forcing: (a) and (b) eastward wind, (c) and (d) northward wind, and (e) and (f) temperature perturbation from the global mean. Plots on the left side represent high source momentum flux ($p = 1.6$), while plots on the right represent low source momentum flux ($p = 1.75$). Red solid lines are positive quantities; blue dashed lines are negative.

In the middle atmosphere, the gravity wave breaking levels were unchanged for both cases. In the breaking level equation, changes in momentum flux were balanced by equivalent changes in horizontal wavenumber. However, the eddy diffusion associated with the wave breaking, and hence the momentum flux divergence, was inversely proportional to the horizontal wavelength. Thus the higher source momentum flux case imparted greater zonal accelerations in the 50-100 km altitude range, resulting in a middle atmosphere winter zonal jet 20 m s^{-1} slower and 10 km lower in altitude than the low source momentum flux case. In both cases, the winter and summer zonal jets were closed around 80 km altitude. In the thermosphere, the magnitude of the zonal acceleration scaled by the magnitude of the source momentum flux. The onset of dissipation from molecular diffusion occurred at comparable altitudes, but the magnitude of the zonal acceleration was greater with larger source momentum flux. Despite the apparent differences in thermospheric forcing, zonal mean flow above 150 km was eliminated in both cases due to offsetting eastward and westward momentum deposition. In the low source magnitude case, the gravity wave forcing enhanced the northward meridional wind at the same altitudes (near 120 km) as the case with zonal mean forcing only. The peak magnitude increased from 40 m s^{-1} to 60 m s^{-1}. In the high momentum flux case, meridional wind speed increased, but at lower heights (70-90 km) to coincide with the increased momentum deposition from gravity wave breaking. Polar warming above the winter pole did not change in either case, but adiabatic cooling at the summer pole due to the ascending branch of the pole-to-pole circulation was greater with larger source momentum flux magnitudes.

As an exercise, the model was run with source momentum flux derived for a constant horizontal wavelength of 200 km. The momentum flux profile scaled directly with the potential energy density profile in Figure 4.5 (a). Near the equator, momentum flux was nearly 6 times greater due to the shorter horizontal wavelength. The momentum flux was sufficient to reverse the direction of the thermospheric jets in both hemispheres. This result demonstrated, following *Alexander et al*. [2002, 2010], that direct scaling of energy density profiles can potentially overestimate gravity wave momentum flux if observability is a function of latitude.

114

5.3 Gravity Wave Effects at Equinox

Figure 5.11 shows the zonal mean wind and temperature fields due to combined zonal mean and gravity wave forcing during northern hemisphere autumn ($L_s = 180°$) with stationary gravity waves only (left) and with gravity waves with phase speeds $|c| \leq 20$ m s^{-1} (right). For each test case in this section, the gravity wave source momentum flux profile was given in Figure 4.6, and the associated zonal accelerations by phase speed can be found in Appendix C. In the case with stationary gravity waves only, gravity waves were only able to propagate upwards between 45°N and 70°N. At other latitudes, stationary gravity waves encountered a critical level near the launch level and were quickly filtered which allowed the westward flow above the equator and the eastward flow in the southern hemisphere to develop with no zonal drag force from gravity waves. In the northern hemisphere, there were some modifications to the eastward flow from 50-80 km altitude where gravity wave breaking occurred. With the development of a retrograde flow above the equator into the thermosphere, this case had started to capture some of the features in *Hartogh et al.* [2005] and *Forget et al.* [1999], but the eastward zonal circulation in those GCMs did not extend into the thermosphere. In this case, meridional circulation was negligible. As phase speeds increased to $|c| \leq 20$ m s^{-1}, more significant gravity wave effects began to emerge. The strengths of the eastward zonal jets in each hemisphere were significantly reduced due to breaking gravity waves, and the middle atmosphere westward flow above the equator was nearly eliminated. Significant meridional flows and temperature perturbations began to develop in the thermosphere. Due to the lower speeds of the background wind field, the equinox case was perhaps more sensitive to gravity phase speed distribution than the solstice case. As in the solstice case, wind speed measurements are needed in the lower atmosphere to calculate or constrain the allowed range of phase speeds and in the middle and upper atmosphere to validate the zonal mean wind fields.

Figure 5.12 and Figure 5.13 show the zonal mean wind and temperature fields due to combined zonal mean and gravity wave forcing during northern hemisphere spring ($L_s = 0°$) and northern hemisphere autumn ($L_s = 180°$) with a phase speed distribution ranging from -60 to 60 m s^{-1}. Deltas to the background atmosphere determined from zonal forcing only are also shown in each figure.

At spring equinox, gravity wave forcing served to decelerate the overall zonal circulation in the middle atmosphere. The strength of the eastward zonal jets in the middle atmosphere of each hemisphere was reduced by 20-40 m s^{-1}, while the vertical extent of the moderate westward flow above the equator was diminished. Due to relatively slow background wind speed and the resulting low intrinsic phase speeds, the bulk of the gravity wave breaking occurred from 40-90 km altitude, lower than breaking levels at solstice. Zonal winds in the thermosphere were significantly reduced as faster westward and eastward propagating waves were able to reach thermospheric heights. Because of the eastward zonal flow, westward gravity waves were able to propagate roughly 10-20 km higher before dissipating than eastward propagating waves. Meridional circulation was significantly enhanced throughout the thermosphere with wind speed magnitudes equal to or exceeding the zonal flow. Multiple cells of overturning circulation were created in the absence of a strong zonal flow, accompanied by net heating or cooling of the atmosphere.

In northern autumn, observed gravity wave energy densities were much stronger, and the resulting source momentum flux profile (see Figure 4.6) was 2 to 4 times higher than northern spring, except at middle and high northern latitudes where flux levels were comparable. Since the background zonal wind fields were the same but with hemispheres swapped, the northern autumn case was essentially a variation of the northern spring case with increased gravity wave source magnitudes. The results at northern autumn equinox ($L_s = 180°$) were similar to the results at northern spring equinox with some gravity wave effects magnified by the increased momentum flux. As in spring, the middle atmosphere eastward jets were reduced to ~20 m s^{-1}, as the top of the jet was closed off by breaking waves around 60-70 km altitude. The retrograde (westward) flow above the equator occurred slightly higher in the middle atmosphere (near 70 km altitude) due to breaking stationary gravity waves at lower altitudes. In the thermosphere, the northern (autumn) hemisphere zonal circulation was reduced to near 0 m s^{-1}, while in the southern (spring) hemisphere, westward zonal flow up to 40 m s^{-1} had developed near the south pole. The strength of the meridional winds in the thermosphere exceeded that of the zonal winds as multiple cells of overturning circulation were again created.

116

Overall, the gravity wave effects moved the zonal mean wind and temperature fields further from the limited GCM published results for equinox conditions [*Hartogh et al.*, 2005; *Forget et al.*, 1999]. Also, wind speed measurements of Mars' middle and upper atmosphere to validate the predicted wind speeds were very limited. In *Moreno et al.* [2009], Doppler-shift measurements of the middle atmosphere near northern autumn equinox showed westward winds ~ 50 m s^{-1} slightly south of the equator, but very strong eastward winds of over 100 m s^{-1} at northern latitudes. The northern hemisphere jet was 3-4 times stronger than even the LMD GCM result [*Forget et al.*, 1999]. These observations occurred during a global dust storm which may have affected zonal mean flow. Given the lack of observations to validate the wind field and limited GCM published results, this test case was viewed as a qualitative exercise to demonstrate that gravity wave effects significantly modify the zonal mean fields at equinox if non-zero phase speeds are assumed.
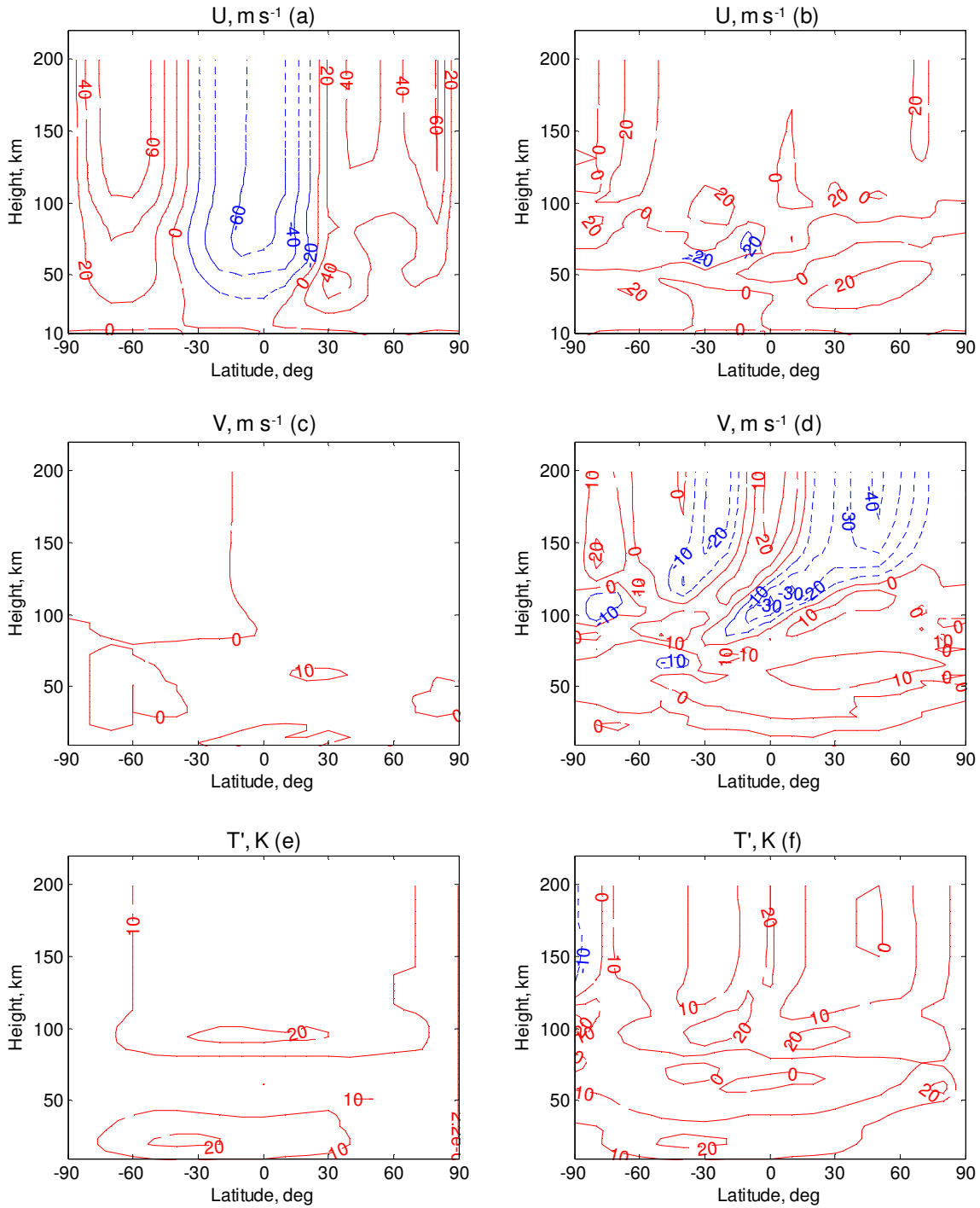
117

Figure 5.11: Zonal mean fields for $L_s = 180°$ (northern hemisphere autumn) with zonal mean and gravity wave forcing: (a) and (b) eastward wind, (c) and (d) northward wind, and (e) and (f) temperature perturbation from the global mean. Phase speed distributions were (left) $c = 0$ m s^{-1} and (right) $c = -20$, 0, and 20 m s^{-1}. Red solid lines are positive quantities; blue dashed lines are negative.
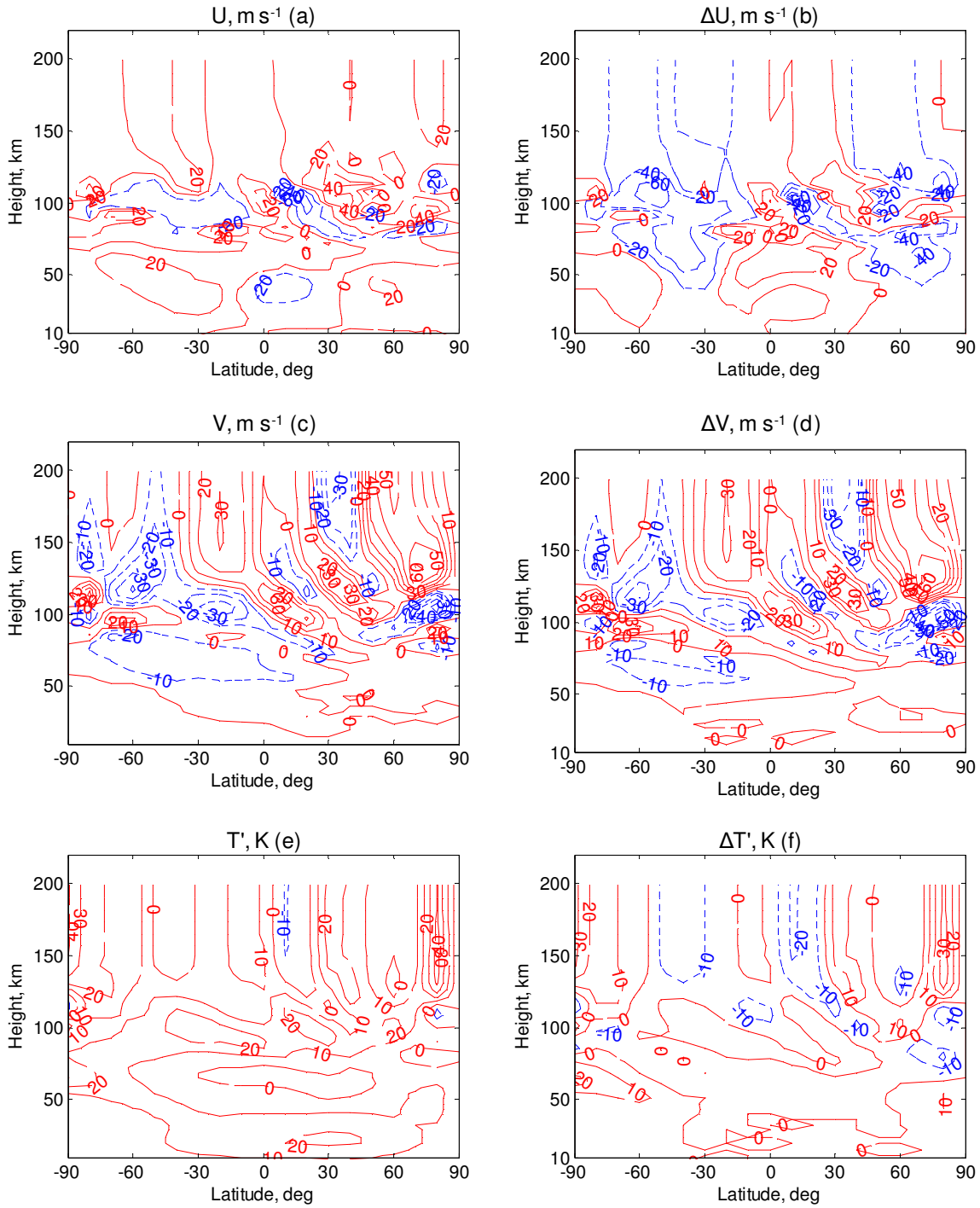
Figure 5.12: Zonal mean fields for $L_s = 0°$ (northern hemisphere spring) with zonal mean and gravity wave forcing: (a) eastward wind, (c) northward wind, and (e) temperature perturbation from the global mean. Differences from zonal mean forcing only are shown in (b), (d), and (f). Red solid lines are positive quantities; blue dashed lines are negative.
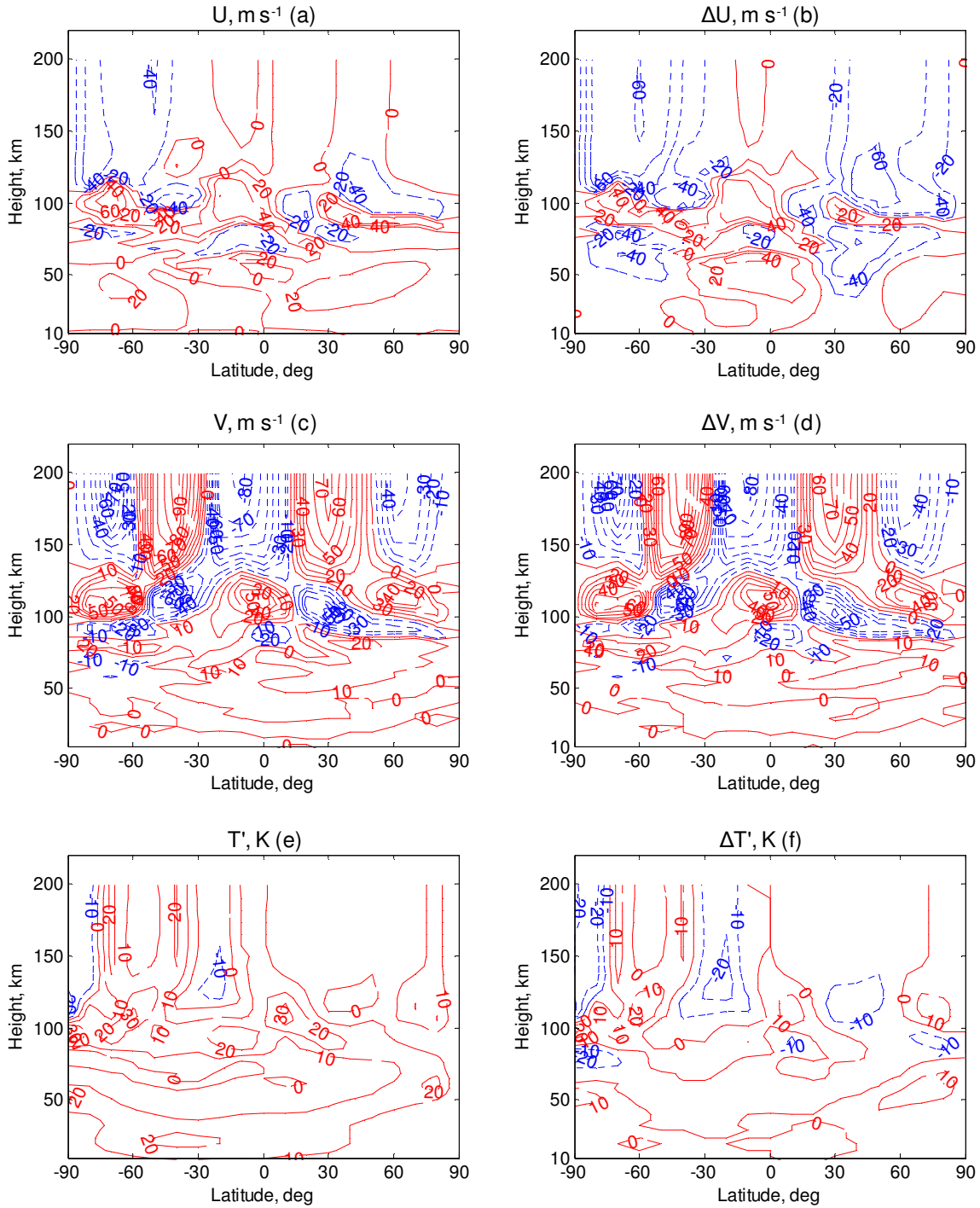
Figure 5.13: Zonal mean fields for $L_s = 180°$ (northern hemisphere autumn) with zonal mean and gravity wave forcing: (a) eastward wind, (c) northward wind, and (e) temperature perturbation from the global mean. Differences from zonal mean forcing only are shown in (b), (d), and (f). Red solid lines are positive quantities; blue dashed lines are negative.

Chapter 6

Summary and Conclusions

Gravity waves have long been thought to play an important role in the dynamics of Mars' atmosphere due to similarities with Earth in the structure and circulation of the atmosphere and due to expected stronger forcing of gravity waves from the large amplitude of Martian topography and stronger low-level winds. Modeling studies have generally supported these assertions but have been limited by observational constraints on gravity wave forcing and by a lack of wind and temperature measurements to validate predicted results. Recent observations of small-scale waves in Mars' atmosphere have allowed this research to begin to quantify the characteristics and variability of gravity waves at Mars. First, from temperature perturbations in MGS radio occultation measurements, global distributions of gravity wave potential energy density in the lower atmosphere were calculated to serve as the observational basis to constrain gravity wave amplitudes in a dynamical model for Mars. The distributions are believed to contain stationary gravity waves from topographic forcing and non-stationary large-wavenumber tidal gravity waves. Secondly, density perturbations found in MGS accelerometer measurements during aerobraking provided evidence that gravity waves reached thermospheric heights and provided insight into the potential variability of source-level forcing or filtering by the background winds.

To assess the effects of gravity waves on the mean state of Mars' atmosphere, a Mars-specific gravity wave parameterization was developed that combined the linear saturation scheme of *Lindzen* [1981] and the atmospheric transmission scheme of *Matsuno* [1982] to create a model for gravity wave effects from the lower atmosphere to the upper thermosphere. The gravity wave parameterization was

121

integrated into the Mars QNLM model, which was run using gravity wave source momentum flux profiles derived directly from the observed energy densities. This marked the first time that numerical simulations of Mars atmosphere were performed using a gravity wave parameterization constrained by observational data. Unlike typical gravity waves studies for Earth, the model results were not tuned to achieve an expected climatology.

When run in a standalone configuration, the gravity wave parameterization reproduced (1) the predicted zonal accelerations of a single breaking gravity wave from *Barnes* [1990] and *Joshi et al.* [1995] and (2) the combined zonal accelerations from a full spectrum of waves propagating against a prescribed background flow from *Medvedev et al.* [2011]. When integrated into QNLM and configured for topographic forcing only, the QNLM results were very similar to the zonal mean parameters from a full Mars GCM [*González-Galindo et al.*, 2009b]. In both models, much of the stationary gravity wave energy encountered a critical level when propagating vertically and was filtered by the background wind.

The observed gravity wave potential energy distributions, which show large energy densities in Mars' tropics not correlated with topography, and the spectral analysis of *Miyoshi et al.* [2011] on high-resolution GCM results indicate that non-stationary tidal gravity waves are included in the source gravity wave data. *Hinson and Wilson* [2004] provided further observational evidence of thermal tides in the occultation data. When associated phase speeds are incorporated into the QNLM gravity wave source spectrum, the effects on the resulting zonal mean parameters are profound. At solstice, the middle atmosphere zonal jets were closed, and upper atmosphere zonal winds were significantly diminished. Meridional circulation was enhanced at altitudes where gravity wave breaking occurred. The model results were particularly sensitive to the prescribed phase speed distribution, and multiple phase speed spectra were evaluated to assess sensitivity. With phase speed spectrums up to only 20 m s^{-1}, the model results differed quite strongly from Mars GCMs, particularly in the upper atmosphere above ~100 km altitude.

In these cases, the differences between model results was due to the propagation and dissipation of the non-stationary gravity wave components. It is expected that the Mars' GCMs resolve the tidal

122

components contained in the QNLM momentum flux profiles. The difference in results suggests that Mars' GCMs may be underestimating the forcing from large zonal wavenumber tidal components. On the other hand, the prescribed phase speed distribution used in QNLM may be overestimating phase speed magnitude or the relative contribution of the stationary components. Thus, many open questions remain: (1) how significant are tidal gravity waves in the source momentum flux distribution?, (2) what are the characteristics (phase speed, horizontal structure, and frequency) of the tidal components?, and (3) are other plausible mechanisms, such as convective activity at boundary layers, geostrophic adjustment, and non-local deep transport, significant sources for non-stationary gravity waves?

Proper specification of the gravity wave phase speed spectrum requires better understanding of the horizontal structure of the gravity waves, the relative contributions of tidal and non-tidal gravity waves in the momentum flux distribution, and upper level wind measurements to validate model results. The altitude regime of Mars' atmosphere where gravity wave effects are expected to occur is poorly observed. Other than Viking lander and Pathfinder missions, the only available wind speed measurements of Mars' atmosphere were derived from Earth-based Doppler shift measurements of CO emission lines near 50 km altitude [e.g. *Moreno et al.*, 2009]. Very few of these measurements have been taken, and they only spanned a small height range in the middle atmosphere. Measurements of low-level and upper atmosphere wind speeds are not available. Overall, the model results provided compelling evidence that gravity waves have the potential to significantly alter the mean zonal state of the atmosphere, but more observational data is needed to better constrain the gravity wave parameters and validate model results.

6.1 Review of Science Questions

The science questions that have been addressed by this research are reviewed in the this section.

1. What are the characteristics of the wave structures observed in MGS radio occultation vertical temperature profiles?

For each gravity wave observed in a radio occultation temperature profile, potential energy density and vertical wavelength were calculated from the temperature perturbation profile. The mean

123

gravity wave potential energy density observed between 10-15 km altitude was 3.9 J kg^{-1}, but large amplitude waves with potential energy densities greater than 100 J kg^{-1} were also observed. Using Fourier analysis, wave power spectrums were computed for each temperature perturbation profile. Mean and median vertical wavelengths were 14.9 km and 14.0 km respectively. The distribution of dominant wavelengths was bimodal with maxima near 8-10 km and 13-15 km. Horizontal wavelength could not be calculated from the radio occultation measurement, but instead was inferred using gravity wave theory. Nominal horizontal wavelengths were estimated to range from 264 km at the pole to 1138 km at the equator, but the uncertainty in the estimate was very high. Other characteristics, such as phase speed, horizontal propagation direction, and wave frequency, could not be determined from the temperature profiles.

2. How do gravity wave energy densities observed in the lower atmosphere vary with latitude, longitude, season, and local time of day?

Global distributions of gravity wave potential energy density were calculated to depict the geographic and seasonal variations of gravity wave energy. Gravity wave energy was elevated above the Martian tropics and to a lesser degree above areas of significant topography, such as the Tharsis region. The highest values of potential energy density were observed near northern autumn equinox ($L_s = 180°$) suggesting a seasonal change in forcing, filtering by background winds, or a combination of both.

The gravity wave vertical flux of horizontal momentum was calculated directly from potential energy density. Due to the latitude-dependent horizontal wavelength profile, zonally averaged momentum flux was more equally spread across all latitudes, except during northern hemisphere autumn when elevated momentum flux was calculated for the southern hemisphere, indicating a possible correlation with the hemisphere's increased orographic variance.

Due to the spacecraft's orbit, daytime occultation profiles were only available at polar latitudes. This data was not used due to difficulty in processing some of the profiles, and diurnal variations in polar regions could not be assessed.

124

3. Do the distributions of observed gravity wave energy densities provide insight on how gravity waves are generated at Mars?

The geographic distribution of gravity wave energy density can be explained reasonably well by the combination of stationary components from topographic forcing and non-stationary tidal components. Additional observations of gravity waves in conjunction with measurements of low-level winds are needed to better understand gravity wave sources.

4. How do density perturbations observed in the thermosphere vary with latitude, longitude, season, and local time of day?

During aerobraking, the progression of accelerometer density measurements through different seasons, latitudes, and local times of day permitted comparisons of thermospheric density perturbations by season, hemisphere, and local time of day. Fractional density perturbation variance in northern autumn was 13 times higher than northern spring, consistent with the seasonal potential energy density distributions from the lower atmosphere. In northern winter, perturbation variance was 50% higher than southern winter. The result suggested that small-scale waves in the thermosphere may not be heavily influenced by the underlying topography, as orographic variance is higher in the southern hemisphere. Finally, perturbation variance was seen to be 2 times greater at 1500 LTST than at 0200 LTST, which may be evidence of a difference between daytime and nighttime filtering by tidal related winds.

5. Do the characteristics of waves seen in the thermosphere differ from those of gravity waves observed in the lower atmosphere?

Given the data averaging of the thermospheric density profiles and the observability constraints on the radio occultation measurement, it is believed that the waves observed in the thermosphere were different than those observed in the lower atmosphere due to differences in horizontal and vertical wavelengths. Nevertheless, the thermospheric density perturbations provided qualitative evidence that gravity waves reach thermospheric heights. Also, elevated gravity wave activity in northern autumn was observed in both the lower atmosphere and thermosphere.

125

6. What are the effects of gravity waves on zonal mean wind and temperature variations in the middle and upper atmosphere of Mars?

At solstice with stationary gravity waves only, most gravity waves encountered a critical level in the lower atmosphere allowing the strong westward flow to develop above the equator and in the southern hemisphere in the absence of any zonal drag from gravity wave dissipation. The strength of the winter (eastward) jet was reduced 20 m s^{-1} by breaking waves, and thermospheric winds at high northern latitudes were significantly reduced. Northward meridional circulation increased by 20-50 m s^{-1}. Adiabatic heating above the winter pole increased due to the increased strength of the Hadley circulation.

With non-zero phase speeds, the middle atmosphere zonal jets in both hemispheres were closed near 80 km altitude. The strength of the winter jet was reduced by 25 m s^{-1}, and the location of the jet's core lowered from 50 to 30 km altitude and moved southward. The strength of the summer (westward) jet was reduced by 10 m s^{-1}. In the thermosphere, the zonal jets were effectively eliminated. Meridional northward winds increased by 20-30 m s^{-1} from 70-100 km altitude where gravity wave breaking occurred. Warming above the winter pole due to adiabatic heating from the descending branch of the pole-to-pole circulation increased due to the enhanced meridional circulation.

At equinox with non-zero phase speeds, gravity waves decelerated the overall zonal circulation in the middle atmosphere. Eastward zonal flow in each hemisphere and westward zonal flow above the equator were reduced to approximately 20 m s^{-1}. Zonal winds in the thermosphere were also significantly reduced.

7. How high in Mars' atmosphere do the effects of gravity waves extend?

Accelerometer density perturbations provided observations of gravity waves up to 140 km altitude. QNLM model results indicated that gravity waves with sufficient phase speed will propagate even higher into the upper thermosphere and that significant modifications to the mean wind and temperature fields extend throughout the thermosphere as well. In nearly all simulations, stationary gravity waves did not propagate above 100 km altitude.

126

8. What are the dependencies of the mean circulation and structure to various characteristics of the source spectrum?

The QNLM model was run varying the magnitude of the source spectrum and also the phase speed spectrum. Changes in source momentum flux magnitude, which were bounded by the observability constraints of the radio occultation experiment, were noticeable but in line with the baseline effects. Phase speed spectrums reflected the range of phase speeds expected from the large wavenumber tidal components in the gravity wave source spectrum. When a stationary gravity wave spectrum was used, the QNLM model results were similar to GCM results using an orographic gravity wave scheme. With phase speeds as low as 20 m s^{-1}, the middle atmosphere jets were closed, and thermospheric winds were significantly reduced indicating that thermal tides may be significant to middle and upper atmosphere forcing

6.2   Recommendations for Future Research

To better understand the circulation and structure of Mars' atmosphere, the interactions of the mean flow and atmospheric waves, and the coupling of the lower and upper atmosphere, direct wind and temperature measurements are needed at all levels and at all locations. In the middle and upper atmosphere, wind speed measurements would be used to validate GCM predictions. In particular, wind speed measurements would address the outstanding question if non-stationary gravity waves are significant in Mars' upper atmosphere. Earth-based Doppler shift measurements of the atmospheric CO emission lines in the middle atmosphere have provided wind measurements that at times disagree strongly with thermal wind estimates based on MGS TES data and with GCM results [*Moreno et al.*, 2009]. In the thermosphere, an improved knowledge of thermospheric winds over the solar cycle and Mars' seasons will increase our understanding of the Mars thermosphere-ionosphere system and its coupling with the lower atmosphere. In addition, upper atmosphere wind measurements will be important to plan aerobraking and aerocapture operations and the safe entry, descent, and landing (EDL) of surface missions.

Instruments planned for NASA's Mars Science Orbiter (MSO), originally envisioned for a late 2013 launch, would have been capable of providing direct wind observations of Mars' atmosphere on a daily basis. The Sub-millimeter Radiometer would measure zonal and meridional components of lower atmosphere winds, and the Retarding Potential Analyzer would measure upper atmosphere winds. Vertical coverage was planned from the surface to 120 km altitude with resolution better than an atmospheric scale height. Due to budget constraints, MSO mission objectives were reduced and merged with ESA's ExoMars mission and then eventually terminated in February 2012 by the Obama administration. A Doppler wind instrument may also be suitable to measure horizontal atmospheric winds on a planetary mission. The Doppler technique has been used by the Wind Imaging Interferometer (WINDII), the High Resolution Doppler Imager (HRDI), and the TIMED Doppler Interferometer (TIDI) to measure winds in Earth's middle and upper atmosphere, but this type of instrument has not flown on an interplanetary mission. It should be noted that even in the higher altitudes of Earth's atmosphere, wind measurements are much harder to obtain and not commonly available.

Radio occultation measurements provide temperature profiles that enable a range of research activities of the structure and circulation of the lower atmosphere. All orbiter missions to Mars should be equipped with a radio science package sufficient to perform radio occultation experiments. Unfortunately, this has not been the case for many recent Mars orbiters. Of recent missions, only the Mars Express Orbiter Radio Science Experiment (MaRS) has been suitable for radio sounding of the neutral atmosphere and ionosphere. MaRS temperature profiles should be combined with the work here to improve the characterization of gravity wave energy and parameters. Another method to improve the quantity and distribution of radio occultation measurements would be to employ radio science experiments on spacecraft-to-spacecraft communication at Mars. Spacecraft-to-spacecraft radio occultations would broaden coverage of atmospheric neutral and ionospheric structure beyond that attainable by Earth communications only. Such a radio science system could be planned into future science and telecommunications mission sent to Mars. Finally, a mission or instrument design that enhances spatial and temporal coverage could better characterize the horizontal scale and wave frequency

of gravity waves, similar to *Ern et al*. [2004], *Alexander et al*. [2008], and *Wang and Alexander* [2010]. Better estimates of horizontal wavelengths and wave frequencies would better constrain the profiles of gravity wave source momentum flux and better constrain the phase speed distribution

With respect to modeling, significant benefits would be realized with improving the specification of the gravity wave source momentum flux. Incorporation of MaRS radio occultation profiles into the MGS gravity wave dataset may improve seasonal and geographic coverage. Another change that could be implemented immediately is the estimation of horizontal wavelength for an individual temperature perturbation profile as opposed to using an estimate based on a zonal average. The gravity wave parameterization could potentially be improved by incorporating other dissipation effects from *Yiğit et al*. [2008] such as nonlinear effects, thermal conduction, and ion drag. The gravity wave parameterization could also be incorporated into a 3-D GCM. Gravity wave intermittency was not addressed in this research, but intermittency effects should be included in future research. It will also be important to understand how gravity waves interact with planetary-scale waves. Using QNLM, the large-scale tidal equations and gravity wave equations could be solved simultaneously with the mean flow to understand how the waves interact with each other and the mean circulation.

Bibliography

Acuña, M. H., et al. (1998), Magnetic field and plasma observations at Mars: Initial results of the Mars Global Surveyor mission, *Science*, *279*, 1676–1680.

Ahmad, B., and G. L. Tyler (1999), Systematic errors in atmospheric profiles obtained from Abelian inversion of radio occultation data: Effects of large-scale horizontal gradients, *J. Geophys. Res.*, *104*(D4), 3971–3992, doi:10.1029/1998JD200102.

Albee, A. L., R. E. Arvidson, F. Palluconi, and T. Thorpe (2001), Overview of the Mars Global Surveyor mission, *J. Geophys. Res.*, *106*, 23,291-23,316.

Alexander, M. J., and T. J. Dunkerton (1999), A Spectral Parameterization of Mean-Flow Forcing due to Breaking Gravity Waves, *J. Atmos. Sci.*, *56*, 4167-4182.

Alexander, M. J., T. Tsuda, and R. A. Vincent (2002), Latitudinal variations observed in gravity waves with short vertical wavelengths, *J. Atmos. Sci.*, *59*, 1394-1404.

Alexander, M. J. and K. H. Rosenlof (2003), Gravity-wave forcing in the stratosphere: Observational constraints from the Upper Atmosphere Research Satellite and implications for parameterization in global models, *J. Geophys. Res.*, *108*(D19), 4597, doi:10.1029/2003JD003373.

Alexander, M. J., J. H. Richter, and B. R. Sutherland (2006), Generation and trapping of gravity waves from convection with comparison to parameterization, *J. Atmos. Sci.*, *63*, 2963-2977.

Alexander, M. J., et al. (2008), Global estimates of gravity wave momentum flux from High Resolution Dynamics Limb Sounder observations, *J. Geophys. Res.*, *113*, D15S18, doi:10.1029/2007JD008807.

Alexander, M. J., S. D. Eckermann, D. Broutman, and J. Ma (2009), Momentum flux estimates for South Georgia Island mountain waves in the stratosphere observed via satellite, *Geophys. Res. Lett.*, *36*, L12816, doi:10.1029/2009GL038587.

Alexander, M. J., M. Geller, C. McLandress, S. Polavarapu, P. Preusse, F. Sassi, K. Sato, S. Eckermann, M. Ern, A. Hertzog, Y. Kawatani, M. Pulido, T. A. Shaw, M. Sigmond, R. Vincent, and S. Watanabe (2010), Recent developments in gravity-wave effects in climate models and the global distribution of gravity-wave momentum flux from observations and models, *Q. J. R. Meteorol. Soc.*, *136*, 1103-1124.

Anderson, E., and C. Leovy (1978), Mariner 9 television limb observations of dust and ice hazes on Mars, *J. Atmos. Sci.*, *35*, 723–734.

Angelats i Coll, M., F. Forget, M. A. López-Valverde, P. L. Read, and S. R. Lewis (2004), Upper atmosphere of Mars up to 120 km: Mars Global Surveyor accelerometer data analysis with the LMD general circulation model, *J. Geophys. Res.*, *109*, E01011, doi:10.1029/2003JE002163.

Angelats i Coll, M., F. Forget, M. A. López -Valverde, and F. González-Galindo (2005), The first Mars thermospheric general circulation model: The Martian atmosphere from the ground to 240 km, *Geophys. Res. Lett.*, *32*, L04201, doi:10.1029/2004GL021368.

Banfield, D., B. J. Conrath, M. D. Smith, P. R. Christensen, and R. J. Wilson (2003), Forced waves in the Martian atmosphere from MGS TES nadir data, *Icarus*, *161*, 319–345.

Barnes, J. (1990), Possible effects of breaking gravity waves on the circulation of the middle atmosphere of Mars, *J. Geophys. Res.*, *95*, 1401-1421.

Benyon, W. J. G. (1948), Evidence of horizontal motion in region F_2 ionization, *Nature*, *162*, 887.

Bougher, S., G. Keating, R. Zurek, J. Murphy, R. Haberle, J. Hollingsworth, and R. T. Clancy (1999), Mars Global Surveyor aerobraking: Atmospheric trends and model interpretation, *Adv. Space. Res.*, *23*, 1887– 1897.

Bougher, S. W., S. Engel, D. P. Hinson, and J. M. Forbes (2001), Mars Global Surveyor radio science electron density profiles : Neutral atmosphere implications, *Geophys. Res. Lett.*, *28*(16), 3091–3094, doi:10.1029/2001GL012884.

Bougher, S. W., S. Engel, D. P. Hinson, and J. R. Murphy (2004), MGS Radio Science electron density profiles: Interannual variability and implications for the Martian neutral atmosphere, *J. Geophys. Res.*, *109*, E03010, doi:10.1029/2003JE002154.

Bougher, S. W., J. M. Bell, J. R. Murphy, M. A. Lopez-Valverde, and P. G. Withers (2006), Polar warming in the Mars thermosphere: Seasonal variations owing to changing insolation and dust distributions, *Geophys. Res. Lett.*, *33*, L02203, doi:10.1029/2005GL024059.

Briggs, G. A. and C. B. Leovy (1974), Mariner 9 observations of the Mars north polar hood, *Bull. Amer. Met. Soc.*, *55*, 278-296.

Cahoy, K. L., D. P. Hinson, and G. L. Tyler (2006), Radio science measurements of atmospheric refractivity with Mars Global Surveyor, *J. Geophys. Res.*, *111*, E05003, doi:10.1029/2005JE002634.

Christensen, P. R., et al. (1992), Thermal Emission Spectrometer Experiment: Mars Observer Mission, *J. Geophys. Res.*, *97*(E5), 7719–7734, doi:10.1029/92JE00453.

Christensen, P. R., et al. (2001), Mars Global Surveyor Thermal Emission Spectrometer experiment: Investigation description and surface science results, *J. Geophys. Res.*, *106*, 23,823–23,871, doi:10.1029/2000JE001370.

Clancy, R. T., B. J. Sandor, M. J. Wolff, P. R. Christensen, M. D. Smith, J. C. Pearl, B. J. Conrath, and R. J. Wilson (2000), An interpretation of ground-based millimeter, MGS TES, and Viking atmospheric temperature measurements and dust loading in the global Mars atmosphere, *J. Geophys. Res.*, *105*, 9553–9571.

Clancy, R. T., M. J. Wolff, and P. R. Christensen (2003), Mars aerosol studies with the MGS TES emission phase function observations: Optical depths, particle sizes, and ice cloud types versus latitude and solar longitude, *J. Geophys. Res.*, *108*(E9), 5098, doi:10.1029/2003JE002058.

Clancy, R. T., M. J. Wolff, B.A. Whitney, B. A. Cantor, M. D. Smith, and T. H. McConnochie (2010), Extension of atmospheric dust loading to high altitudes during the 2001 Mars dust storm: MGS TES limb observations, *Icarus*, *207*, 98-109.

Collins, M., S. R. Lewis, and P. L. Read (1997), Gravity wave drag in a global circulation model of the Martian atmosphere: Parametrisation and validation, *Adv. Space. Res.*, *44*, 1395–1409.

Conrath, B. J. (1975), Thermal structure of the martian atmosphere during the dissipation of the dust storm of 1971, *Icarus*, *24*, 36–46.

Creasey, J. E., J. M. Forbes, and D. P. Hinson (2006a), Global and seasonal distribution of gravity wave activity in Mars' lower atmosphere derived from MGS radio occultation data, *Geophys. Res. Lett.*, *33*, L01803, doi:10.1029/2005GL024037.

Creasey, J. E., J. M. Forbes, and G. M. Keating (2006b), Density variability at scales typical of gravity waves observed in Mars' thermosphere by the MGS accelerometer, *Geophys. Res. Lett.*, *33*, L22814, doi:10.1029/2006GL027583.

Delacourt, C., N. Gros, P. Allemand, and D. Baratoux (2003), Online Mars digital elevation model derived from profiles, *Eos Trans. AGU*, *84*(52), 583, doi:10.1029/2003EO520003.

Deming, D., M. J. Mumma, F. Espenak, and T. Kostiuk (1986), Polar warming in the middle atmosphere of Mars, *Icarus*, *66*, 366-379.

Eckermann, S. D., I. Hirota, and W. K. Hocking (1994), Gravity wave and equatorial wave morphology of the stratosphere derived from long-term rocket soundings, *Q. J. R. Meteorol. Soc.*, 121, 149– 186.

Eliassen, A. and E. Palm (1961), On the transfer of energy in stationary waves, *Geofys. Publ.*, *22*, 1-23.

Ern, M., P. Preusse, M. J. Alexander, and C. D. Warner (2004), Absolute values of gravity wave momentum flux derived from satellite data, *J. Geophys. Res.*, *109*, D20103, doi:10.1029/2004JD004752.

Fjeldbo, G., A. Kliore, and B. Seidel (1970), The Mariner 1969 Occultation Measurements of the Upper Atmosphere of Mars, *Radio Sci.*, *5*(2), 381–386, doi:10.1029/RS005i002p00381.

Fjeldbo, G., A. J. Kliore, and V. R. Eshleman (1971), The neutral atmosphere of Venus as studied with the Mariner V radio occultation experiments, *Astron. J.*, *76*, 123–140.

Fjeldbo, G., D. Sweetnam, J. Brenkle, E. Christensen, D. Farless, J. Mehta, B. Seidel, W. Michael jr., A. Wallio, and M. Grossi (1977), Viking Radio Occultation Measurements of the Martian Atmosphere and Topography: Primary Mission Coverage, *J. Geophys. Res.*, *82*(28), 4317–4324, doi:10.1029/JS082i028p04317.

Forbes, J. M., F. A. Marcos, and F. Kamalabadi (1995), Wave structures in lower thermosphere density from Satellite Electrostatic Triaxial Accelerometer (SETA) measurements, *J. Geophys. Res.*, *100*, 14,693–14,701.

Forbes, J. M. (1996), Troposphere-MLT coupling due to deep convective activity: modeling perspectives, Winds 96 Workshop, York University, Toronto.

Forbes, J. M., and M. E. Hagan (2000), Diurnal Kelvin wave in the atmosphere of Mars: Towards an understanding of 'stationary' density structures observed by the MGS accelerometer, *Geophys. Res. Lett.*, *27*(21), 3563–3566, doi:10.1029/2000GL011850.

Forbes, J. M., A. F. C. Bridger, S. W. Bougher, M. E. Hagan, J. L. Hollingsworth, G. M. Keating, and J. Murphy (2002), Nonmigrating tides in the thermosphere of Mars, *J. Geophys. Res.*, *107*(E11), 5113, doi:10.1029/2001JE001582.

Forbes, J. M., and S. Miyahara (2006), Solar Semidiurnal Tide in the Dusty Atmosphere of Mars, *J. Atmos. Sci.*, *63*, 1798-1817.

Forget, F., F. Hourdin, R. Fournier, C. Hourdin, O. Talagrand, M. Collins, S. R. Lewis, P. L. Read, and J.-P. Huot (1999), Improved general circulation models of the Martian atmosphere from the surface to above 80 km, *J. Geophys. Res.*, *104*, 24,155– 24,176.

Fritts, D. C. (1984), Gravity wave saturation in the middle atmosphere: A review of theory and observations, *Rev. Geophys.*, *22*, 275– 308.

Fritts, D. C., and R. A. Vincent (1987), Mesospheric momentum flux studies at Adelaide, Australia: Observations and a gravity wave/tidal interaction model, *J. Atmos. Sci.*, *44*, 605-619.

Fritts, D. C., R. C. Blanchard, and L. Coy (1989), Gravity wave structure between 60 and 90 km inferred from space shuttle reentry data, *J. Atmos. Sci.*, *46*, 423– 434.

Fritts, D. C., and Z. Luo (1992), Gravity wave excitation by geostrophic adjustment of the jet stream. Part I: Two-dimensional forcing, *J. Atmos. Sci.*, *49*, 681-697.

Fritts, D. C., and T. E. Van Zandt (1993), Spectral estimates of gravity wave energy and momentum fluxes, I: Energy dissipation, acceleration, and constraints, *J. Atmos. Sci.*, *47*, 51– 66.

Fritts, D. C., D. Wang, and R. C. Blanchard (1993), Gravity wave and tidal structures between 60 and 140 km inferred from space shuttle reentry data, *J. Atmos. Sci.*, *50*, 837–849.

Fritts, D. C., and M. J. Alexander (2003), Gravity wave dynamics and effects in the middle atmosphere, *Rev. Geophys.*, *41*(1), 1003, doi:10.1029/2001RG000106.

Fritts, D. C., L. Wang, and R. H. Tolson (2006), Mean and gravity wave structures and variability in the Mars upper atmosphere inferred from Mars Global Surveyor and Mars Odyssey aerobraking densities, *J. Geophys. Res.*, *111*, A12304, doi:10.1029/2006JA011897.

Garcia, R. R. and S. Solomon (1985), The effect of breaking gravity waves on the dynamics and chemical composition of the mesosphere and lower thermosphere, *J. Geophys. Res.*, *92*, 3850-3868.

Garcia, R. R. and B. A. Boville (1994), Downward control of the mean meridional circulation and temperature distribution of the polar winter stratosphere, *J. Atmos. Sci.*, *15*, 2238-2245.

González-Galindo, F., F. Forget, M. A. López-Valverde, M. Angelats i Coll, and E. Millour (2009a), A ground-to-exosphere Martian general circulation model: 1. Seasonal, diurnal, and solar cycle variation of thermospheric temperatures, *J. Geophys. Res.*, *114*, E04001, doi:10.1029/2008JE003246.

González -Galindo, F., F. Forget, M. A. López-Valverde, and M. Angelats i Coll (2009b), A ground-to-exosphere Martian general circulation model: 2. Atmosphere during solstice conditions - Thermospheric polar warming, *J. Geophys. Res.*, *114*, E08004, doi:10.1029/2008JE003277.

Hartogh, P., A. S. Medvedev, T. Kuroda, R. Saito, G. Villanueva, A. G. Feofilov, A. A. Kutepov, and U. Berger (2005), Description and climatology of a new general circulation model of the Martian atmosphere, *J. Geophys. Res.*, *110*, E11008, doi:10.1029/2005JE002498.

Heavens, N. G., M. I. Richardson, W. G. Lawson, C. Lee, D. J. McCleese, D. M. Kass, A. Kleinböhl, J. T. Schofield, W. A. Abdou, and J. H. Shirley (2010), Convective instability in the martian middle atmosphere, *Icarus*, *208*, 574–589.

Hines, C. O. (1961), Internal gravity waves at ionospheric heights, *Can. J. Phys.*, *38*, 1441-1481.

Hines, C. O. (1963), The upper atmosphere in motion, *Q. J. R. Meteorol. Soc.*, *89*, 1-42.

Hines, C. O. (1997), Doppler-spread parameterization of gravity wave momentum deposition in the middle atmosphere. Part 1: Basic formulation, *J. Atmos. Sol. Terr. Phys.*, *59*, 371–386.

Hinson, D. P., and G. L. Tyler (1983), Internal gravity waves in Titan's atmosphere observed by Voyager radio occultation, *Icarus*, *54*, 337-352.

Hinson, D. P., and J. M. Jenkins (1995), Magellan radio occultation measurements of atmospheric waves on Venus, *Icarus*, *114*, 310– 327.

Hinson, D. P., R. A. Simpson, J. D. Twicken, G. L. Tyler, and F. M. Flasar (1999), Initial results from radio occultation measurements with Mars Global Surveyor, *J. Geophys. Res.*, *104*, 26,997– 27,012.

Hinson, D. P., G. L. Tyler, J. L. Hollingsworth, and R. J. Wilson (2001), Radio occultation measurements of forced atmospheric waves on Mars, *J. Geophys. Res.*, *106*, 1463–1480, doi:10.1029/2000JE001291.

Hinson, D. P., and R. J. Wilson (2002), Transient eddies in the southern hemisphere of Mars, *Geophys. Res. Lett.*, *29*(7), 1154, doi:10.1029/2001GL014103.

Hinson, D. P., and R. J. Wilson (2004), Temperature inversions, thermal tides, and water ice clouds in the Martian tropics, *J. Geophys. Res.*, *109*, E01002, doi:10.1029/2003JE002129.

Hinson, D. P., M. D. Smith, and B. J. Conrath (2004), Comparison of atmospheric temperatures obtained through infrared sounding and radio occultation by Mars Global Surveyor, *J. Geophys. Res.*, *109*, E12002, doi:10.1029/2004JE002344.

Hinson, D. P. (2006), Radio occultation measurements of transient eddies in the northern hemisphere of Mars, J. Geophys. Res., 111, E05002, doi:10.1029/2005JE002612.

Hinson, D.P. (2008), Mars Global Surveyor Radio Occultation Profiles of the Neutral Atmosphere - Reorganized, MGS-M-RSS-5-TPS-V1.0, NASA Planetary Data System.

Hinson, D. P., M. Pätzold, R. J. Wilson, B. Häusler, S. Tellmann, and G. L. Tyler (2008), Radio occultation measurements and MGCM simulations of Kelvin waves on Mars, *Icarus*, *193*, 125-138.

Holton, J. R. (1982), The role of gravity wave induced drag and diffusion in the momentum budget of the mesosphere, *J. Atmos. Sci.*, *39*, 791-799.

Holton, J. R. (1983), The influence of gravity wave breaking on the general circulation of the middle atmosphere, *J. Atmos. Sci.*, *40*, 2497-2507.

Howard, L. N. (1961), Note on a paper of John W. Miles, *J. Fluid Mech.*, *10*, 509-512.

Joshi, M. M., B. N. Lawrence, and S. R. Lewis (1995), Gravity wave drag in three-dimensional atmospheric models of Mars, *J. Geophys. Res.*, *100*, 21,235– 21,245.

Joshi, M. M., J. L. Hollingsworth, R. M. Haberle, and A. F. C. Bridger (2000), An interpretation of Martian thermospheric waves based on analysis of a general circulation model, *Geophys. Res. Lett.*, *27*, 613– 616.

Kasprzak, W. T., A. E. Hedin, H. G. Mayr, and H. B. Niemann (1988), Wavelike perturbations observed in the neutral thermosphere of Venus, *J. Geophys. Res.*, *93*, 11,237– 11,245.

Keating, G. M., et al. (1998), The structure of the upper atmosphere of Mars: In situ accelerometer measurements from Mars Global Surveyor, *Science*, *279*, 1672–1676.

Keating, G. M., R. H. Tolson, J. L. Hanna, R. F. Beebe, J. R. Murphy, and L. F. Huber (2002), MGS-M-ACCEL-5-PROFILE-V1.2, http://atmos.nmsu.edu/PDS/data/mgsa_0002/, NASA Planetary Data System.

Kliore, A., D. L. Cain, G. S. Levy, V. R. Eshleman, G. Fjeldbo and F. D. Drake (1965), Occultation Experiment: Results of the First Direct Measurement of Mars's Atmosphere and Ionosphere, *Science*, *149*, 1243-1248.

Kliore, A. J., D. L. Cain, G. Fjeldbo, B. L. Seidel, and M. J. Sykes (1972), The atmosphere of Mars from Mariner 9 radio occultation measurements, *Icarus*, *17*, 484-516.

Kliore, A. J., G. Fjeldbo, B. L. Seidel, M. J. Sykes, and P. M. Woiceshyn (1973), S Band Radio Occultation Measurements of the Atmosphere and Topography of Mars with Mariner 9: Extended Mission Coverage of Polar and Intermediate Latitudes, *J. Geophys. Res.*, *78*(20), 4331–4351, doi:10.1029/JB078i020p04331.

Kuettner, J. P., P. A. Hildebrand, and T. L. Clark (1987), Convection waves: Observations of gravity wave systems over convectively active boundary layers, *Q. J. R. Meteorol. Soc.*, *113*, 445-467.

LaPrise, J. P. R. (1993), An Assessment of the WKBJ Approximation to the Vertical Structure of Linear Mountain Waves: Implications for Gravity-Wave Drag Parameterization, *J. Atmos. Sci.*, *50*, 1469-1487.

Lellouch, E., J. Rosenqvist, J. J. Goldstein, S. W. Bougher, and G. Paubert (1991). First absolute wind measurements in the middle atmosphere of Mars, *Astrophys. J.*, *383*, 401–406.

Leovy, C. B. (1964), Simple models of thermally driven mesospheric circulation, *J. Atmos. Sci.*, *21*, 327-341.

Leovy, C. B., and R. W. Zurek (1979), Thermal Tides and Martian Dust Storms: Direct Evidence for Coupling, *J. Geophys. Res.*, *84*(B6), 2956–2968, doi:10.1029/JB084iB06p02956.

Lewis, S. R., M. Collins, P. L. Read, F. Forget, F. Hourdin, R. Fournier, C. Hourdin, O. Talagrand, and J.-P. Huot (1999), A climate database for Mars, *J. Geophys. Res.*, *104*, 24,177–24,194.

Lindal, G. F., H. B. Hotz, D. N. Sweetnam, Z. Shippony, J. P. Brenkle, G. V. Hartsell, R. T. Spear, and W. H. Michael Jr. (1979), Viking Radio Occultation Measurements of the Atmosphere and Topography of Mars: Data Acquired During 1 Martian Year of Tracking, *J. Geophys. Res.*, *84*(B14), 8443–8456, doi:10.1029/JB084iB14p08443.

Lindzen, R. S. (1967), Planetary waves on beta-planes, *Mon. Weather. Rev.*, *95*, 441-451.

Lindzen, R. S. (1981), Turbulence and stress owing to gravity wave and tidal breakdown, *J. Geophys. Res.*, *86*, 9707–9714.

Lyons, D. T. (1994), Aerobraking Magellan: Plan Versus Reality, *Adv. Astronaut. Sci.*, *87*, 663–680.

Malin, M. C., G. E. Danielson, A. P. Ingersoll, H. Masursky, J. Veverka, M. A. Ravine, and T. A. Soulanille (1992), Mars Observer Camera, *J. Geophys. Res.*, *97*, 7699–7718.

Malin, M. C. and K. S. Edgett (2001), Mars Global Surveyor Mars Orbiter Camera: Interplanetary cruise through primary mission, *J. Geophys. Res.*, *106*, 23,429–23,570, doi:10.1029/2000JE001455.

Martin, T. Z., and M. I. Richardson (1993), New Dust Opacity Mapping From Viking Infrared Thermal Mapper Data, *J. Geophys. Res.*, *98*(E6), 10,941–10,949, doi:10.1029/93JE01044.

Matsuno, T. (1982), A quasi one-dimensional model of the middle atmosphere circulation interacting with internal GWs, *J. Meteorol. Soc. Japan*, *60*, 215-226.

Mayr, H. G., J. G. Mengel, K. L. Chan, and H. S. Porter (1998), Seasonal variations of the diurnal tide induced by gravity wave filtering, *Geophys. Res. Lett.*, *25*(7), 943–946, doi:10.1029/98GL00637.

McLandress, C. and W. E. Ward (1994), Tidal/gravity wave interactions and their influence on the large-scale dynamics of the middle atmosphere: Model results, *J. Geophys. Res.*, *99*(D4), 8139–8155, doi:10.1029/94JD00486.

McLandress, C. (1998), On the importance of gravity waves in the middle atmosphere and their parameterization in general circulation models, *J. Atmos. Sol. Terr. Phys.*, *60*, 1357–1383.

Medvedev, A. S., and G. P. Klaassen (2000), Parameterization of gravity wave momentum deposition based on nonlinear wave interactions: Basic formulation and sensitivity tests, *J. Atmos. Sol. Terr. Phys.*, *62*, 1015–1033.

Medvedev, A. S., and P. Hartogh (2007), Winter polar warmings and the meridional transport on Mars simulated with a general circulation model, *Icarus*, *186*, 97-110.

Medvedev, A. S., E. Yiğit, and P. Hartogh (2011), Estimates of gravity wave drag on Mars: Indication of a possible lower thermospheric wind reversal, *Icarus*, *211*, doi:10.1016/j.icarus2010.10.013, 909–912.

Meyer, C. K. (1999a), GW interactions with the diurnal propagating tide, *J. Geophys. Res.*, *104*, 4223-4239.

Meyer, C. K. (1999b), GW interactions with mesospheric planetary waves: A mechanism for penetration into the thermosphere-ionosphere system, *J. Geophys. Res.*, *104*, 28,181-28,196.

Mitchell, D. L., R. P. Lin, C. Mazelle, H. Rème, P. A. Cloutier, J. E. P. Connerney, M. H. Acuna, and N. F. Ness (2001), Probing Mars' crustal magnetic field and ionosphere with the MGS Electron Reflectometer, *J. Geophys. Res.*, *106*, 23,419–23,427, doi:10.1029/2000JE001435.

Miyahara, S. and D.-H. Wu (1989), Effects of solar tides on the zonal mean circulation in the lower thermosphere: Solstice condition. *J. Atmos. Sol.-Terr. Phys.*, *51*, 635–648.

Miyahara, S. and J. M. Forbes (1991), Interactions between gravity waves and the diurnal tide in the mesosphere and the lower thermosphere, *J. Met. Soc. Japan*, *69*, 523-531.

Miyoshi, Y., and H. Fujiwara (2009), Gravity waves in the equatorial thermosphere and their relation to the lower atmospheric variability, *Earth Planets Space*, *61*(4), 471–478.

Miyoshi, Y., J. M. Forbes, and Y. Moudden (2011), A new perspective on gravity waves in the Martian atmosphere: Sources and features, *J. Geophys. Res.*, *116*, E09009, doi:10.1029/2011JE003800.

Moreno, R., E. Lellouch, F. Forget, T. Encrenaz, S. Guilloteau, and E. Millour (2009), Wind measurements in Mars' middle atmosphere: IRAM Plateau de Bure interferometric CO observations, *Icarus*, *201*, 549-563.

Moudden, Y, and J. C. McConnell (2005), A new model for multiscale modeling of the Martian atmosphere, GM3, *J. Geophys. Res.*, *110*, E04001, doi:10.1029/2004JE002354.

Munro, G. H. (1948), Short-period changes in the F region of the ionosphere, *Nature*, *162*, 886-887.

Munro, G.H. (1950), Traveling disturbances in the ionosphere, *Proc. R. Soc. Ser. A*, *202*, 208-223.

Nappo, C. J. (2002), An Introduction to Atmospheric Gravity Waves, Academic Press, San Diego, CA.

Oppenheim, A. V., and R. W. Schafer (1989), Discrete-Time Signal Processing, Prentice-Hall, Upper Saddle River, N. J.

Palmer, T. N., G. J. Shutts, and R. Swinbank (1986), Alleviation of a systematic westerly bias in general circulation and numerical weather prediction models through an orographic gravity wave drag parametrisation, *Q. J. R. Meteorol. Soc.*, *112*, 1001–1039.

Pätzold, M., et al. (2004), MaRS: Mars Express Orbiter Radio Science, Mars Express: The Scientific Payload, ESA SP-1240. European Space Research and Technology Centre, Noordwijk, 141–163.

Peralta, J., R. Hueso, A. Sánchez-Lavega, G. Piccioni, O. Lanciano, and P. Drossart (2008), Characterization of mesoscale gravity waves in the upper and lower clouds of Venus from VEX-VIRTIS images, *J. Geophys. Res.*, *113*, E00B18, doi:10.1029/2008JE003185.

Plumb, R. A., and A. D. McEwan (1978), The Instability of a Forced Standing Wave in a Viscous Stratified Fluid: A Laboratory Analogue of the Quasi-Biennial Oscillation, *J. Atmos. Sci.*, *35*, 1827-1839.

137

Pollack, J. B., D. S. Colburn, F. M. Flasar, R. Kahn, C. E. Carlston, and D. Pidek (1979), Properties and Effects of Dust Particles Suspended in the Martian Atmosphere, *J. Geophys. Res.*, *84*(B6), 2929–2945, doi:10.1029/JB084iB06p02929.

Preusse, P., A. Dörnbrack, S. D. Eckermann, M. Riese, B. Schaeler, J. T. Bacmeister, D. Broutman, and K. U. Grossmann (2002), Space-based measurements of stratospheric mountain waves by CRISTA, 1. Sensitivity, analysis method, and a case study, *J. Geophys. Res.*, *107*(D23), 8178, doi:10.1029/2001JD000699.

Preusse, P., et al. (2006), Tropopause to mesopause gravity waves in August: Measurement and modeling, *J. Atmos. Solar Terr. Phys.*, *68*, 1730– 1751.

Preusse, P., S. D. Eckermann, and M. Ern (2008), Transparency of the atmosphere to short horizontal wavelength gravity waves, *J. Geophys. Res.*, *113*, D24104, doi:10.1029/2007JD009682.

Rafkin, S. C. R. (2012), The potential importance of non-local, deep transport on the energetics, momentum, chemistry, and aerosol distributions in the atmospheres of Earth, Mars, and Titan, *Planet. Space Sci.*, *60*, 147-154.

Read, P. L. and S. R. Lewis (2004), The Martian Climate Revisted, Praxis Publishing, Chichester, UK.

Sato, K. (1994), A statistical study of the structure, saturation and sources of inertio-gravity waves in the lower stratosphere observed with the MU radar, *J. Atmos. Terr. Phys.*, *56*, 755-774.

Scaife, A. A., N. Butchart, C. D. Warner, R. Swinbank (2002), Impact of a spectral gravity wave parameterization on the stratosphere in the Met Office Unified Model., *J. Atmos. Sci.*, *59*, 1473–1489.

Scorer, R. S. (1949), Theory of waves in the lee of mountains, *Q. J. R. Meteorol. Soc.*, *75*, 41-56.

Seiff, A., and D. B. Kirk (1977), Structure of the atmosphere of Mars in summer mid-latitudes, *J. Geophys. Res.*, *82*, 4364-4378.

Smith, D. E., et al. (2001a), Mars Orbiter Laser Altimeter: Experiment summary after the first year of global mapping of Mars, *J. Geophys. Res.*, *106*, 23,689–23,722, doi:10.1029/2000JE001364.

Smith, M. D., J. C. Pearl, B. J. Conrath, and P. R. Christensen (2000), Mars Global Surveyor Thermal Emission Spectrometer (TES) observations of dust opacity during aerobraking and science phasing, *J. Geophys. Res.*, *105*, 9539–9552.

Smith, M. D., J. C. Pearl, B. J. Conrath, and P. R. Christensen (2001b), Thermal Emission Spectrometer results: Mars atmospheric thermal structure and aerosol distribution, *J. Geophys. Res.*, *106*, 23,929–23,945, doi:10.1029/2000JE001321.

Smith, M. D., J. C. Pearl, P. R. Christensen, and B. J. Conrath (2002), Thermal Emission Spectrometer Observations of Martian Planet-Encircling Dust Storm 2001A, *Icarus*, *157*, 259-263.

Smith, M. D. (2003), TES limb-geometry observations of aerosols, paper presented at Sixth International Conference on Mars, Lunar and Planet. Inst., Pasadena, Calif.

Théodore, B., E. Lellouch, E. Chassefière, and A. Hauchecorne (1993), Solstitial temperature inversions in the Martian middle atmosphere: Observational clues and 2-D modeling, *Icarus*, *105*, 512–528.

Tolson, R. H., G. M. Keating, G. J. Cancro, J. S. Parker, S. N. Noll, and B. L. Wilkerson (1999), Application of Accelerometer Data to Mars Global Surveyor Aerobraking Operations, *J. Spacecr. Rockets*, *36*, 323– 329.

Tolson, R. H., G. M. Keating, S. N. Noll, D. T. Baird, and T. J. Shellenberg (2000), Utilization of Mars Global Surveyor accelerometer data for atmospheric modeling, *Adv. Astronaut. Sci*., 103, 1329– 1346.

Tolson, R. H., A. M. Dwyer, J. L. Hanna, G. M. Keating, B. E. George, P. E. Escalera, and M. R. Werner (2005), Application of accelerometer data to Mars Odyssey aerobraking and atmospheric modeling, *J. Spacecr. Rockets*, *42*, 435– 443.

Tolson, R. H., G. M. Keating, R. W. Zurek, S. W. Bougher, C. G. Justus, and D. C. Fritts (2007), Application of accelerometer data to atmospheric modeling during Mars aerobraking operations, *J. Spacecr. Rockets*, *44*, 1172-1179.

Tsuda, T., T. Inoue, D. C. Fritts, T. E. VanZandt, S. Kato, T. Sato, and S. Fukao (1989), MST radar observations of a saturated gravity wave spectrum, *J. Atmos. Sci*., *46*, 2440-2447.

Tsuda, T,. S. Kato, T. Yokoi, T. Inoue, M Yamamoto, T. E. VanZandt, S. Fukao, and T. Sato (1990), Gravity waves in the mesosphere observed with the middle and upper atmosphere radar, *Radio Sci*., *25*, 1005-1018.

Tsuda, T., M. Nishida, C. Rocken, and R. H. Ware (2000), A global morphology of gravity wave activity in the stratosphere revealed by the GPS occultation data (GPS/MET), *J. Geophys. Res*., *105*, 7257– 7273.

Tyler, G. L., G. Balmino, D. P. Hinson, W. L. Sjogren, D. E. Smith, R. Woo, S. W. Asmar, M. J. Connally, C. L. Hamilton, and R. A. Simpson (1992), Radio Science Investigations With Mars Observer, *J. Geophys. Res*., *97*(E5), 7759–7779, doi:10.1029/92JE00513.

Tyler, G. L., G. Balmino, D. P. Hinson, W. L. Sjogren, D. E. Smith, R. A. Simpson, S. W. Asmar, P. Priest, and J. D. Twicken (2001), Radio science observations with Mars Global Surveyor: Orbit insertion through one Mars year in mapping orbit, *J. Geophys. Res*., *106*, 23, 327-23, 348.

VanZandt, T. E. (1982), A universal spectrum of buoyancy waves in the atmosphere, *Geophys. Res. Lett*., *9*(5), 575–578, doi:10.1029/GL009i005p00575.

Van Zandt, T. E. (1985), A model for gravity wave spectra observed by Doppler sounding system, *Radio Sci*., *20*, 1323– 1330.

VanZandt, T. E., and D. C. Fritts (1989), A Theory of Enhanced Saturation of the Gravity Wave Spectrum Due to Increases in Atmospheric Stability, *Pure Appl. Geophys*., *130*, 399-420.

Vincent, R. A. and I. M. Reid (1983), HF Doppler measurements of mesospheric momentum fluxes, *J. Atmos. Sci*., *40*, 1321-1333.

Wang, L., D. C. Fritts, and R. H. Tolson (2006), Nonmigrating tides inferred from the Mars Odyssey and Mars Global Surveyor aerobraking data, *Geophys. Res. Lett*., *33*, L23201, doi:10.1029/2006GL027753.

Wang, L., and M. J. Alexander (2010), Global estimates of gravity wave parameters from GPS radio occultation temperature data, *J. Geophys. Res.*, *115*, D21122, doi:10.1029/2010JD013860.

Wilson, R. J. (2000), Evidence for diurnal period Kelvin waves in the Martian atmosphere from Mars Global Surveyor TES data, *Geophys. Res. Lett.*, *27*(23), 3889–3892, doi:10.1029/2000GL012028.

Withers, P., S. W. Bougher, and G. M. Keating (2003), The effects of topographically-controlled thermal tides in the Martian upper atmosphere as seen by the MGS accelerometer, *Icarus*, *164*, 14– 32.

Yiğit, E., A. D. Aylward, and A. S. Medvedev (2008), Parameterization of the effects of vertically propagating gravity waves for thermosphere general circulation models: Sensitivity study, *J. Geophys. Res.*, *113*, D19106, doi:10.1029/2008JD010135.

Young, R. E., R. L. Walterscheid, G. Schubert, A. Seiff, V. M. Linkin, and A. N. Lipatov (1987), Characteristics of gravity waves generated by surface topography on Venus - Comparison with the VEGA Balloon results, *J. Atmos. Sci.*, *44*, 2628-2639.

Young, L. A., R. V. Yelle, R. Young, A. Seiff, and D. B. Kirk (1997), Gravity waves in Jupiter's thermosphere, *Science*, *276*, 108-111.

Yuan, D.-N., W. L. Sjogren, A. S. Konopliv, and A. B. Kucinskas (2001), Gravity field of Mars: A 75th Degree and Order Model, *J. Geophys. Res.*, *106*, 23,377–23,401, doi:10.1029/2000JE001302.

Zhu, X., and J. R. Holton (1987), Mean fields induced by gravity-wave forcing in the middle atmosphere, *J. Atmos. Sci.*, *44*, 620-630.

Zuber, M. T., D. E. Smith, S. C. Solomon, D. O. Muhleman, J. W. Head, J. B. Garvin, J. B. Abshire, and J. L. Bufton (1992), The Mars Observer Laser Altimeter investigation, *J. Geophys. Res.*, *97*, 7781–7798.

Zuber, M. T., F. G. Lemoine, D. E. Smith, A. S. Konopliv, S. E. Smrekar, and S. W. Asmar (2007), Mars Reconnaissance Orbiter Radio Science Gravity Investigation, *J. Geophys. Res.*, *112*, E05S07, doi:10.1029/2006JE002833.

Zurek, R. W. (1982), Martian great dust storms: An update, *Icarus*, *50*, 288-310.

Zurek, R. W. (1986), Atmospheric tidal forcing of the zonal mean circulation: The Martian dusty atmosphere, *J. Atmos. Sci.*, *43*, 652-670.

Zurek, R. W., and R. M. Haberle (1988), Zonally symmetric response to atmospheric tidal forcing in the dusty Martian atmosphere, *J. Atmos. Sci.*, *45*, 2469–2485.

Appendix A

Derivation of Gravity Wave Potential Energy Density

This appendix first derives the gravity wave total energy equation from the equations of state, following *Nappo* [2004], and then uses the first law of thermodynamics to express gravity wave potential energy per unit mass in its common form as a function of temperature perturbation.

We start with the two-dimensional Euler equations for irrotational and inviscid flow. The Boussinesq approximation, which assumes $|\rho'/\rho_0| \ll 0$ where ρ' is the density perturbation from the mean state, is used here to eliminate acoustic waves from the solution. The equations below are the horizontal and vertical momentum equations, the mass continuity equation, and the equation for conservation of thermal energy respectively.

$$\frac{\partial u}{\partial t} + u\frac{\partial u}{\partial x} + w\frac{\partial u}{\partial z} = -\frac{1}{\rho}\frac{\partial p}{\partial x} \ , \tag{A.1}$$

$$\frac{\partial w}{\partial t} + u\frac{\partial w}{\partial x} + w\frac{\partial w}{\partial z} = -\frac{1}{\rho}\frac{\partial p}{\partial z} - g \ , \tag{A.2}$$

$$\frac{\partial u}{\partial x} + \frac{\partial w}{\partial z} = 0 \ , \tag{A.3}$$

$$\frac{\partial \rho}{\partial t} + u\frac{\partial \rho}{\partial x} + w\frac{\partial \rho}{\partial z} = 0 \ . \tag{A.4}$$

After linearizing about a mean background state ($q(x,z,t) = q_0(z) + q'(x,z,t)$), assuming hydrostatic balance ($\partial p/\partial z = -\rho g$), and eliminating terms ($\partial q_0/\partial t = 0$ and perturbation products), the above equations become

$$\frac{\partial u'}{\partial t} + u_0\frac{\partial u'}{\partial x} + w'\frac{du_0}{dz} = -\frac{1}{\rho_0}\frac{\partial p'}{\partial x} \ , \tag{A.5}$$

141

$$\frac{\partial w'}{\partial t} + u_0 \frac{\partial w'}{\partial x} = -\frac{1}{\rho_0}\frac{\partial p'}{\partial z} - \frac{\rho'}{\rho_0}g \ , \tag{A.6}$$

$$\frac{\partial u'}{\partial x} + \frac{\partial w'}{\partial z} = 0 \ , \tag{A.7}$$

$$\frac{\partial \rho'}{\partial t} + u_0 \frac{\partial \rho'}{\partial x} + w'\frac{d\rho_0}{dz} = 0 \ . \tag{A.8}$$

Multiplying (A.5) by u' and (A.6) by w', adding the two equations, then multiplying by ρ_0, and rearranging gives

$$\rho_0 \left[u'\frac{Du'}{Dt} + w'\frac{Dw'}{Dt} \right] + u'\frac{\partial p'}{\partial x} + w'\frac{\partial p'}{\partial z} + \rho' g w' = -\rho_0 u'w'\frac{du_0}{dz}, \tag{A.9}$$

where $D/Dt = \partial/\partial t + u\,\partial/\partial x + w\,\partial/\partial z$ is the total derivative. The first term in (A.9) can be written as

$$\rho_0 \left[u'\frac{Du'}{Dt} + w'\frac{Dw'}{Dt} \right] = \frac{D}{Dt}\left[\frac{1}{2}\rho_0(u'^2 + w'^2) \right], \tag{A.10}$$

and the second and third terms as

$$u'\frac{\partial p'}{\partial x} + w'\frac{\partial p'}{\partial z} = \frac{\partial}{\partial x}(u'p') + \frac{\partial}{\partial z}(w'p') - p'\left(\frac{\partial u'}{\partial x} + \frac{\partial w'}{\partial z} \right). \tag{A.11}$$

From the continuity equation (A.7), the last term on the right hand side is zero, and substituting (A.10) and (A.11) into (A.9) gives us the initial form of the gravity wave total energy equation:

$$\frac{D}{Dt}\left[\frac{1}{2}\rho_0(u'^2 + w'^2) \right] + \rho' g w' = -u'\frac{\partial p'}{\partial x} - w'\frac{\partial p'}{\partial z} - \rho_0 u'w'\frac{du_0}{dz}. \tag{A.12}$$

Next, we define the Brunt-Väisälä frequency N, , and the vertical velocity perturbation as

$$N^2 = -\frac{g}{\rho_0}\frac{d\rho_0}{dz}, \tag{A.13}$$

$$w' = \frac{D\zeta}{Dt}, \tag{A.14}$$

where ζ is the vertical displacement of an air parcel from equilibrium. Using (A.14) in (A.8) and integrating both sides gives an expression for the density perturbation, which when combined with (A.13) gives

$$\rho' = -\frac{d\rho_0}{dz}\zeta = \frac{N^2\rho_0}{g}\zeta \,. \tag{A.15}$$

Using (A.15) in (A.8) gives a new expression for the linearized form of the conservation of thermal energy

$$\frac{D}{Dt}\left(\frac{\rho_0 N^2 \zeta}{g}\right) + \frac{\rho' w'}{\zeta} = 0 \,. \tag{A.16}$$

Multiplying by ζg and rearranging gives

$$\rho' g w' = \frac{D}{Dt}\left(\frac{1}{2}\rho_0 N^2 \zeta^2\right), \tag{A.17}$$

which, when plugged back into (A.12), gives an updated form of the perturbation total energy equation.

$$\frac{D}{Dt}\left[\frac{1}{2}\rho_0(u'^2 + w'^2) + \frac{1}{2}\rho_0 N^2 \zeta^2\right] = -u'\frac{\partial p'}{\partial x} - w'\frac{\partial p'}{\partial z} - \rho_0 u' w' \frac{du_0}{dz} \,. \tag{A.18}$$

On the left hand side, the first term is the perturbation kinetic energy, and the second term is the perturbation potential energy. The first two terms on the right hand side are the divergence of flux of wave energy.

The next step is to express perturbation potential energy in terms of a temperature perturbation versus a vertical displacement, and for that we start with the first law of thermodynamics, which states that the change in temperature and rate of work done by a fluid is equal to the heat input:

$$c_p \frac{DT}{Dt} - \alpha \frac{Dp}{Dt} = J \,, \tag{A.19}$$

where c_p is specific heat at constant pressure, $\alpha = \rho^{-1}$, and J is diabatic heating. Using an isobaric system with $Dp/Dt = \omega$ and expanding DT/Dt, equation (A.19) can be rewritten as

$$c_p\left(\frac{\partial T}{\partial t} + u\frac{\partial T}{\partial x} + \omega\frac{\partial T}{\partial p}\right) - \alpha\omega = J \,. \tag{A.20}$$

Next, we define the static stability parameter S_p for the isobaric system:

$$S_p \equiv \frac{RT}{c_p p} - \frac{\partial T}{\partial p} = \frac{\alpha}{c_p} - \frac{\partial T}{\partial p}, \tag{A.21}$$

where R is the gas constant. Plugging (A.21) into (A.20) and dividing through by c_p, we obtain

143

$$\frac{\partial T}{\partial t} + u\frac{\partial T}{\partial x} - S_p \omega = \frac{J}{c_p} . \tag{A.22}$$

Using Poisson's equation for potential temperature θ in (A.23) and the relationship between atmospheric lapse rate $\bar{\Gamma}$ and the dry adiabatic lapse rate Γ_d in (A.24)

$$\theta = T\left(\frac{p_s}{p}\right)^{R/c_p} , \tag{A.23}$$

$$\Gamma_d - \bar{\Gamma} = \frac{T}{\theta}\frac{\partial \theta}{\partial z} = \frac{\partial \bar{T}}{\partial z} + \frac{g}{c_p}, \tag{A.24}$$

the static stability parameter can be written as

$$S_p = -\frac{T}{\theta}\frac{\partial \theta}{\partial p} = \frac{(\Gamma_d - \bar{\Gamma})}{\rho g}. \tag{A.25}$$

Letting $\omega = -\rho g w$, defining $\Gamma = \Gamma_d - \bar{\Gamma}$, and assuming the process is adiabatic, substituting (A.25) into (A.22) gives

$$\frac{\partial T}{\partial t} + u\frac{\partial T}{\partial x} + \Gamma w = 0 . \tag{A.26}$$

Next we linearize using $T = \bar{T}(z) + T'(z,t)$, $u = \bar{u}(z) + u'(x,z,t)$, and $w = w'(z,t)$. This assumes $\bar{w} = 0$. From (A.14), $w' = D\zeta/Dt$. After expanding and eliminating terms, we get

$$\frac{\partial T'}{\partial t} + \bar{u}\frac{\partial T'}{\partial x} + \Gamma\left(\frac{\partial \zeta}{\partial t} + \bar{u}\frac{\partial \zeta}{\partial x}\right) = 0 . \tag{A.27}$$

Integrating over t gives us

$$T' + \Gamma\zeta = 0 . \tag{A.28}$$

Using an alternate form of the Brunt-Väisälä frequency

$$N^2 = \frac{g}{\bar{T}}\left(\frac{\partial \bar{T}}{\partial z} + \frac{g}{c_p}\right) = \frac{g}{\bar{T}}\Gamma, \tag{A.29}$$

in (A.28) and solving for ζ, we obtain

$$\zeta = -\frac{g}{N^2}\left(\frac{T'}{\bar{T}}\right). \tag{A.30}$$

From the total energy equation (A.18), the perturbation potential energy E_p was defined as

$$E_p = \frac{1}{2}\rho_0 N^2 \zeta^2 \,. \tag{A.31}$$

Plugging (A.30) into (A.31) and expressing as energy per unit mass gives us the common form for gravity wave potential energy density used in *Creasey et al.* [2006a].

$$E_p = \frac{1}{2}\left(\frac{g}{N}\right)^2 \left(\frac{T'}{\overline{T}}\right)^2 \,. \tag{A.32}$$

Appendix B

Gravity Wave Potential Energy Distribution by Martian Month

This appendix provides global distributions of gravity wave potential energy density at 10-15 km altitude by Martian month. Each month is defined as 30° of solar longitude. Due to the eccentricity of Mars' orbit, Martian months range from 46 to 67 sols in duration. Mars is furthest from the Sun near northern summer solstice (L_s = 71°) and closest to the Sun near northern winter solstice (L_s = 251°). White areas represent locations with no data available.

146
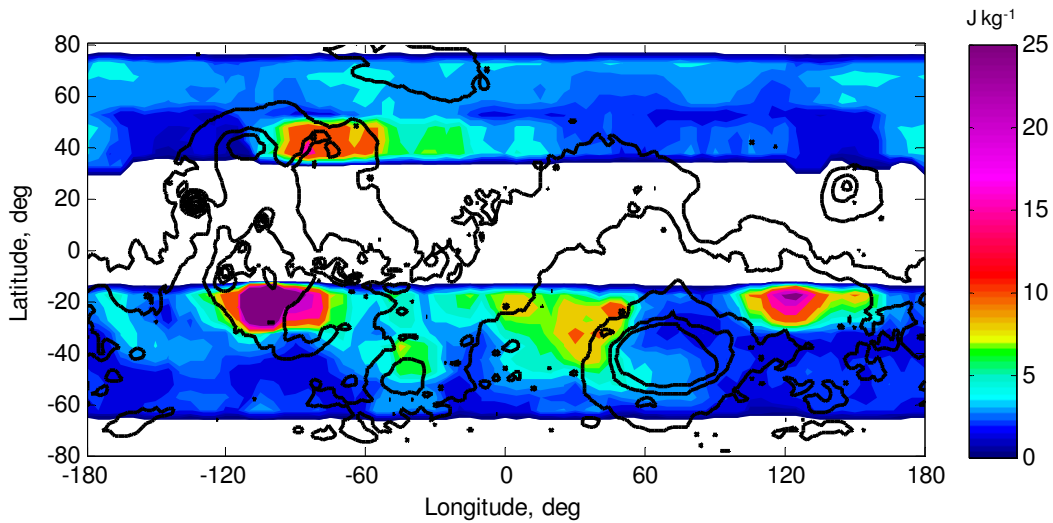
Figure B.1: Global distribution of E_p, gravity wave potential energy per unit mass, at 10-15 km height for L_s = 0-30 deg. Number of temperature profiles = 1608.
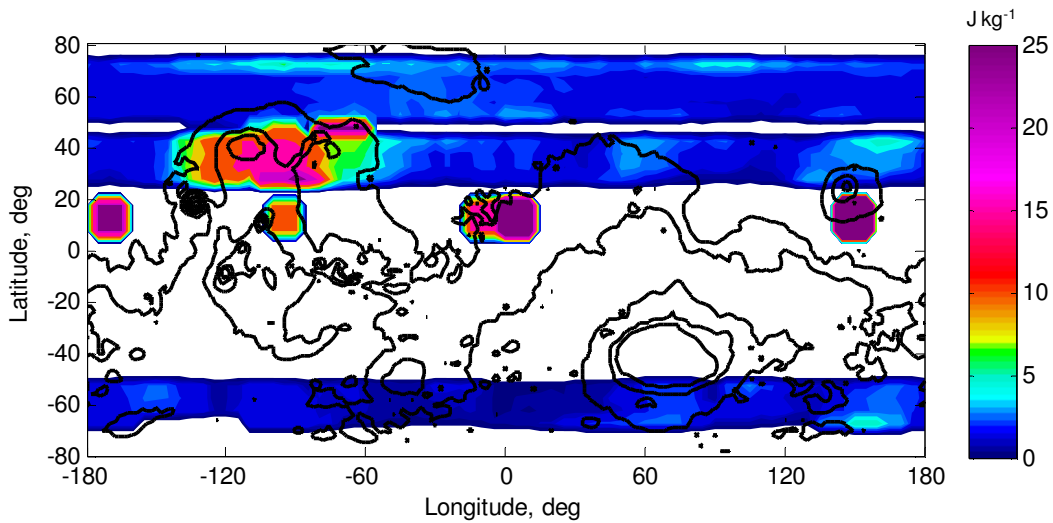
Figure B.2: Global distribution of E_p, gravity wave potential energy per unit mass, at 10-15 km height for L_s = 30-60 deg. Number of temperature profiles = 1534.
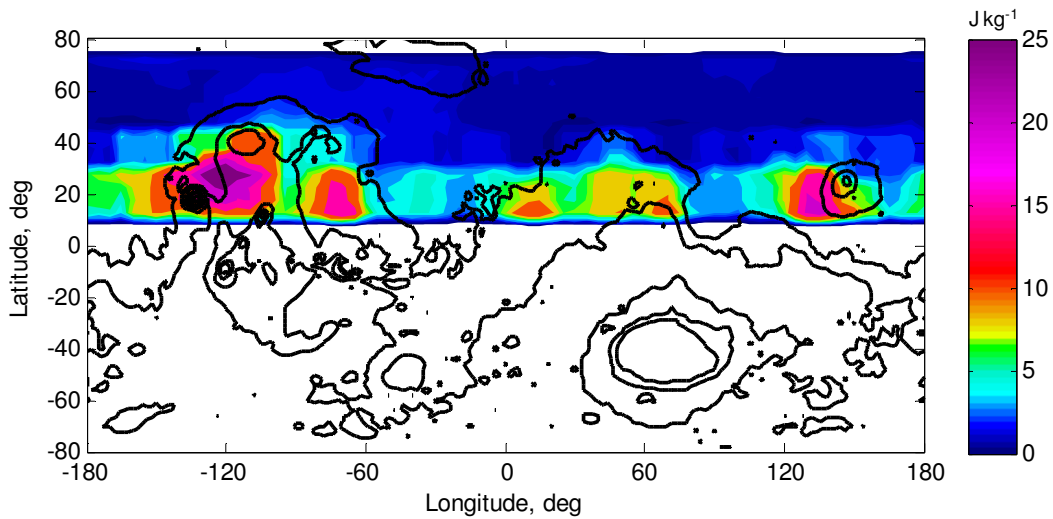
Figure B.3: Global distribution of E_p, gravity wave potential energy per unit mass, at 10-15 km height for L_s = 60-90 deg. Number of temperature profiles = 1773.
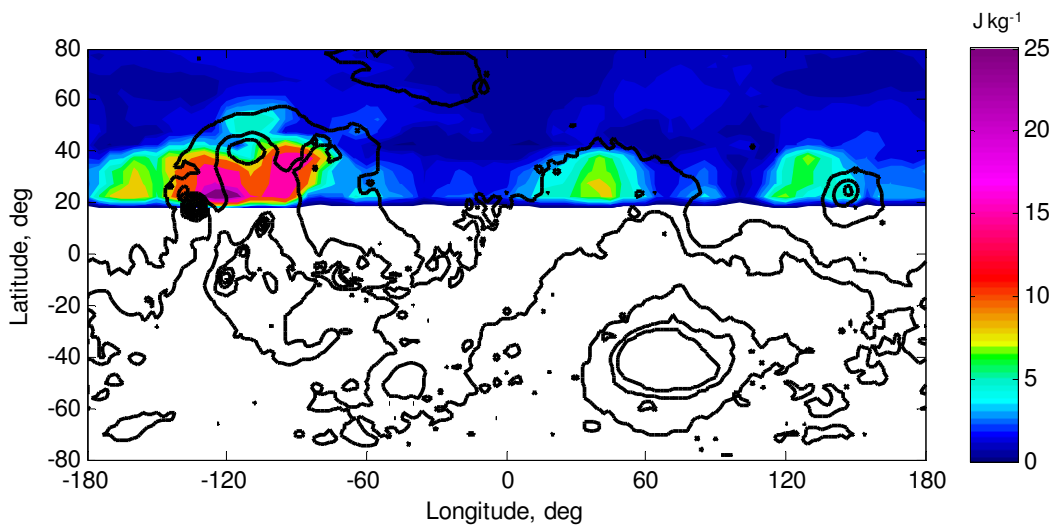
Figure B.4: Global distribution of E_p, gravity wave potential energy per unit mass, at 10-15 km height for L_s = 90-120 deg. Number of temperature profiles = 1973.
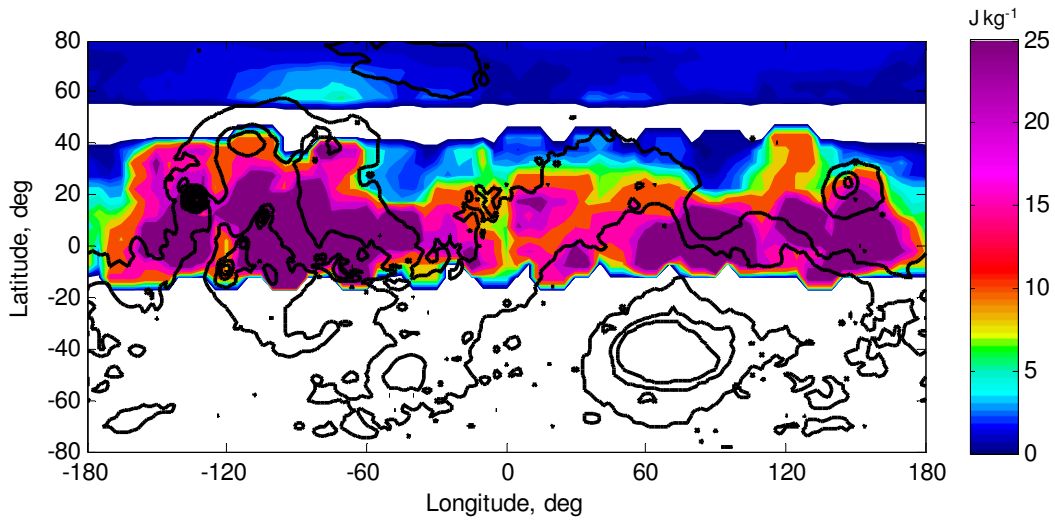
Figure B.5: Global distribution of E_p, gravity wave potential energy per unit mass, at 10-15 km height for L_s = 120-150 deg. Number of temperature profiles = 1101.
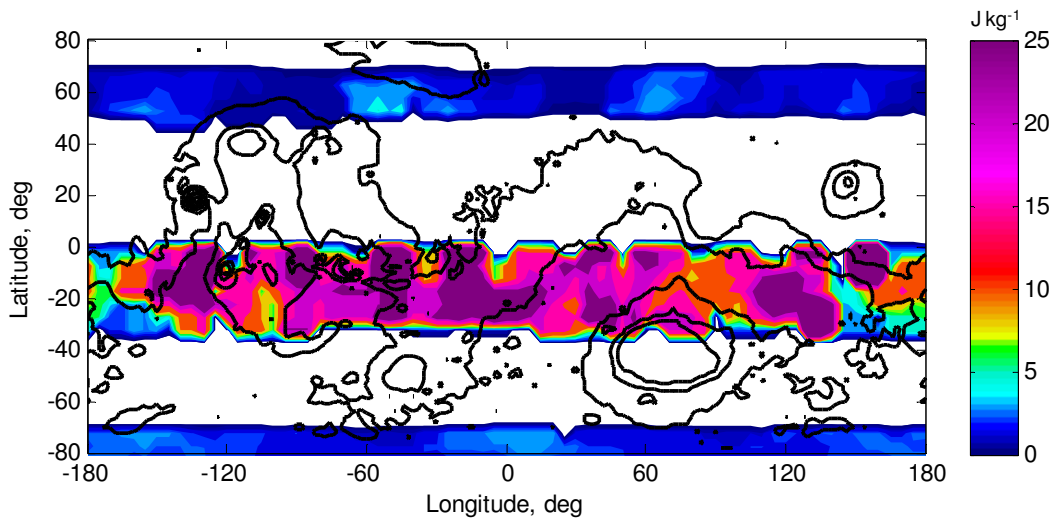
Figure B.6: Global distribution of E_p, gravity wave potential energy per unit mass, at 10-15 km height for L_s = 150-180 deg. Number of temperature profiles = 201.
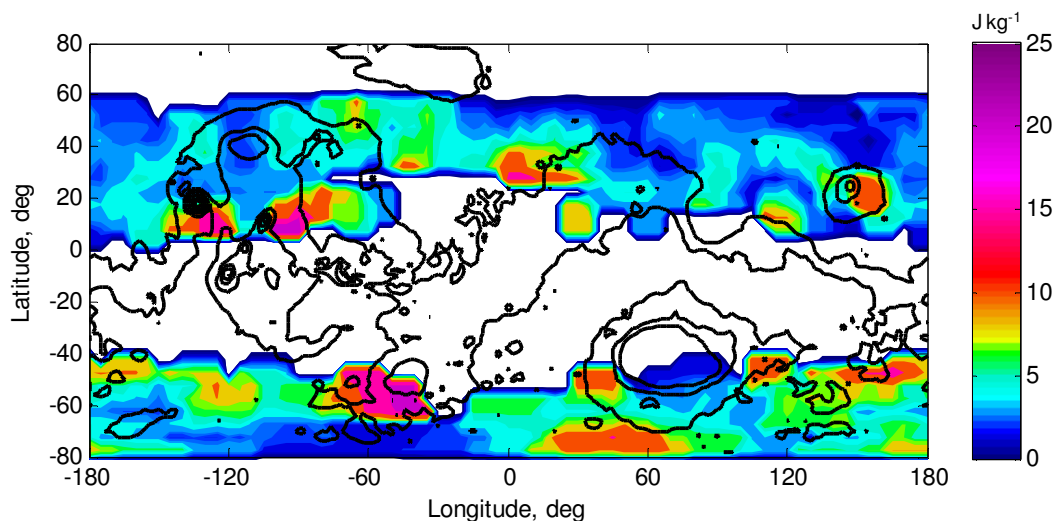
Figure B.7: Global distribution of E_p, gravity wave potential energy per unit mass, at 10-15 km height for L_s = 180-210 deg. Number of temperature profiles = 301.
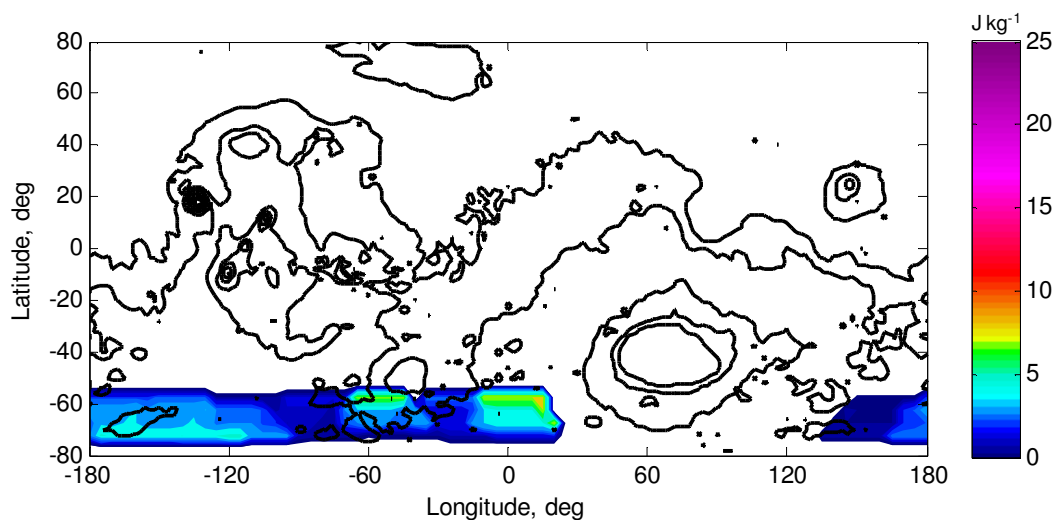
Figure B.8: Global distribution of E_p, gravity wave potential energy per unit mass, at 10-15 km height for L_s = 210-240 deg. Number of temperature profiles = 16.
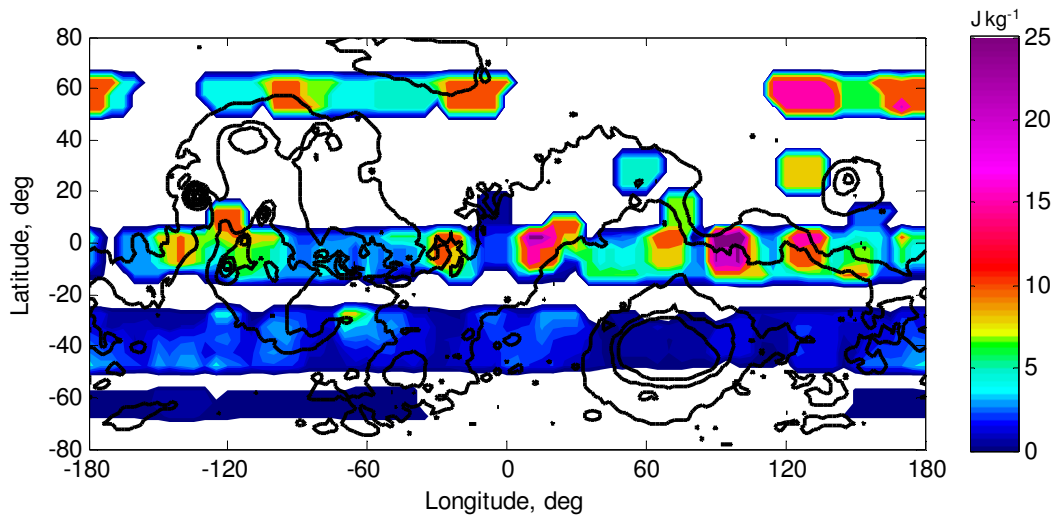
Figure B.9: Global distribution of E_p, gravity wave potential energy per unit mass, at 10-15 km height for L_s = 240-270 deg. Number of temperature profiles = 195.
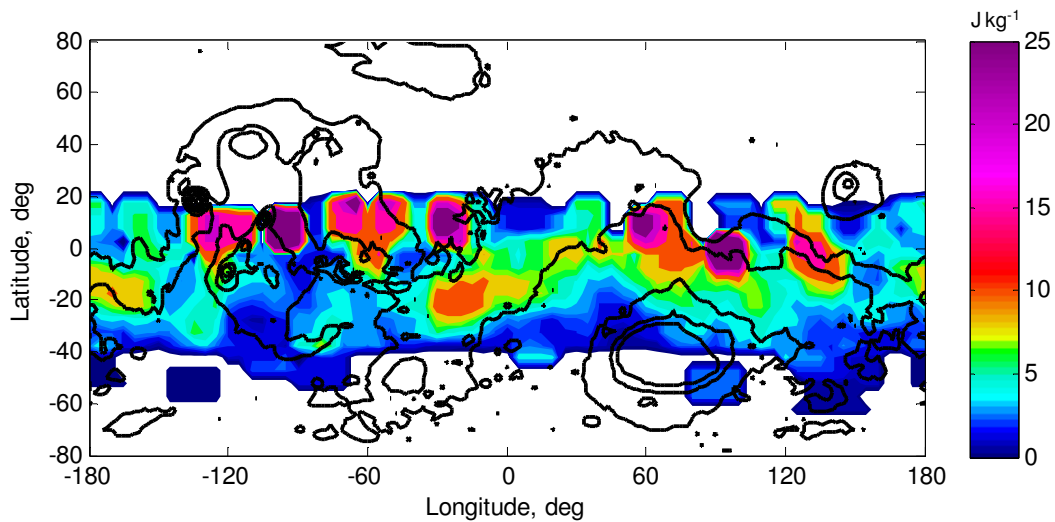
Figure B.10: Global distribution of E_p, gravity wave potential energy per unit mass, at 10-15 km height for L_s = 270-300 deg. Number of temperature profiles = 536.
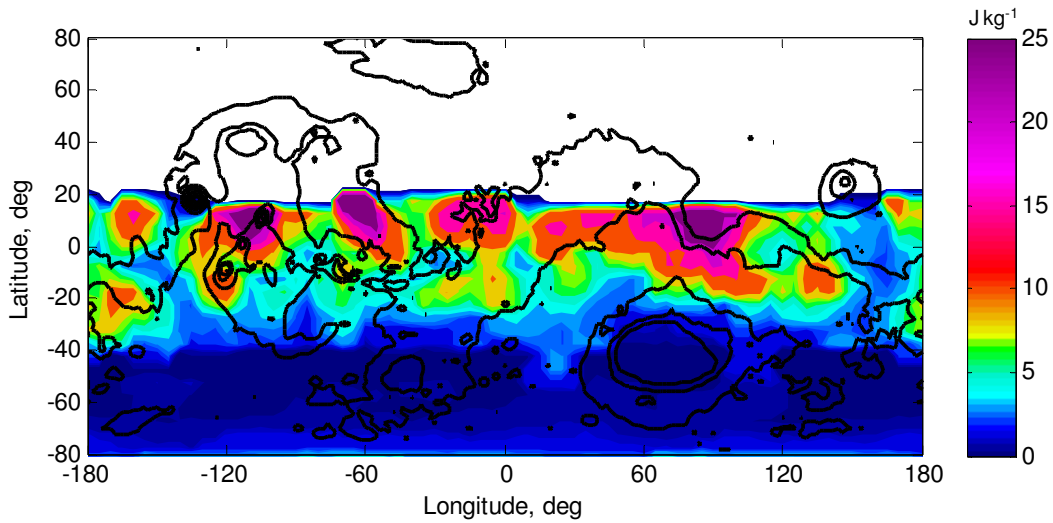
Figure B.11: Global distribution of E_p, gravity wave potential energy per unit mass, at 10-15 km height for L_s = 300-330 deg. Number of temperature profiles = 1043.
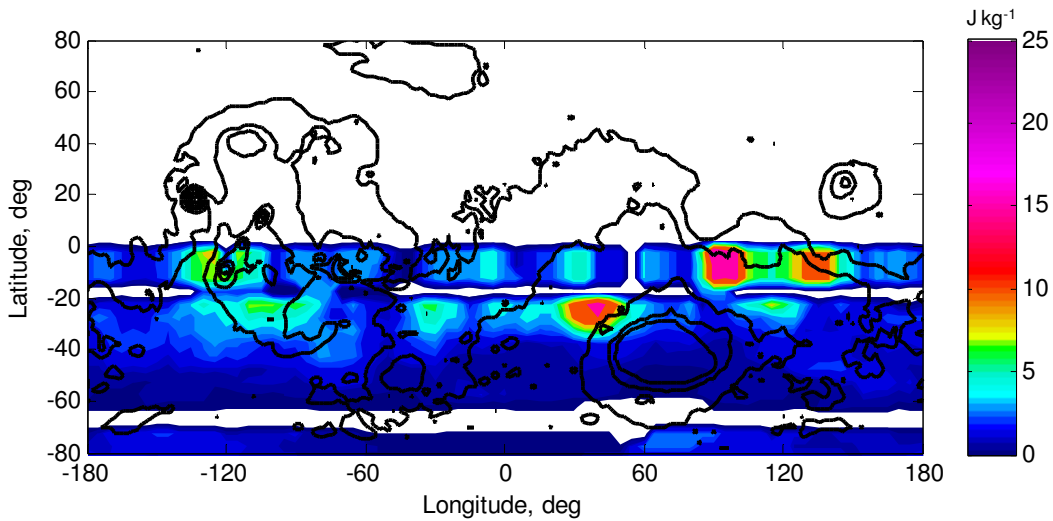
Figure B.12: Global distribution of E_p, gravity wave potential energy per unit mass, at 10-15 km height for L_s = 330-0 deg. Number of temperature profiles = 678.
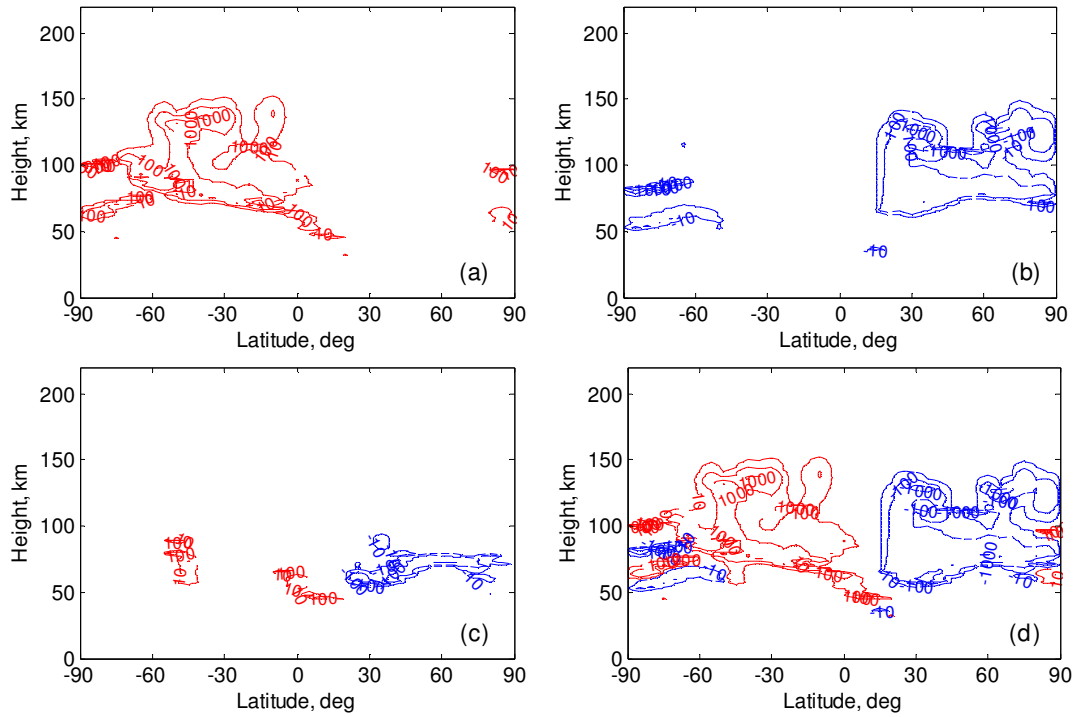
Appendix C

Gravity Wave Zonal Forcing by Wave Phase Speed
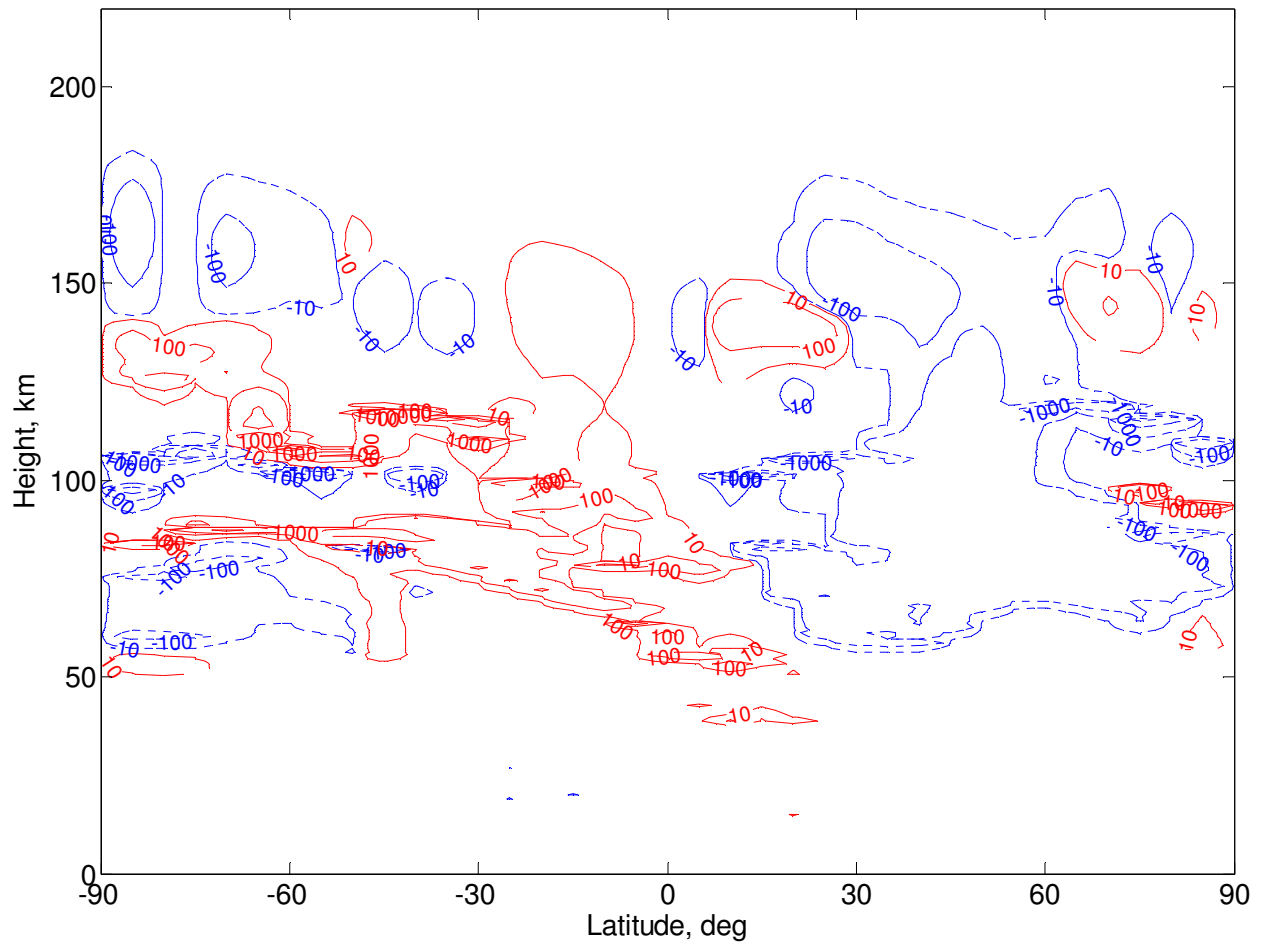
Figure C.1: Gravity wave acceleration (m s^{-1} sol^{-1}) of the zonal mean flow for $L_s = 270°$ and spectral index $p = 5/3$ with phase speed distribution -60, -40, -20, 0, 20, 40, and 60 m s^{-1}. Red (blue) contour lines depict eastward (westward) acceleration.
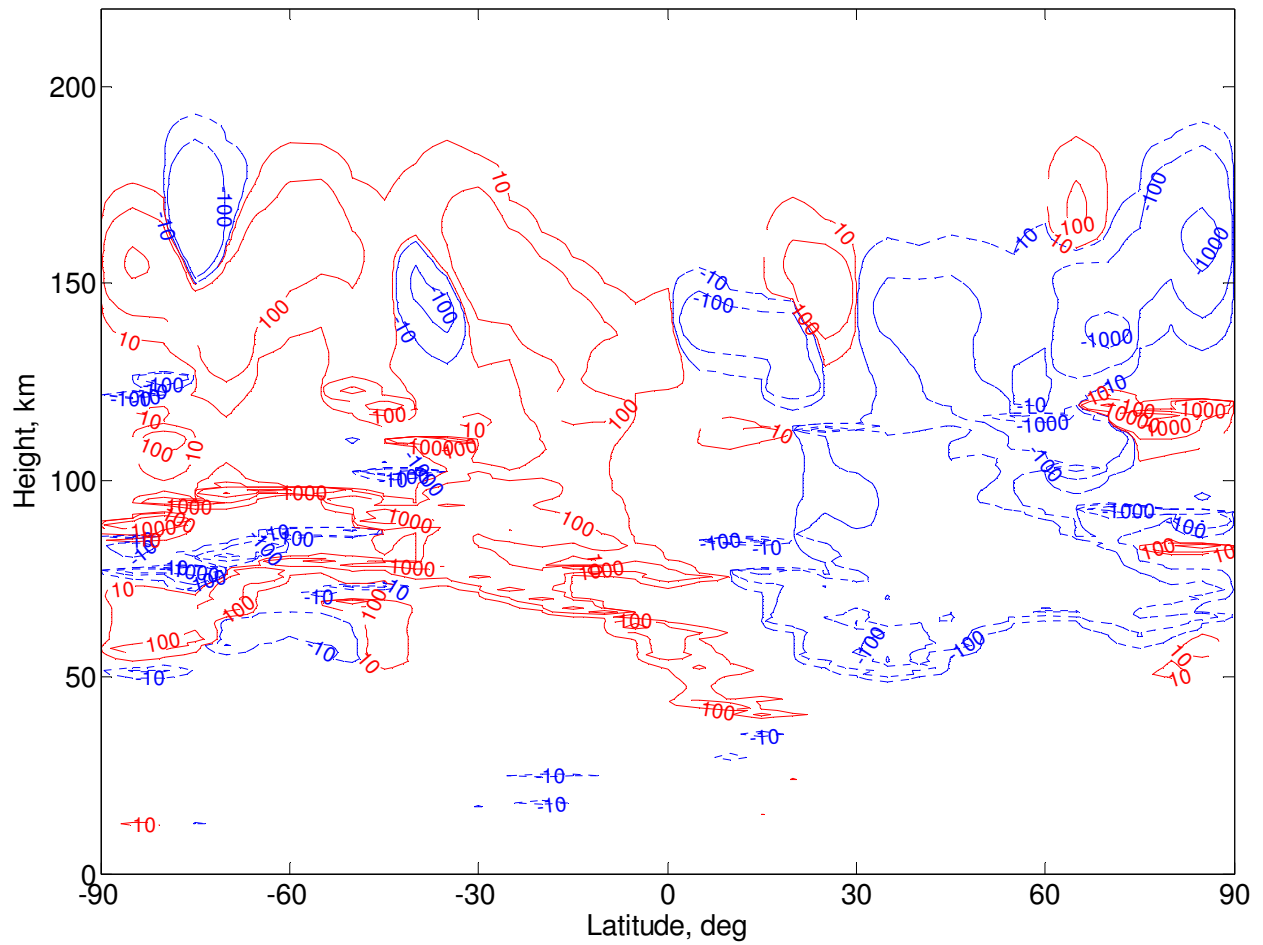
Figure C.2: Gravity wave acceleration (m s^{-1} sol^{-1}) of the zonal mean flow for $L_s = 270°$ and spectral index $p = 1.6$ with phase speed distribution -60, -40, -20, 0, 20, 40, and 60 m s^{-1}. Red (blue) contour lines depict eastward (westward) acceleration.
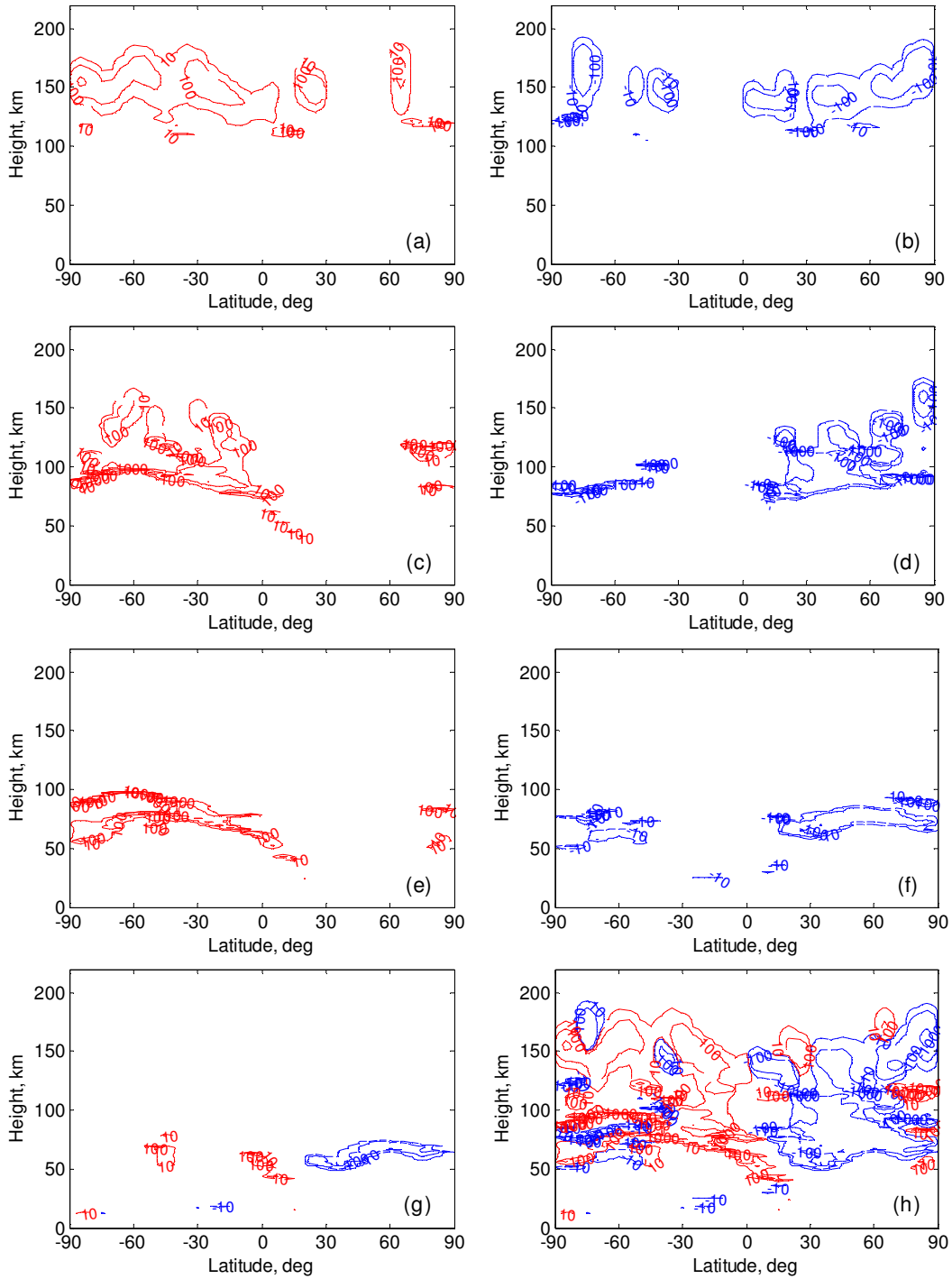
Figure C.3: Gravity wave acceleration (m s^{-1} sol^{-1}) of the zonal mean flow for $L_s = 270°$ and spectral index $p = 1.6$ with phase speed distribution (a) 60 m s^{-1}, (b) -60 m s^{-1}, (c) 40 m s^{-1}, (d) -40 m s^{-1}, (e) 20 m s^{-1}, (f) -20 m s^{-1}, (g) 0 m s^{-1}, and (h) all phase speeds. Red (blue) contour lines depict eastward (westward) acceleration.
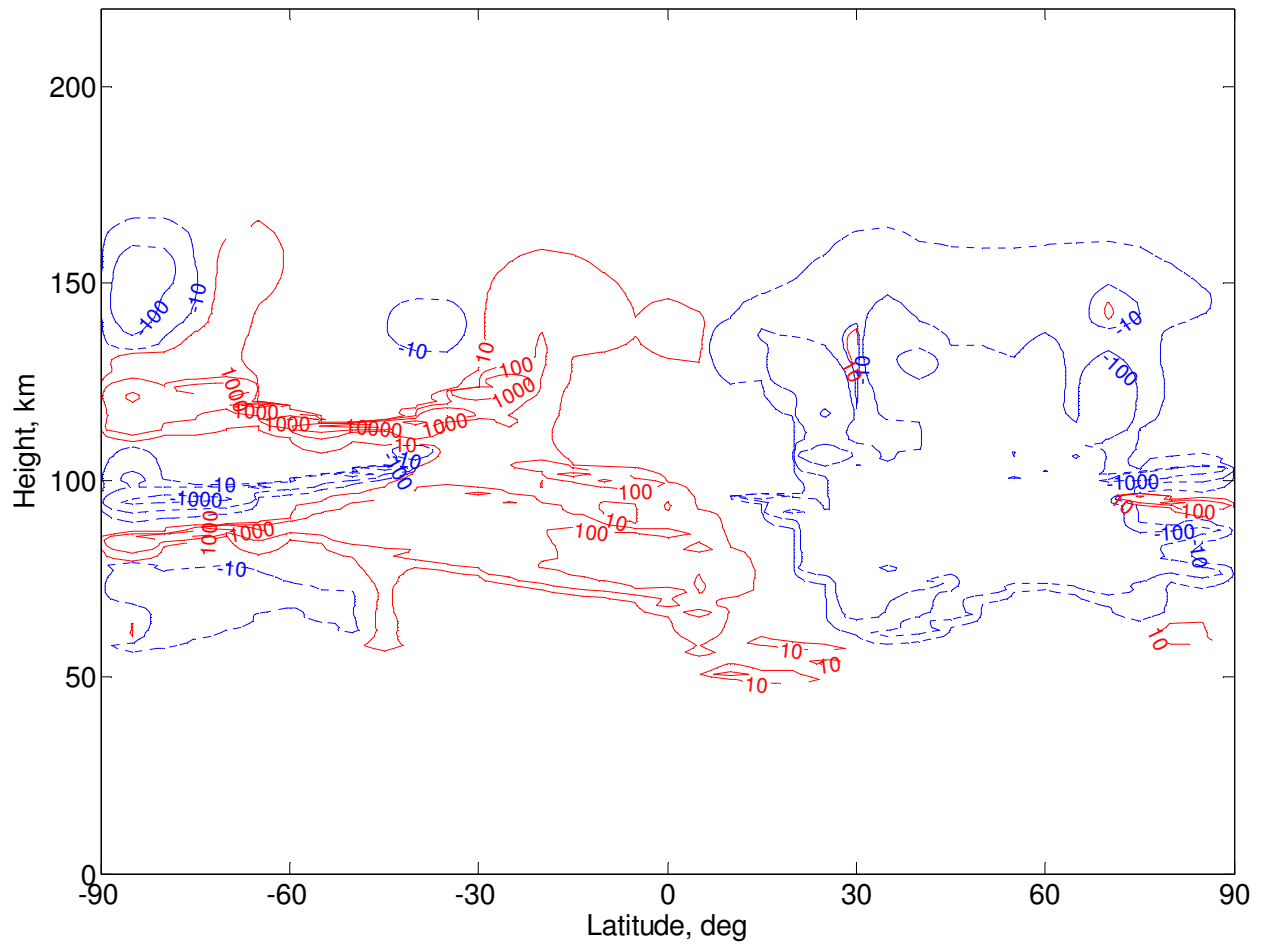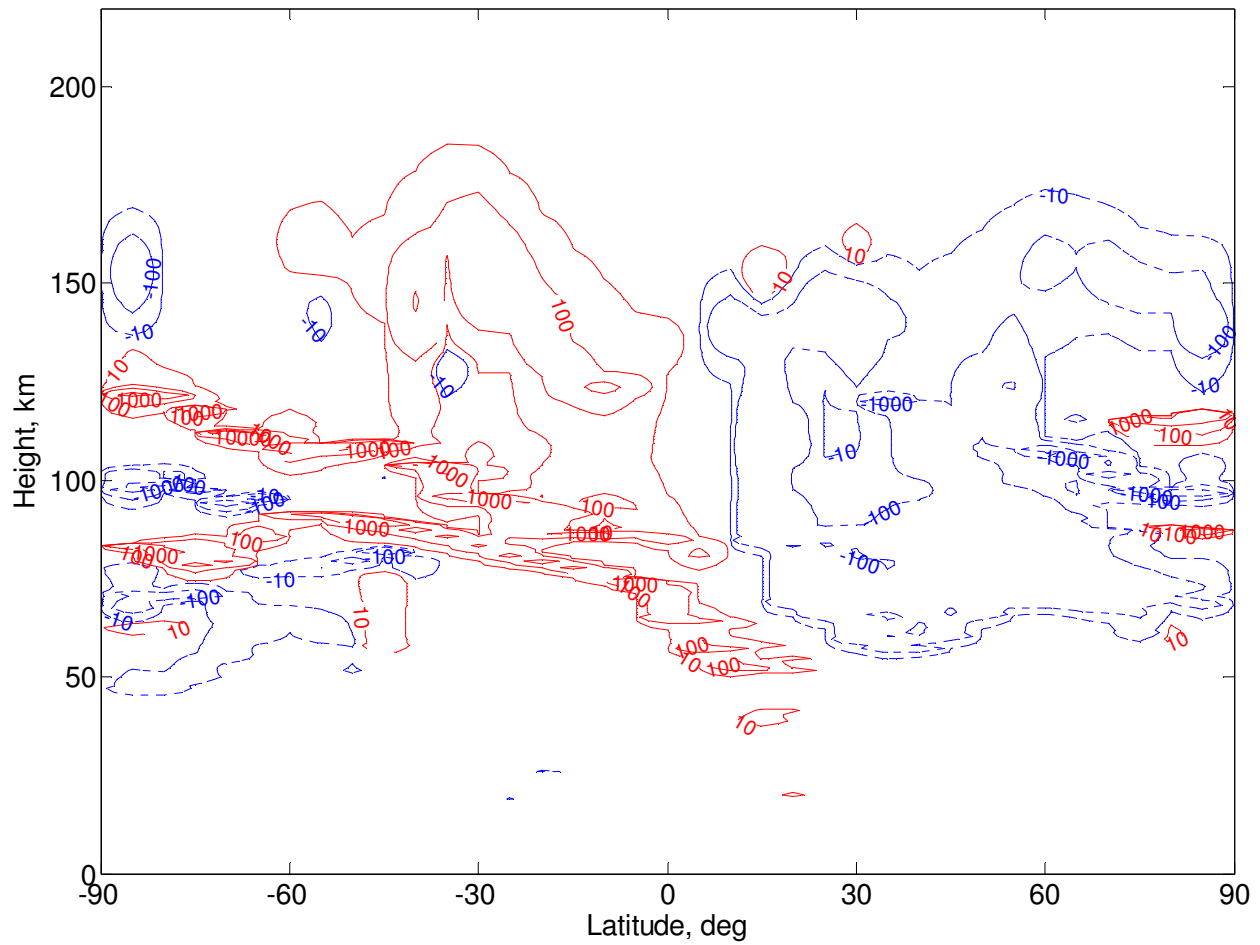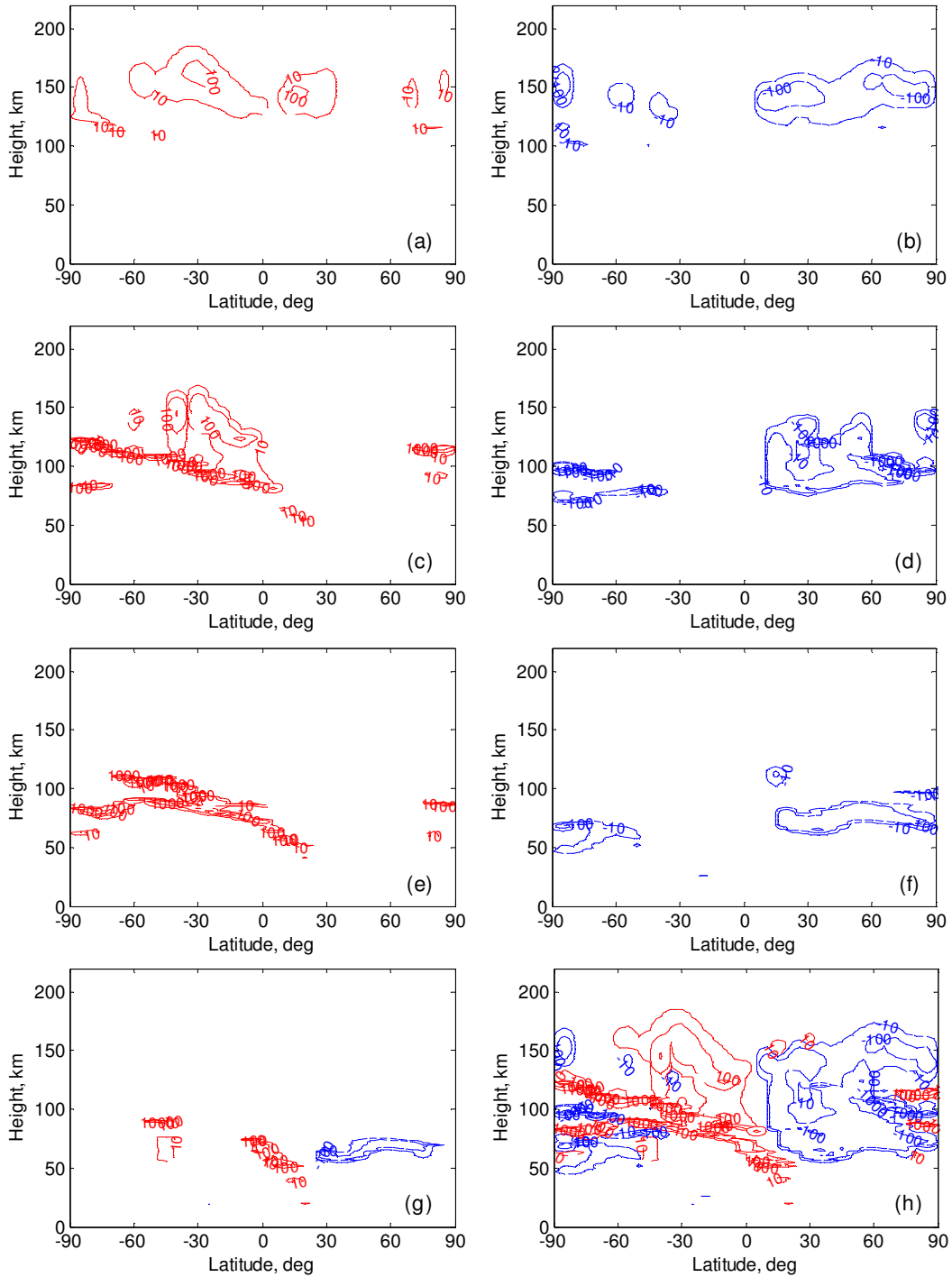
Figure C.4: Gravity wave acceleration (m s^{-1} sol^{-1}) of the zonal mean flow for $L_s = 270°$ and spectral index $p = 1.75$ with phase speed distribution -60, -40, -20, 0, 20, 40, and 60 m s^{-1}. Red (blue) contour lines depict eastward (westward) acceleration.
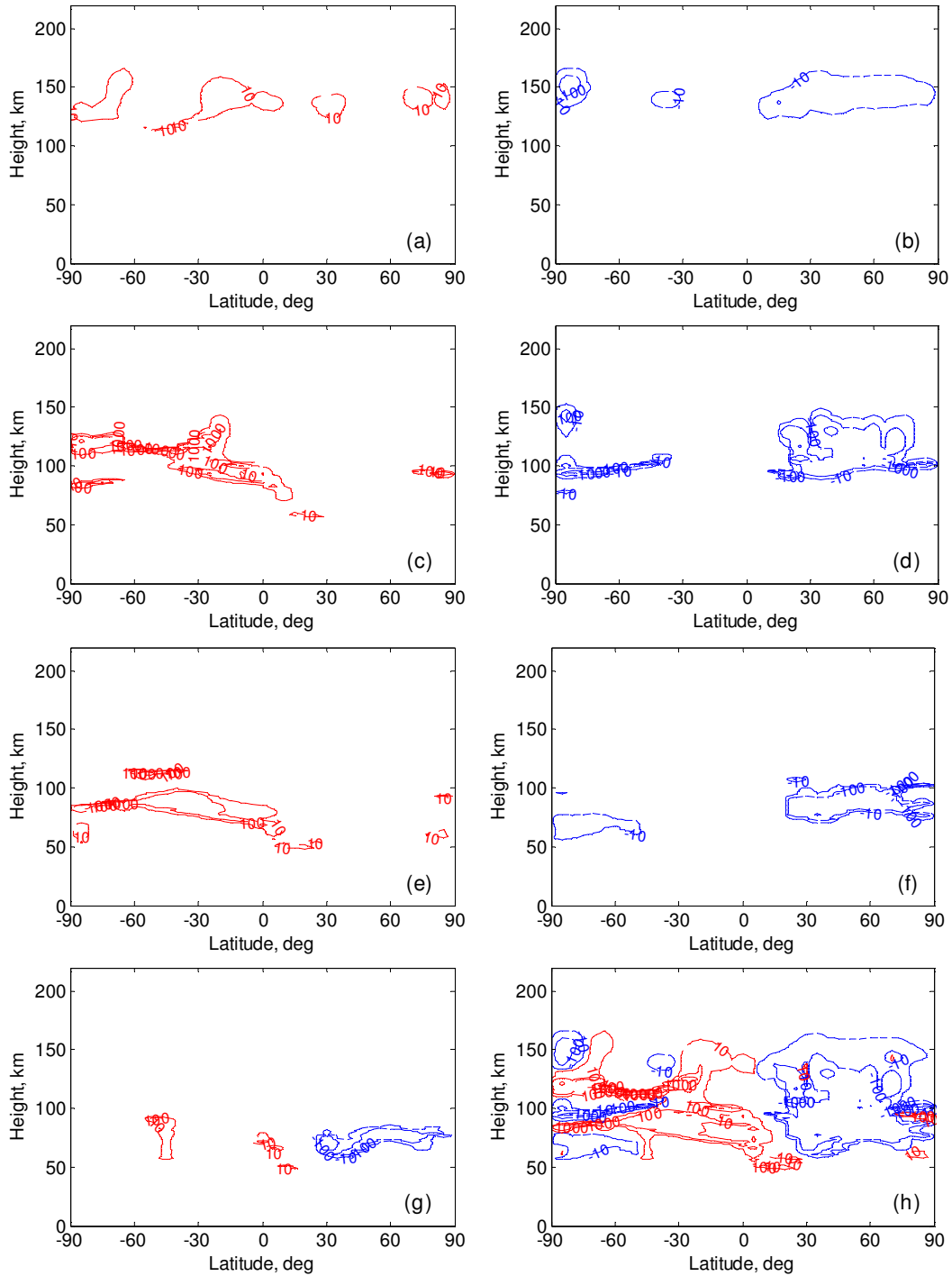
Figure C.5: Gravity wave acceleration (m s^{-1} sol^{-1}) of the zonal mean flow for $L_s = 270°$ and spectral index $p = 1.75$ with phase speed distribution (a) 60 m s^{-1}, (b) -60 m s^{-1}, (c) 40 m s^{-1}, (d) -40 m s^{-1}, (e) 20 m s^{-1}, (f) -20 m s^{-1}, (g) 0 m s^{-1}, and (h) all phase speeds. Red (blue) contour lines depict eastward (westward) acceleration.
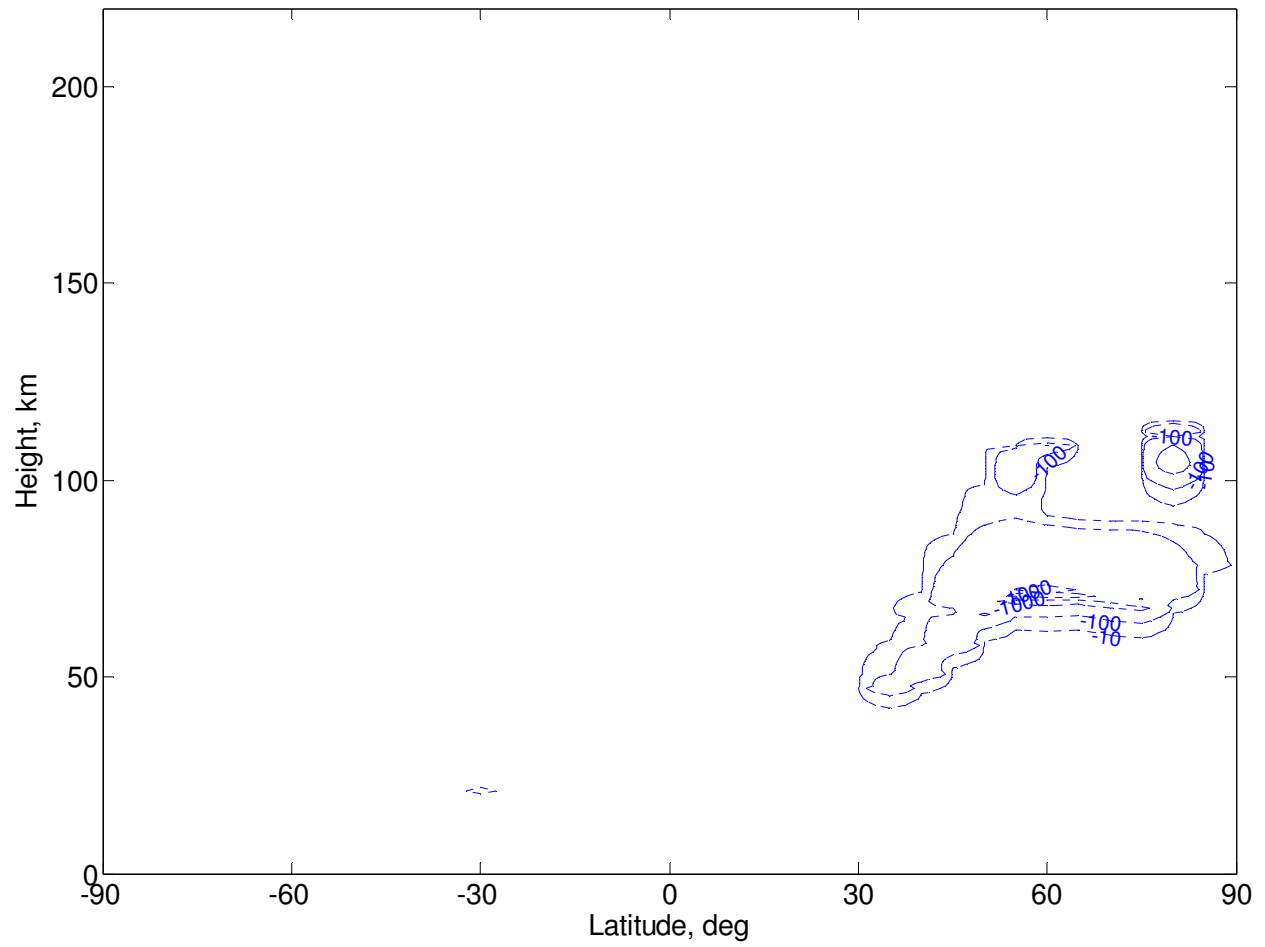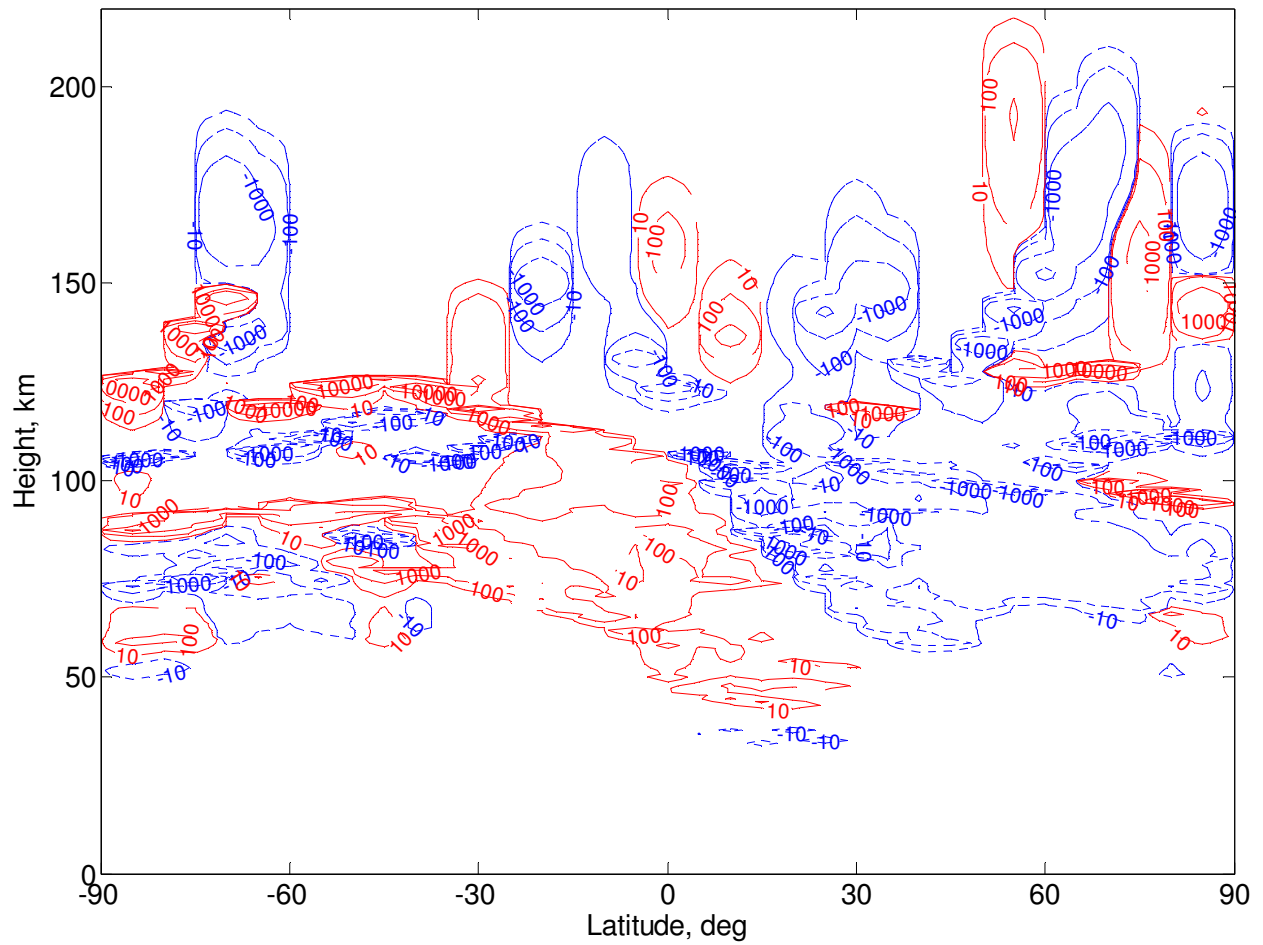
Figure C.6: Gravity wave acceleration (m s^{-1} sol^{-1}) of the zonal mean flow for $L_s = 270°$ and spectral index $p = 5/3$ with phase speed $c = 0$ m s^{-1}. Red (blue) contour lines depict eastward (westward) acceleration.
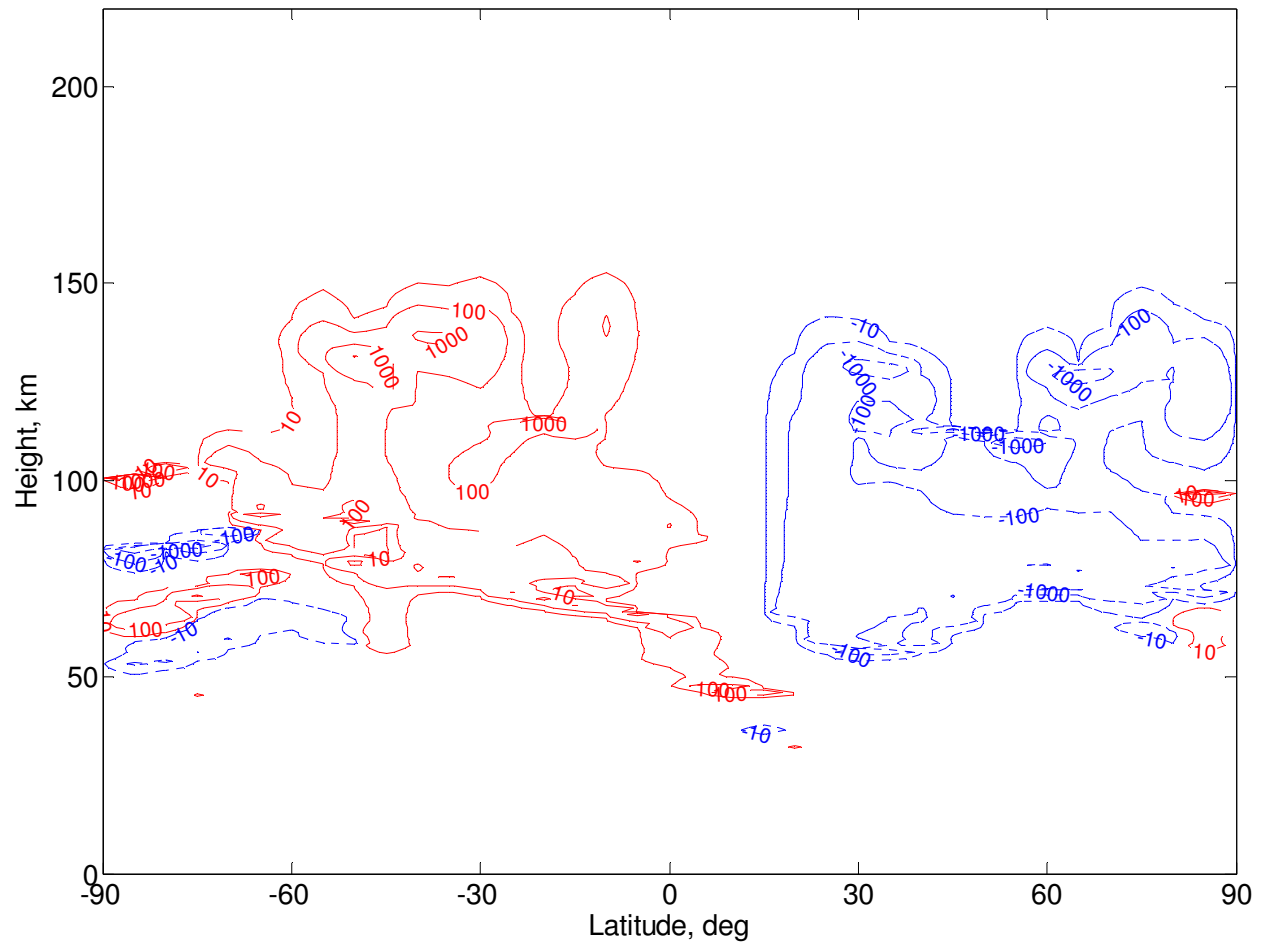
Figure C.7: Gravity wave acceleration (m s^{-1} sol^{-1}) of the zonal mean flow for $L_s = 270°$ and spectral index $p = 5/3$ with phase speed distribution -20, 0, and 20 m s^{-1}. Red (blue) contour lines depict eastward (westward) acceleration.
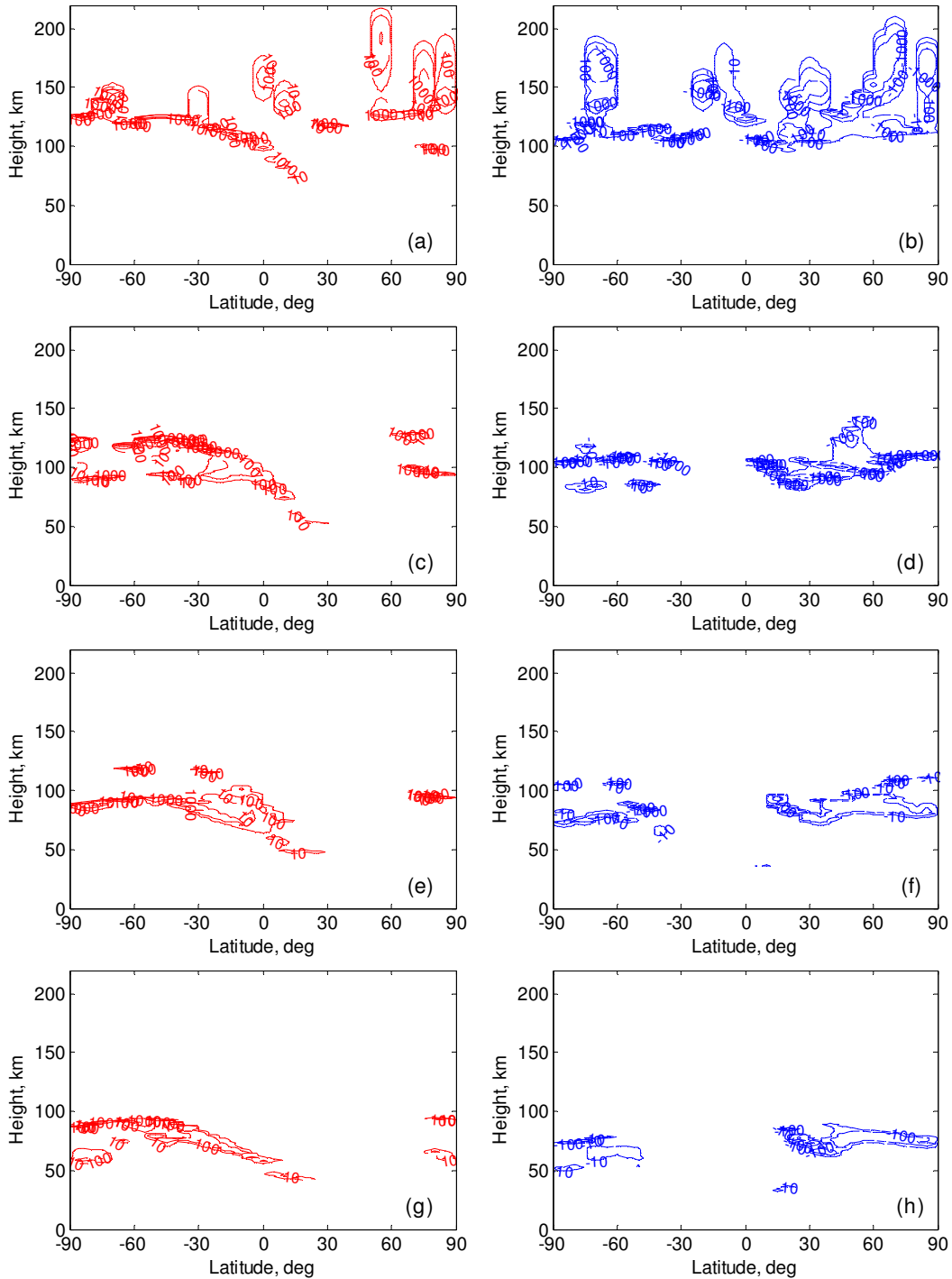
Figure C.8: Gravity wave acceleration (m s^{-1} sol^{-1}) of the zonal mean flow for $L_s = 270°$ and spectral index $p = 5/3$ with phase speed distribution (a) 20 m s^{-1}, (b) -20 m s^{-1}, (c) 0 m s^{-1}, and (d) all phase speeds. Red (blue) contour lines depict eastward (westward) acceleration.

Figure C.9: Gravity wave acceleration (m s^{-1} sol^{-1}) of the zonal mean flow for $L_s = 270°$ and spectral index $p = 5/3$ with phase speed distribution -60, -40, -20, 0, 20, 40, and 60 m s^{-1}. Westward momentum flux at the source level was 3 times greater than eastward momentum flux. Red (blue) contour lines depict eastward (westward) acceleration.
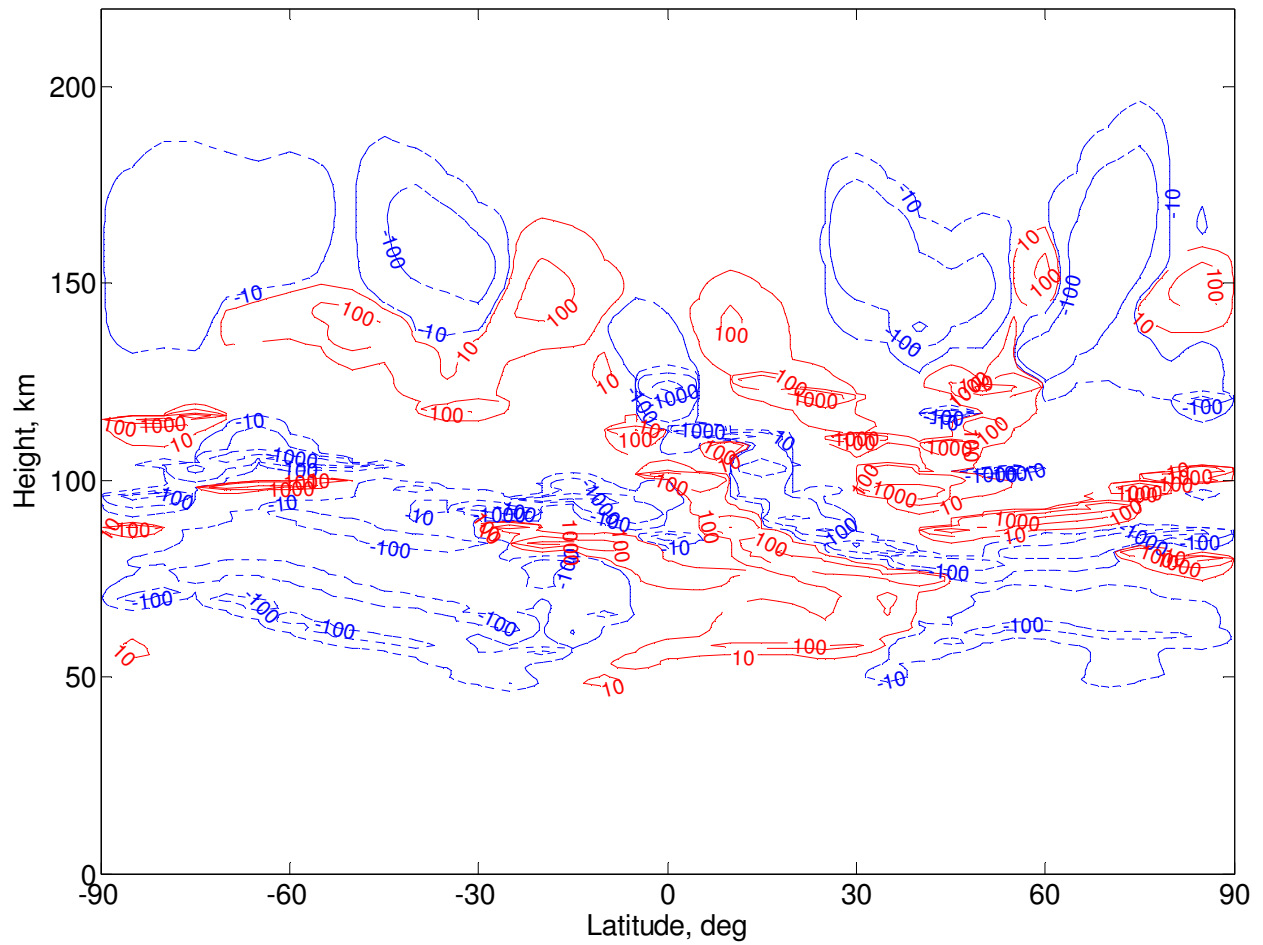
Figure C.10: Gravity wave acceleration (m s^{-1} sol^{-1}) of the zonal mean flow for L_s = 270° and spectral index p = 5/3 with phase speed distribution (a) 60 m s^{-1}, (b) -60 m s^{-1}, (c) 40 m s^{-1}, (d) -40 m s^{-1}, (e) 20 m s^{-1}, (f) -20 m s^{-1}, (g) 0 m s^{-1}, and (h) all phase speeds. Westward momentum flux at the source level was 3 times greater than eastward momentum flux. Red (blue) contour lines depict eastward (westward) acceleration.

Figure C.11: Gravity wave acceleration (m s^{-1} sol^{-1}) of the zonal mean flow for $L_s = 270°$ and spectral index $p = 5/3$ with phase speed distribution -80, -60, -40, -20, 0, 20, 40, 60, and 80 m s^{-1}. Red (blue) contour lines depict eastward (westward) acceleration.
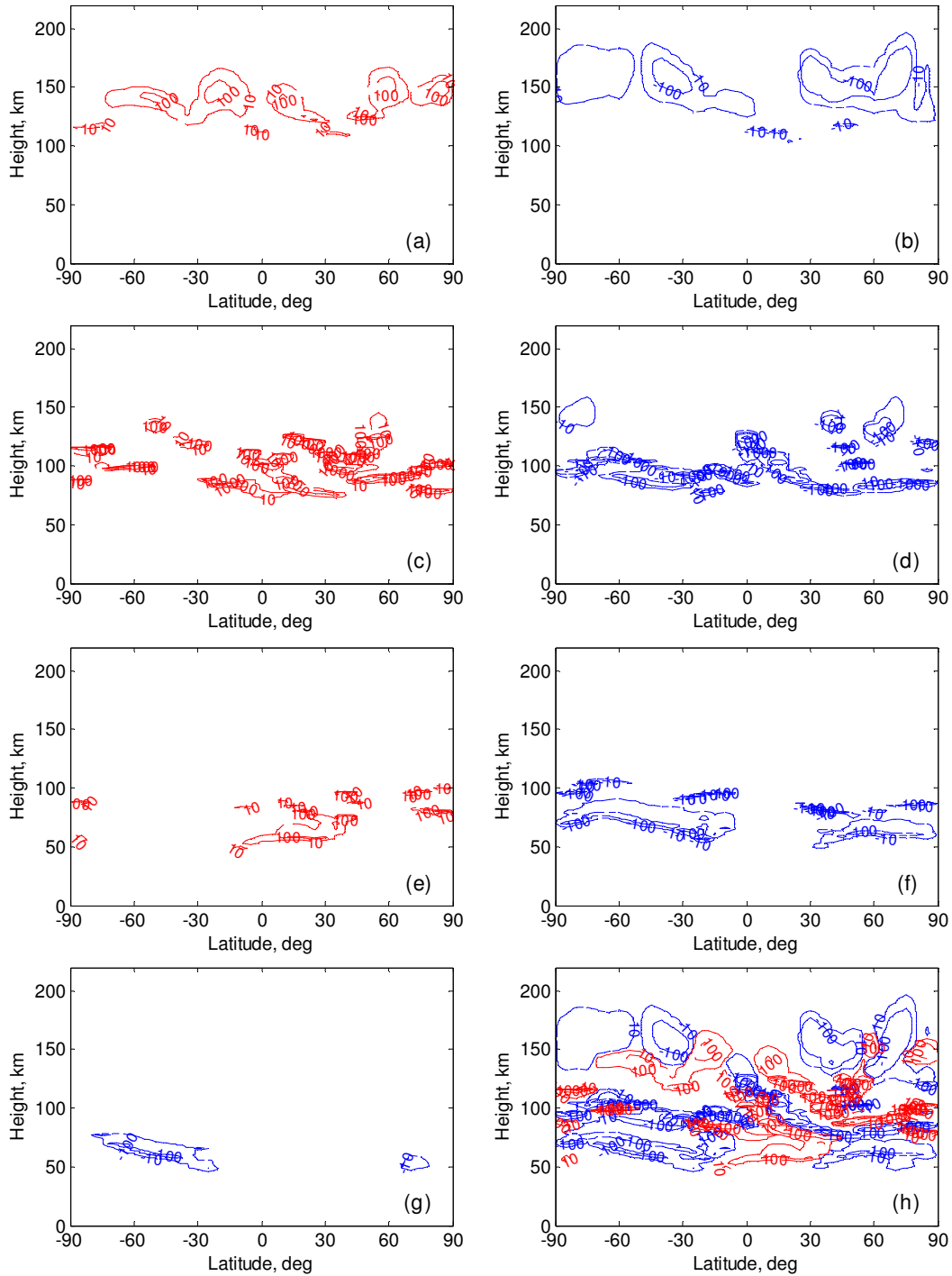
Figure C.12: Gravity wave acceleration (m s^{-1} sol^{-1}) of the zonal mean flow for L_s = 270° and spectral index p = 5/3 with phase speed distribution (a) 80 m s^{-1}, (b) -80 m s^{-1}, (c) 60 m s^{-1}, (d) -60 m s^{-1}, (e) 40 m s^{-1}, (f) -40 m s^{-1}, (g) 20 m s^{-1}, (h) -20 m s^{-1}, and 0 m s^{-1} (not shown). Westward momentum flux at the source level was 3 times greater than eastward momentum flux. Red (blue) contour lines depict eastward (westward) acceleration.
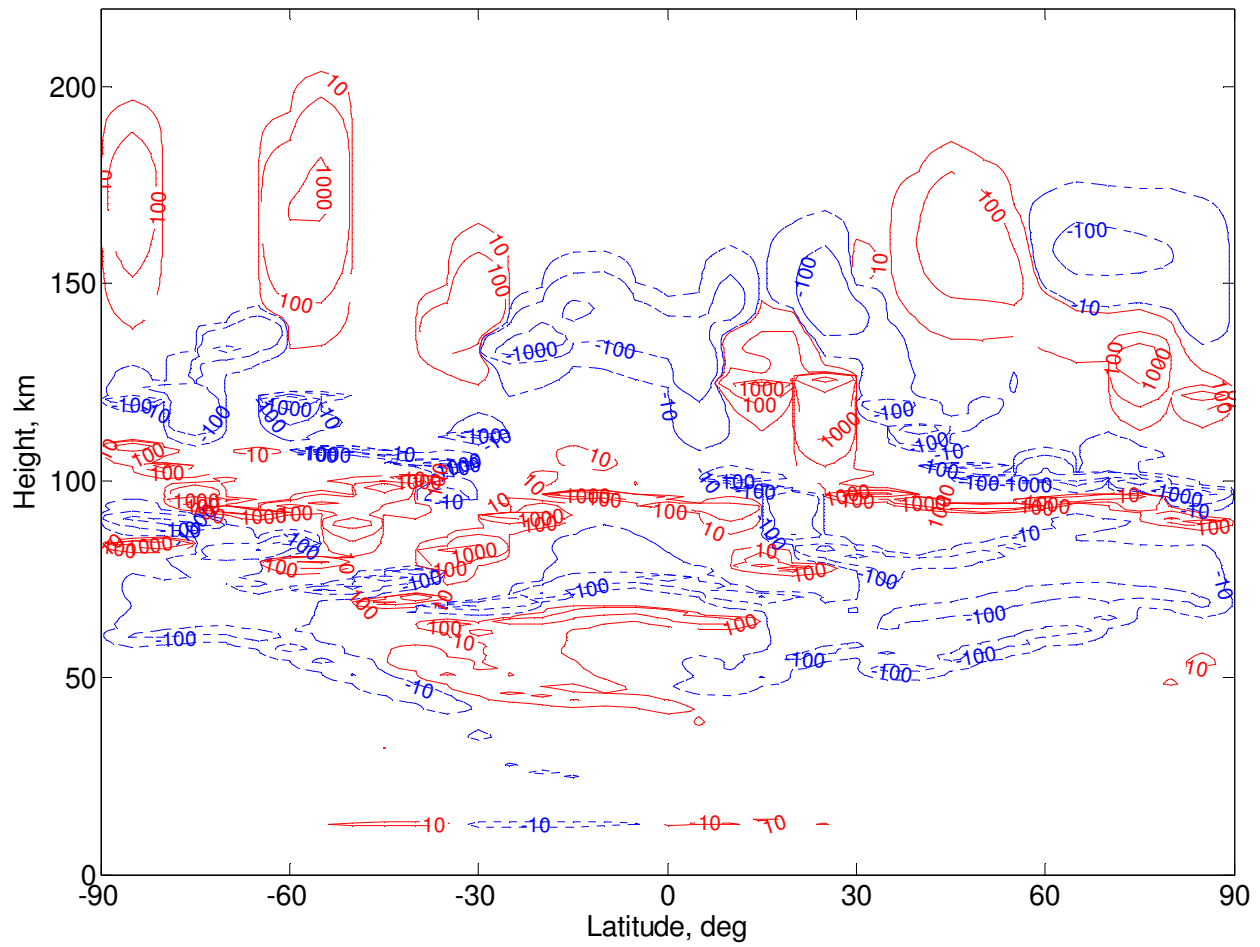
Figure C.13: Gravity wave acceleration (m s^{-1} sol^{-1}) of the zonal mean flow for $L_s = 0°$ and spectral index $p = 5/3$ with phase speed distribution -60, -40, -20, 0, 20, 40, and 60 m s^{-1}. Red (blue) contour lines depict eastward (westward) acceleration.
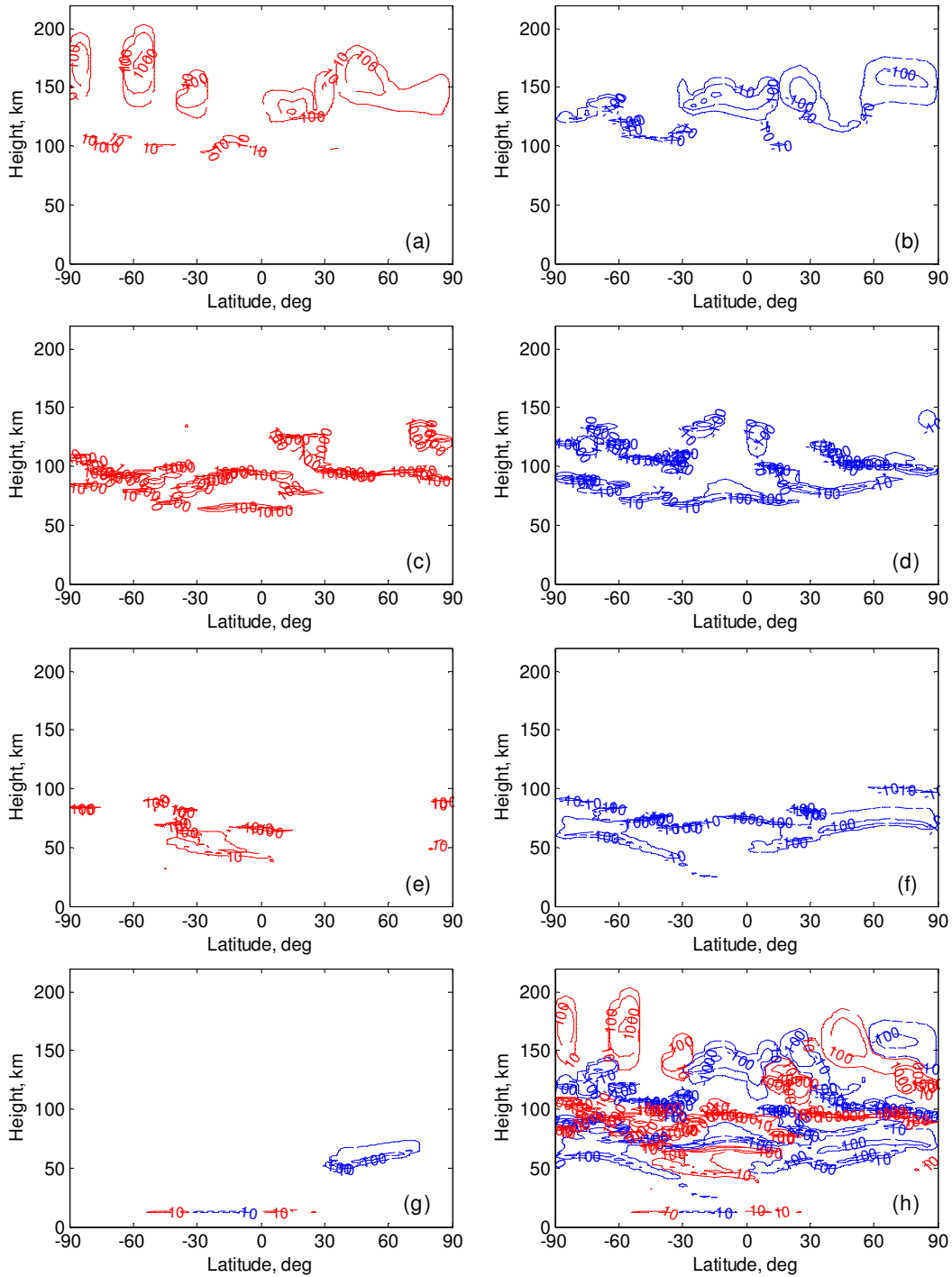
Figure C.14: Gravity wave acceleration (m s^{-1} sol^{-1}) of the zonal mean flow for $L_s = 0°$ and spectral index $p = 5/3$ with phase speed distribution (a) 60 m s^{-1}, (b) -60 m s^{-1}, (c) 40 m s^{-1}, (d) -40 m s^{-1}, (e) 20 m s^{-1}, (f) -20 m s^{-1}, (g) 0 m s^{-1}, and (h) all phase speeds. Red (blue) contour lines depict eastward (westward) acceleration.

Figure C.15: Gravity wave acceleration (m s^{-1} sol^{-1}) of the zonal mean flow for L_s = 180° and spectral index p = 5/3 with phase speed distribution -60, -40, -20, 0, 20, 40, and 60 m s^{-1}. Red (blue) contour lines depict eastward (westward) acceleration.

Figure C.16: Gravity wave acceleration (m s^{-1} sol^{-1}) of the zonal mean flow for L_s = 180° and spectral index p = 5/3 with phase speed distribution (a) 60 m s^{-1}, (b) -60 m s^{-1}, (c) 40 m s^{-1}, (d) -40 m s^{-1}, (e) 20 m s^{-1}, (f) -20 m s^{-1}, (g) 0 m s^{-1}, and (h) all phase speeds. Red (blue) contour lines depict eastward (westward) acceleration.
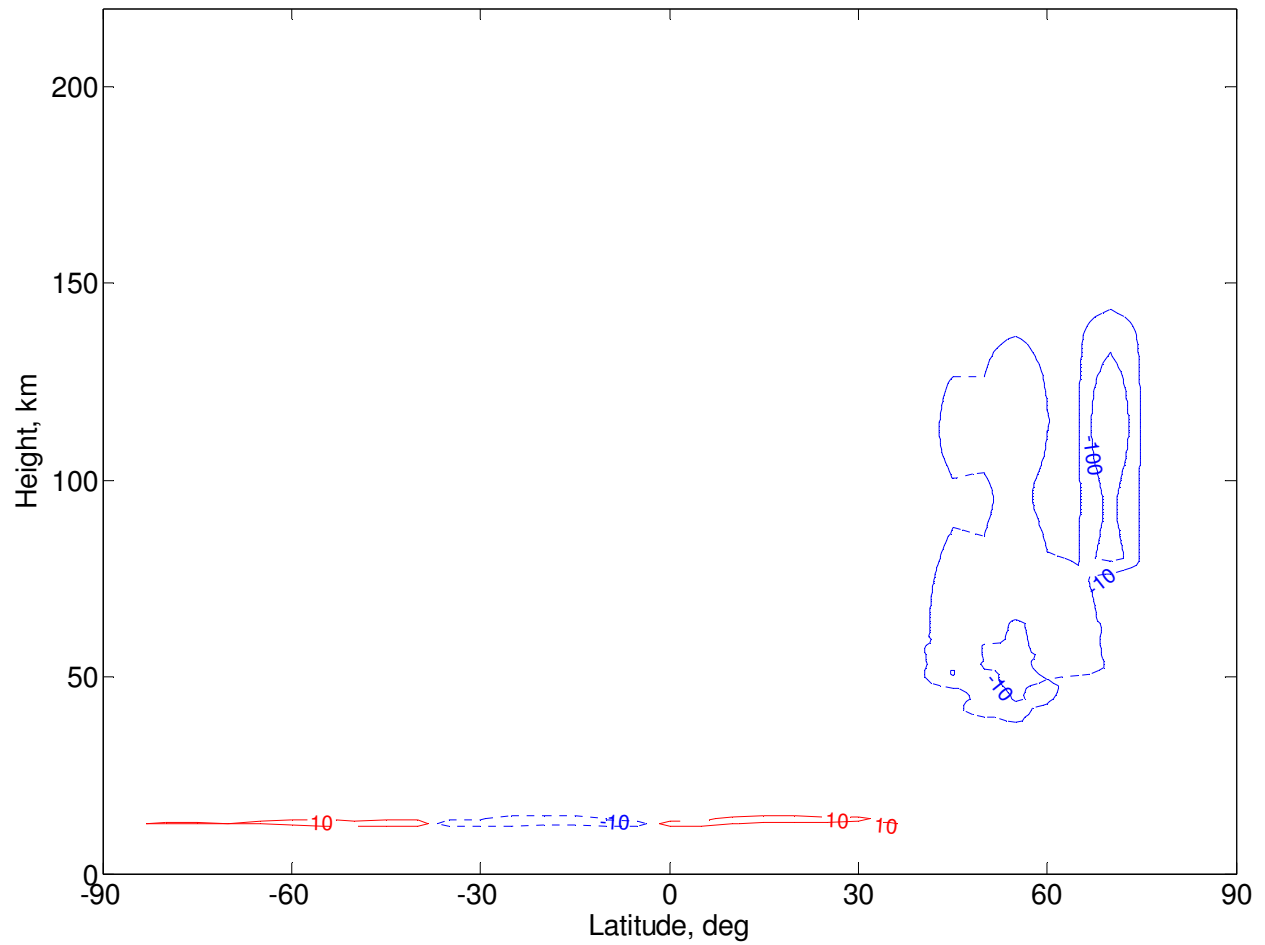
Figure C.17: Gravity wave acceleration (m s^{-1} sol^{-1}) of the zonal mean flow for $L_s = 180°$ and spectral index $p = 5/3$ with phase speed $c = 0$ m s^{-1}. Red (blue) contour lines depict eastward (westward) acceleration.
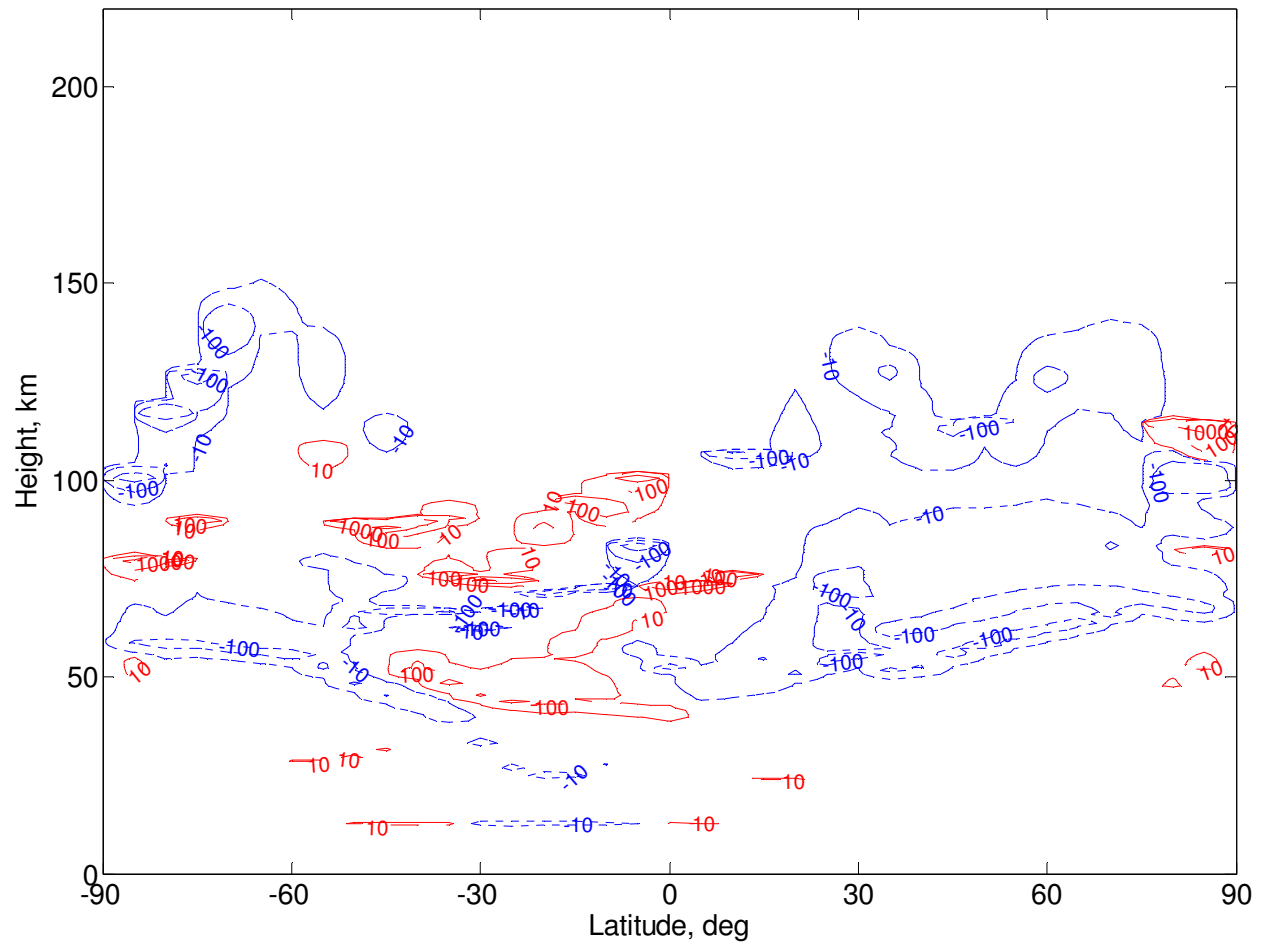
Figure C.18: Gravity wave acceleration (m s^{-1} sol^{-1}) of the zonal mean flow for L_s = 180° and spectral index p = 5/3 with phase speed distribution -20, 0, and 20 m s^{-1}. Red (blue) contour lines depict eastward (westward) acceleration.
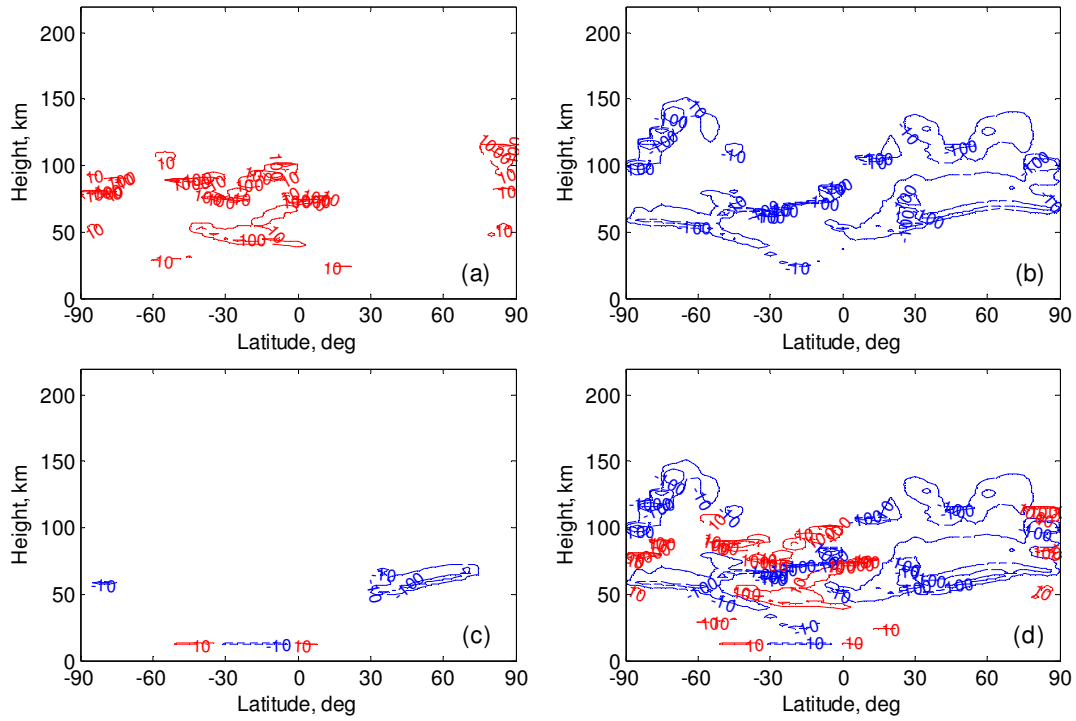
Figure C.19: Gravity wave acceleration (m s^{-1} sol^{-1}) of the zonal mean flow for L_s = 180° and spectral index p = 5/3 with phase speed distribution (a) 20 m s^{-1}, (b) -20 m s^{-1}, (c) 0 m s^{-1}, and (d) all phase speeds. Red (blue) contour lines depict eastward (westward) acceleration.